

**SELECTIVE CONVERSION OF BIOMASS MODEL COMPOUNDS
USING PROMOTED METAL CATALYSTS**

Cong Wang

A DISSERTATION

in

Chemical and Biomolecular Engineering

Presented to the Faculties of the University of Pennsylvania

in

Partial Fulfillment of the Requirements for the

Degree of Doctor of Philosophy

2019

Supervisor of Dissertation

Raymond J. Gorte,

Russell Pearce and Elizabeth Crimian Heuer Professor, CBE, MSE

Graduate Group Chairperson

John C. Crocker,

Professor, CBE

Dissertation Committee

John M. Vohs, Carl V. S. Patterson Professor and Chair, CBE, MSE

Aleksandra Vojvodic, Skirkanich Assistant Professor of Innovation, CBE

Bingjun Xu, Assistant Professor, Chemical Engineering, University of Delaware

ACKNOWLEDGMENTS

First and foremost, I would like to sincerely thank my advisor, Prof. Raymond Gorte, for the advice, guidance and support he has provided me in the past four years. It goes without saying that our project owes a major part of success to his expertise, judgment and experience. I am also indebted to my senior mentors, Dr. Jing Luo and Dr. Matteo Monai, for the attentive training, as well as to my collaborators from the Vohs Group and the Murray Group at the University of Pennsylvania and the Vlachos Group and the Caratzoulas Group at the University of Delaware for the generosity of sharing their expertise in surface science, catalyst synthesis and theory. This project would not have been possible without their proficiency. I also wanted to thank all my colleagues, friends in our lab for sharing their knowledge, happiness and everything that makes me proud of being one part of this great research team. Lastly, I am incredibly blessed to have my amazing family - my wife Peidi, son Mason, and parents Fujun and Jinghui. Without their love and support in my life, I would not be who I am or where I am today.

ABSTRACT

SELECTIVE CONVERSION OF BIOMASS MODEL COMPOUNDS USING PROMOTED METAL CATALYSTS

Cong Wang

Raymond J. Gorte

Extensive research and development have gone into modern biomass upgrading in order to mitigate the environmental concerns and other impending challenges associated with conventional fuels and chemicals. The phenolic and furanic compounds produced by primary upgrading processes represent a collection of biomass intermediates that still preserve the valuable chemical structures, but they require further upgrading due to unfavorable oxygen contents and unstable functional groups. This dissertation seeks to demonstrate the viability of utilizing bimetallic and metal-oxide-promoted metal catalysts to further upgrade biomass-derived oxygenates by selective C-O bond scissions. Useful fuels and chemicals are produced from model compounds (2-hydroxymethylfurfural, furfural, tetrahydrofurfuryl alcohol and *m*-cresol) which represent the main fractions of lignocellulosic biomass. In all studies featured in this thesis, promoted metal catalysts exhibit special activity, selectivity and stability to produce desired products, even though the individual components are not active, selective or stable. In order to bridge the gap between these enhanced catalytic performances and their mechanistic fundamentals, well-defined catalysts synthesized by either solvothermal method (for bimetallic nanocrystals)

or atomic layer deposition (for metal-oxide-promoted metal catalysts) were also used to characterize the structure-activity relationships. Notably, I will demonstrate in this dissertation that the active form of the Pt-WO_x catalyst exists as a thin, submonolayer film of the oxide on the Pt surface. Direct bonding between the Pt and supported WO_x complexes both stabilizes the oxide and lowers the barrier to oxygen vacancy formation. The latter plays a pivotal role in the formation of redox sites on the WO_x which are active for direct C-O bond hydrogenolysis. These contributions from the fundamentals should help developing catalysts that are suitable for practical applications.

TABLE OF CONTENTS

ACKNOWLEDGMENTS	II
ABSTRACT.....	III
TABLE OF CONTENTS	V
LIST OF TABLES	XI
LIST OF FIGURES	XIV
CHAPTER 1. INTRODUCTION	1
1.1 Background	1
<i>1.1.1 Biomass – the momentum to leverage the future energy structure.....</i>	<i>1</i>
<i>1.1.2 Lignocellulose – the most promising biomass for upgrades</i>	<i>2</i>
<i>1.1.3 Primary upgrades of lignocellulosic biomass</i>	<i>4</i>
1.2 Upgrades for biomass model compounds	6
<i>1.2.1 C-O bond chemistry – the avenue towards useful fuels and chemicals... 6</i>	
<i>1.2.2 Hydrodeoxygenation..... 9</i>	
<i>1.2.3 Ring-opening reactions..... 14</i>	
1.3 Thesis Outline	16
CHAPTER 2. EXPERIMENTAL METHODS	20
Summary	20
2.1 Reactor Design and Reactivity Measurements	20
<i>2.1.1 Three-phase Continuous Flow Reactor..... 21</i>	

2.1.2	<i>Gas-phase Continuous Flow Reactor</i>	23
2.2	Catalyst Preparation	24
2.2.1	<i>Incipient Wetness Impregnation</i>	24
2.2.2	<i>Well-defined Nano-crystals (NCs)</i>	26
2.2.3	<i>Atomic Layer Deposition (ALD)</i>	27
2.3	Characterization Techniques	29
2.3.1	<i>TPD-TGA Measurement</i>	29
2.3.2	<i>Other Characterization Techniques</i>	31
CHAPTER 3. UNRAVELING THE SURFACE STATE AND COMPOSITION OF HIGHLY SELECTIVE NANOCRYSTALLINE NI-CU ALLOY CATALYSTS FOR HYDRODEOXYGENATION OF HMF		33
	Summary	33
3.1	Introduction	34
3.2	Experimental	36
3.2.1	<i>Catalyst synthesis</i>	36
3.2.2	<i>Catalyst characterization</i>	36
3.3	Results	38
3.3.1	<i>Nanocrystal catalyst characterization</i>	38
3.3.2	<i>HDO studies</i>	43
3.3.3	<i>Reaction of DMF</i>	50

3.4	Discussion	52
CHAPTER 4. A COMPARISON OF FURFURAL HYDRODEOXYGENATION OVER PT-CO AND NI-FE CATALYSTS AT HIGH AND LOW H₂ PRESSURES ...		55
	Summary	55
4.1	Introduction	55
4.2	Experimental	58
	4.2.1 <i>Catalyst Synthesis</i>	58
	4.2.2 <i>Reactivity Measurements and Catalyst Characterization</i>	59
4.3	Results	61
	4.3.1 <i>HDO of Furfural at 1 Bar</i>	61
	4.3.2 <i>HDO of Furfural at 33 Bar</i>	67
4.4	Discussion	74
CHAPTER 5. A STUDY OF TETRAHYDROFURFURYL ALCOHOL TO 1,5- PENTANEDIOL OVER PT-WO_x/C		76
	Summary	76
5.1	Introduction	76
5.2	Experimental	78
	5.2.1 <i>Catalyst Synthesis</i>	78
	5.2.2 <i>Reactivity Measurements and Catalyst Characterization</i>	80

5.3	Results	82
	5.3.1 <i>Ring-opening of THFA over M^I-M^2O_x/C</i>	82
	5.3.2 <i>Ring-opening of THFA over ALD-prepared Pt-WO_x NCs</i>	91
5.4	Discussion	92

CHAPTER 6. MECHANISTIC STUDY OF THE DIRECT HYDRODEOXYGENATION OF M-CRESOL OVER WO_x -DECORATED PT/C CATALYSTS 95

	Summary	95
6.1	Introduction.....	96
6.2	Experimental	98
	6.2.1 <i>Catalyst Synthesis and Characterization</i>	98
	6.2.2 <i>Reactivity Measurements and Catalyst Characterization</i>	98
	6.2.3 <i>Theoretical Approaches</i>	99
6.3	Results	101
	6.3.1 <i>Reactivity Studies</i>	101
	6.3.2 <i>Additional Catalyst Characterization</i>	110
	6.3.3 <i>Computational Studies</i>	113
6.4	Discussion	119

CHAPTER 7. HYDRODEOXYGENATION OF M-CRESOL OVER PT- WO_x /C USING H_2 GENERATED IN-SITU BY N-HEXANE DEHYDROGENATION.... 125

Summary	125
7.1 Introduction	126
7.2 Experimental	128
7.2.1 <i>Catalyst synthesis</i>	128
7.2.2 <i>Reactivity study</i>	129
7.3 Results	129
7.4 Discussion	135
CHAPTER 8. A CHARACTERIZATION STUDY OF REACTIVE SITES IN ALD-SYNTHESIZED WO_x/ZRO₂ CATALYSTS	138
Summary	138
8.1 Introduction	138
8.2 Experimental	141
8.2.1 <i>Catalyst Synthesis</i>	141
8.2.2 <i>Catalyst Characterization</i>	142
8.3 Results	143
8.3.1 <i>Characterization of ALD-prepared W-Zr</i>	143
8.3.2 <i>Reactive sites on ALD-prepared W-Zr</i>	150
8.4 Discussion	159

CHAPTER 9. H-D EXCHANGE OF SIMPLE AROMATICS AS A MEASURE OF BRØNSTED-ACID SITE STRENGTHS IN SOLIDS.....	164
Summary	164
9.1 Introduction.....	164
9.2 Experimental	167
9.2.1 <i>Catalyst Synthesis and Characterization</i>	167
9.2.2 <i>Theoretical Approaches</i>	169
9.3 Results.....	170
9.3.1 <i>TPD-TGA Measurements</i>	170
9.3.2 <i>Steady-State Reaction Measurements</i>	174
9.3.3 <i>DFT calculations</i>	179
9.4 Discussion	181
CHAPTER 10. CONCLUSIONS.....	184
BIBLIOGRAPHY	189

LIST OF TABLES

Table 2.1 A listing of IMP-prepared catalysts that have been reported in this thesis.....	24
Table 3.1 XPS results summary. The relative contributions are calculated with respect to the whole area of the Ni 2p _{3/2} or Cu 2p _{3/2} region (100 %). The Ni:Cu ratio is calculated by integrating the area of Ni 2p _{3/2} corrected for the photoionization cross-section divided by the Cu 2p _{3/2} area, corrected in the same way.....	42
Table 3.2 B and D group product distribution for HDO of HMF over 10-wt% Ni/C in 1-propanol, under 180 °C and 33 bar. (Yield %).....	45
Table 3.3 B and D group product distribution for HDO of HMF over 10-wt% impregnated NiCu/C in 1-propanol, under 180 °C and 33 bar. (Yield %).....	47
Table 4.1 Conversion and product yields for HDO of furfural ^a over carbon-supported, 10-wt% catalysts at 1 bar at the highest space times.....	63
Table 4.2 Conversion and product yields for HDO of furfural ^a over carbon-supported, 10-wt% catalysts at 33 bar at the highest space times.....	71
Table 5.1 A listing of M ¹ -M ² O _x /C catalysts and their precursors used in this study.....	78
Table 5.2 Detail conversion and selectivity for THFA hydrogenolysis over 10-wt% Pt/C, 6.3-wt% WO _x /C, and 10-wt% M ¹ -M ² O _x /C (1:0.5).....	84
Table 5.3 Redox data for the pulse-reactor measurements performed at 473 K using CO-O ₂ pulses over the as-prepared samples. While WO _x /C alone cannot be reduced under this condition, WO _x with the presence of Pt can be reduced to an averaged	

valence of ~5.1. Atomic oxygen released on as-prepared Pt/C catalyst is due to the reduction of surface PtO ₂	90
Table 6.1 Metal dispersions for carbon supported catalysts after 573K reduction, assuming CO/Pt = 1. Conversion and selectivity for high-pressure HDO reaction of <i>m</i> -cresol. Reaction conditions: 573 K, 36 bar, 2-mol% <i>m</i> -cresol/dodecane solution, WHSV = 0.6 hr ⁻¹	112
Table 6.2 Concerted C-O scission DFT energies on various catalyst surfaces. BHMF stands for 2,5-bis(hydroxymethyl) furan, HMMF - 2-hydroxymethyl-5-methyl furan, TOL – toluene, O* - surface oxygen, V – oxygen vacancy. B1 and B3 refer to corresponding structures in Figure 6.10.	117
Table 6.3 Conversion and selectivity for high-pressure HDO reaction of <i>m</i> -cresol, anisole and guaiacol over Pt-WO _x /C and Pt/C catalysts. Reaction conditions: 623K, 36 bar, 2-mol% reagent/dodecane solution, WHSV = 0.6 hr ⁻¹	124
Table 7.1 Equilibrium conversions of <i>n</i> -hexane at 773 K and a range of total pressures. Data obtained from ASPEN PLUS™ using the Peng-Robinson equation of state.	134
Table 7.2 Selectivities for DHY reaction of <i>n</i> -hexane in the tandem reactions of <i>m</i> -cresol HDO using <i>n</i> -hexane as H-donor at 673 K and 36 bar. Reagent concentration: 5.7-mol% <i>m</i> -cresol/ <i>n</i> -hexane; space time = 1 min·gcat·mL ⁻¹ . Data obtained at 3 h on stream.	135

Table 8.1 Weight gain, surface area, and calculated layer thickness for W-Zr and W-Si materials. The layer thickness was calculated using a WO_3 density of 7.16 g/cm^3 . The nomenclature $x\text{W-Zr}$ is used to refer to a sample exposed to x ALD cycles.	144
Table 8.2 Reaction site densities determined from the desorption features of 2-propanamine TPD, determined as described in the text. W/B = number of W atoms per Brønsted site.....	155
Table 9.1 A summary of strong Brønsted-site densities (determined by TPD-TGA of 2-propanamine) and onset temperatures for H-D exchange of toluene and chlorobenzene on the samples tested in this study.....	168

LIST OF FIGURES

Figure 1.1 Structure of lignocellulosic biomass with cellulose, hemicellulose, and lignin represented (adapted from ref. [14]).	3
Figure 1.2 Current processing techniques for primary upgrading of lignocellulosic biomass (adapted from ref. [14,20]).....	4
Figure 1.3 Catalytic pathways for the conversion of 2-hydroxymethylfurfural. Reprinted from ref. [30], with permission from Informa plc.....	8
Figure 1.4 Reaction network for HMF hydrodeoxygenation using alcohols as solvent. Reprinted from ref. [38], with permission from Elsevier.	11
Figure 1.5 Different mechanisms proposed for the HDO reaction of phenolic compounds with <i>m</i> -cresol as an example. Direct hydrogenolysis mechanisms; (right) mechanism involving a keto tautomer. Reprinted with permission from ref. [81]. Copyright (2015) American Chemical Society.....	13
Figure 1.6 Proposed mechanism of THFA hydrogenolysis over Rh-ReO _x /SiO ₂ . Reprinted from ref. [96], with permission from Elsevier.	15
Figure 2.1 Schematic diagram of three-phase continuous flow reactor.....	22
Figure 2.2 Schematic diagram of gas-phase continuous flow reactor with two feeding alternatives using a bubbler or a syringe pump.....	24
Figure 2.3 Cartoon depicting the stages of nucleation and growth for the preparation of monodisperse NCs with the following steps of deposition and ligand removal.	

Adapted from ref. [104], with permission from Annual Reviews. TEM image of Pt₃Co₂ NCs/C was used as an example. Adapted with permission from ref. [45]. Copyright (2016) American Chemical Society..... 26

Figure 2.4 Schematic of one ALD cycle in a pore structure. (a) Introduction of precursor molecules and adsorption on the surface; (b) purge of the unreacted precursor molecules and reaction products; (c) introduction of ligand removal reactants, which react with the chemisorbed precursor molecules; and (d) purge of the excess reactants and reaction products. This schematic is an example of an ideal ALD process for TiO₂ deposition using the TiCl₄/H₂O system. Reprinted from ref. [108]..... 28

Figure 2.5 Schematic diagram of TPD-TGA system..... 30

Figure 3.1 The TEM images of (a) NiCu and (d) NiCu₃ and their corresponding size distributions (b and e) and diffraction patterns (c and f). The powder X-ray diffraction patterns are shown in (g), with pure Cu and Ni patterns included. Scale bars are 100 nm. Model colors: light blue = Cu atoms, green = Ni atoms. 39

Figure 3.2 SEM micrographs of graphite supported Ni-Cu nanoparticles. (A) NiCu nanoparticles after deposition and (B) NiCu nanoparticles after plasma treatment and annealing to 700 °C. (C) NiCu₃ nanoparticles after deposition and (D) NiCu₃ nanoparticles after plasma treatment and annealing to 700 °C. The size of the

images is $1 \times 1 \mu\text{m}^2$. Model colors: light blue = Cu atoms, green = Ni atoms, red = oxygen atoms. 40

Figure 3.3 NAP-XPS spectra of Cu 2p and Ni 2p core levels of NiCu and NiCu₃ nanoparticles measured in UHV and under 1 mbar of H₂ at 250 °C. The spectra are normalized to the metallic Cu 2p_{3/2} signal and offset for clarity. XPS colors: light blue = Cu (0), green = Ni (0), red = oxidized metals, grey = satellite signals; model colors: light blue = Cu atoms, green = Ni atoms, red= oxygen atoms.. 41

Figure 3.4 Reaction network for HDO of HMF using alcohols as solvent..... 44

Figure 3.5 Conversion and product yield for the HDO reaction of HMF over 10-wt% impregnated (a) Ni/C, (b) Cu/C, as a function of reactor space time. Reaction conditions: 33 bar and 180 °C. (▼) HMF conversion, (▲) product group B, (●) DMF, (■) product group D, (◄) 5-methyl furfural (MF), (◆) 2,5-bis(propoxymethyl) furan (BEF), (×) 2-hydroxymethyl-5-methyl furan (HMMF)..... 45

Figure 3.6 Conversion and product distribution for the HDO reaction of HMF over 10-wt% (a) IMP NiCu/C, (b) IMP NiCu₃/C, as a function of reactor space time. Reaction conditions: 33 bar and 180 °C. (▼) HMF conversion, (▲) product group B, (●) DMF, (■) product group D. 47

Figure 3.7 Conversion and product distribution for the HDO reaction of HMF over 10-wt% (a) NCs NiCu/C, (b) NCs NiCu₃/C, as a function of reactor space time. Reaction

conditions: 33 bar and 180 °C. (▼) HMF conversion, (▲) product group B, (●) DMF, (■) product group D.	49
Figure 3.8 The size distributions of (a) NiCu and (b) NiCu ₃ before (black) and after (red) catalytic reactions.....	50
Figure 3.9 Conversion and product distribution for the reaction of DMF over 10-wt% (a) IMP NiCu/C, (b) IMP NiCu ₃ /C, (c) NCs NiCu/C, (d) NCs NiCu ₃ /C, as a function of space time. Reaction conditions: 33 bar and 180 °C. (▼) DMF conversion, (□) DMTHF, (▽) 2-hexanone, (△) 2,5-hexandione.....	51
Figure 4.1 TEM images of 10-wt% impregnated NiFe/C: (a) as-prepared; (b) after HDO reaction with furfural at 1 bar; and (c) after reaction at a pressure of 33 bar. The scale bars are 50 nm.	60
Figure 4.2 TEM images of 10-wt% PtCo ₃ /C: (a) as-prepared; (b) after HDO reaction with furfural at 1 bar; and (c) after reaction at a pressure of 33 bar. The scale bars are 50 nm. The average sizes and size distributions were presented as (diameter) ± (standard deviation) nm.	61
Figure 4.3 Conversion and product distributions for HDO of furfural over 10-wt% impregnated (a) Ni/C and (b) NiFe/C as a function of reactor space time (mass of catalyst divided by mass flow rate of furfural and H ₂). Reaction condition: 180 °C and 1 bar. (▼) furfural conversion; (▲) furan yield; (■) FAL yield; (●) MF yield; (◆) over-hydrogenation products.	62

Figure 4.4 Conversion and product distributions for HDO of furfural over 10-wt% impregnated (a) Pt/C; and (b) NCs PtCo₃/C as a function of reactor space time (mass of catalyst divided by mass flow rate of furfural and H₂). Reaction condition: 180 °C and 1 bar. (▼) furfural conversion; (▲) furan yield; (■) FAL yield; (●) MF yield; (◆) over-hydrogenation products..... 65

Figure 4.5 Time on Stream for HDO of furfural over 10-wt% (a) impregnated Co/C; and (b) NCs PtCo₃/C as a function of reaction time. Space time: 5 min·g/g; Reaction condition: 180 °C and 1 bar. (▼) furfural conversion; (▲) furan yield; (■) FAL yield; (●) MF yield; (◆) over-hydrogenation products..... 66

Figure 4.6 Reaction network for 1-bar HDO of furfural carried by H₂. Reaction routes in gray color are suppressed by NiFe and PtCo₃ bimetallics. 66

Figure 4.7 Conversion and product distributions for HDO of furfural over 10-wt% impregnated (a) Ni/C and (b) NiFe/C as a function of reactor space time, (mass of catalyst divided volumetric flow rate of liquid feed). Reaction condition: 180 °C and 33 bar. (▼) furfural conversion; (■) FAL yield; (◆) sum of FAct and FEther yields; (●) MF yield; (◆) over-hydrogenation products..... 68

Figure 4.8 Conversion and product distributions for HDO of furfural over 10-wt% impregnated (a) Pt/C, (b) Co/C and (c) NCs PtCo₃/C as a function of reactor space time (mass of catalyst divided volumetric flow rate of liquid feed). Reaction condition: 180 °C and 33 bar. (▼) furfural conversion; (■) FAL yield;

(◆) sum of FAct and FEther yields; (●) MF yield; (◆) over-hydrogenation products..... 69

Figure 4.9 Time on Stream for HDO of furfural over 10-wt% NCs PtCo₃/C as a function of reaction time. Space time: 0.25 min·g/mL; Reaction condition: 180 °C and 33 bar. (▼) furfural conversion; (■) FAL yield; (◆) FAct and FEther yield; (●) MF yield; (◆) over hydrogenation products..... 73

Figure 4.10 Reaction network for high pressure HDO of furfural in 1-propanol solvent. R represents propyl group. Reaction routes in gray color are suppressed by NiFe and PtCo₃ bimetallics. 74

Figure 5.1 TEM images of 10-wt% Pt NCs (a) as-deposited on carbon support, (b) after 1 ALD cycle ((1R) Pt|WO_x/C) and (c) after 5 ALD cycles ((5R) Pt|WO_x/C) of WO_x. The scale bars represent 50 nm. 81

Figure 5.2 Proposed reaction scheme for THFA hydrogenolysis. Experimentally observed species: (1) tetrahydrofurfuryl alcohol (THFA); (2) 1,5-pentanediol (1,5-PeD); (3) 1-pentanol (1-PeOH); (4) tetrahydropyran (THP); (5) tetrahydro-2-pyranone (THP-2-one); (6) methyl tetrahydrofuran; (7) 2-pentanol; (8) tetrahydrofuran; (9) 1-butanol (1-BuOH); (10) 1,2-pentanediol. Reaction pathway I undergoes direct ring-opening with 1,5-PeD as an intermediate; reaction pathway II and III undergo hydrodeoxygenation (HDO) and decarbonylation (DCO) respectively prior to ring-opening; reaction pathway IV undergoes direct ring-opening. ... 83

Figure 5.3 Conversion for THFA hydrogenolysis over 10-wt% M^1 - M^2O_x/C (1:0.5) (a) Pt-based catalysts and (b) other catalysts. M^2 in Pt- $M^2O_x^*$ includes Ce, Cr, Mn, Y, Zn, Al and Co. Reaction conditions: 473 K, 36 bar, 1-wt% THFA aqueous solution, space time = 1.67 min·g/mL. 86

Figure 5.4 Selectivity for THFA hydrogenolysis over 10-wt% M^1 - M^2O_x/C (1:0.5) catalysts with detectable activities. Selectivity bars are grouped in pathway I and a sum of pathway II, III and IV. Reaction conditions: 473 K, 36 bar, 1-wt% THFA aqueous solution, space time = 1.67 min·g/mL. 87

Figure 5.5 Conversion and selectivity for THFA hydrogenolysis over 10-wt% Pt- WO_x/C (1:0.5) catalyst as a function of (a) space time at 473 K and (b) reaction temperature at space time = 1.67 min·g/mL. (▼) THFA conversion; (●) 1,5-PeD selectivity; (◆) Pathway I excl. 1,5-PeD selectivity; (■) Pathway III selectivity. Reaction conditions: 36 bar, 1-wt% THFA aqueous solution. 88

Figure 5.6 Effects of tungsten leaching on THFA hydrogenolysis over Pt and WO_x containing catalysts. (a) 10-wt% Pt- WO_x/C (1:0.5) catalyst; (b) 10-wt% Pt- WO_x/C (1:0.5) catalyst with a 30-min H_2 treatment at 773 K prior to the reaction; (c) 10-wt% Pt/C and 6.3-wt% WO_x/C physical mixture; (d) dual bed with WO_x/C upstream of Pt/C; (e) dual bed with WO_x/C upstream of Pt/C, and with a 30-min H_2 treatment at 773 K prior to the reaction; (f) 10-wt% Pt /C catalyst. Selectivity bars are grouped in pathway I and a sum of pathway II, III and IV.

Reaction conditions: 473 K, 36 bar, 1-wt% THFA aqueous solution, space time = 1.67 min·g/mL.	89
Figure 5.7 Thermodynamic calculation of the boundaries of tungsten oxides as a function of temperatures and water/hydrogen pressure ratios. (●) represents the reaction condition at 473 K and 36 bar.	90
Figure 5.8 HAADF-STEM images and EDS elemental mapping of (5R) Pt WO _x /C. The scale bars represent 10 nm.	91
Figure 5.9 Conversion and selectivity for THFA hydrogenolysis over (1R) and (5R) Pt WO _x /C catalysts. Selectivity bars are grouped in pathway I and a sum of pathways II, III and IV. Reaction conditions: 473 K, 36 bar, 1-wt% THFA aqueous solution, space time = 1.67 min·g/mL.	92
Figure 6.1 Structure optimization trajectory of W ₂ O ₆ /3-layer Pt(111) at the standard (high) level of theory. The initial cluster structure was predicted by ab initio molecular dynamics/simulated annealing at the low level of theory.	101
Figure 6.2 Reaction network for HDO of <i>m</i> -cresol. Species detected in the catalytic measurements are included. The products in grey were only observed during the 1-bar HDO reaction of pure <i>m</i> -cresol at 623K. ONE – methyl cyclohexanone; OL – methyl cyclohexanol; MCH – methyl cyclohexane; TOL – toluene; PhOH – phenol; BZ – benzene; 1 – alkyltoluenes; 2 – tolylethers; 3 – cresols; 4 – xylenols; 5 – xylenes.	102

Figure 6.3 Conversion and selectivity for high-pressure HDO reaction of <i>m</i> -cresol over Pt-WO _x /C, Pt/C and WO _x /C catalysts. Reaction conditions: 573 K, 36 bar, 2-mol% <i>m</i> -cresol/dodecane solution, WHSV = 0.6 hr ⁻¹	103
Figure 6.4 Time-on-stream experiments for high-pressure HDO reaction of <i>m</i> -cresol over (a) Pt-WO _x /C and (b) Pt/C catalyst. Reaction conditions: 573K, 36 bar, 2-mol% <i>m</i> -cresol/dodecane solution, WHSV = 0.6 hr ⁻¹ . Conversion of <i>m</i> -cresol (■); selectivity of TOL (●), MCH (▲) and the sum of ONE and OL (◆).....	105
Figure 6.5 Conversion and selectivity for 1-bar HDO reaction of pure <i>m</i> -cresol over Pt-WO _x /C and Pt/C catalysts. Reaction conditions: 623 K, 1 bar. H ₂ flow rate: 12 mL/min, WHSV = 60 hr ⁻¹	106
Figure 6.6 Conversion (■) and selectivity of toluene (●) as a function of temperature for high-pressure HDO reaction of <i>m</i> -cresol over Pt-WO _x /C catalyst. Reaction condition: 36 bar, 2-mol% <i>m</i> -cresol/dodecane solution, WHSV = 0.6 hr ⁻¹ . ..	107
Figure 6.7 High-pressure HDO reaction of (a) <i>m</i> -cresol, (b) ONE and (c) OL over Pt-WO _x /C and Pt/C catalyst. Products are grouped as hydrocarbons (HC) and oxygen-containing hydrocarbons (O-HC). Reaction conditions: 573 K, 36 bar, 2-mol% <i>m</i> -cresol/dodecane solution, WHSV = 0.6 hr ⁻¹	109
Figure 6.8 XPS spectra of the Pt(4f) and W(4f) energy regions of WO _x -decorated Pt model catalysts (a and c) before and (b and d) after exposing to <i>m</i> -cresol HDO reaction	

conditions (H ₂ plus 2-mol% <i>m</i> -cresol in dodecane, 36 bar total pressure, 573 K) for 5 h.	111
Figure 6.9 X-ray diffraction (XRD) pattern of (a) pristine Pt/C, (b) pristine Pt-WO _x /C and (c) consumed Pt-WO _x /C after exposing to <i>m</i> -cresol HDO reaction conditions (H ₂ plus 2-mol% <i>m</i> -cresol in dodecane, 36 bar total pressure, 573 K) for 5 h. XRD patterns are normalized and referenced to graphite feature (■) at 26.5°. Pt facets are labeled by ▲.	113
Figure 6.10 Simulated annealing-optimized W ₂ O ₆ (A1), W ₃ O ₉ (A2), and W ₄ O ₁₂ (A3) clusters, supported on Pt (111). (B1 – B3): partially reduced Pt (111)-W ₂ O ₅ . B1/B2 and B3 correspond to O removal at WO ₄ and WO ₃ Pt tetrahedral units, respectively.	114
Figure 6.11 Computed reaction pathway for the concerted C-O bond scission/C-H bond formation in <i>m</i> -cresol on Pt(111)-W ₂ O ₅ -B3. Energy is plotted relative to the initial state energy, set to zero.	118
Figure 6.12 Comparison of simplified reaction networks and DFT-optimized adsorption structures for HDO reaction of <i>m</i> -cresol over Pt/C and Pt-WO _x /C catalysts.	121
Figure 7.1 Reaction scheme for the tandem reactions of <i>m</i> -cresol HDO using <i>n</i> -hexane as H-donor.	128
Figure 7.2 Reaction rates for high pressure tandem reactions of HDO of <i>m</i> -cresol (■) and DHY of <i>n</i> -hexane (■) over Pt-WO _x /C, Pt/C and WO _x /C catalysts at 673 K and	

36 bar. The corresponding conversions are tabulated. Red dash line indicates equilibrium conversion (1%) of <i>n</i> -hexane determined by repeated experiments. Reagent concentration: 5.7-mol% <i>m</i> -cresol/ <i>n</i> -hexane; space time = 1 min·g _{cat} ·mL ⁻¹ . Data obtained at 3 h on stream.....	130
Figure 7.3 (a) Conversions and (b) reaction rates for high pressure tandem reactions of HDO of <i>m</i> -cresol (■) and DHY of <i>n</i> -hexane (●) as a function of space time at 673 K and 36 bar. Reagent concentration: 5.7-mol% <i>m</i> -cresol/ <i>n</i> -hexane. Data obtained at 3 h on stream.	131
Figure 7.4 Time evolution for the HDO reaction rate over Pt-WO _x /C at 673 K and 36 bar using 5.7-mol% (■) and 19.8-mol% (▲) <i>m</i> -cresol/ <i>n</i> -hexane solutions. space time = 1 min·g _{cat} ·mL ⁻¹	133
Figure 7.5 Time evolution for the conversions of the DHY reaction of <i>n</i> -hexane over Pt/C catalyst at 773 K and under total pressures of 1 bar (■), 8 bar (▲), 21 bar (◆), and 36 bar (●). Reaction condition: pure <i>n</i> -hexane feed, space time = 0.25 min·g _{cat} ·mL ⁻¹	134
Figure 7.6 Proposed reaction mechanism for the tandem reactions of <i>m</i> -cresol HDO using <i>n</i> -hexane as H-donor.	137
Figure 8.1 XRD patterns for (a) ZrO ₂ , (b) 5W-Zr (5 ALD cycles), and (c) 40W-Zr (40 ALD cycles). Monoclinic phase (■); tetragonal phase (◆).....	144

Figure 8.2 BF (Bright-Field) scanning transmission electron microscopy (STEM) image and energy-dispersive spectroscopy (EDS) elemental mapping of the 40W-Zr sample. The scale bars represent 20 nm.	146
Figure 8.3 Raman spectra of (a) ZrO ₂ , (b) impW-Zr (10-wt% WO _x), and (c) 5W-Zr samples under ambient conditions.	148
Figure 8.4 TPD-TGA of 2-propanol over (a) ZrO ₂ , (b) 5W-Zr, and (c) impW-Zr. The desorption features correspond to propene ($m/e = 41$) and unreacted 2-propanol ($m/e = 45$). The graphic symbols are a schematic of the WO _x (purple) over the ZrO ₂ support (gray).	149
Figure 8.5 FTIR spectra of pyridine adsorbed on (a) ZrO ₂ and (b) 5W-Zr. The samples were pretreated with helium at 373 K before pyridine was adsorbed onto the samples at room temperature.	150
Figure 8.6 A summary of reaction pathways for the conversion of 2-propanamine on the WO _x /ZrO ₂ samples observed in the TPD-TGA measurements.	151
Figure 8.7 TPD-TGA of 2-propanamine over (a) ZrO ₂ , (b) 5W-Zr, (c) impW-Zr, and (d) 20W-Zr. The desorption features correspond to hydrogen ($m/e = 2$), ammonia ($m/e = 17$), a mixture of butenes and acetonitrile ($m/e = 41$), acetone ($m/e = 43$), propene ($m/e = 41$ and 42), and unreacted 2-propanamine ($m/e = 44$).	154

Figure 8.8 TPD-TGA of 1- propanamine over ZrO₂. The desorption features correspond to hydrogen (m/e = 2), unreacted 1-propylamine (m/e = 30) and propionitrile (m/e = 54). The graphic symbols represent schematic ZrO₂ support (gray). 154

Figure 8.9 Reaction site densities of (▲) dehydrogenation sites, (●) Brønsted sites, and (■) oxidation sites as a function of the number of WO_x ALD cycles. 157

Figure 8.10 The 2-propanol conversions on *x*W-Zr (where *x* is the number of ALD cycles) samples for the steady-state dehydration reaction at 403 K. Reaction conditions: 2-propanol WHSV = 0.40 h⁻¹. 158

Figure 8.11 Conversions for H - D exchange of toluene (in red) and chlorobenzene (in blue) on (●) 5W-Zr and (■) H-ZSM-5 (280) as a function of temperature. The Brønsted-site densities for both materials were 80 μmol/g. Reaction conditions: 100 mg of catalyst, 1% toluene/chlorobenzene, and 1% D₂O in 20 mL/min He. 159

Figure 9.1 TPD-TGA of toluene-h₈ over deuterated (a) H-[Al]ZSM-5(50), (b) H-[Fe]ZSM-5, and (c) P-SPP. 172

Figure 9.2 TPD-TGA of chlorobenzene-h₅ over deuterated (a) H-[Al]ZSM-5(50) and (b) H-[Fe]ZSM-5. 174

Figure 9.3 Onset-of-reaction temperatures for steady-state H-D exchange between toluene-h₈ and D₂O in a continuous flow reactor over a series of MFI-structured zeolites. 10% conversion of H-D exchange was observed on each material at the

highlighted temperature. Reaction conditions: 100-mg catalyst, 1% toluene-h₈ and 1% D₂O in a 20-mL/min He flow. 176

Figure 9.4 Onset-of-reaction temperatures for steady-state H-D exchange between toluene-h₈ and D₂O in a continuous flow reactor over 5W-Zr, P-SPP, ZrO₂, and Al₂O₃. 10% conversion of H-D exchange was observed on each material at the highlighted temperatures. Reaction conditions: 100-mg catalyst, 1% toluene-h₈ and 1% D₂O in a 20-mL/min He flow. 177

Figure 9.5 Onset-of-reaction temperatures for steady-state H-D exchange between chlorobenzene-h₅ and D₂O in a continuous flow reactor. 10% conversion of H-D exchange was observed on each material at the highlighted temperature. Reaction conditions: 100-mg catalyst, 1% chlorobenzene-h₅ and 1% D₂O in a 20-mL/min He flow. 178

Figure 9.6 Free energy profiles of the H-D exchange reaction between deuterated H-[Al]ZSM-5 and toluene at the *para* (red line) and *meta* (blue line) positions, at 60 °C. The zero-energy reference is gas-phase toluene at infinite separation from deuterated H-[Al]ZSM-5. The reaction follows the two-step mechanism via the Wheland intermediate. 180

Figure 9.7 Transition state geometry of deuterium cation transfer from the D-[Al]ZSM-5 active site to the *para* position of toluene. The deuterium-donor/acceptor distances are shown in Å. For clarity, only toluene and the active site atoms are

shown in the ball-and-stick representation; the rest of the system is shown in the wireframe representation. Color codes: pink, Al; red, O; white, H; grey, C. 181

CHAPTER 1. INTRODUCTION

1.1 Background

1.1.1 *Biomass – the momentum to leverage the future energy structure*

Biomass is a renewable, plant-based energy source that contributes to an estimated 10 to 15% of the worldwide energy consumption worldwide. Unlike other forms of sustainable energy that will not likely contribute until the second half of the 20th century, there has been a long history of using the captured energy in plants. In the past, photosynthesized energy was mainly collected through uncontrolled thermal activation (e.g. fire) and natural biochemical reactions (e.g. livestock), which, unfortunately, have a very low efficiency.

More recently, environmental concerns and other impending challenges associated with fossil fuels have received growing attention. These challenges have led to extensive research and development into alternative, cleaner production technologies. Modern biomass upgrading has been subsequently identified as an important approach to complement conventional energy and chemicals production from petroleum, coal, and natural gas [1–7]. The advantages of this substitution are potentially very important. Bio-fuels are potentially biodegradable and non-toxic, and they have low sulfur contents and a zero greenhouse-gas (GHG) balance. Besides the environmental advantages, they could create other social benefits such as job creation, rural revitalization, *etc.* [8]. Compared to the traditional ways of using biomass as an energy source, modern processes could be much

more reliable and energy efficient, since they first convert the biomass feedstock into high performance biofuels and additives prior to combustion for heating, transportation, and electricity generation. Not surprisingly, bioenergy (excluding traditional use of biomass) accounts for roughly 50% of all renewables consumed on earth at the present time, which is equivalent to hydropower, geothermal, wind, and solar combined [9]. The critical position of biomass here makes it key resource to address the challenges associated with the diminishing fossils that we have relied on for hundreds of years.

1.1.2 Lignocellulose – the most promising biomass for upgrades

As the most bountiful polymer in nature, lignocellulosic biomass is produced on an estimated scale of 200 billion metric tons per year [10]. Unlike starch or corn, this type of biomass can come from the non-edible portion of plants, so that it does not directly compete with food production.

Depending on the plant species, lignocellulosic biomass typically consists of 33- to 51-wt% cellulose, 15- to 36-wt% hemicellulose, and 21- to 32-wt% lignin, with smaller amounts of organic extractives and inorganic compounds [11]. As is shown in Figure 1.1, cellulose is a linear, long-chain polymer that predominantly contains $\beta(1,4)$ -linked, D-glucose units with crystalline arrangements; by comparison, hemicellulose consists of more random, amorphous and branched structures; it comprises multiple pentose and hexose sugars, such as D-xylose, D-mannose, D-galactose and D-rhamnose [12]. The building units of lignin are mostly phenolics, sinapyl alcohol, coniferyl alcohol, and

coumaryl alcohol [13], packed into three-dimensional polymers with various types of linkage between them.

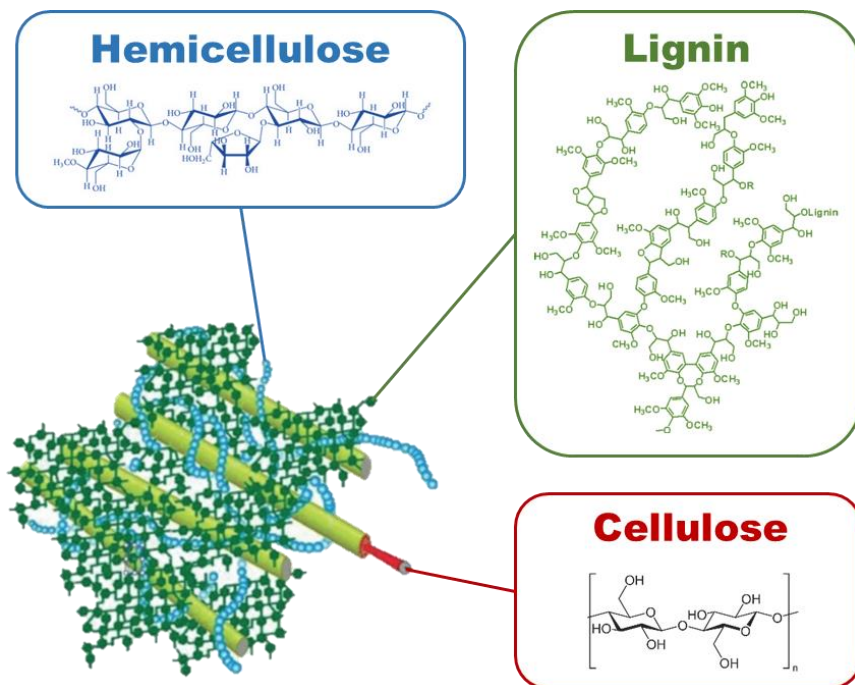


Figure 1.1 Structure of lignocellulosic biomass with cellulose, hemicellulose, and lignin represented (adapted from ref. [14]).

On a molecular level, the building blocks of lignocellulose contain useful chemical structures and functionalities that are particularly advantageous in value-added upgrades [15–19]. For example, furanic features derived from cellulose and hemicellulose have a high energy density and octane rating, which indicates that they have potential to make renewable fuels. Aromatic functionalities in the lignin portion of biomass could be of great importance in various downstream applications such as the production of organic solvents, synthetic polymers, pharmaceuticals, pesticides, *etc.*

1.1.3 Primary upgrades of lignocellulosic biomass

Various upgrading routes have been developed for converting biomass into products that can then be handled in more conventional ways. In general, these primary processing technologies can be classified into three categories: gasification, hydrolysis, and pyrolysis (See Figure 1.2) [20].

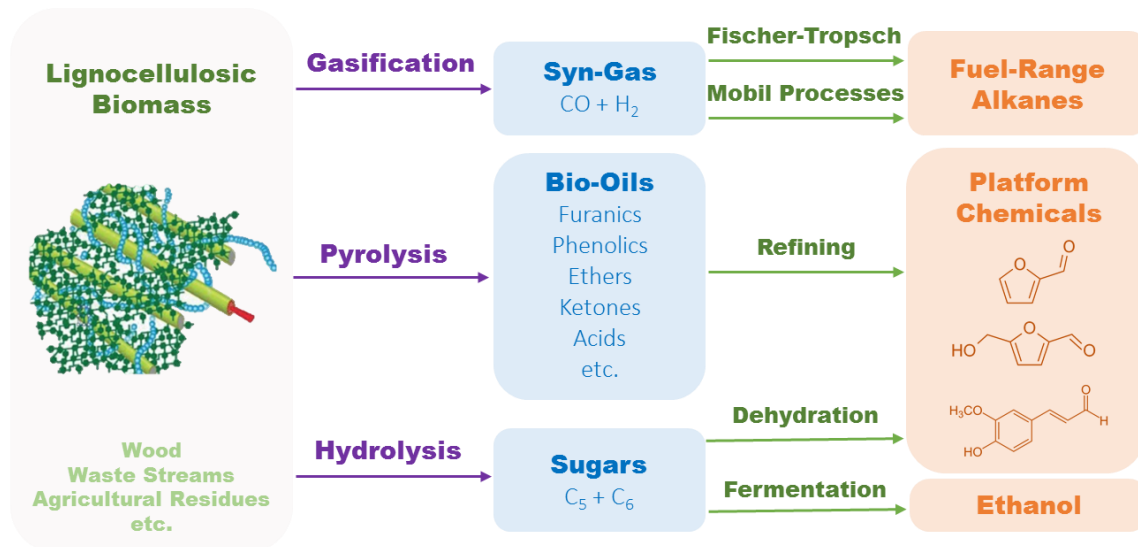


Figure 1.2 Current processing techniques for primary upgrading of lignocellulosic biomass (adapted from ref. [14,20]).

Gasification breaks biomass material down into syngas, which can be subsequently reassembled into useful chemicals and fuels. This is a fairly simple and brute-force approach that does not require complex pretreatment or separation. The fact that biomass feedstocks are first converted to CO and H₂ makes the production lines versatile for incorporation into conventional syngas streams and established processing technologies such as Fischer-Tropsch and Mobil Methanol-To-Gasoline processes. However, this method is energy intensive. Syngas production is expensive, as are the processes required

to convert syngas into other fuels and chemicals. Furthermore, breaking all of the organic functionalities wastes the valuable chemical structures associated with biomass building blocks.

Acid-catalyzed hydrolysis is useful for deconstruction of cellulose and hemicellulose so long as one avoids decomposing the resulting pentose and hexose sugars. These sugars may either be fermented into bioethanol [4] (a process which decomposes the potentially valuable chemical functionalities in the same way as syngas production) or dehydrated to make platform intermediates, such as furfural and 2-hydroxymethylfurfural (HMF) [4,21]. The hydrolysis-dehydration route, pioneered by the Quaker Oat Company, is a relatively mature process that has been commercialized for almost a hundred years [22]. In this early application, 98+ % purity furfural is produced from pentose sugars by flowing steam through sulfuric-acid-saturated, oat hulls, followed by the appropriate separations. Unfortunately, the process was developed at a time when one ton of oat hulls would fulfill the annual world demand for furfural [22]. In 2013, the surging demand for furfural increased to 300 kilotons per year thanks to the strong shift toward sustainable chemistry [23]. This sharp rise in market demand has resulted in a significant effort for finding ways to selectively produce furfural derivatives from polysaccharides and their sugar monomers [24–26]. One example of the results from this research is a process capable of achieving a 99% yield of HMF from glucose over a 12-molybdophosphoric acid catalyst in a solution of 1-ethyl-3-methylimidazolium chloride and acetonitrile [27].

The third processing technique, pyrolysis, involves thermal degradation of organic compounds in the absence of molecular oxygen. Depending on the desired ratio of gas/liquid/solid products, pyrolysis may produce a variety of products that differ because of the reaction temperature, ramping rate, and residence time [13,28]. The most common method for upgrading lignocellulosic biomass is fast pyrolysis, using ~500 °C for the reaction temperature, ~1000 °C/s for the ramping rate, and ~1 s for the residence time [13]. These conditions allow the yields to be maximized to between 50 and 95% of the liquid components in products [29]. The product from this process is referred to as bio-oil or pyrolysis oil. Besides having a considerable water content (~40 wt%), pyrolysis oil consists of phenolics, furfurals, sugar and lignin building blocks, ketones, aldehydes, and carboxylic acids. Many of these compounds are also produced in the hydrolysis-dehydration route, making them of extra importance in the upgrading chains.

However, the chemicals mentioned above are not ready for the final applications, mainly due to the presence of highly reactive, oxygen-containing functional groups. Therefore, further upgrading is necessary to produce fuels by reducing the oxygen content and specialty chemicals by tailoring the functionalities as desired.

1.2 Upgrades for biomass model compounds

1.2.1 C-O bond chemistry – the avenue towards useful fuels and chemicals

The phenolic and furanic compounds produced by the above processes represent the majority of intermediates that still preserve the valuable chemical structures contained

in lignocellulosic biomass, but these compounds still require further upgrading due to unfavorable oxygen contents and unstable functional groups. Therefore, most of this upgrading should involve reactions that focus on the C-O chemical bonds. Among these reaction pathways, hydrodeoxygenation reduces excess oxygen content for the productions of renewable fuels [30]. Ring-opening and partial oxidations can produce polyols and dicarboxylic acids that are alternative building blocks for polymer synthesis [6,31]. Etherification has also been proposed as a route to make pharmaceutical precursors [32].

Other commonly proposed upgrading pathways, such as aldol condensation, alkylation, and acylation, do not directly involve C-O bond scission or creation, but can be incorporated with C-O bond chemistry to make valuable final products. For example, Vlachos *et al.* have recently demonstrated a synthesis strategy to make renewable lubricants using biomass-derived 2-alkylfurans [33]. With this method, they condense 2-pentylfuran with lauraldehyde via hydrodeoalkylation, followed by ring-opening and HDO, to produce a C-30 branched lubricant. In another example, our group has recently demonstrated a selective route for carbon-carbon bond formation by acylation of furans with long-chain acids over H-ZSM-5 catalyst [34]. The ultimate goal here was to make renewable oleo-furan surfactants. HDO is required to remove the oxygen from the ketone to make the final products. Using HMF as an example, the aforementioned catalytic pathways of upgrading this model compound are summarized in Figure 1.3.

1.2.2 Hydrodeoxygenation

Hydrodeoxygenation (HDO) is arguably the most commonly studied method for produce useful lignocellulose derivatives [16,35,36]. This process aims to reduce the amount of oxygen atoms in the intermediate compounds. For fuel production, HDO increases the energy density and miscibility of the products for incorporation into convention fuels, while mitigating issues associated with high corrosivity and viscosity [37]. The three most commonly studied, model compounds to represent the families of furfurals and phenolics are 2-hydroxymethylfurfural (HMF), furfural, and *m*-cresol. HDO reactions of these compounds have attracted tremendous attention from research groups worldwide for purposes of developing and understanding catalysts for selective HDO.

The desired HDO products from furfural and HMF are 2-methylfuran (MF) and 2,5-dimethylfuran (DMF), respectively. They share many similarities. DMF, for example, has been recognized as an excellent fuel additive in terms of energy density (30 MJ/L), boiling point (93 °C) and octane rating (119), even compared to commercial bio-ethanol (23 MJ/L, 78 °C and 113, respectively). However, the reactions to produce these two products are usually performed under very different conditions due to the fact that furfural is easily vaporized, while HMF cannot be.

Previous work has shown that the HDO reaction of HMF occurs through a sequential reaction network with DMF formed as an intermediate (See Figure 1.4) [38]. Selective production of DMF is difficult on monometallic catalysts, such as supported Pt, Ni, Pd, Ir, Ru, and Rh, because the monometallic metals further convert DMF to ring-

saturated and ring-opened products at high space times [38]. In contrast to this, certain bimetallic alloys are able to achieve much higher selectivity towards DMF by suppressing the reaction of DMF to other products [39–46]. Some early work from Dumesic and coworkers [47] reported a 71% yield of DMF from HMF over a Cu-Ru/C catalyst. Unfortunately, this catalyst suffered from severe deactivation due in part to coking and chloride poisoning. More recently, Ebitani *et al.* [40] developed a Pd-Au/C catalysts that could achieve 96% yield to DMF under optimal conditions with the presence of HCl media. This same catalyst was also shown to be selective for the direct synthesis of DMF from ketoses where it also required promotion by HCl. Around the same time, the Schüth group [48] demonstrated a 98% yield of DMF from HMF using hollow carbon nanospheres encapsulated Pt-Co catalysts. It was suggested that the carbon nanospheres could assist the formation of ultra-small Pt-Co nanoparticles which were believed to be essential for the high reactivity. This outstanding performance (98% yield to DMF) of Pt-Co alloy was subsequently confirmed by our group [45] using Pt-Co nanocrystals (NCs) with well-defined compositions, crystallinity, and particle size. It was mechanistically understood that a honeycomb-like CoO_x overlayer was responsible for preventing over-hydrogenation of DMF, while providing openings that allow for selective HDO on the underlying Pt. In a follow-up study [46], we further demonstrated that yields approaching 100% DMF could be achieved over a series of Pt-based, bimetallic catalysts, including Pt-Ni, Pt-Cu, and Pt-Zn.

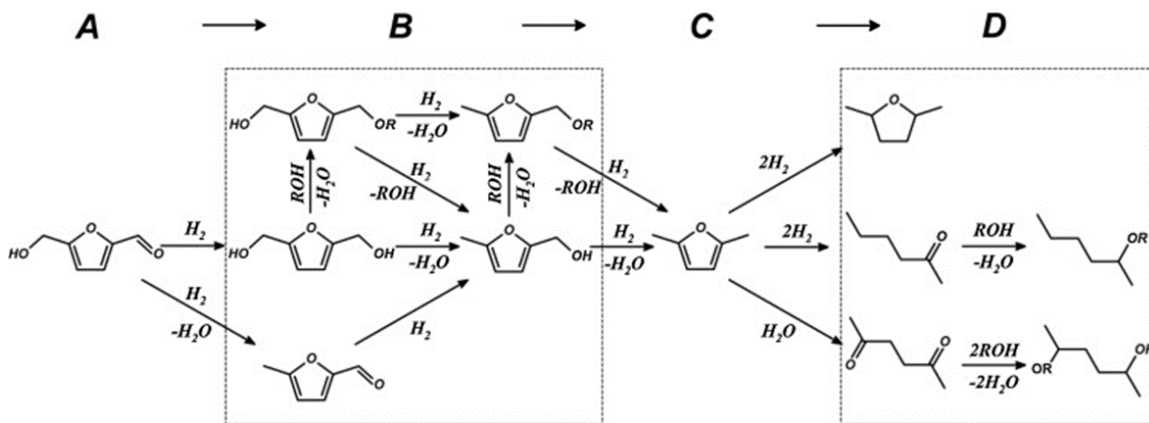


Figure 1.4 Reaction network for HMF hydrodeoxygenation using alcohols as solvent. Reprinted from ref. [38], with permission from Elsevier.

The results demonstrated clear evidence that alloying a second metal with Pt can suppress the unfavorable over-hydrogenation of the furan ring. The mechanisms behind the high selectivity for the various metal alloys appear to differ. With the Pt-Cu alloy, it is commonly agreed that Cu alloying produces Cu ensembles that repel the furan ring by means of the filled 3-d orbitals that overlap with the π orbitals of the furan ring [30]. With the Pt-Zn alloy, the furan ring is believed to tilt away from the catalyst surface because the oxygen-containing functional groups bond strongly to oxophilic Zn sites [49].

The selective conversion of *m*-cresol to toluene represents another important category of HDO reaction that produces valuable aromatic hydrocarbons from the lignin building blocks. The fundamentals and recent advances in this category of reactions have been discussed in greater detail in recent excellent review articles, most notably the two reported by Zhang *et al.* [50] and Rahimpour *et al.* [36].

The top challenge that differentiates the HDO reaction of *m*-cresol (and other lignin model compounds) from HDO of HMF and furfural is the difficulty in breaking the C(sp²)-O conjugations while still preserving the aromaticity of the molecule. As early as 1980s, molybdenum-based oxides, sulfides, nitrides, and carbides were investigated for the HDO of phenolics due to the use of these catalysts in hydrotreating processes in petroleum refining [51]. Among these catalysts, most early studies focused on using commercial MoS₂-based hydrotreating catalysts [52–54], but these were found to suffer from rapid deactivation due in part to coking [55,56] and to promote the formation of less desirable over-hydrogenated products. Although supported Group 10 metals have been shown to be active for HDO reactions, they are not ideal choices for phenolics, since these catalysts are also prone to deactivation and strongly promote ring saturation [57–62]. In an attempt to address these issues, some recent studies have focused on bimetallic catalysts, composed of a group 10 metal, such as Ni or Pt, alloyed with a second, more oxophilic metal, such as Fe, Zn or Mo [49,63–68]. For some reaction conditions, these catalysts have demonstrated enhanced HDO activity and good selectivity for maintaining aromaticity of the molecule, although a range of both aromatic and ring-saturated products are typically still formed [63,64,66]. Alternatively, bifunctional catalysts consisting of a transition metal supported on or modified by an acidic metal oxide have shown some promise for selective HDO of phenolics and other aromatic oxygenates [69–76]. Examples here include Pt/F–Al₂O₃ [69], Pt/H-Beta [70], and Ru/WO_x-ZrO₂ [76].

It should be noted that the mechanism for HDO on these supported metal catalysts is not well understood. Generally, HDO of phenolic compounds are believed to proceed through two main routes shown in Figure 1.5: (1) direct hydrogenolysis of the targeted C–O bond [68,72–74,77–80] or (2) more complex pathways that proceed via tautomerization and partial hydrogenation of the aromatic ring, followed by a dehydration/dehydrogenation step to remove the oxygen. In this latter pathway, the group 10 metal is thought to catalyze partial ring hydrogenation, whereas the more oxophilic/acidic metal or metal oxide modifier provides sites for the subsequent dehydration reaction and stabilizes the tautomer intermediate [59,64,67,68].

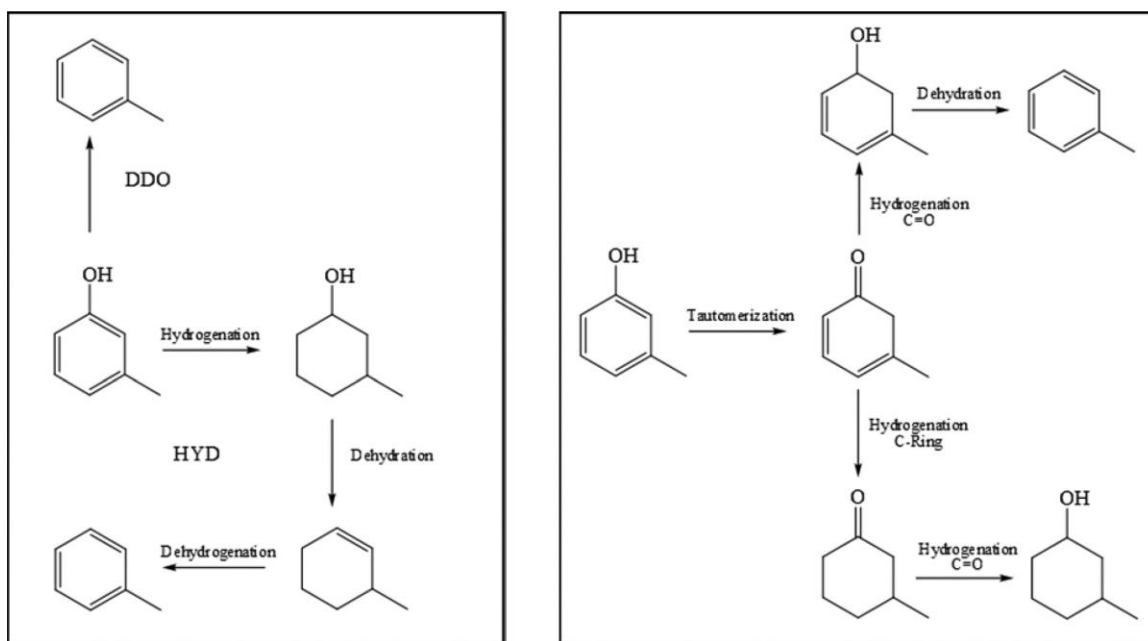


Figure 1.5 Different mechanisms proposed for the HDO reaction of phenolic compounds with *m*-cresol as an example. Direct hydrogenolysis mechanisms; (right) mechanism involving a keto tautomer. Reprinted with permission from ref. [81]. Copyright (2015) American Chemical Society.

1.2.3 Ring-opening reactions

Ring opening is another potentially important route for upgrading that requires selective scission of C-O bonds. Depending on the reagents and the desired degree of hydrogenolysis, selective opening of the cyclic ether bond may produce polyols, monoalcohols or aliphatic hydrocarbons [82–85]. This chemistry is particularly important for the syntheses of α,ω -diols [31,86] and renewable diesel-to-lubricant-range alkanes [33,87].

In the former application, the selective conversions of tetrahydrofurfuryl alcohol (THFA) to 1,5-pentandiol (1,5-PeD) and of 2,5-bis-hydroxymethyltetrahydrofuran to 1,6-hexanediol have received the most attention because these products are in large-scale demand as monomers in the production of polyesters and polyurethanes [88]. Early work with THFA involved a three-step process in which THFA was first converted to dihydropyran and then δ -hydroxyvaleraldehyde, before ultimately producing 1,5-PeD [89]. More recently, one-pot conversions of both THFA and BHMTHF to their respective α,ω -diols were reported over a number of bifunctional catalysts, including supported Rh–ReO_x [31,90,91], Pt–WO_x [92–95], and other M¹–M²O_x pairs [96–100]. In these systems, the simultaneous presence of both the hydrogenation metal (M¹) and the promoting metal oxide (M²O_x) has been shown to be critical for achieving high activity and selectivity to terminal diols.

The Tomishige group has done seminal work in this area [2,31,96–98] and has made substantial effort to elucidate the mechanism of M¹-M²O_x synergy. As is shown in Figure 1.6, they proposed that one critical role of M²O_x, including both ReO_x and MoO_x,

is to provide a binding site for the hydroxyl group of the substrate in order to anchor the molecule adjacent to the reactive interface via etherification (*step i*) [98]. The positively charged M^2 then assists M^1 , which in their work was either Ir or Rh, to heterolytically dissociate H_2 (*step ii*). The negatively charged hydride species formed here first opens the cyclic ether C-O bond (*step iii*), followed by protonation to release the final product 1,5-PeD (*step iv*) [101]. In this picture, direct evidence for the heterolytic activation of hydrogen is lacking; it is also not clear why this unique chemistry occurs only on some hydrogenation catalysts, such as Ir and Rh, but not others, such as Pt, Pd, or Ni [99,101].

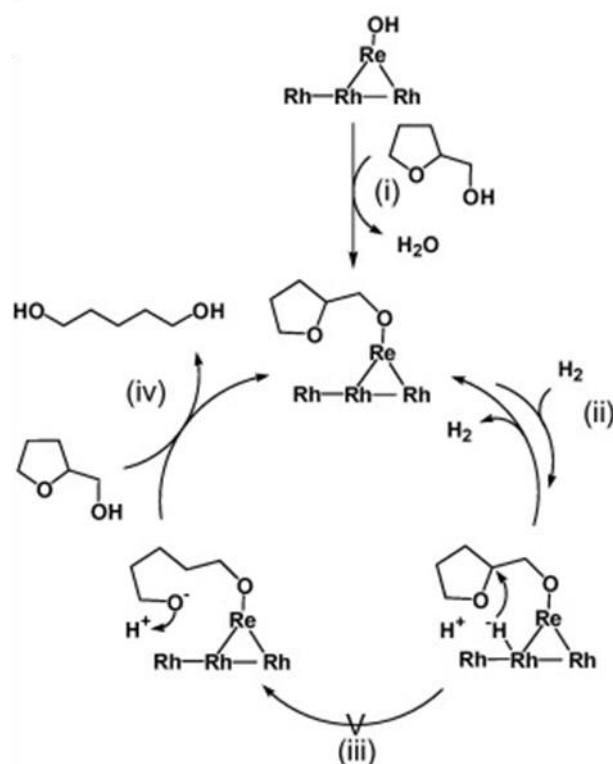


Figure 1.6 Proposed mechanism of THFA hydrogenolysis over Rh-ReO_x/SiO₂. Reprinted from ref. [96], with permission from Elsevier.

The other leading hypothesis, first proposed by Dumesic *et al.*, is that hydroxyls on the metal oxide are Brønsted sites [90]. According to this, donation of a proton from the Brønsted site stabilizes an oxocarbenium-ion transition state that forms upon ring-opening reactions. That the metal oxides form Brønsted sites was shown primarily through ammonia-adsorption measurements; however, it should be noted that ammonia can adsorb on almost any oxide, including ones that are usually considered solid bases, such as CaO [102]. Furthermore, the metal oxides that seem to exhibit the best performance are not necessarily the ones that would most obviously lead to Brønsted acidity.

1.3 Thesis Outline

The first chapter in this dissertation aimed to provide general background upon which the remainder of the thesis can be better understood. A review of the fundamentals and recent advances that are relevant to the projects was presented in Section 1.2, where I have mainly discussed three specific biomass model reactions that are required for selective C-O bond cleavage. They are (1) the HDO reaction of HMF and furfural to make DMF and MF; (2) the HDO reaction of *m*-cresol to produce toluene and (3) the ring-opening reaction of THFA to produce 1,5-PeD. Despite the large volume of research and the critical contributions of previous workers, important aspects required further investigation.

Chapter 2 summarizes the experimental methods I have implemented throughout my research projects. I start off by describing the designs for the high- and low-pressure continuous flow reactors that I used. I then discuss the synthesis methods I used for preparing catalysts. First, catalysts were prepared by solvothermal methods to produce

bimetallic nanocrystals; Second, I used atomic layer deposition to make overlayer oxides. Finally, key instruments used in the analysis are introduced.

My new research work started with a collaborative research project together with Dr. Jing Luo. This work involved the selective HDO reaction of HMF and furfural over bimetallic alloys. Chapter 3 and 4 present the results from this collaboration. While our previous work had mostly focused on Pt-based bimetallics, the work featured in Chapter 3 presents results from a base metal alloy, Ni-Cu, that also leads to unprecedentedly high yields of DMF from HMF. High selectivity in this case may, in fact, be different from that for Pt-Co catalysts that were investigated in the past.

The experimental conditions may also have profound influence on the HDO reaction network. Chapter 4 investigates the HDO reaction of furfural under low and high reaction pressures and shows that the products are indeed different. This study shows that the Ni-Fe [41] and Pt-Co [45] catalysts, which have previously been demonstrated to be selective under low and high pressures, respectively, also suppress undesirable side reactions under the opposite conditions. The implications for the underlying relationships in these reactions are discussed.

Chapter 5 presents a study on the ring opening reaction of THFA, a platform chemical that is produced by hydrogenation of furfural. Catalyst screening was first performed to identify active and selective M^1 - M^2O_x combination, then a discussion is made to narrow down the possible synergy between the metal and the metal oxide. Using a well-defined Pt- WO_x/C catalyst synthesized by ALD of WO_x onto Pt NCs, this study

demonstrates the importance of the geometry required to achieve an active interface to facilitate 1,5-PeD selectivity.

Chapter 6 discusses my work on the HDO reaction of lignin-derived *m*-cresol. Catalysts that were previously shown to be selective for HMF and furfural are not effective in this reaction. The Pt-WO_x/C catalyst, on the other hand, is unusually active, stable, and selective to toluene as compared to Pt/C or WO_x/C. An in-depth mechanistic study was done to decipher why this catalyst exhibits its unusual properties.

All the selective HDO catalysts presented above make the most efficient uses of H₂ as they suppress unfavorable hydrogenation such as ring saturation. However, the cost of H₂ is still a significant impediment to the development of commercial processes that convert these compounds. To address this, results in Chapter 7 demonstrate that it is possible to perform HDO of *m*-cresol on Pt-WO_x/C using in-situ generated H₂ formed by dehydrogenation of *n*-hexane. I will demonstrate that the stability is related to a strong pressure dependence on the deactivation rate for Pt.

This thesis also features results from two additional studies aimed at developing characterization methods for the solid-acid catalysts. Chapter 8 reports a novel synthesis method to prepare tungstated zirconia (W-Zr), a well-known solid acid, using atomic layer deposition. The ZrO₂ with uniform, ultra-thin WO_x layer is demonstrated to have three different types of catalytic sites, the concentrations of which clearly correlate with the WO_x coverage. Chapter 9 reports on my work aimed at quantifying the relative Brønsted-acid strengths of a series of solids acid materials using H-D exchange with simple aromatics.

The project was motivated in part by testing the commonly accepted argument that W-Zr has super acidity which is stronger than many silicoaluminate zeolites.

Finally, Chapter 10 summarizes the key findings I have explored thus far and concludes this thesis dissertation.

CHAPTER 2. EXPERIMENTAL METHODS

Summary

The goal of this chapter is to complement the experimental sections in each of the other chapters of this dissertation. I assume that the reader is already familiar with the basic concepts behind rate measurements and catalyst characterization but an overview is required to show the specific methods used here. The experiments included work on three-phase, continuous-flow reactors, atomic layer deposition (ALD), and simultaneous temperature program desorption and thermal gravimetric analysis (TPD-TGA). For other tools that are less critical, but still important for my studies, a procedural description is given in order to provide operational details.

2.1 Reactor Design and Reactivity Measurements

Reactors can be divided into two broad categories: batch and continuous. In general, batch reactors are more versatile but the fact that things scale linearly with size makes it much more difficult to use batch systems for large-scale production. In the laboratory, batch reactors also pose issues that are particularly problematic for multi-phase catalysis. Since most of the biomass model reactions described in this thesis are three-phase, consisting of gas phase molecular hydrogen, a liquid-phase reagent in a solvent, and a solid-phase catalyst, the top challenge for reactor design is to ensure sufficient contact among the three phases at steady state. Picturing a conventional batch reactor in which ~100 mg solid catalyst is immersed in a ~100 mL liquid solution, contact with the hydrogen

gas to the exterior of the catalyst particles is obviously difficult, even in the absence of internal heat and mass transfer within the porous materials.

2.1.1 Three-phase Continuous Flow Reactor

The drawback of insufficient contact motivated me to perform my reactions in a three-phase, continuous-flow reactor. Another advantage of using flow systems is that reaction kinetics can be measured easily, since the residence time is well-defined. One can also observe catalyst deactivation, if it occurs. A difficulty with tubular reactors is that operating at high pressures is more challenging.

To demonstrate the reliability of this high pressure flow unit, Dr. Jing Luo [103] performed a comparative study of flow and batch reactors using HDO reaction of HMF over a simple Pt/C catalyst. The kinetics obtained from the flow system clearly showed that the HDO of HMF is a sequential reaction in which DMF is an intermediate. This conclusion would have been much more difficult from the batch-reactor data due to the fact reaction occurred during heat-up and cool-down times required to reach reaction conditions.

Figure 2.1 shows a schematic diagram of this custom-built, high-pressure, continuous-flow unit. The stainless-steel tubular reactor was 200 mm in length and 4.6 mm in inner diameter and was configured horizontally inside a cylindrical furnace. Between 50 and 200 mg of the catalyst powder were packed between quartz-wool plugs at the center and were supported by two inert rods at each end. When lower space times were desired, the catalyst bed was diluted with carbon support material while maintaining a total

bed size of 50 mg. High-pressure H₂ was fed through a 244-cm long, 51- μ m i.d. capillary tube that was calibrated to provide a 12 mL/min gas flow at STP when the pressure drop across the capillary was 550 psi. The liquid feed, a solution of the desired biomass compound (typically at concentrations between 1 and 20 mol%), was introduced into the reactor at 0.05 mL/min using an HPLC pump (Series I+, Scientific Systems Inc.). A back-pressure regulator (KPB series, Swagelok) was connected to the reactor exit to adjust the total pressure.

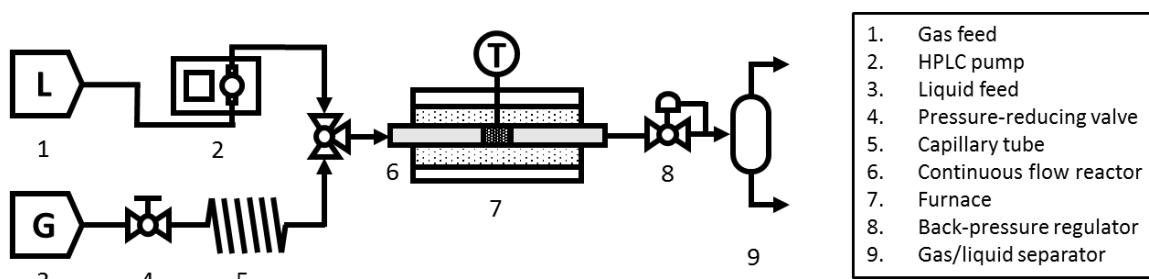


Figure 2.1 Schematic diagram of three-phase continuous flow reactor.

In a typical reactivity run, a catalyst was pretreated *in-situ* under flowing H₂ at 1 bar and 533 K for 30 min prior to the experiments. It was initiated by co-feeding pure liquid solvent and H₂ while pressuring and heating the system to the reaction conditions. The liquid feed was then switched from pure solvent to the reactant containing solution. Both gas- and liquid-phase products were collected and injected into a GC-MS (QP5000, Shimadzu, equipped with an Agilent HP-Innowax GC column) using a syringe. Due in part to the use of low flow rates, it typically took ~3 h for the system to reach steady state. Conversions and product selectivities were quantified using by calibrating the GC-MS with

known compounds. Unless otherwise noted, carbon balances in the high-pressure measurements were always better than 90%.

2.1.2 *Gas-phase Continuous Flow Reactor*

An ambient-pressure, gas-phase flow reactor was built to serve in a comparative study of furfural HDO (Chapter 4). This unit was also used to measure light-off temperatures for H-D exchange with *h*₈-toluene and *h*₅-chlorobenzene over solid acids (Chapter 9). A schematic of this flow reactor is shown in Figure 2.2. It had the same dimensions and similar catalyst loadings as the high-pressure unit. The main difference in these experiments was that the feed to this reactor consisted of reactant vapor(s) in a carrier gas (H₂ or He). In the furfural HDO work, this feed was prepared by passing the H₂ carrier through a temperature-controlled bubbler containing pure furfural; in the H-D exchange experiments, the feed consisted of aromatic and D₂O liquids added into a He stream by two syringe pumps (PHD 2000, Harvard Apparatus). All lines were kept at high temperature to avoid condensation. Product quantification was carried out on the same GC-MS described above, but using an on-line gas-sampling valve.

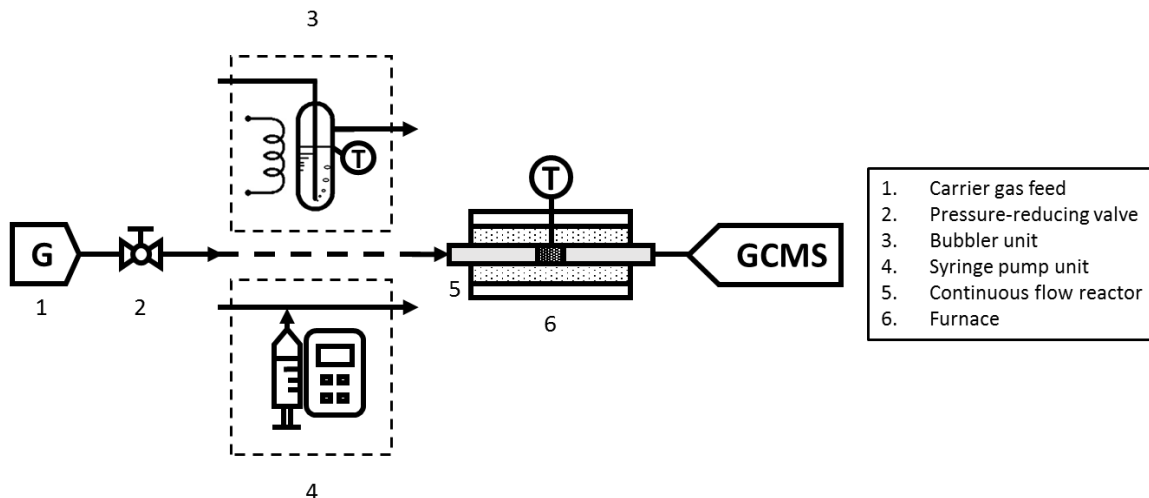


Figure 2.2 Schematic diagram of gas-phase continuous flow reactor with two feeding alternatives using a bubbler or a syringe pump.

2.2 Catalyst Preparation

2.2.1 Incipient Wetness Impregnation

Incipient wetness impregnation (IMP) is a simple, robust, and economical synthesis method for heterogeneous catalyst preparation. All carbon-supported catalysts reported in this thesis were at least initially prepared by IMP method. Depending on the need for further investigation, I then used solvothermal or ALD methods to prepare better defined materials. A listing of these IMP-prepared catalysts is given in Table 2.1.

Table 2.1 A listing of IMP-prepared catalysts that have been reported in this thesis.

monometallic (M^1/C) catalysts						
Pt	Ni	Ir	Ru	Pd	Co	-
bimetallic (M^1-M^2/C) catalysts						
Pt-Co	Ni-Cu	Ni-Fe	-	-	-	-

metal-metal oxide ($M^1-M^2O_x/C$) catalysts						
Pt-WO _x	Pt-ReO _x	Pt-MoO _x	Pt-NbO _x	Pt-VO _x	Pt-CeO _x	-
Pt-CrO _x	Pt-MnO _x	Pt-ZnO	Pt-YO _x	Pt-Al ₂ O ₃	Pt-CoO _x	-
Ir-WO _x	Ir-MoO _x	Ir-VO _x	Ru-WO _x	Ni-WO _x	Co-WO _x	Pd-WO _x

When a M^1/C catalyst was prepared, the M^1 precursor was first dissolved in a water/ethanol (3:1) mixture under vigorous stirring. Carbon black (225 m²/g, Vulcan XC-72R) was then added to form a slurry, which was dried in air at 333 K for 12 h. The resulting powder was reduced in a flow reactor in a 5-vol % H₂/He carrier (60 mL/min) at 773 K for 2 h with ramping rate at 10 K/min. The bimetallic M^1-M^2 alloys were made by the same procedure used for M^1/C catalysts, except that the two precursors were first co-dissolved in the solvent prior to the latter steps.

$M^1-M^2O_x/C$ catalysts were prepared by impregnating M^2O_x onto as-prepared M^1/C . The precursor for the M^2O_x component was first dissolved in a water/ethanol (3:1) mixture. Then, M^1/C was added to make a slurry before drying in air at 333 K for 12 h. Finally, the resulting power was calcined in a muffle furnace at 473 K for 12 h.

2.2.2 Well-defined Nano-crystals (NCs)

Well-defined Pt-Co¹ and Ni-Cu NCs were synthesized by solvothermal methods in the two studies featured in Chapter 3 and 4. Figure 2.3 shows a schematic diagram to illustrate this synthesis strategy.

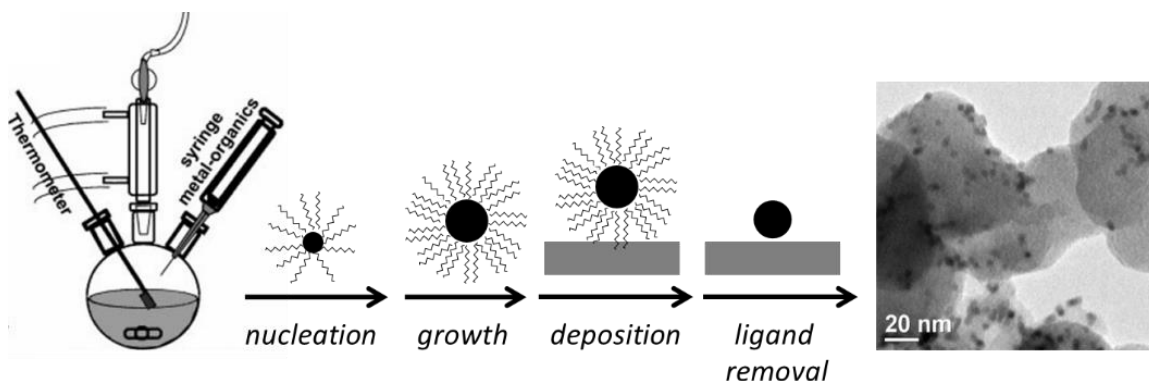


Figure 2.3 Cartoon depicting the stages of nucleation and growth for the preparation of monodisperse NCs with the following steps of deposition and ligand removal. Adapted from ref. [104], with permission from Annual Reviews. TEM image of Pt₃Co₂ NCs/C was used as an example. Adapted with permission from ref. [45]. Copyright (2016) American Chemical Society.

The procedure used for Pt-Co NCs synthesis involved dissolving platinum (II) acetylacetonate (Acros, 98%), 1-adamantanecarboxylic acid (Sigma-Aldrich, 99%), and 1,2-hexadecanediol (Sigma-Aldrich, 90%) in a solution of oleylamine (Sigma-Aldrich, 70%) and 1-octadecene (Acros, 90%). It was carried out in a 150-mL three-necked, round-

¹ The carbon supported Pt-Co NCs catalyst was synthesized by Jennifer D. Lee from the Chris Murray lab in the Chemistry Department at University of Pennsylvania

bottomed flask and connected to a Schlenk line. This reaction mixture was kept at 343 K for 30 min under vacuum and then heated to 503 K at a rate of 10 K/min under a N₂ atmosphere. Co₂(CO)₈ (Acros, 95%), dissolved in 1,2-dichlorobenzene (Acros, 99%) at room temperature, was then injected into the reaction solution at 443 K with a needle and syringe. This mixture was held at 503 K under a N₂ atmosphere for 30 min before cooling to room temperature. The resulting NCs were purified by precipitation with isopropanol and centrifugation at 6000 rpm for 2 min. The precipitate was washed twice with hexane/isopropanol mixtures before dispersing onto carbon black, followed by a drying process under vacuum.

When Ni-Cu NCs were prepared, Nickel acetylacetonate (95%, Alfa Aesar) and copper acetylacetonate (97%, Alfa Aesar) were dissolved in oleylamine (70%, Sigma Aldrich) and degassed at 373 K for 15 min. Trioctylphosphine (90%, Sigma Aldrich) was then added under a N₂ atmosphere. The system temperature was ramped up and kept at 503 K for 10 min before cooling to room temperature. Methanol and hexane were used to precipitate and re-disperse the NCs, respectively, in the rinsing steps. Finally, the NCs were dispersed onto the carbon support, followed by the drying process described above. Organic ligands from the surface of the NCs were removed by exposing the sample to an O₂ plasma for 15 min, followed by rapid thermal annealing (RTA) at 773 K for 1 min.

2.2.3 Atomic Layer Deposition (ALD)

The concept of using ALD to synthesize novel heterogeneous catalysts is relatively new, but the advantages have already been highly recognized in a number of excellent

literature reviews [105–108]. ALD is used to design catalysts with improved activity, selectivity, and stability, especially under extreme conditions. They are also used to elucidate reaction mechanisms and structure-performance relationship [106].

A typical ALD cycle consists of four key steps: (1) adsorption of excess gaseous precursors onto the substrate; (2) removal of excess precursors that are weakly bound; (3) Addition of oxidizing reactant to decompose the precursor and create binding sites for the next ALD cycle; and (4) removal of excess reactant and by-products. A schematic diagram of TiO₂ ALD on porous materials is shown in Figure 2.4 to illustrate these four steps [108].

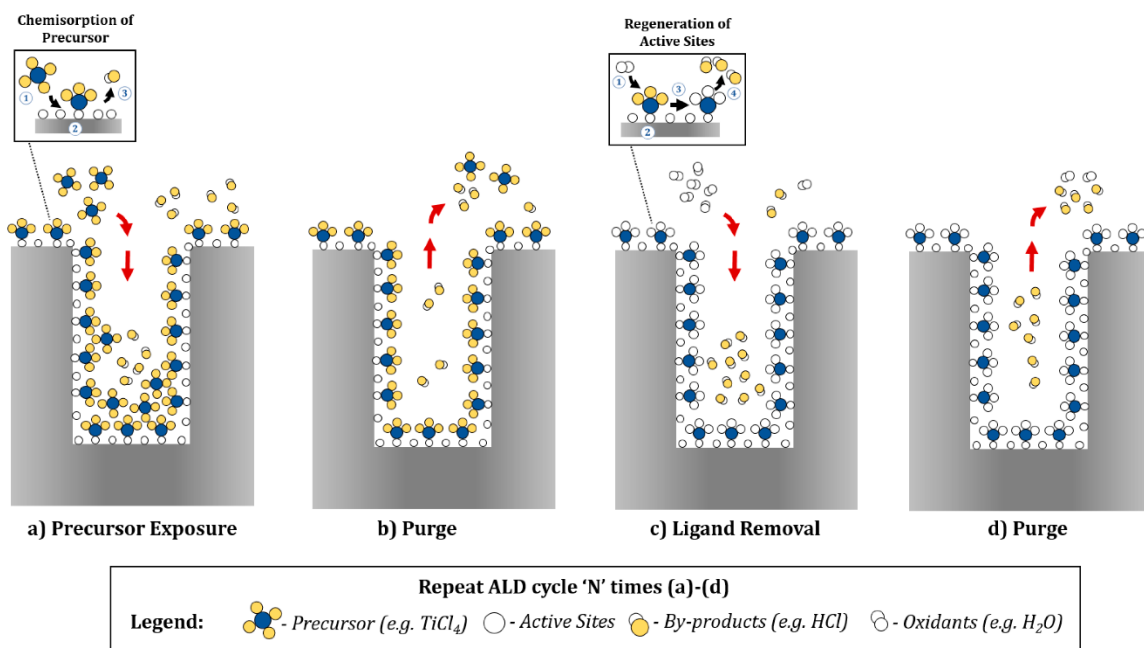


Figure 2.4 Schematic of one ALD cycle in a pore structure. (a) Introduction of precursor molecules and adsorption on the surface; (b) purge of the unreacted precursor molecules and reaction products; (c) introduction of ligand removal reactants, which react with the chemisorbed precursor molecules; and (d) purge of the excess reactants and reaction products. This schematic is an example of an ideal ALD process for TiO₂ deposition using the TiCl₄/H₂O system. Reprinted from ref. [108].

While these four general steps are true for all ALD systems, the operating parameters for synthesis of porous materials can be complex. While ALD has been successfully employed in the semiconductor industry for relatively flat materials, application to porous materials requires different equipment and operating conditions. As is pointed out by Onn *et al.*, a conventional ALD procedure that uses rapid cycling (typically 0.5-s exposure per reagent per cycle) can lead to serious issues due to gas-phase diffusion limitations in the highly porous microstructures [108].

In order to mitigate the diffusion limitations and achieve thin, uniform coverages in a reasonable time, ALD was performed here in a custom-built, static system that could be evacuated by a mechanical pump. The precursor [e.g. tungsten hexacarbonyl (99%, Strem)], was first evacuated at room temperature to remove air, then heated to 403 K to produce a vapor. In an ALD cycle, 300 mg of sample was exposed to the $W(CO)_6$ vapor at 473 K for 3 min, evacuated for 5 min, and then exposed to excess air for 6 min. This cycle was repeated until desired coverage has obtained.

2.3 Characterization Techniques

2.3.1 TPD-TGA Measurement

The temperature programmed desorption and thermogravimetric analysis (TPD-TGA) measurements were performed to characterize solid-acid, reactive sites in the studies featured in Chapter 8 and 9. Since the early development in the 1980s [109–111]. TPD-TGA of simple alcohols and amines has been demonstrated to be a reliable characterization

technique for determining Lewis- and Brønsted-site densities [112–115]. TPD-TGA of amines can be used to quantify Brønsted-site densities by measuring the desorption of propene and ammonia. These products are produced via the Hofmann-elimination decomposition of stoichiometrically adsorbed alky-ammonium complexes on the Brønsted-acid sites.

A schematic diagram of the custom-built, TPD-TGA instrument is shown in Figure 2.5. This unit consists of an evacuated CAHN 2000 microbalance equipped with an SRI quadrupole mass spectrometer (RGA100). In a typical TPD-TGA experiment, 50-mg samples were first heated in a vacuum to 823 K before being cooled to room temperature and then exposed to the vapor of the probe adsorbate, either 2-propanol (99.9%, Fisher), 1-propanamine (99+%, Alfa Aesar), or 2-propanamine (99%, Alfa Aesar). After 1-h evacuation, the TPD and TGA measurements were obtained while ramping the temperature at 10 K/min.

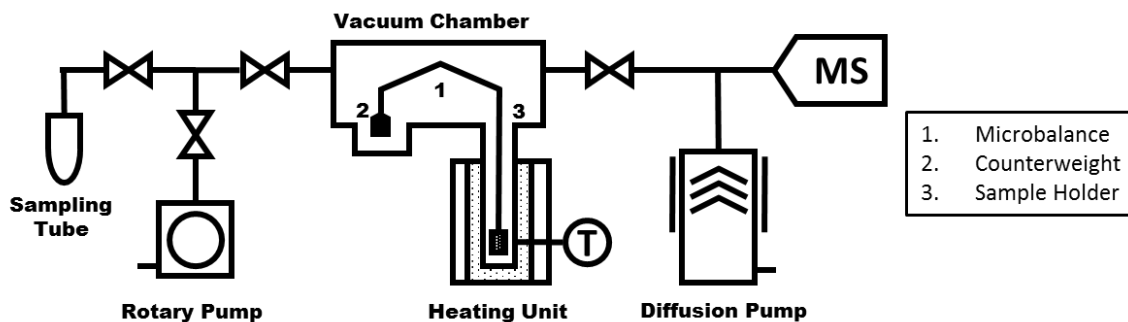


Figure 2.5 Schematic diagram of TPD-TGA system

In the study featured in Chapter 9, less commonly used adsorbates, toluene- h_8 (99.9%, Fisher Scientific) or chlorobenzene- h_5 (99.5%, Acros), were used to probe the

relative strength of Brønsted site. In this variation, the 50-mg catalyst samples were deuterated by being degassed in vacuum at 823 K, exposed to 10 torr D₂O at 298 K for 30 min, and evacuated at 523 K to remove excess D₂O. The samples were then cooled *in vacuo* to 243 K by immersing the sample tube in ethanol that was cooled to that temperature with dry ice. The samples were dosed *in vacuo* to vapor from the desired adsorbate until the sample coverage was between 500 and 1000 μmol/g. After 1-h evacuation at 243 K, TPD–TGA measurements were performed, using the mass spectrometer to look for H–D exchange in the products.

2.3.2 Other Characterization Techniques

This section aims to provide brief procedural descriptions for a collection of characterization methods that served in supporting roles in my studies.

Catalyst total surface areas were measured using a custom-built Brunauer–Emmett–Teller (BET) apparatus with N₂ as the adsorbent. This apparatus was also used for selective CO chemisorption measurements, which were used to estimate the Pt dispersion in each catalyst. The samples used for dispersion measurements were degassed *in vacuo* at 473 K and pretreated in 200 torr H₂ at 473 K for 30 min prior to adsorbing CO at room temperature.

Powder X-ray Diffraction (XRD) was used for phase identification of crystalline metals and metal oxides. Sample powders were first dispersed into a 2-propanol suspension and then drop-casted onto a glass slide. The XRD patterns were collected from a Rigaku Smartlab diffractometer equipped with a Cu K source ($\lambda=1.5405 \text{ \AA}$).

Infrared spectra of adsorbed pyridine were performed on a Mattson Galaxy FTIR (Madison Instruments Inc.) with a diffuse-reflectance attachment (Collector II™) in order to confirm the presence of Brønsted sites. In the FTIR cell, the samples were initially heated to 373 K in flowing He to remove any adsorbed water. After cooling the samples to room temperature, pyridine vapors were exposed to the sample. The samples were then flushed with flowing He to remove excess pyridine prior to collecting the infrared spectra.

Raman spectra were obtained with an NTEGRA Spectra system (NT-MDT) with an excitation laser wavelength of 532 nm. The experiments were carried out with a laser power of 15 mW (10% of 150 W from the natural-density filter setting) at the samples and a collection time of 60 s.

CHAPTER 3. UNRAVELING THE SURFACE STATE AND COMPOSITION OF HIGHLY SELECTIVE NANOCRYSTALLINE NI-CU ALLOY CATALYSTS FOR HYDRODEOXYGENATION OF HMF²

Summary

This publication was a continuation of an early collaboration with Dr. Jing Luo in our group, who sought to demonstrate a selective HDO reaction of HMF to DMF over a series of bimetallic oxophilic catalysts. While all the selective catalysts we had previously looked into were Pt-based alloys, here we reported base-metal Ni-Cu NCs that also led to unprecedentedly high yields to the desired product, DMF. Near ambient-pressure X-ray photoelectron spectroscopy (NAP-XPS) was used to characterize the surface composition of these highly selective catalysts. Evidence indicates that the catalysts were completely reduced under the reaction conditions. It suggests that the high selectivity, in this case, may be different from that for Pt-Co catalysts, in which partially oxidized CoO_x overlayer is thought to be critical in the selective mechanism.

² This chapter was published as J. Luo, M. Monai, **C. Wang**, J.D. Lee, T. Duchoň, F. Dvořák, V. Matolín, C.B. Murray, P. Fornasiero, R.J. Gorte, *Catalysis Science & Technology* 7 (2017) 1735–1743.

3.1 Introduction

As I have discussed in Chapter 1, a number of groups have demonstrated that monometallic catalysts are not selective for DMF production from HMF [27,38,40,116]. At high hydrogen pressures, HDO of HMF has been shown to be a sequential reaction over carbon-supported Pt, Pd, Ir, Ni, Ru, and Co catalysts, with DMF itself reacting to form either ring-opened (e.g. 2-hexanone, 2,5-hexanedione) or ring-hydrogenated (e.g. 2,5-dimethyltetrahydrofuran, DMTHF) byproducts [103,117,118]. However, some bimetallic catalysts have shown significantly improved HDO selectivities. For example, Schüth and co-workers [48] synthesized a carbon-sphere-encapsulated Pt–Co catalyst that gave DMF yields as high as 98%. The conclusion that Pt–Co alloys could be selective for DMF production was supported by a study of Pt–Co alloy nanocrystals (NCs) [45], which further demonstrated that the reactivity of DMF was greatly suppressed on the alloy compared to monometallic Pt or Co. In the latter case, it was argued that the superior HDO selectivity of this catalyst is due to the formation of a CoO_x monolayer that dramatically weakens the interactions between the furan ring and the catalyst surface so that over-hydrogenation of DMF is suppressed [45]. Similarly for Ni–Fe alloys, it was suggested that the effect of Fe on the bonding of the furans is likely due to the oxophilicity of Fe [41]. However, other Pt/base-metal (Pt–Cu, Pt–Zn) alloy catalysts were also shown to give high yields of DMF due to suppressed reactions of DMF (>95%) [46]; and the alloying metal in the case of Cu is not as oxophilic as Fe or Co. It remains unclear whether an oxide overlayer is needed in order to obtain high DMF yields.

Base-metal alloys have also been shown to be more selective relative to monometallic catalysts for the vapor-phase reaction of furfural to methyl furan. For example, Resasco and coworkers have demonstrated that Ni–Fe catalysts are superior to monometallic Ni [41]. In the vapor-phase reaction, furan, obtained from decarbonylation of furfural, is the major side product but there is evidence that catalysts which are selective for HMF conversion to DMF are also selective for furfural conversion to methyl furan [119]. Higher yields of DMF from HMF have been reported for Ni–W₂C [39] and Cu–Co@C [120] catalysts, but there is no indication about the catalysts' surface composition under the reaction conditions or about the role of the carbon overlayer in controlling the HDO selectivity. In the work described this chapter, I report on the reaction of HMF to form DMF over Ni–Cu NC catalysts in a continuous flow reactor at high H₂ pressures. DMF yields as high as 98.7% were achieved with the NiCu₃ NC catalyst due to the fact that this catalyst exhibits very low reactivity towards DMF over-hydrogenation. Catalysts prepared by conventional infiltration methods were not as selective as the ones prepared from alloy NCs because the composition of the conventional supported metals was not as uniform. The preparation of alloy NCs via solvothermal methods eliminates catalyst heterogeneity, which also makes it easier to understand how catalyst composition and particle size affect activity and selectivity [121]. Near ambient pressure X-ray photoelectron spectroscopy (NAP-XPS) revealed that the Ni–Cu NCs are completely reduced to the metallic state under the reaction conditions. Possible reasons for the high selectivity of this bimetallic alloy catalyst is discussed in this Chapter.

3.2 Experimental

3.2.1 Catalyst synthesis

NiCu and NiCu₃ NCs were synthesized by solvothermal method. These catalysts were also prepared via conventional impregnation (IMP) to demonstrate the importance of compositional uniformity on the alloy surface. Detailed synthesis procedures have been described in Chapter 2. All the catalysts used carbon black (225 m²/g, Vulcan XC-72R) as the support and all had 10-wt% metal loading. In solvothermal method, 3:1 and 1:1 precursor molar ratios were used In order to obtain 1:1 and 1:3, Ni:Cu molar ratios in the final products.

3.2.2 Catalyst characterization

The TEM images and electron diffraction patterns of the NCs were collected on a JEOL JEM-1400 microscope operating at 120 kV. Particle-size distributions were determined by measuring >200 particles per sample with ImageJ software. The elemental compositions of the NCs were determined by inductively coupled plasma optical emission spectrometry (ICPOES) performed on a Spectro Genesis spectrometer with a concentric nebulizer. Powder X-ray diffraction patterns were collected in the 2 θ range of 20–120° on a Panalytical X'Pert diffractometer with Co K α radiation ($\lambda = 0.178901$ nm).

NAP-XPS experiments were carried out in a custom-built system (SPECS Surface Nano Analysis, GmbH Germany) equipped with a PHOIBOS 150 hemispherical energy analyzer, coupled with a differentially pumped electrostatic prelens system. The reaction

NAP cell was installed in an analysis chamber that had a base pressure of $\sim 10^{-10}$ mbar and allowed in situ XPS studies at pressures up to 20 mbar. A high-intensity monochromatized Al K α X-ray source (1486.6 eV) was used to record the spectra of Cu 2p, Ni 2p, O 1s, P 2p, N 1s and C 1s core levels. Binding energies are reported after correction for charging, using the metallic Cu 2p $_{3/2}$ signal (932.4 eV) as a reference. Before the XPS investigation, the NiCu and NiCu $_3$ NCs were first deposited on a graphite foil.

SEM measurements were performed on a field-emission scanning electron microscope (SEM) (Model Tescan Mira 3). High resolution was achieved using an acceleration voltage of 30 kV and a working distance of less than 3 mm.

The HDO reactions were carried out in a three-phase continuous-flow reactor that has been described in Chapter 2. Quantification of the major products was accomplished by calibration with standard solutions of HMF, DMF, DMTHF, 2-hexanone, 2-hexanol, and 2,5-hexanedione (all purchased from Sigma Aldrich). For quantification of other furan-based intermediate products, the GC sensitivity was assumed to be the same as that for HMF. For open-ring ether products, the GC sensitivity was assumed to be the same as that for 2-hexanone or 2,5-hexanedione. The typical time for an experiment was 4 h. For each sample injection, the GC analysis required 30 min. The catalyst required no activation but most of the catalysts underwent deactivation to some extent, so that the data which referred to as the “initial performance” were typically chosen from the second or third measurement (40 to 60 min after starting the reaction). The space times (W/F) in this work are given as

the weight of the metal catalyst divided by the volumetric flow rates of the liquid. Although determining mass-transfer limitations in three-phase systems is difficult, several experiments were performed in which W/F was fixed while varying the catalyst loading and reactant flow rate. This had no effect on either the conversions or the selectivities.

3.3 Results

3.3.1 Nanocrystal catalyst characterization

The TEM images of the NiCu and NiCu₃ NCs synthesized by solvothermal methods are shown in Figure 3.1(a) and (d). In each case, the particles were uniform, with a slightly faceted morphology. The average sizes and size distributions of the NiCu and NiCu₃ NCs were 13 ± 1.0 nm and 15 ± 1.2 nm, respectively. The slight difference in the particle sizes of NiCu and NiCu₃ NCs is due to the amount of precursors used during the synthesis. The XRD patterns in Figure 3.1(g) demonstrate that the NCs have a face-centered-cubic (FCC) crystal structure. As a reference, the diffraction patterns of pure Cu (JCPDS 00-004-0836) and pure Ni (JCPDS 03-065-0380) are also shown. The diffraction peaks of the NiCu NCs were shifted to slightly higher angles compared to those of the NiCu₃ NCs, as expected for well-mixed alloys. An extra 2θ peak between (111) and (200) planes was observed for NiCu NCs, and this is likely indicative of the presence of hcp-like stacking faults [122,123]. The elemental compositions of Ni–Cu alloys were determined by ICP-OES. The metal compositions from these measurements were 45 : 55 for NiCu NCs and 22 : 78 for NiCu₃ NCs, respectively.

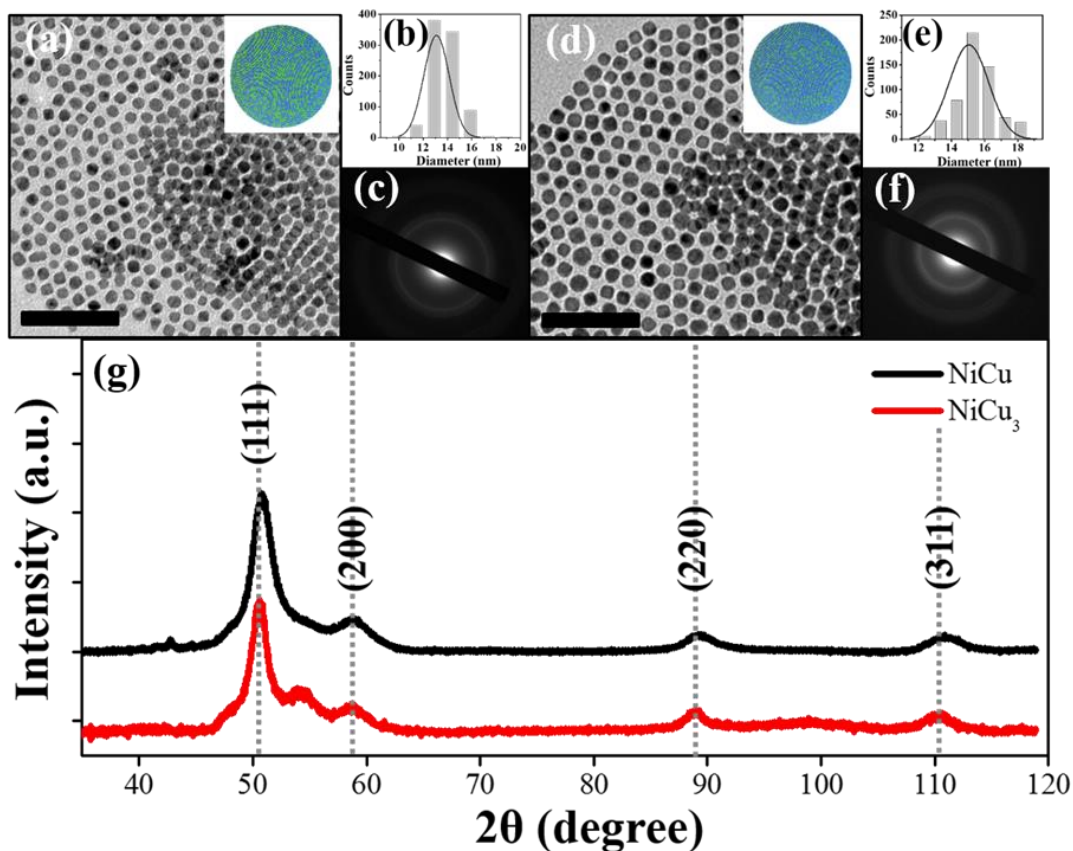


Figure 3.1 The TEM images of (a) NiCu and (d) NiCu₃ and their corresponding size distributions (b and e) and diffraction patterns (c and f). The powder X-ray diffraction patterns are shown in (g), with pure Cu and Ni patterns included. Scale bars are 100 nm. Model colors: light blue = Cu atoms, green = Ni atoms.

For SEM and NAP-XPS investigation, the NiCu and NiCu₃ nanocrystals were deposited on a graphite foil. The SEM micrographs (Figure 3.2) show that the nanoparticles were homogeneously distributed over the surface in a side-by-side fashion, forming a single discontinuous layer. No evidence for second (or higher) layer formation was observed. The XPS spectra taken after treating the NCs with oxygen plasma and rapid-thermal annealing (RTA) show that the pretreatment effectively removed the protecting

ligands, so that both N and P signals were below the detection limit in the spectra (not shown).

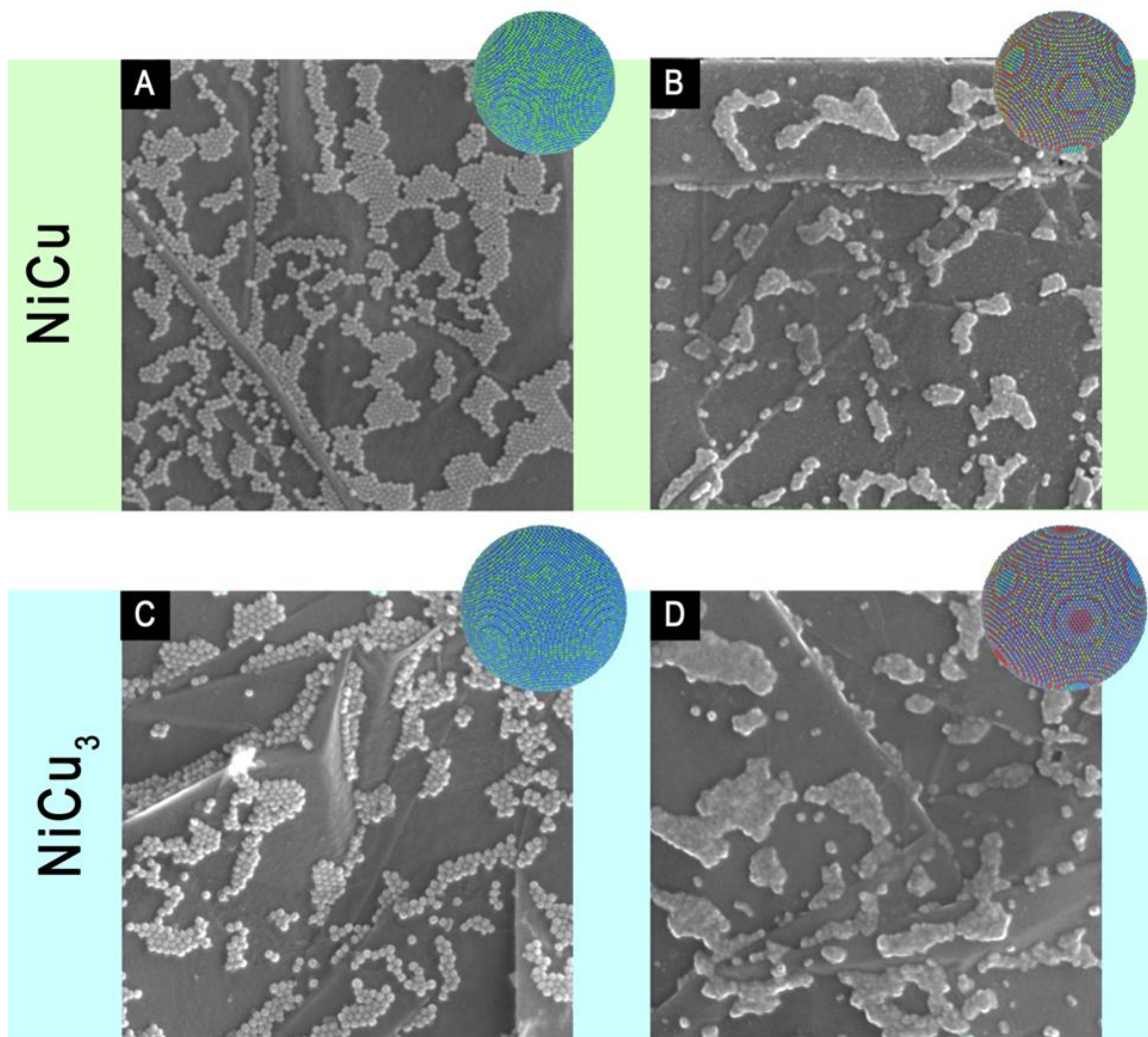


Figure 3.2 SEM micrographs of graphite supported Ni-Cu nanoparticles. (A) NiCu nanoparticles after deposition and (B) NiCu nanoparticles after plasma treatment and annealing to 700 °C. (C) NiCu₃ nanoparticles after deposition and (D) NiCu₃ nanoparticles after plasma treatment and annealing to 700 °C. The size of the images is 1 × 1 μm². Model colors: light blue = Cu atoms, green = Ni atoms, red = oxygen atoms.

In order to understand the structure and chemical state of the NC particles under the reaction conditions, we performed NAP-XPS characterization for both the NiCu and

NiCu₃ NCs, with their spectra shown in Figure 3.3. Additional XPS information about binding energies and the contributions of surface species are listed in Table 3.1. Immediately after evacuating the samples at room temperature, the spectra of Cu and Ni show that both elements were mostly oxidized. For Ni, the XPS signals can be assigned to Ni²⁺ (853.7 eV), indicative of NiO, and Ni³⁺ (855.6 eV), indicative of Ni(OOH) or Ni₂O₃. While the Cu signal has significant contributions from Cu²⁺ (934.7) and metallic Cu⁰ (932.4 eV), the presence of Cu¹⁺ cannot be ruled out due to its overlap with the metallic signal.

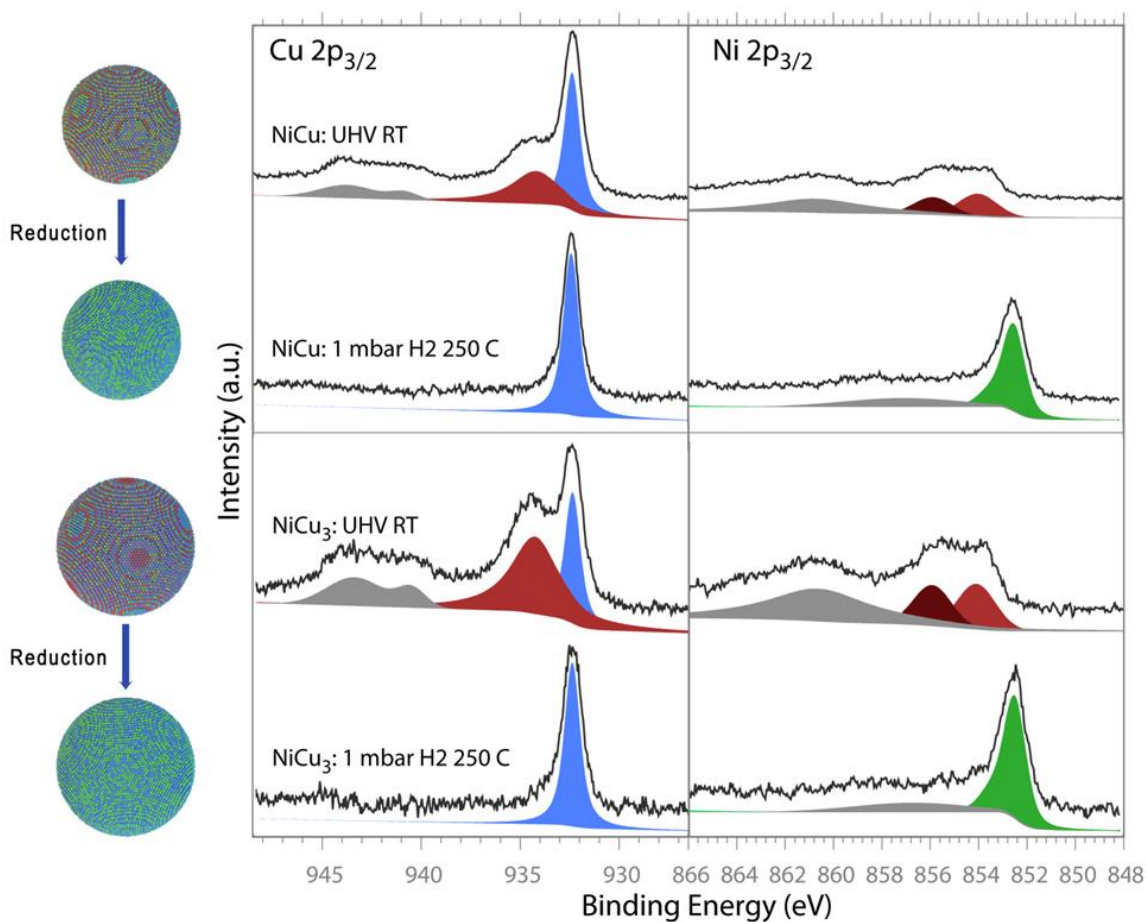


Figure 3.3 NAP-XPS spectra of Cu 2p and Ni 2p core levels of NiCu and NiCu₃ nanoparticles measured in UHV and under 1 mbar of H₂ at 250 °C. The spectra are

normalized to the metallic Cu 2p_{3/2} signal and offset for clarity. XPS colors: light blue = Cu (0), green = Ni (0), red = oxidized metals, grey = satellite signals; model colors: light blue = Cu atoms, green = Ni atoms, red= oxygen atoms.

Table 3.1 XPS results summary. The relative contributions are calculated with respect to the whole area of the Ni 2p_{3/2} or Cu 2p_{3/2} region (100 %). The Ni:Cu ratio is calculated by integrating the area of Ni 2p_{3/2} corrected for the photoionization cross-section divided by the Cu 2p_{3/2} area, corrected in the same way.

	BE (eV)	Relative contribution to the Ni 2p or Cu 2p signal (%)			
		NiCu (UHV)	NiCu (H ₂)	NiCu ₃ (UHV)	NiCu ₃ (H ₂)
Ni ⁰	852.5	0	100	0	100
Ni ²⁺	853.7	56	0	52	0
Ni ³⁺	855.6	44	0	48	0
Cu ⁰	932.4	70	100	33	100
Cu ²⁺	934.7	30	0	67	0
Ni:Cu	-	0.8	0.9	0.8	0.9

The spectra obtained in 1 mbar of H₂ at 250 °C are also shown in Figure 3.3 and are more indicative of the surfaces under the reaction conditions. The reduction treatment led to the complete reduction of both Cu and Ni to their metallic states in both the NiCu and NiCu₃ NCs. Based on photoionization cross-section analysis, both the NiCu and NiCu₃ NCs exhibit a Ni : Cu molar ratio close to 1 : 1, as indicated in Table 3.1, in the surface region mapped by XPS. This result implies that Ni segregates to the surface in the NiCu₃ nanoparticles, leading to the formation of a Ni-rich shell on a Cu-rich core. The formation of such a core–shell structure is not surprising. During the sample preparation, the NCs

were mildly oxidized by oxygen-plasma and rapid-thermal-annealing treatments in order to remove the surface organic ligands. Since Ni is easier to be oxidized than Cu, there is a driving force to segregate Ni on the particle surface. After reduction, Ni forms an alloy with Cu, resulting in a Cu-rich core and Ni-rich shell structure. Similar observations have been reported for Pt–Co [45]. However, with Pt–Co NCs spectroscopic data suggested the formation of a stable CoO_x layer at the surface that could not be reduced under the conditions of that study [45].

3.3.2 HDO studies

High-pressure HDO of HMF in alcohol solvents is a sequential reaction in which DMF is an intermediate product that can further react to form secondary products, as shown in Figure 3.4 [38,103]. HMF (A) is first partially hydrogenated into a group of intermediate species (B), including 5-methylfurfural (MF), 2,5-bis-hydroxymethyl)furan (BHMF), 2-propoxymethyl-5-furanmethanol (ether-furfuryl alcohol, or EFA), 2-propoxymethyl-5-methylfuran (ether-methyl furan, or EMF), 2-hydroxymethyl-5-methylfuran (HMMF), and 2,5-bis(propoxymethyl)furan (BEF). All these intermediates can react further to produce DMF (C), which in turn reacts to form over-hydrogenated products (D), such as DMTHF, 2-hexanone and 2,5-hexanedione. Hexanone and hexanedione can undergo reductive etherification to form other derivatives, such as 1-propoxy-1-methylpentane (2-propoxyhexane) and 1,4-dipropoxy-1,4-dimethylbutane (2,5-dipropoxyhexane), which are not shown in Figure 3.4.

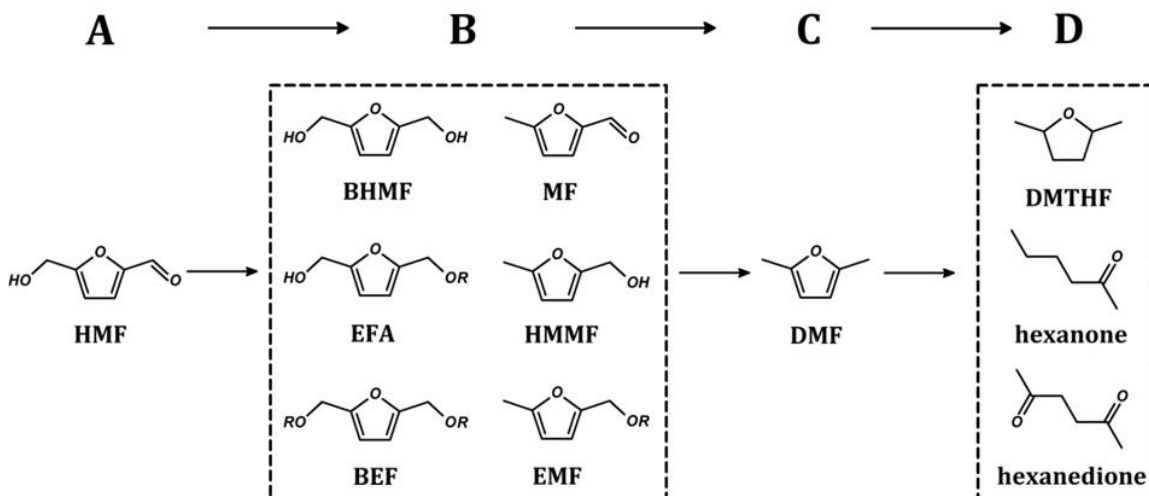


Figure 3.4 Reaction network for HDO of HMF using alcohols as solvent.

The product distributions as a function of reactor space time over 10 wt% monometallic Ni/C and Cu/C catalysts are shown in Figure 3.5 for the reaction at 180 °C and 33 bar total pressure. The results for Ni/C, shown in Figure 3.5(a), are similar to what has been reported previously and are consistent with the sequential reaction scheme discussed above [38,103]. Partially hydrogenated products (B) are formed only at the lowest space times and these rapidly diminish. DMF production initially increases with space time, and then declines, while the over-hydrogenated products are formed only at longer space times. The maximum DMF yield was about 55%. A more detailed list of the other products and their yields is reported in Table 3.2. Cu/C was much less reactive, as shown in Figure 3.5(b). The maximum conversion of HMF was less than 40% at the longest space time and the products were primarily the partially-hydrogenated compounds (B). No DMF was observed on the Cu catalyst under the conditions used here. The results are consistent with the fact that Cu-based catalysts are used to hydrogenate furfural to furfural

alcohol [124,125]. Although the 1-propanol solvent can serve as a hydrogen donor in catalyzed transfer hydrogenation (CTH), no propanal was observed in the products. Considering the fact that CTH is commonly catalyzed by Lewis acid catalysts [126,127], the transfer hydrogenation likely did not interfere with the HDO reaction in this work.

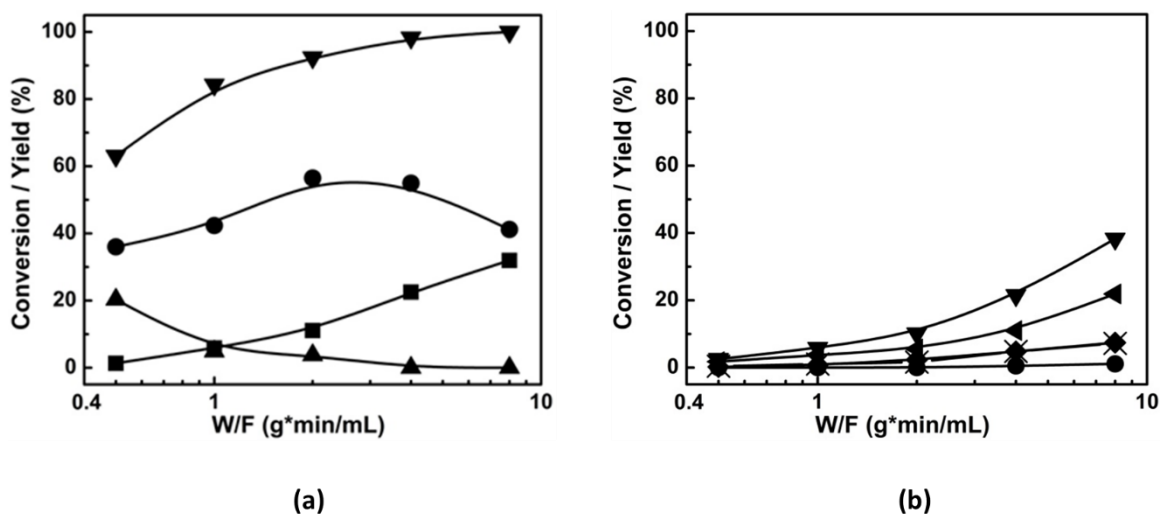
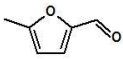
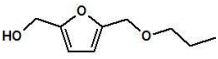
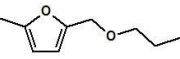


Figure 3.5 Conversion and product yield for the HDO reaction of HMF over 10-wt% impregnated (a) Ni/C, (b) Cu/C, as a function of reactor space time. Reaction conditions: 33 bar and 180 °C. (▼) HMF conversion, (▲) product group B, (●) DMF, (■) product group D, (◄) 5-methyl furfural (MF), (◆) 2,5-bis(propoxymethyl) furan (BEF), (×) 2-hydroxymethyl-5-methyl furan (HMMF).

Table 3.2 B and D group product distribution for HDO of HMF over 10-wt% Ni/C in 1-propanol, under 180 °C and 33 bar. (Yield %)

W/F (g·min/mL)	B group products			D group products	
					
0.5	2.3	14.8	3.2	0.2	1.1
1	1.2	2.6	1.1	0.4	5.4

2	<1	1.5	<1	0.3	10.7
4	0	0	0	1.5	21.0
8	0	0	0	6.0	23.1

Several bimetallic Pt-based catalysts have been shown to be very selective for the production of DMF, with yields above 98% [45,46], even though Pt and some of the metals with which it was alloyed were not selective. To determine how Ni–Cu bimetallic catalysts would perform, similar continuous-flow reaction experiments were carried out over the NiCu and NiCu₃ bimetallic catalysts. Figure 3.6 presents data for HMF conversion and product yields as a function of space time at 180 °C and 33 bar for 10 wt% NiCu/C and NiCu₃/C catalysts prepared by conventional impregnation methods. The product curves for NiCu, Figure 3.6(a), and NiCu₃, Figure 3.6(b), are qualitatively similar to the results shown earlier for the monometallic Ni catalyst, but with different yields. Surprisingly, the rates on all three catalysts were similar as shown by the fact that conversions at any given space time were similar. For example, at a space time of 0.5 g min mL⁻¹, the conversion over NiCu/C was 85% and 60% on both NiCu₃ and Ni catalysts. This relatively small difference could be due to differences in metal dispersions, which are difficult to measure on Ni–Cu alloys in general [128], especially when using a carbon support.

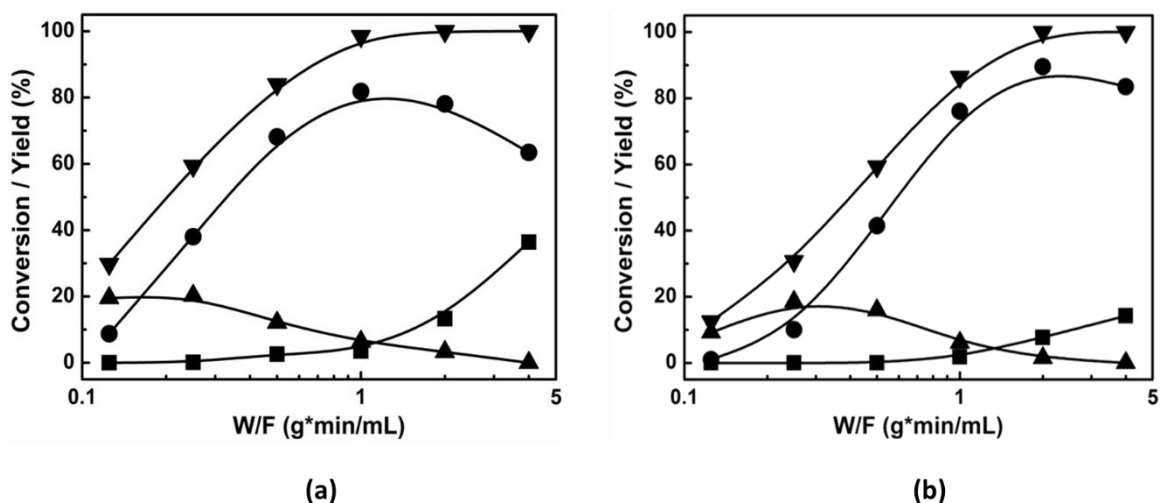
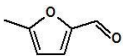
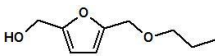
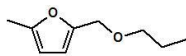


Figure 3.6 Conversion and product distribution for the HDO reaction of HMF over 10-wt% (a) IMP NiCu/C, (b) IMP NiCu₃/C, as a function of reactor space time. Reaction conditions: 33 bar and 180 °C. (▼) HMF conversion, (▲) product group B, (●) DMF, (■) product group D.

Both the NiCu and NiCu₃ catalysts exhibited greatly improved DMF selectivities, with maximum yields in the range of 80 to 90%. However, at longer space time, the DMF yields on both Ni–Cu catalysts decreased, an indication that DMF was reacting to form over-hydrogenated products (D group). While a detailed analysis of the B and D compounds from NiCu/C is given in Table 3.3, the main over-hydrogenated products on the Ni–Cu catalysts were 2,5-hexanedione and DMTHF, which were also the primary products formed by the reaction of DMF on Ni/C. Unlike the reaction of HMF on Pt [38], I did not observe significant amounts of the etherification by-products, 2-propoxyhexane or 2,5-dipropoxyhexane, on the Ni-based catalysts, which were formed by reaction with the alcohol solvent.

Table 3.3 B and D group product distribution for HDO of HMF over 10-wt% impregnated NiCu/C in 1-propanol, under 180 °C and 33 bar. (Yield %)

W/F (g·min/mL)	B group products			D group products	
					
0.125	8.4	9.4	1.7	0	0
0.25	7.7	10	2.5	0	<1
0.5	4.8	7.1	<1	0	2.1
1	1.2	5.2	0	<1	3.2
2	0	3.3	0	5.3	8
4	0	0	0	17.5	18.9

In previous HDO studies of Pt–Ni and Pt–Co catalysts, compositional uniformity was shown to be a critical factor in determining selectivity [45,46], and NC catalysts prepared by solvothermal methods with the optimal composition showed greatly improved yields compared to catalysts having the same overall composition but prepared by conventional impregnation. To determine whether this would also be true with the Ni–Cu catalysts, I investigated the HDO reaction on the highly uniform 10 wt% NiCu and NiCu₃ NC catalysts, with the conversions and yields shown in Figure 3.7. Both NC catalysts achieved better DMF selectivities compared to impregnated catalysts, with yields of 96.1% for the NiCu/C catalyst and 98.3% for the NiCu₃/C catalyst.

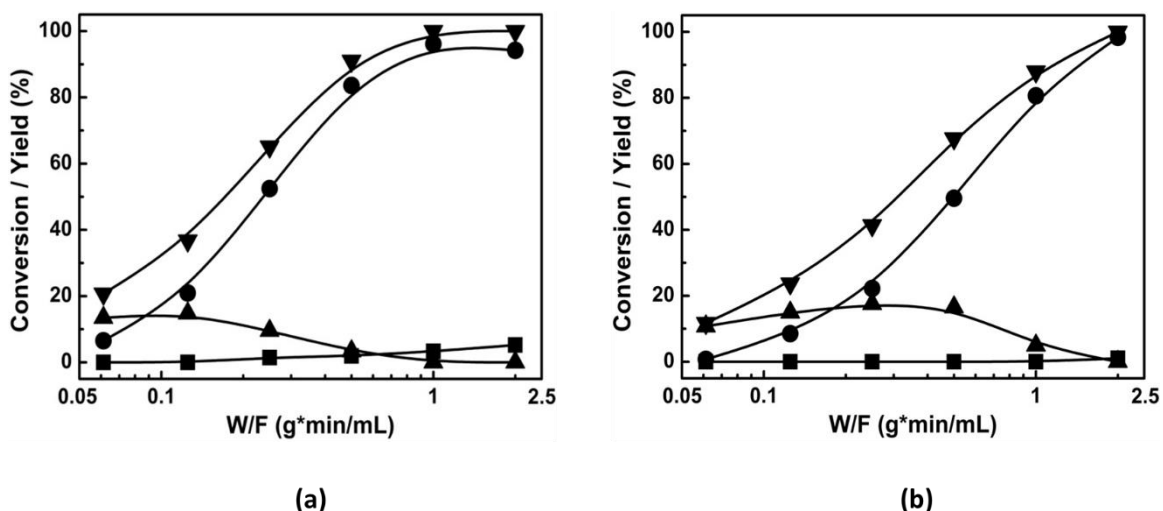


Figure 3.7 Conversion and product distribution for the HDO reaction of HMF over 10-wt% (a) NCs NiCu/C, (b) NCs NiCu₃/C, as a function of reactor space time. Reaction conditions: 33 bar and 180 °C. (▼) HMF conversion, (▲) product group B, (●) DMF, (■) product group D.

Some deactivation of the HDO activities was observed over the Ni–Cu NCs. For example, at 180 °C, 33 bar and 0.5 g min L⁻¹ W/F, the HMF conversion after 4 h decreased by about 10% over the NiCu NCs and nearly 50% over a conventional Ni catalyst. However, the selectivity was not affected by time on stream. To demonstrate that deactivation was not due to sintering, I analyzed the NC particle-size distributions before and after reaction, as shown in Figure 3.8. Within experimental uncertainty, there was no change in the particle size. In previous work [38], it was argued that the deactivation is due to the formation of humins that block the metal active sites, based on the fact that stability scaled with the carbon balances on various catalysts.

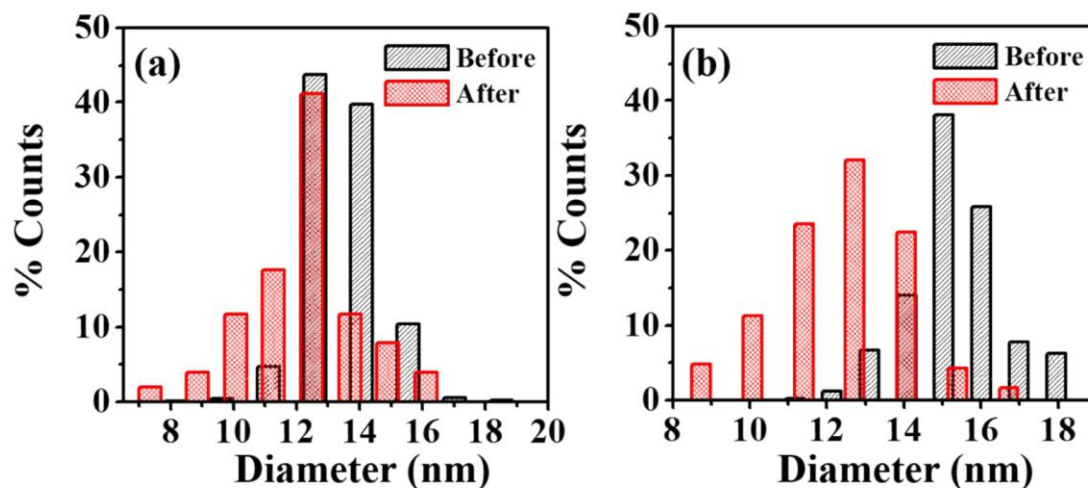


Figure 3.8 The size distributions of (a) NiCu and (b) NiCu₃ before (black) and after (red) catalytic reactions.

3.3.3 Reaction of DMF

Because HDO of HMF is a sequential reaction in which DMF can undergo additional reaction, high selectivities for DMF require that DMF be unreactive. Therefore, I investigated the reaction of DMF over the various Ni–Cu alloy catalysts by feeding DMF in a solution with 1-propanol at the same molar concentration as that used in the HMF reaction studies. The experiments were carried out under the same reaction conditions, 180 °C with 33 bar H₂; and the data are summarized in Figure 3.9. The most notable difference between the catalysts was their activity, following the order: IMP NiCu/C > IMP NiCu₃/C > NC NiCu/C > NC NiCu₃/C.

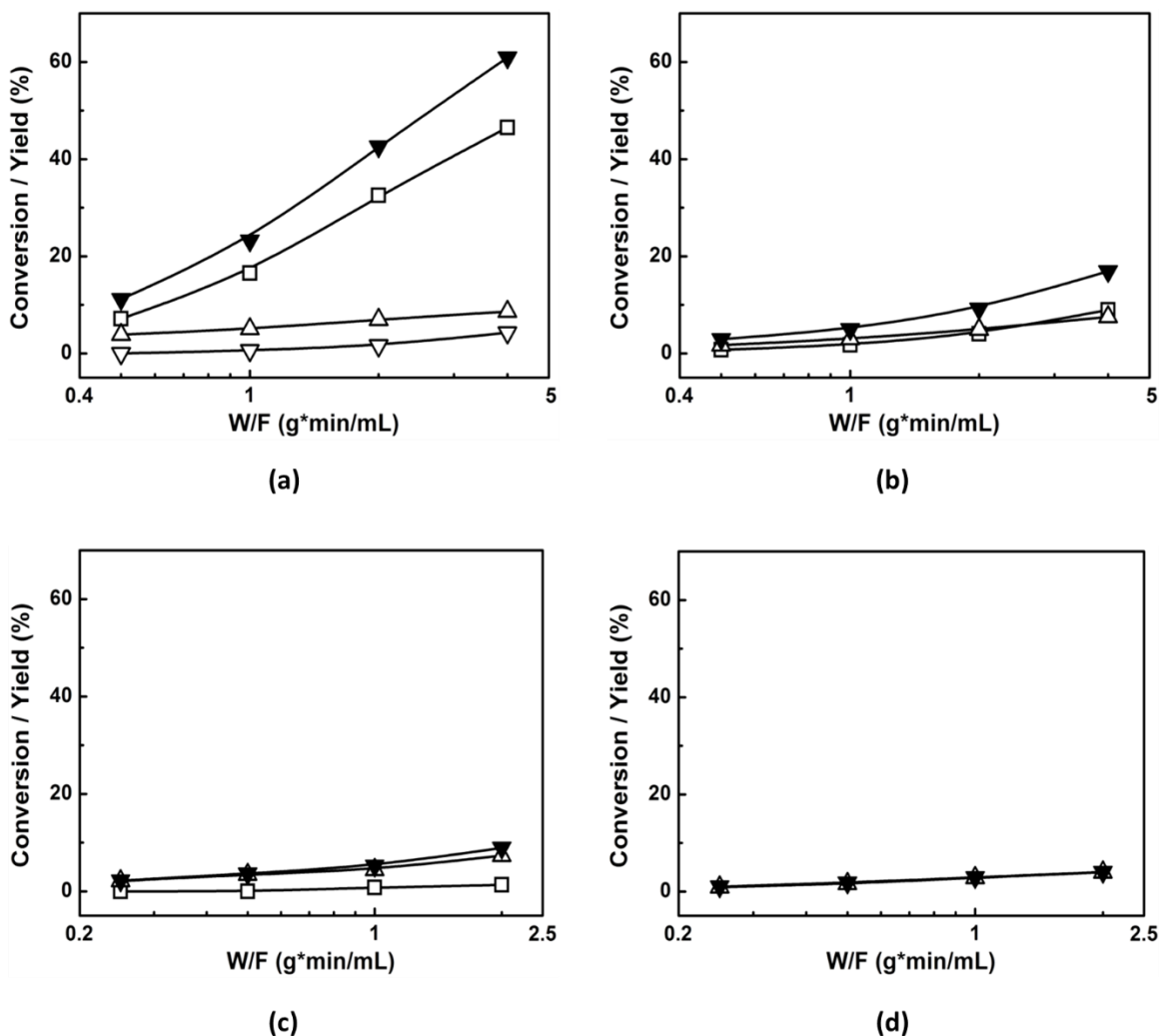


Figure 3.9 Conversion and product distribution for the reaction of DMF over 10-wt% (a) IMP NiCu/C, (b) IMP NiCu₃/C, (c) NCs NiCu/C, (d) NCs NiCu₃/C, as a function of space time. Reaction conditions: 33 bar and 180 °C. (▼) DMF conversion, (□) DMTHF, (▽) 2-hexanone, (△) 2,5-hexanedione.

The data in Figure 3.9 are consistent with the sequential reaction mechanism and the reaction data for HMF. There is a direct relationship between the catalyst selectivity and the reactivity of DMF. Furthermore, the products from the reaction of DMF were primarily DMTHF and 2,5-hexanedione, which were also the primary products that formed

from HMF on these catalysts at longer space times. Since less water is formed in the reaction of DMF, the yields of hexanedione tend to be lower with DMF.

3.4 Discussion

The results of the present chapter confirm that alloy catalysts are capable of higher DMF selectivities for HDO of HMF. DMF yields above 95% have been achieved over Pt–Co, Pt–Ni, Pt–Zn, Pt–Cu, and, now, Ni–Cu alloy catalysts [45,46]. In each of these cases, high selectivities have been shown to be related to the suppressed reaction of DMF to form over hydrogenated products. Ni–Fe [41] and Co–Cu [120] alloys have also been reported to show high selectivities for HDO reactions. Although suppressed reactivity of DMF has not been confirmed in those cases, it seems likely that the Ni–Fe and Co–Cu systems would show this similarity as well. The important question is that why do all of these alloys exhibit reaction properties that are so different from their monometallic counterparts. It seems likely that the alloying metal in each case prevents the furan ring from lying down on the catalyst surface. Previous studies suggested that the alloying metal's oxophilicity was the key to achieve such conditions [41] or that surface oxides of the alloy catalyst can prevent the further interaction of the furan ring [46]. Since Cu is not normally considered an oxophilic metal and since NAPXPS analysis indicates that the particles have a completely reduced surface at 250 °C even at low H₂ pressure, similar explanations cannot apply to the Ni–Cu NCs of the study presented in this Chapter.

The role of Cu in the Ni–Cu alloys may be to decrease the ensemble size at the Ni surface [129]. An alternative explanation is based on the results from Xiong *et al.* [130]

who investigated the HDO reactions by adsorption of furfural on Cu(111), Ni(111), and Ni–Cu model surfaces. On Cu(111), they observed that furfural adsorbed only weakly via an $\eta^1(\text{O})$ configuration, whereas furfural was strongly bonded on the Ni(111) surface through an $\eta^2(\text{C},\text{O})$ configuration and decomposed nonselectively. Selective reaction of furfural to 2-methyl furan was observed on a Cu(111) surface with a Ni overlayer.

The differences between the Ni–Cu catalysts prepared by conventional impregnation and those prepared from nanocrystals are likely due to catalyst homogeneity. The individual metal particles in the impregnated catalysts almost certainly have varying compositions and the presence of some Ni-rich particles will limit the selectivities, similar to what was found with Pt–Co catalysts prepared by conventional impregnation [45]. This inhomogeneity problem is particularly serious when dealing with sequential reactions in which the desired product is an intermediate. Even if the majority of the catalyst is selective, that part of the catalyst that is not can further promote the reaction of the desired product. Compared to alloys like Pt–Ni and Pt–Co, Cu-based alloys will be less sensitive to compositional heterogeneity because Cu is relatively unreactive. However, the advantages of the nanocrystal catalysts prepared by solvothermal methods were still apparent with the Ni–Cu system.

The oxidation state of the catalyst surface during reaction is important to consider. Our present XPS results demonstrate that the Ni–Cu catalysts are reduced with very mild pretreatments, so that the catalyst is certainly reduced before reaction. A calculation of the bulk thermodynamics for the reaction $\text{Ni} + \text{H}_2\text{O} \rightleftharpoons \text{NiO} + \text{H}_2$ shows that equilibrium will

occur at a $P(\text{H}_2) : P(\text{H}_2\text{O})$ ratio of $\sim 10^{-3}$ at 180 °C. Since the $P(\text{H}_2) : P(\text{H}_2\text{O})$ ratio was never less than 25 in our reactor, the thermodynamics of the nanoparticles would have to be dramatically different from that of the bulk for the particles to be oxidized under the reaction conditions. In previous work on Pt–Co NCs catalysts, where a surface CoO_x was observed [45], bulk thermodynamics would again suggest that Co should be in its metallic form. In addition to the fact that the thermodynamics of surface Co reduction may be somewhat different from that of the bulk [131], it appears that the reduction may have been kinetically limited in that case, since the catalyst was not reduced, even by the initial pretreatments. The fact that Ni–Cu alloys are capable of providing high selectivities for DMF production demonstrates that reasonably inexpensive catalysts can be used for selective HDO of HMF. It is interesting to know whether these base-metal alloys could also be used for other HDO reactions, as such would be important in the processing of lignin. There are indeed indications for this [49].

CHAPTER 4. A COMPARISON OF FURFURAL HYDRODEOXYGENATION OVER PT-CO AND NI-FE CATALYSTS AT HIGH AND LOW H₂ PRESSURES³

Summary

This chapter reports the results of HDO of furfural at high and low H₂ pressures, using catalysts that were previously identified as exhibiting some of the best selectivities for furfural at low pressures (Ni-Fe) and for HMF at high pressures (Pt-Co). The goal of this work was to demonstrate the correspondence between these two reactants. A key finding in this study is that catalysts which are selective for HDO as opposed to decarbonylation at low pressures also suppress the reaction of DMF to over-hydrogenated products at high pressures (*vice versa*). The implications for the underlying relationships in these reactions are discussed.

4.1 Introduction

Furfural, similar to HMF which I have discussed in Chapters 1 and 3, is another biomass-derived, platform molecule that can be upgraded and stabilized to produce

³ This chapter was published as **C. Wang**, J. Luo, V. Liao, J.D. Lee, T.M. Onn, C.B. Murray, R.J. Gorte, *Catalysis Today* 302 (2018) 73–79.

derivatives that can be used in various chemical applications or added to conventional fuels [28,30]. Selective upgrading is necessary for most applications because the carbonyl group in furfural is highly susceptible to oligomerization and reaction with other functional groups. One important product formed from furfural is furfural alcohol, which is used directly in the polymer industry and as an intermediate in the production of various fine chemicals [132]. Commercial catalysts based on Cu chromite are reasonably effective for this hydrogenation reaction. Another potentially important reaction for stabilizing furfural is hydrodeoxygenation (HDO) to 2-methyl furan (MF), which can also be used as an intermediate for chemicals production or as a fuel additive due to its high octane number and low water solubility [133]. HDO consumes a relatively small amount of H₂, maintains the aromatic furan ring, and avoids loss of carbon from the final product via decarbonylation [41,134].

Significant effort has gone into developing catalysts for selective HDO of furfural to MF [2]. Most studies of transition-metal catalysts have shown decarbonylation to furan to be a major side reaction; but bimetallic catalysts, particularly ones based on Ni-Fe bimetallics, have been identified as being much more selective than the pure metals [41]. Product distributions also exhibit a strong H₂ pressure dependence [135], apparently due to the effects of hydrogen coverage on the metal [136] as well as the surface crowding of the furanic compounds [137]. For example, a Pt/C catalyst that produced primarily the decarbonylation product, furan, at low pressures produced no measurable furan at high H₂ pressures. Unfortunately, furfural reacted to form various open-ring, over-hydrogenated

compounds, in addition to MF, at high pressures. The evolution of the product distribution with contact time at high H₂ pressures indicated that the reaction is sequential, with MF forming selectively as an initial product that is itself further hydrogenated.

An important conclusion of the earlier study of the H₂-pressure dependence on HDO of furfural is that there are strong similarities between HDO of furfural and of HMF. HDO of HMF to form DMF has also been shown to be a sequential reaction over various transition-metal catalysts [38]. Again, changes in the product distribution with time indicate that HMF first forms a group of partially hydrogenated products which in turn go on to form DMF. DMF can react further to form a range of species that depend on the particular catalyst that is used. For example, a Pt/C catalyst formed largely open-ring molecules while Pd/C produced dimethyl-tetrahydrofuran. Similar to results with HDO of furfural, various bimetallics, including Ni-Cu (see Chapter 3) and a series of Pt-based bimetallic NCs catalysts, were found to exhibit much better selectivity towards DMF [45,46]. The high selectivity in the case of the bimetallic catalysts resulted from suppressed reaction of DMF.

Even though similarities in the HDO of HMF and furfural should be anticipated, research efforts to upgrade these two biomass-based have largely proceeded in parallel. This is due to the fact that HMF has a much lower vapor pressure than furfural, so that reaction studies of HMF are typically carried out in an autoclave at high pressures in the presence of a solvent, while most reported HDO studies of furfural have been performed in vapor-phase flow reactors at lower pressures. As pointed out earlier, reaction pathways

and products for furfural can be different in the presence of high H₂ pressures, making it difficult to compare results from HDO studies of furfural and HMF since most experiments were performed under very different conditions with different catalysts.

This chapter reports the results of HDO of furfural at high and low H₂ pressures, using catalysts that were previously identified as exhibiting some of the best selectivities for furfural at low pressures (Ni-Fe) and for HMF at high pressures (Pt-Co). The results again demonstrate the correspondence between these two reactants. Catalysts that are selective for HDO as opposed to decarbonylation at low pressures also suppress the reaction of DMF to over-hydrogenated products at high pressures.

4.2 Experimental

4.2.1 Catalyst Synthesis

Carbon-supported NiFe, Ni, Fe, Pt and Co catalysts were prepared to have 10-wt% metal loadings by incipient-wetness impregnation, as reported in Chapter 2. PtCo₃ nanocrystals (NC) were synthesized by solvothermal methods that were also described in more detail in Chapter 2. The as-synthesized NCs were mixed with carbon black (Vulcan XC-72R) to a loading of 10-wt% metal.

The surface treatments to remove the ligands for the PtCo₃/C were performed following a previously published procedure [46]. The catalysts were first exposed to O₂ plasma for 15 minutes, followed by thermal treatment at 500 °C for 1 minute for ligand

removal. The elemental composition and concentration of PtCo₃ NCs were determined by Inductively Coupled Plasma-Optical Emission spectrometry (ICP-OES) performed on a Spectro Genesis spectrometer with a concentric nebulizer.

4.2.2 *Reactivity Measurements and Catalyst Characterization*

The high-pressure reactions were conducted in a tubular flow reactor that has been described in Chapter 2. The liquid feed used in this work was a solution of 1-propanol (99+%, Acros) and furfural (99%, Sigma-Aldrich) at a concentration of 1 g/100 mL (solvent-based). The molar ratio of H₂ to furfural in these experiments was fixed at 100. The product distributions were measured as a function of space time, defined as the mass of the catalyst divided by the volumetric flow rate of the furfural-containing liquid (g-cat/mL liquid feed). For all of the experiments conducted in this study, the space time was varied by changing the amount of catalyst in the reactor. Blank experiments with only 1-propanol in the liquid feed produced only small quantities (less than 1%) 1,1-dipropoxypropane over the catalysts used in this study.

Ambient-pressure HDO of furfural was conducted in a separate tubular reactor which has also been described in Chapter 2. The feed to this reactor consisted of 1.0% furfural (99%, Sigma-Aldrich) vapor in pure H₂ (UHP grade, Airgas). Unless otherwise noted, the data reported in this chapter were all acquired 2 hours after starting the reaction. Product distributions were again measured as a function of reactor space time. In the ambient-pressure measurements, this is defined as the mass of the catalyst divided by the

total mass flow rate of furfural and H₂. Carbon balances in the ambient-pressure experiments were greater 90%.

TEM images of the carbon-supported bimetallic catalysts were collected on a JEOL JEM-1400 microscope operating at 120 kV, before and after HDO reaction measurements. The NiFe/C catalyst, shown prior to reaction in Figure 4.1a), was highly non-uniform and had a large distribution of metal particle sizes (average particle size ~12-nm). TEM images following reaction for 3 h, Figure 4.1b), suggested that high-pressure reaction caused a loss of smaller particles due to formation of larger aggregates. The PtCo₃/C NC catalysts were much more homogeneous, consisting of uniform particles, 4-nm in diameter. There was no significant change in size or shape of the NC following reaction. Figure 4.2a)-2c) show images of the initial catalyst following reduction, the catalyst after ambient-pressure HDO at 180 °C for 7 h, and the catalyst after high-pressure HDO at 180 °C for 4 h. All of the images were similar and there were no significant differences following reaction.

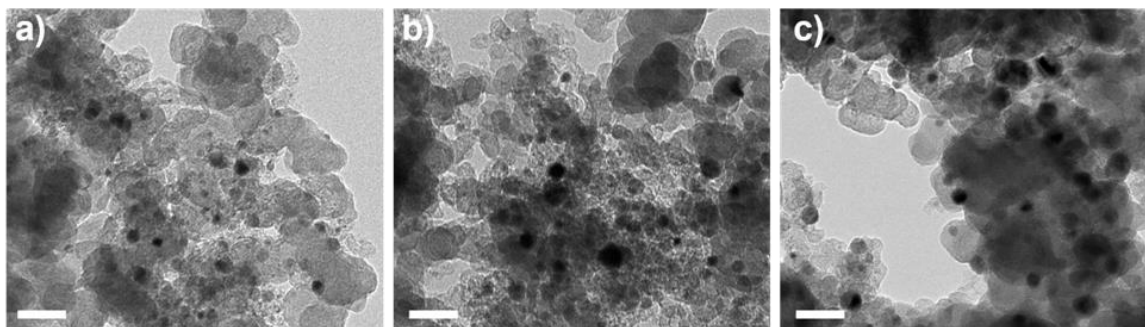


Figure 4.1 TEM images of 10-wt% impregnated NiFe/C: (a) as-prepared; (b) after HDO reaction with furfural at 1 bar; and (c) after reaction at a pressure of 33 bar. The scale bars are 50 nm.

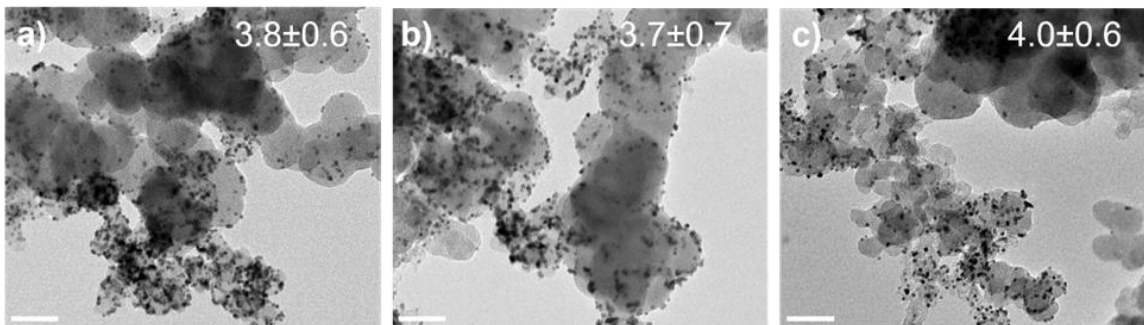


Figure 4.2 TEM images of 10-wt% PtCo₃/C: (a) as-prepared; (b) after HDO reaction with furfural at 1 bar; and (c) after reaction at a pressure of 33 bar. The scale bars are 50 nm. The average sizes and size distributions were presented as (diameter) ± (standard deviation) nm.

4.3 Results

4.3.1 HDO of Furfural at 1 Bar

The initial HDO experiments were performed on 10-wt% Ni/C, Fe/C, and NiFe/C catalysts at 1 bar and 180 °C in order to verify previous reports that the Ni-Fe bimetallics exhibit superior selectivity compared to the monometallic catalysts under these conditions [41]. Because conversions on the Fe/C sample were very low, even when the temperature was increased to 250 °C, product distributions are reported only for the Ni/C and NiFe/C catalysts. These are shown as a function of space time in Figure 4.3. For Ni/C, Figure 4.3a), the major product at low space times was furfural alcohol (FAL), which reached a maximum yield of 25% before decreasing monotonically at higher space times. The methyl furan (MF) yield also went through a maximum of about 33% at a space time of 10 min·g/g before decreasing to form over-hydrogenated products, primarily tetrahydrofurfuryl alcohol (THFA, 31%) and 2-methyl tetrahydrofuran (MTHF, 14%). A more complete listing of products at the highest space time is given in Table 4.1. In addition to these

products, significant amounts of furan, the decarbonylation product, also formed. Unlike FAL and MF, which showed maxima in their yields, the yield for furan reached a nearly steady value for space times greater than about 2.5 min·g/g, increasing from 16% at 2.5 min·g/g to 18% at 20 min·g/g. The maxima in the yields for FAL and MF imply that these are intermediate products in the HDO of furfural to THFA and MTHF. Decarbonylation of furfural to furan occurs in parallel and production of furan stops when all of the furfural has been converted.

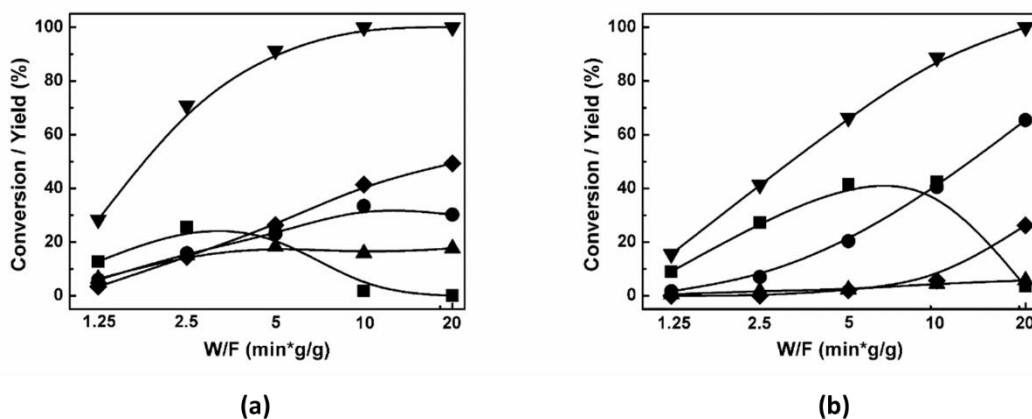


Figure 4.3 Conversion and product distributions for HDO of furfural over 10-wt% impregnated (a) Ni/C and (b) NiFe/C as a function of reactor space time (mass of catalyst divided by mass flow rate of furfural and H₂). Reaction condition: 180 °C and 1 bar. (▼) furfural conversion; (▲) furan yield; (■) FAL yield; (●) MF yield; (◆) over-hydrogenation products.

Table 4.1 Conversion and product yields for HDO of furfural^a over carbon-supported, 10-wt% catalysts at 1 bar at the highest space times.

	Space Time ^c (min·g/g)	Conv. (%)	Yield (%)								
			Furan	FAL ^b	MF	MTHF	THFA	2PON	2POL	PE	1BOL
Ni	20	100	17.6	-	30.3	14.2	30.8	-	-	-	3.1
NiFe	20	100	5.7	3.5	65.4	9.2	12.3	-	-	-	3.3
Pt	10	80.7	49.4	1.9	27.1	2.4	-	-	-	-	-
Co	10	100	-	-	33.7	11.5	-	16.7	30.5	5.1	2.3
PtCo₃	5	100	4.5		80.8	5.4	-	6.4	-	-	2.1

^a Reaction conditions: Temp. = 180 °C, pressure = 1 bar, H₂-to-furfural ratio = 100; ^b FAL = furfuryl alcohol; MF = 2-methyl furan; MTHF = 2-methyl tetrahydrofuran; THFA = tetrahydrofurfuryl alcohol; 2POL = 2-pentanol; 2PON= 2-pentanone; PE = 1-pentane; 1BOL = 1-butanol. ^c Space time is defined as mass of catalyst divided by mass flow rate of furfural and H₂.

Figure 4.3b) shows the conversion and product distributions for the NiFe/C catalyst. While the conversions at a given space time were lower on the bimetallic catalyst, the product yields to MF were significantly better. First, the formation of furan was significantly suppressed on the bimetallic catalyst and the maximum yield was only 5%. Production of FAL again showed a maximum in the yield, suggesting that it is converted to MF in a sequential reaction. The yield of MF reached 65% at the highest space time; because the furfural conversion was nearly complete at this point, that is also likely the maximum yield. Significant amounts of over-hydrogenated products, primarily THFA (12.3%) and MTHF (9.2%), were only observed at the highest space times, probably due to the reaction of MF, since these only begin to form in quantity after MF is formed. Based on a comparison of results for Ni/C and NiFe/C, the bimetallic catalyst shows greatly improved selectivities, suppressing both decarbonylation of furfural and over-hydrogenation of MF, in agreement with previous reports [41].

HDO of furfural at 1 bar total pressure and 180 °C was also studied on the Pt/C, Co/C, and PtCo₃/C catalysts, with results for Pt/C and PtCo₃/C shown as a function of space time in Figure 4.4. The results for Pt/C in Figure 4.4a) show that decarbonylation is the primary reaction pathway on this metal, in agreement with a previous report [135]. The selectivity to furan was greater than 60% at all conversions. The yield for MF was only 16% at the highest space time shown but over-hydrogenation was not significant, perhaps because of the low MF yields. , Although decarbonylation to furan was not a major pathway for the Co/C catalyst and the selectivities to FAL or MF at lower space times were

reasonably good (Figure 4.5), rapid deactivation of this catalyst made the results unreliable, especially at the higher space times. The catalyst showed a 50% and 4-fold reduction in activity and MF yield, respectively, after 3 h. Ring-opened products, including 2-pentanone (2PON), 2-pentanol (2POL), and pentane (PE) were produced in quantity from MF at the highest space time, 10 min·g/g, so that the maximum yield of MF was only 34% at 100% furfural conversion (See Table 4.1).

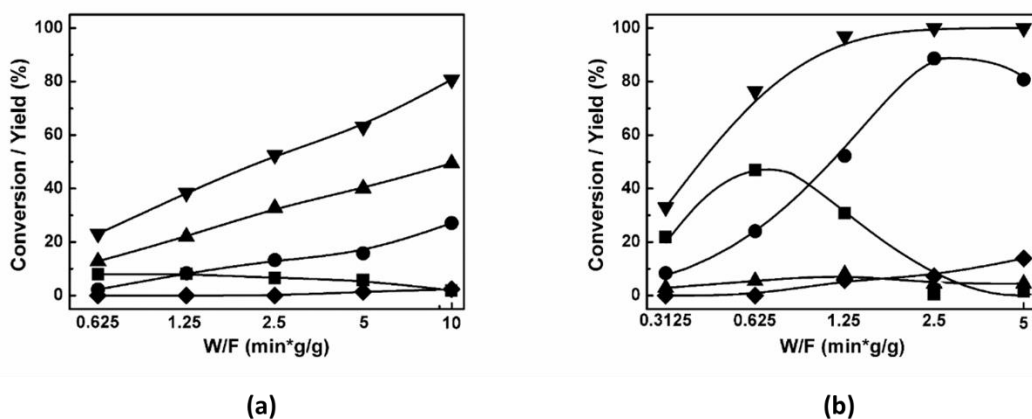


Figure 4.4 Conversion and product distributions for HDO of furfural over 10-wt% impregnated (a) Pt/C; and (b) NCs PtCo₃/C as a function of reactor space time (mass of catalyst divided by mass flow rate of furfural and H₂). Reaction condition: 180 °C and 1 bar. (▼) furfural conversion; (▲) furan yield; (■) FAL yield; (●) MF yield; (◆) over-hydrogenation products.

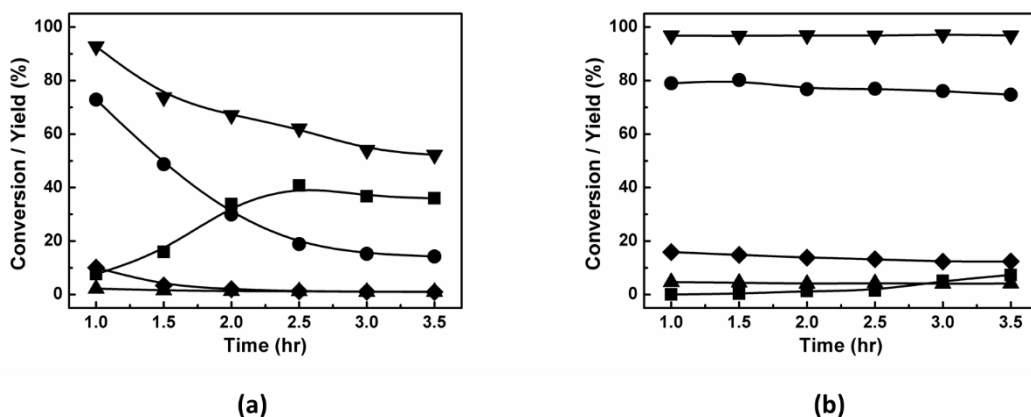


Figure 4.5 Time on Stream for HDO of furfural over 10-wt% (a) impregnated Co/C; and (b) NCs PtCo₃/C as a function of reaction time. Space time: 5 min·g/g; Reaction condition: 180 °C and 1 bar. (▼) furfural conversion; (▲) furan yield; (■) FAL yield; (●) MF yield; (◆) over-hydrogenation products.

A complete reaction network for 1-bar HDO of furfural over catalysts applied in this study is shown in Figure 4.6. NiFe and PtCo₃ bimetallics effectively suppress the reaction routes in gray color, resulting in selective yields of MF.

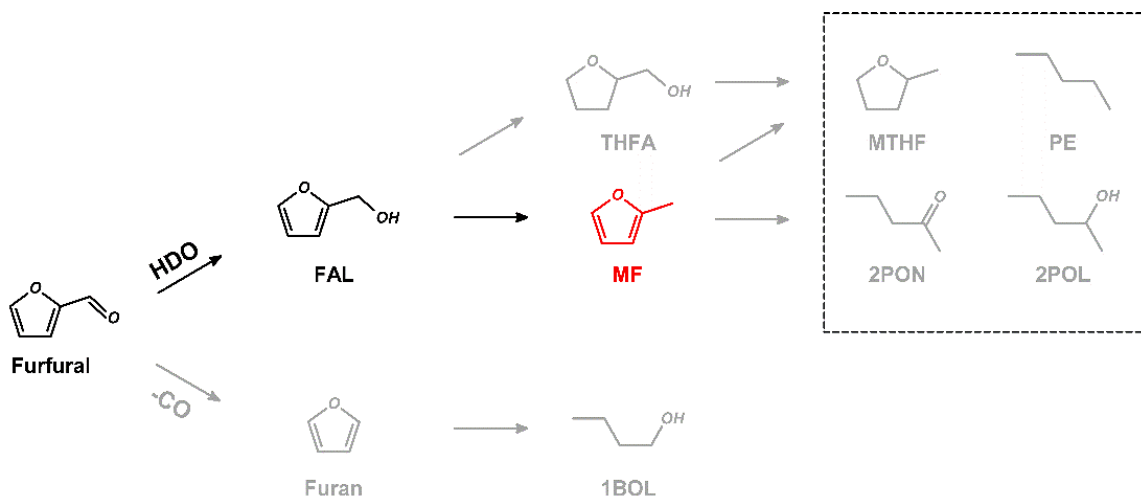


Figure 4.6 Reaction network for 1-bar HDO of furfural carried by H₂. Reaction routes in gray color are suppressed by NiFe and PtCo₃ bimetallics.

Prior HDO studies of HMF at high pressures have shown that Pt-Co NC catalysts exhibit better selectivity and stability than Pt-Co catalysts prepared by conventional methods [45]. Since catalysts prepared from Pt NCs showed similar selectivities to their conventional counterparts, the higher selectivity of the Pt-Co NCs must be due to the compositional uniformity of the NCs, together with the fact that Pt/C and Co/C catalysts are not as selective as the bimetallic catalysts. Therefore, this work presented in Chapter 4 was performed with PtCo₃/C NC catalysts and the conversion and product yields are shown as a function of space time in Figure 4.4b). Because the catalyst was so much more active, measurements were performed at shorter space times. The improved activity of the NCs is likely because of higher metal dispersions. For very short space times, the main product was FAL but FAL then reacted to form MF. The MF yield reached 88% before falling at the longest space times. It is noteworthy that the furan yield never exceeded 8.0% and the over-hydrogenation products only formed at the longest space times, implying that both of these reaction pathways were blocked in bimetallic, compared to the pure-metal catalysts. Compared to Co/C, this catalyst was also stable with time and deactivation over a 3-h period was negligible (See Figure 4.5b).

4.3.2 *HDO of Furfural at 33 Bar*

The high-pressure HDO reactions were carried out at 180 °C and 33 bar, using 1-wt% of furfural in 1-propanol, and results for the different catalysts are shown in Figure 4.7 and Figure 4.8. Again, data are not reported for Fe/C because its HDO activity was very low under these conditions. One major difference between furfural and HMF is that

furfural reacts easily with 1-propanol, forming furfuryl-dipropylacetal (FAct) and furfuryl-propyl ether (FEther). Because of this, the furfural conversions were high at even the lowest space times on all of the catalysts. Since furfural, FAct, and FEther all underwent HDO to form FAL and MF, conclusions regarding the selectivities of the various catalysts are not affected by their production.

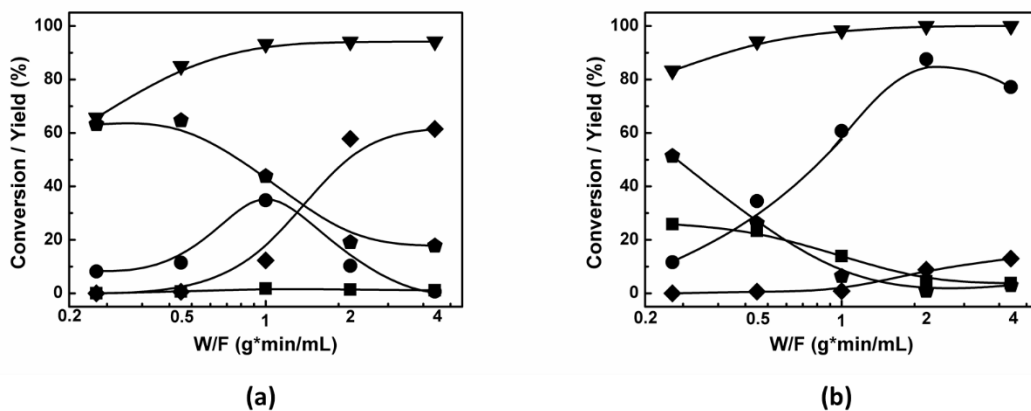


Figure 4.7 Conversion and product distributions for HDO of furfural over 10-wt% impregnated (a) Ni/C and (b) NiFe/C as a function of reactor space time, (mass of catalyst divided volumetric flow rate of liquid feed). Reaction condition: 180 °C and 33 bar. (▼) furfural conversion; (■) FAL yield; (◆) sum of FAct and FEther yields; (●) MF yield; (♦) over-hydrogenation products.

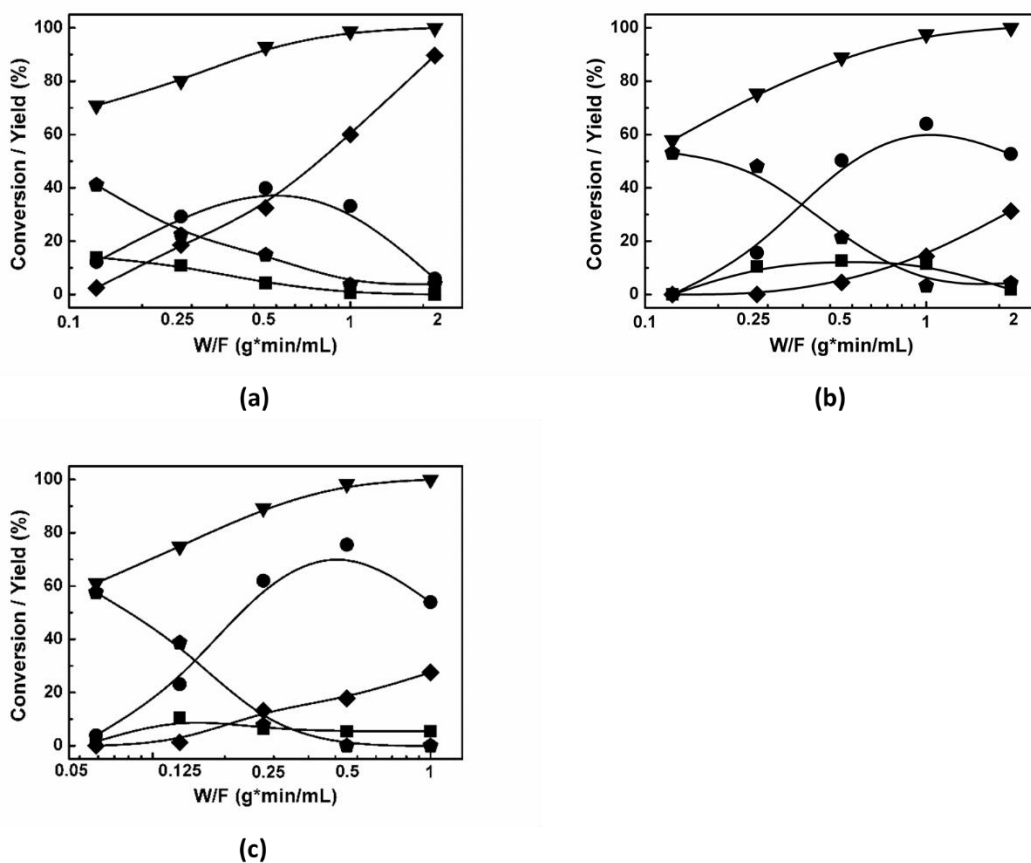


Figure 4.8 Conversion and product distributions for HDO of furfural over 10-wt% impregnated (a) Pt/C, (b) Co/C and (c) NCs PtCo₃/C as a function of reactor space time (mass of catalyst divided volumetric flow rate of liquid feed). Reaction condition: 180 °C and 33 bar. (▼) furfural conversion; (■) FAL yield; (◆) sum of FAct and FEther yields; (●) MF yield; (◆) over-hydrogenation products.

Results for the Ni/C catalyst are shown in Figure 4.7a). Similar to what was reported for HDO of HMF on Pt/C [103], decarbonylation was completely suppressed at these higher pressures. The evolution of the product distribution also implies that reaction of furfural is sequential, similar to what has been reported previously for HDO of HMF. At shorter space times, furfural, FAct, and FEther react to form FAL, which in turn reacts to form MF. The yield of MF reaches a maximum yield of 35% at 1 g·min/mL and then

reacts to form the over-hydrogenated products, listed in detail in Table 4.2. Consistent with the 1-bar experiments, the Ni/C catalyst tends to leave the ring intact (few open-ring products), although the alcohol functionality is removed at the higher pressures and not at the lower pressures.

Table 4.2 Conversion and product yields for HDO of furfural^a over carbon-supported, 10-wt% catalysts at 33 bar at the highest space times

	Space Time ^c (g·min/mL)	Conv. (%)	Yield (%)							
			FAL ^b	MF	MTHF	THFA	2POL	2PON	FEther	FAct
Ni	4	94.2	1.1	0.6	56.2	5.2	-	-	17.8	0
NiFe	4	98.2	3.8	77.2	6.0	2.3	4.7	-	2.9	-
Pt	2	96.8	1.1	11.3	48.2	4.2	23.6	8.4	-	-
Co	2	100	1.9	52.7	15.5	8.7	7.2	-	-	4.2
PtCo₃	1	100	5.5	53.9	19.6	2.2	5.8	-	-	-

^a Reaction condition: temp. = 180 °C, pressure = 33 bar, H₂-to-furfural ratio = 100; ^b FAL = furfuryl alcohol; MF = 2-methyl furan; THFA = tetrahydrofurfuryl alcohol; 2POL = 2-pentanol; 2PON= 2-pentanone; FEther = furfuryl-propyl ether; FAct = furfuryl-dipropylacetal. ^c Space time is defined as mass of catalyst divided volumetric flow rate of liquid feed

The high-pressure results on the NiFe/C bimetallic catalyst, shown in Figure 4.7b), are quantitatively very different from that for Ni/C. Decarbonylation was again nonexistent at 33 bar. The biggest difference between Ni/C and NiFe/C was in the MF yields that were achieved. Based on the yields of MF at lower space times (e.g. 0.5 g·min/mL), the rate of MF formation appears to be somewhat higher on the bimetallic catalyst. Furthermore, the fact that over-hydrogenated products were only formed in small quantities, at the highest space times, implies that the reaction of MF is strongly suppressed relative to what occurs on Ni/C. Because of this, the maximum yield for MF on the bimetallic catalyst was 88%. The results on the Ni-Fe bimetallic are similar to what was reported with HDO of HMF, where other bimetallic catalysts were shown to suppress reaction of DMF [45,46].

The conversion and product yields for HDO of furfural over Pt/C and Co/C catalysts at 180°C and 33 bar, shown in Figure 4.8a) and b), are similar to what has been reported previously for HDO of HMF on these catalysts at the same reaction conditions [38]. (Deactivation of the Co/C catalyst was less severe at these higher pressures, but still significant, similar to what was reported previously for reaction with HMF [38]). The clear patterns for a sequential-reaction mechanism, with an absence of decarbonylation, are observed for both metals. The maximum MF yields were 40% for Pt/C and 64% for Co/C and over-hydrogenated products were observed for both metals at the highest space times. The relatively high yields and the favorable product distributions observed for Co/C were surprising, since Co/C was not as selective as either Pt/C or Ni/C in the reaction of HMF to DMF [38]. Pt/C tended to form more of the open-ring products with furfural, while Co/C preferred to maintain the ring (See Table 4.2) upon over-hydrogenation of MF.

The catalyst prepared from PtCo₃ NCs was more active and selective than either the Pt/C or Co/C catalysts. The higher activity is likely related to the NCs exhibiting a higher dispersion, as discussed earlier; but the higher selectivity must be due to alloy formation. As shown in Figure 4.8c), the maximum yield for the Pt-Co catalyst was 76% and the rates of over hydrogenation were suppressed. Although the selectivity observed here is not dramatically better than that observed on the Co/C catalyst, the Pt-Co catalyst was much more stable. There was no observable loss of activity on the PtCo₃ NCs, even after 6 h (See Figure 4.9). A complete reaction network for high-pressure HDO of furfural can be found in Scheme 2.

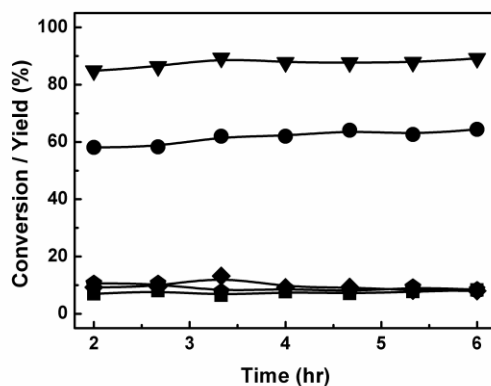


Figure 4.9 Time on Stream for HDO of furfural over 10-wt% NCs PtCo₃/C as a function of reaction time. Space time: 0.25 min·g/mL; Reaction condition: 180 °C and 33 bar. (▼) furfural conversion; (■) FAL yield; (◆) FAct and FEther yield; (●) MF yield; (♦) over hydrogenation products.

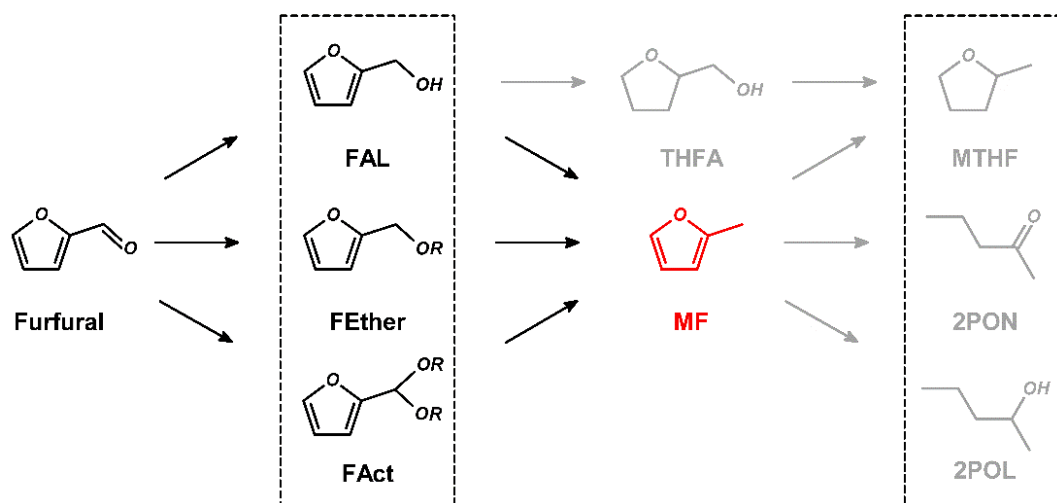


Figure 4.10 Reaction network for high pressure HDO of furfural in 1-propanol solvent. **R** represents propyl group. Reaction routes in gray color are suppressed by NiFe and PtCo₃ bimetallics.

4.4 Discussion

Most hydrodeoxygenation (HDO) studies of furfural are performed at H₂ pressures below one atmosphere and focus on the selectivity of HDO to methyl furan (MF) against decarbonylation to furan, while most HDO studies of 5-hydroxymethylfurfural (HMF) are performed at higher H₂ pressures and focus on the selectivity of dimethyl furan (DMF) against over hydrogenation and ring opening. Previous work demonstrated that the differences in the nonselective pathways observed for furfural and HMF are related to the H₂ pressure and not to differences between the furfural and HMF [135]. High H₂ pressures result in higher coverages of hydrogen on the catalyst surfaces and theoretical calculations have shown that this should change the way in which furfural and HMF bond to the surface [136]. Surface crowding at high pressures has also been suggested to contribute to the suppression of decarbonylation due to formation of a densely packed furfural adlayer [137].

In work from this chapter, I have demonstrated that catalysts which suppress decarbonylation also suppress over hydrogenation of MF and DMF. This implies that there

must be a relationship between the decarbonylation reaction and the over-hydrogenation reactions. Since over hydrogenation involve reactions of MF, while decarbonylation involves reaction of furfural itself, it is not immediately obvious that these two reactions should be so strongly related. Indeed, the fact that the PtCo₃/C was not as selective as the Ni-Fe catalyst in the high-pressure reactions, even though it was the most selective in 1-bar experiments, is further evidence that these pathways are not identical, even though they must be related.

The mechanisms that have been suggested for increased selectivities in alloy catalysts mostly focus on how the alloying metal stabilizes adsorption of the aldehyde, arguing that the alloy stabilizes the furfural adsorbate in such a way as to prevent the furan ring from lying down on the catalyst surface. For example, it has been reported that the oxophilicity of Fe in Ni-Fe can stabilize the $\eta^2(\text{C},\text{O})$ adsorption of furfural, suppressing the acyl intermediates that undergo decarbonylation and tilting the furan ring away from the catalyst surface [41,138]. For Pt-Co bimetallic catalysts, previous work has observed a formation of CoO_x monolayer on catalyst surface [45]; and it was suggested that this overlayer suppresses interactions of the furan ring with the catalyst surface. The fact that over-hydrogenation of MF and DMF are suppressed on the bimetallic surface suggests that the metals must have a similar effect on the adsorption of these adsorbates, perhaps suppressing their adsorption completely when the surface is covered in hydrogen.

Regardless of the differences in the two reaction pathways, it is rather clear that bimetallic catalysts can effectively suppress both decarbonylation and over-hydrogenation. These materials will likely also prove to be selective for other HDO reactions.

CHAPTER 5. A STUDY OF TETRAHYDROFURFURYL ALCOHOL TO 1,5-PENTANEDIOL OVER Pt-WO_x/C⁴

Summary

The publication featured in this chapter investigated the ring opening reaction of THFA. Different from the HDO chemistry I have discussed in Chapter 3 and 4, the selective C-O scission presented here does not involve oxygen removal, but instead to transform the ring structure into the corresponding alkyl diols. In this work, it was first and foremost a demonstration that certain M¹-M²O_x combination exhibited high activity and selectivity to 1,5-PeD. A more comprehensive study of the Pt-WO_x system then indicated that the active form of the catalyst exists as a thin, submonolayer film of the oxide on the Pt surface. This film could be formed by Atomic Layer Deposition (ALD) of W(CO)₆ onto the Pt nanocrystals (NCs) and STEM-EDS mapping demonstrated that ALD deposition occurred selectively on the Pt.

5.1 Introduction

As I have discussed in Chapter 1, the selective conversion of tetrahydrofurfuryl alcohol (THFA) to 1,5-pentandiol (1,5-PeD) has received a significant amount of attention as a means for producing α,ω -diols from biomass-derived chemicals. Bimetallic HDO

⁴ This chapter was published as **C. Wang**, J.D. Lee, Y. Ji, T.M. Onn, J. Luo, C.B. Murray, R.J. Gorte, *Catalysis Letters* 148 (2018) 1047–1054. Reprinted by permission from Springer Nature.

catalysts, including those that I have tested in the studies reported in Chapter 3 and 4, are not active or selective for this ring-opening reaction. On the other hand, selective conversions were reported over a number of bifunctional catalysts, including supported Rh-ReO_x [31,90,91], Pt-WO_x [92–95] and other M¹-M²O_x pairs [96–100]. In these systems, the simultaneous presence of both the metal (M¹) and the metal oxide (M²O_x) has been shown to be critical for achieving high activity and selectivity to terminal diols in these reactions.

It is not entirely clear what role the metal oxide plays in these reactions. Although it is often times not explicitly stated, the leading hypothesis is that hydroxyls on the metal oxide are Brønsted sites [90]. According to this, donation of a proton from the Brønsted site stabilizes an oxocarbenium-ion transition state that forms upon ring-opening reactions. That the metal oxides form Brønsted sites was shown primarily through ammonia-adsorption measurements; however, it should be noted that ammonia can adsorb on almost any oxide, including ones that are usually considered solid bases, such as CaO [102]. Furthermore, the metal oxides that seem to exhibit the best performance are not necessarily the ones that would most obviously lead to Brønsted acidity.

In the study presented in this chapter, I investigated further the role of metal oxide promoter. I started by confirming earlier observations that only reducible oxides were able to improve activity and selectivity [31]. Focusing on the Pt-WO_x system, I demonstrate that the active and selective phase appears to be one in which the oxide covers the metal in a near-monolayer form. The results suggest that promoter reducibility may be important for stabilizing the monolayer oxide structure.

5.2 Experimental

5.2.1 Catalyst Synthesis

All of the catalysts examined in this study were supported on carbon (Vulcan XC-72R). A listing of these catalysts and the precursors used to make them is given in Table 5.1. Most of the samples were prepared by conventional, incipient wetness, as discussed in Chapter 2.

Table 5.1 A listing of $M^1-M^2O_x/C$ catalysts and their precursors used in this study

$M^1-M^2O_x/C$ catalysts						
Pt-WO_x	Pt-ReO _x	Pt-MoO _x	Pt-NbO _x	Pt-VO _x	Pt-CeO _x	-
Pt-CrO_x	Pt-MnO _x	Pt-ZnO	Pt-YO _x	Pt-Al ₂ O ₃	Pt-CoO _x	-
Ir-WO_x	Ir-MoO _x	Ir-VO _x	Ru-WO _x	Ni-WO _x	Co-WO _x	Pd-WO _x
Precursors						
Pt	tetraammineplatinum(II) nitrate (Pt basis 99.99%, Alfa Aesar)					
Pd	tetraamminepalladium(II) nitrate solution (Pd 5%, Alfa Aesar)					
Ir	iridium(III) chloride hydrate (reagent grade, Aldrich)					
Ru	ruthenium (III) chloride hydrate (Ru basis 99.99%, Alfa Aesar)					
Ni	nickel(II) nitrate hexahydrate (98%, Alfa Aesar)					
Co	cobalt(II) nitrate hexahydrate (99%, Aldrich)					
W	ammonium tungsten oxide pentahydrate (W basis 99.999%, Alfa Aesar)					
Mo	ammonium molybdate (para) tetrahydrate (99%, Alfa Aesar)					
Re	ammonium perrhenate (99%, Aldrich)					
V	ammonium vanadium oxide (99%, Alfa Aesar)					
Nb	niobium(V) oxalate hydrate (19.9% Nb ₂ O ₅ min, Alfa Aesar)					
Mn	manganese(II) nitrate hydrate (99.98%, Alfa Aesar)					

Al	aluminum nitrate nonahydrate (98%, Aldrich)
Y	yttrium nitrate tetrahydrate (99.99%, Aldrich)
Zn	zinc nitrate hexahydrate (99%, Alfa Aesar)
Cr	chromium(III) nitrate nonahydrate (98.5%, Alfa Aesar)
Ce	Cerium(III) nitrate hexahydrate (99%, Aldrich)

In the case of Pt|WO_x/C, a separate, additional catalyst was prepared by Atomic Layer Deposition (ALD) of WO_x onto pre-synthesized, carbon-supported Pt nanocrystals (NC). The Pt NCs were synthesized by modifying a previously reported method [45]. Platinum (II) acetylacetonate (0.4 mmol, Pt(acac)₂, Acros, 98%) was dissolved in a mixture of benzyl ether (15 mL, Sigma-Aldrich, 98%), oleylamine (5 mmol, Sigma-Aldrich, 70%), oleic acid (2.5 mmol, Sigma-Aldrich, 90%) and trioctylphosphine (0.6 mmol, Sigma-Aldrich, 97%). The reaction mixture was kept under vacuum at 373 K for 30 min before heating to 573 K at a rate of 15 K/min in flowing N₂. After cooling to room temperature the NCs were purified by adding 2-propanol, followed by centrifugation at 8000 rpm for 2 min. The precipitate was washed three times with hexane/isopropanol (1:3) mixtures and the final NCs were dispersed in hexane. The as-synthesized NCs were dispersed onto the C support to a loading of 10-wt%. To remove the ligands, the samples were treated with an O₂ plasma for 15 min, then placed in a muffle furnace at 773 K for 1 min [45].

ALD was performed in a custom-built, static system that could be evacuated with a mechanical pump and has been described in Chapter 2. The precursor, tungsten hexacarbonyl (W(CO)₆, 99%, Strem), was first evacuated at room temperature, then heated to 403 K to produce a vapor. In an ALD cycle, 100 mg of sample was exposed to the

W(CO)₆ vapor at 473 K for 3 min, evacuated for 5 min, and then exposed to excess air for 6 min. Sample weight changes were used to determine the WO_x loading and the weight increases were found to be linear with the number of cycles [139]. I will show later in this chapter that WO_x deposits preferentially on the Pt and the weight change following 5 ALD cycles on the 10-wt% Pt/C sample was 8.2-wt%. Although some deposition likely occurred at functional groups on the carbon, this does provide an upper limit for the deposition amount of 1.6-wt% WO_x per cycle.

5.2.2 *Reactivity Measurements and Catalyst Characterization*

THFA hydrogenolysis was performed in a high-pressure tubular flow reactor that is described in Chapter 2. The liquid feed, an aqueous solution of 1-wt% THFA (99%, Sigma Aldrich), was introduced to the reactor at 0.03 mL/min using HPLC pump. The reaction products were analyzed using a GC-MS (QP-5000, Shimadzu), with standard solutions of THFA, 1,5-PeD and other products for external calibration.

The transmission electron microscopy (TEM) images were collected on a JEOL JEM-1400 microscope operating at 120 kV. The size and size distribution for the Pt/C catalyst prepared from the NCs was determined by averaging over 100 particles with ImageJ software. As shown in Figure 5.1a, the Pt particles were uniform, spherical in shape, and 3.0±0.4 nm in diameter. A uniform particle growth was observed following 1 and 5 ALD cycles with WO_x (Figure 5.1b and c). High-angle annular dark-field scanning transmission electron microscopy (HAADF-STEM) measurements and energy dispersive X-ray spectroscopy (EDS) chemical mapping were performed using a FEI Talos F200X

TEM operated at 200 kV. Elemental EDX maps of 1024×1024 pixels were acquired with a 20 min acquisition time.

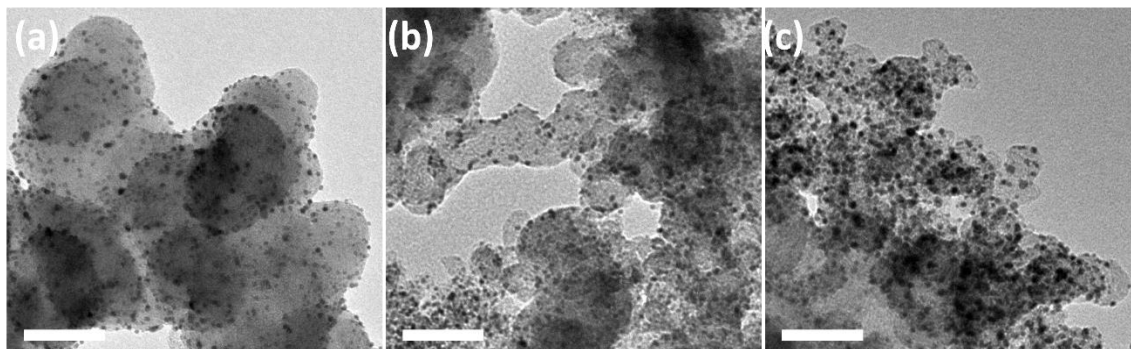


Figure 5.1 TEM images of 10-wt% Pt NCs (a) as-deposited on carbon support, (b) after 1 ALD cycle ((1R) Pt|WO_x/C) and (c) after 5 ALD cycles ((5R) Pt|WO_x/C) of WO_x. The scale bars represent 50 nm.

The CO-O₂ transient-pulse experiments were performed to determine reducibility of Pt-WO_x/C catalysts. The system consists of computer-controlled solenoid valves that allow step changes in the composition of the inlet gases into the tubular reactor. Reactant gases were passed over 200-mg samples in a 1/4 -inch quartz tube. The reactor effluent was monitored continuously using an online quadrupole mass spectrometer (RGA100). The total flow rate was kept constant at 25 mL/min with He as the carrier gas, while the concentrations of the reactive component (either CO or O₂) was chosen to be 10% of the total gas stream. The amounts of CO₂ formed during a CO pulse was determined by the integration of the partial pressures with time. The pulse data was obtained from the reduction in 10% CO in Helium at 473 K for 10 min and then re-oxidation in 10% O₂ for an additional 15 min. The amount ($\mu\text{mol/g}$) of atomic oxygen released from the samples during each cycle is determined by first calibrating the relative intensities of CO and CO₂ and then finding the relative areas of the two peaks.

5.3 Results

5.3.1 Ring-opening of THFA over M^1 - M^2O_x/C

Before discussing the results on the various catalysts, it is important to recognize that a range of products can be formed in the reaction of THFA and that these can be understood as having been formed by one of four pathways that are summarized in Figure 5.2. The desired reaction, Pathway I, produces the 1,5-PeD. 1,5-PeD can undergo further reaction to 1-pentanol (1-PeOH), tetrahydropyran (THP), and tetrahydro-2-pyranone (THP-2-one); but, for purposes of this study, I will sum all the other products produced by this pathway, with a more detailed product distribution provided in Table 5.2. In Pathway II, the first step is dehydroxylation of the alcohol to methyl tetrahydrofuran, which can subsequently ring-open to 2-pentanol. Removal of the hydroxymethyl group in Pathway III produces tetrahydrofuran, which then forms 1-butanol. In Pathway IV, the THFA ring opens to form 1,2-pentanediol.

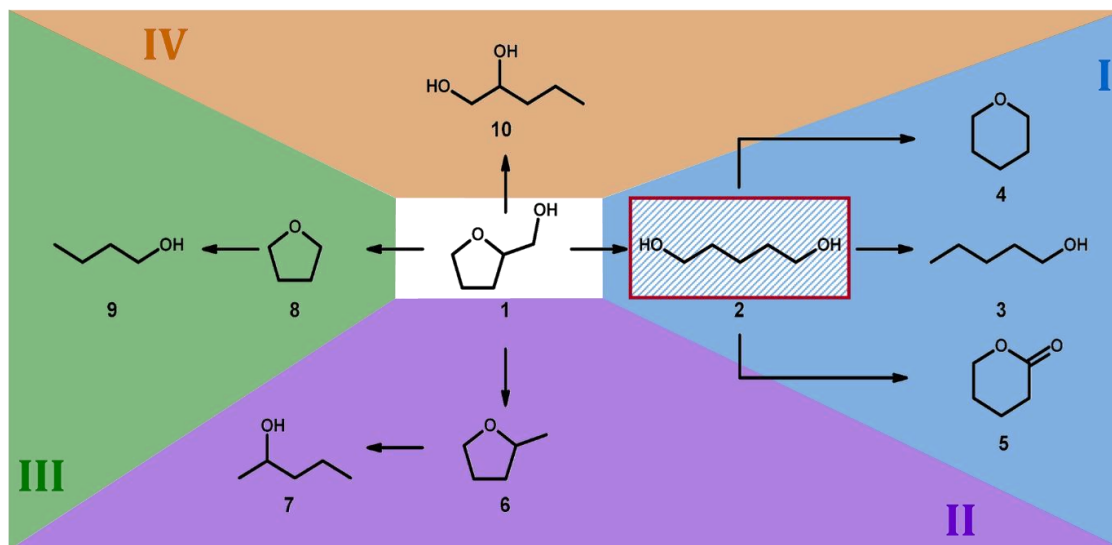


Figure 5.2 Proposed reaction scheme for THFA hydrogenolysis. Experimentally observed species: (1) tetrahydrofurfuryl alcohol (THFA); (2) 1,5-pentanediol (1,5-PeD); (3) 1-pentanol (1-PeOH); (4) tetrahydropyran (THP); (5) tetrahydro-2-pyranone (THP-2-one); (6) methyl tetrahydrofuran; (7) 2-pentanol; (8) tetrahydrofuran; (9) 1-butanol (1-BuOH); (10) 1,2-pentanediol. Reaction pathway I undergoes direct ring-opening with 1,5-PeD as an intermediate; reaction pathway II and III undergo hydrodeoxygenation (HDO) and decarbonylation (DCO) respectively prior to ring-opening; reaction pathway IV undergoes direct ring-opening.

Table 5.2 Detail conversion and selectivity for THFA hydrogenolysis over 10-wt% Pt/C, 6.3-wt% WO_x/C, and 10-wt% M¹-M²O_x/C (1:0.5)

Catalysts	Conversion (%)	Product Selectivity (%)							
		1,5-PeD	1-PeOH	1-BuOH	THP	2-MTHF	THF	THP-2-one	1,2-PeD
Pt	4.0	23	20	15	-	-	-	-	42
WO _x	0	-	-	-	-	-	-	-	-
Pt-WO _x	28	76	10	4	7	-	3	-	-
Pt-ReO _x	55	53	12	11	5	-	-	19	-
Pt-MoO _x	26	69	16	7	3	5	-	-	-
Ir-WO _x	25	71	22	2	3	-	2	-	-
Ir-MoO _x	19	68	20	2	4	6	-	-	-
Ir-VO _x	15	65	19	-	-	16	-	-	-
Pt-NbO _x	4.8	38	10	31	5	-	16	-	-
Pt-VO _x	1.4	57	21	7	-	8	7	-	-
Pt-CeO _x	2.2	45	-	28	-	-	27	-	-
^a Ru-WO _x	33	-	-	5	-	-	31	-	-

List of inactive catalysts

Ni-WO_x Co-WO_x Pd-WO_x Pt-CrO_x Pt-MnO_x Pt-ZnO_x Pt-YO_x Pt-AlO_x Pt-CoO_x

Reaction conditions: 473 K, 36 bar, 1-wt% THFA aqueous solution, space time = 1.67 min·g/mL. ^a Carbon balance on Ru-WO_x/C is 79%.

To screen the catalysts, THFA hydrogenolysis was performed at 473 K and a total pressure of 36 bar over 50-mg samples, all prepared by impregnation, with the fixed flow rate and reactant concentrations reported in the Experimental section. The reaction conversions and products were measured under steady-state reaction conditions, with the reported data obtained 2 h after reactants were first introduced to the catalysts; however, conversions and selectivities did not change significantly on any of the catalysts over a period of at least 5 h. The carbon-supported catalysts all had M^1 -metal loadings of 10-wt%. In samples containing M^2O_x -oxide promoters, the elemental mass ratio of M^1 to M^2 is 1:0.5.

THFA conversions are reported in Figure 5.3, with Pt-based catalysts shown in Figure 5.3a) and catalysts based on other metals shown in Figure 5.3b). With the Pt catalysts, only those samples containing ReO_x , WO_x , and MoO_x showed significant activity. The conversion on the Pt/C catalysts was only 4% but this increased around ten-fold upon the addition of the activating oxides. Compared to the Pt-only catalyst, there may have been a slight increase in the conversion when NbO_x was added; but VO_x , CeO_x , CrO_x , YO_x , MnO_x , ZnO , Al_2O_3 and CoO_x had a negligible influence on the conversion. With regards to the non-Pt catalysts that were tested, WO_x again had a positive influence on the rates with Ru and Ir but did not accelerate rates with Pd, Ni, or Co. With Ir, MoO_x and VO_x also increased conversions.

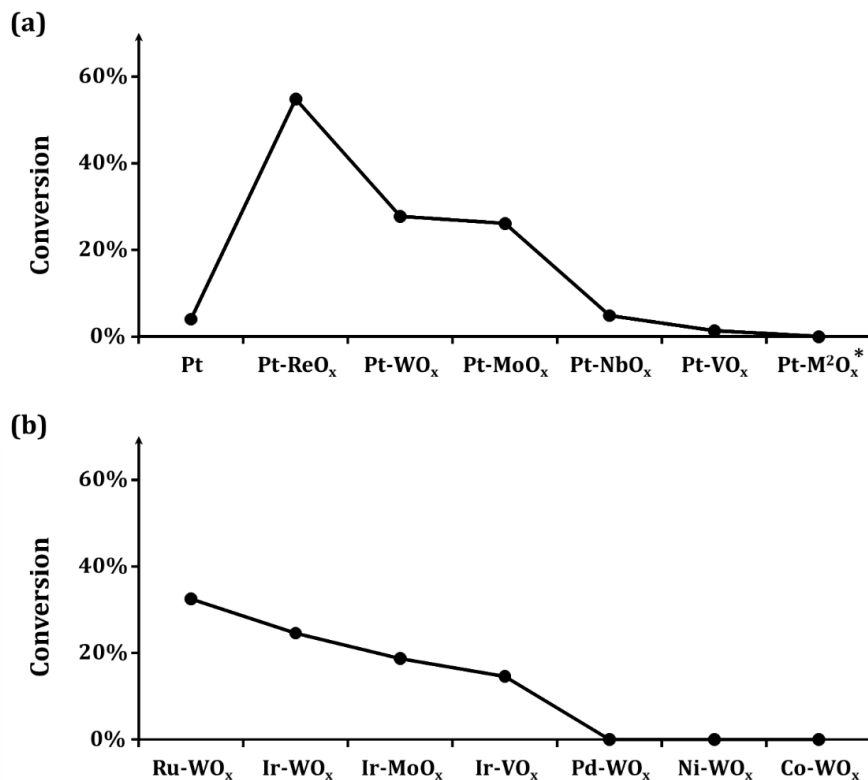


Figure 5.3 Conversion for THFA hydrogenolysis over 10-wt% M^1 - M^2O_x/C (1:0.5) (a) Pt-based catalysts and (b) other catalysts. M^2 in $Pt-M^2O_x^*$ includes Ce, Cr, Mn, Y, Zn, Al and Co. Reaction conditions: 473 K, 36 bar, 1-wt% THFA aqueous solution, space time = 1.67 min·g/mL.

Reaction selectivities are reported in Figure 5.4 for materials that showed measurable conversions. On Pt/C, the majority of products proceeded according to Reaction Pathways III and IV but the addition of WO_x , MoO_x , ReO_x , and VO_x dramatically shifted the reaction to desired Pathway I. Although conversions were slightly higher with Pt-NbO_x/C, the selectivity of this catalyst was poor, similar to that of Pt/C. Ir catalysts with WO_x , MoO_x , and VO_x also showed good selectivity to the desired pathway. It is noteworthy that the Ru- WO_x/C catalysts exhibited reasonably high reaction rates but was completely non-selective for Pathway I.

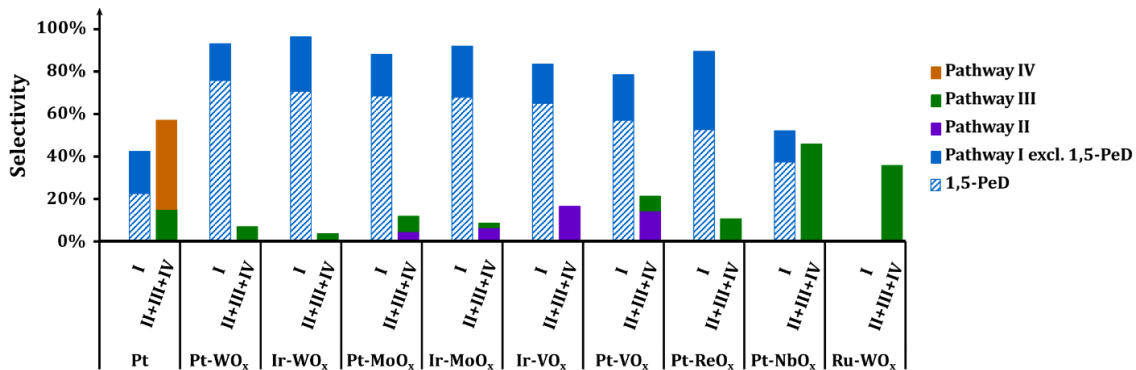


Figure 5.4 Selectivity for THFA hydrogenolysis over 10-wt% M^1 - M^2O_x/C (1:0.5) catalysts with detectable activities. Selectivity bars are grouped in pathway I and a sum of pathway II, III and IV. Reaction conditions: 473 K, 36 bar, 1-wt% THFA aqueous solution, space time = 1.67 min·g/mL.

In order to demonstrate that selectivities observed Figure 5.4 are not dependent on the particular reaction conditions, I measured the conversions and selectivities over the Pt-WO_x/C catalyst as a function of reactor space time and temperature, with results reported in Figure 5.5. Figure 5.5a) demonstrates that Reaction Pathway I dominates at both short and long space times and at higher conversions. At the longer space times, where more 1,5-PeD is formed, more of the secondary products from Pathway I are also formed but the pathway does not change. The effect of temperature at a fixed reactor space time is shown in Figure 5.5b). At 515 K, Reaction Pathway III becomes more important but Reaction Pathway I still dominates.

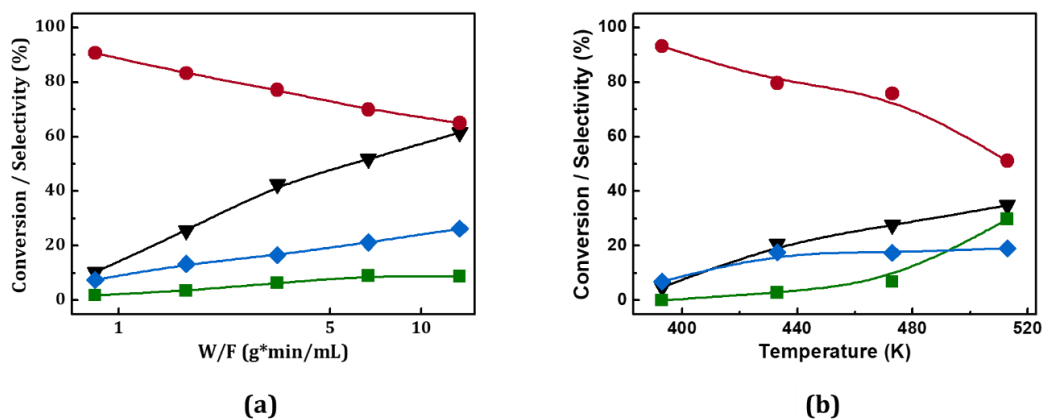


Figure 5.5 Conversion and selectivity for THFA hydrogenolysis over 10-wt% Pt-WO_x/C (1:0.5) catalyst as a function of (a) space time at 473 K and (b) reaction temperature at space time = 1.67 min·g/mL. (▼) THFA conversion; (●) 1,5-PeD selectivity; (◆) Pathway I excl. 1,5-PeD selectivity; (■) Pathway III selectivity. Reaction conditions: 36 bar, 1-wt% THFA aqueous solution.

In the reaction measurements over Pt-WO_x/C, I observed that the initial products exhibited an intense blue color due to leaching of some of the WO_x. Exposure of the sample to air produced a small amount of WO₃ precipitate, and caused the solutions to gradually revert back to colorless. When the Pt-WO_x/C was pre-reduced in H₂ at 773 K before introducing reactants, the leaching stopped. All of this suggests that the species responsible for the colored solutions was a slightly reduced, homogeneous H_xWO_x species. It is noteworthy that ReO_x and MoO_x have also been reported to leach during similar reactions in aqueous phase [31,100,140]. This led me to ask whether movement of the promoters could be important in producing the active forms of the catalysts. To test for this, I examined the effect on the reaction of THFA of placing Pt and WO_x on separate carbon supports and in different parts of the reactor, with results summarized in Figure 5.6. Again, the measurements were all performed at 473 K and a fixed reactor space time.

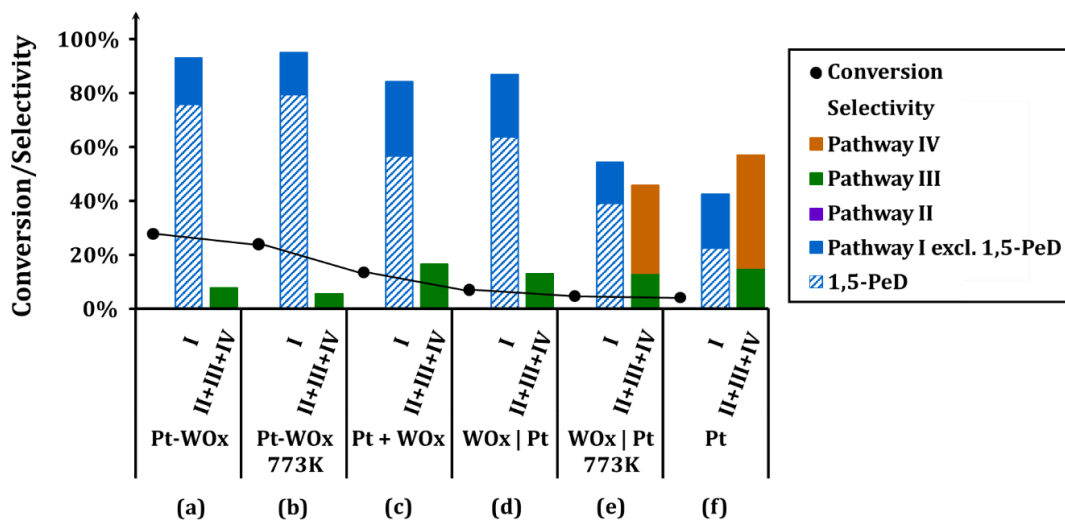


Figure 5.6 Effects of tungsten leaching on THFA hydrogenolysis over Pt and WO_x containing catalysts. (a) 10-wt% Pt-WO_x/C (1:0.5) catalyst; (b) 10-wt% Pt-WO_x/C (1:0.5) catalyst with a 30-min H₂ treatment at 773 K prior to the reaction; (c) 10-wt% Pt/C and 6.3-wt% WO_x/C physical mixture; (d) dual bed with WO_x/C upstream of Pt/C; (e) dual bed with WO_x/C upstream of Pt/C, and with a 30-min H₂ treatment at 773 K prior to the reaction; (f) 10-wt% Pt /C catalyst. Selectivity bars are grouped in pathway I and a sum of pathway II, III and IV. Reaction conditions: 473 K, 36 bar, 1-wt% THFA aqueous solution, space time = 1.67 min·g/mL.

First, pre-reduction the catalyst at 773 K, a pretreatment that appears to stop WO_x leaching, had a minimal effect on both the conversion and the selectivity, suggesting that the WO_x is partially reduced in the active form of the catalyst. This is consistent with thermodynamic calculation shown in Figure 5.7, and it is also supported by the reducibility measurements obtained from CO-O₂ pulse studies shown in Table 5.3. When the reactor was loaded with a physical mixture of WO_x/C and Pt/C, the conversion was somewhat lower, ~13%, but the selectivity was similar. Loading the reactor with separate beds of WO_x/C and Pt/C, with the WO_x/C upstream of the Pt/C, again caused a decrease in the conversion but the selectivity remained high; however, pre-reducing this dual-bed or having the Pt/C upstream of the WO_x/C gave results that were essentially indistinguishable from that achieved with Pt/C alone.

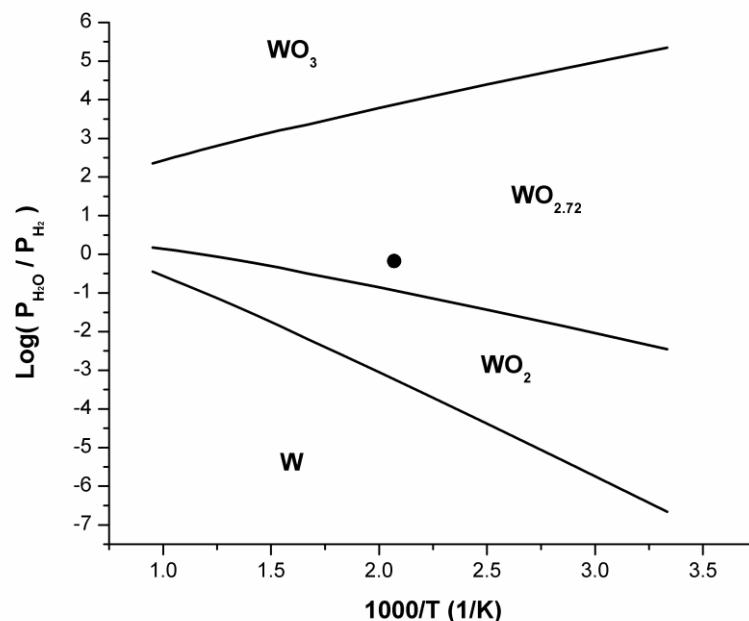


Figure 5.7 Thermodynamic calculation of the boundaries of tungsten oxides as a function of temperatures and water/hydrogen pressure ratios. (●) represents the reaction condition at 473 K and 36 bar.

Table 5.3 Redox data for the pulse-reactor measurements performed at 473 K using CO-O₂ pulses over the as-prepared samples. While WO_x/C alone cannot be reduced under this condition, WO_x with the presence of Pt can be reduced to an averaged valence of ~5.1. Atomic oxygen released on as-prepared Pt/C catalyst is due to the reduction of surface PtO₂.

Sample	Atomic oxygen released (μmol/g)
6.3-wt% WO _x /C	5
10-wt% Pt/C	70
10-wt% Pt-WO _x /C (1:0.5)	176

5.3.2 Ring-opening of THFA over ALD-prepared Pt-WO_x NCs

The fact that a selective catalyst can be produced by exposure of a Pt/C catalyst to the leached solution of H_xWO₃ suggests that the WO_x may be covering the Pt surface when the catalyst is in its active state. In order to prepare samples with better Pt-WO_x interfacial control, I examined Pt|WO_x/C catalyst samples in which the WO_x was added by ALD over pre-synthesized Pt NCs/C. HAADF STEM images and EDS elemental mapping were used to examine the 10-wt% Pt NCs/C catalyst after 5 ALD cycles with WO_x. The image shows some agglomeration of the Pt, possibly due to the thermal sintering during the ALD process. Figure 5.8 also shows elemental distributions of Pt and W determined from EDS, along with a superposition of the Pt and W signals. The superimposition of these two elements reveals that W preferentially deposits on the Pt NCs in ALD.

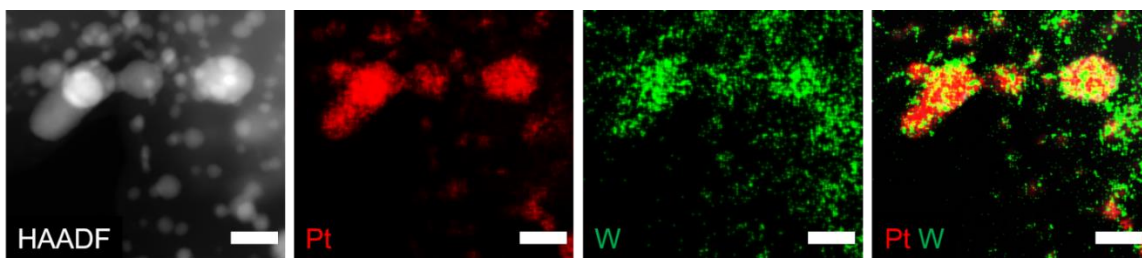


Figure 5.8 HAADF-STEM images and EDS elemental mapping of (5R) Pt|WO_x/C. The scale bars represent 10 nm.

The reaction of THFA was performed over ALD-prepared Pt|WO_x/C catalysts following 1 or 5 ALD cycles. The measurements were again performed at 473 K, 36 bar, and a space time of 1.67 min·g/mL, with results summarized in Figure 5.9. The initial results on the sample prepared with 1 ALD cycle showed 20% conversion of THFA and better than 95% selectivity to the desired Reaction Pathway I, which is higher than what was achieved on the conventional Pt-WO_x/C catalyst, even though the WO_x loading was

much lower, only 1.6-wt%. This catalyst did show some loss in activity with time, likely due to leaching of some of the WO_x . Interestingly, the THFA conversion and selectivity over the catalyst prepared with 5 ALD cycles of WO_x were significantly worse. The conversion on this catalyst was only 6% and the selectivity Reaction Pathway I decreased to 68%. It suggests that the WO_x coating was too thick in this sample.

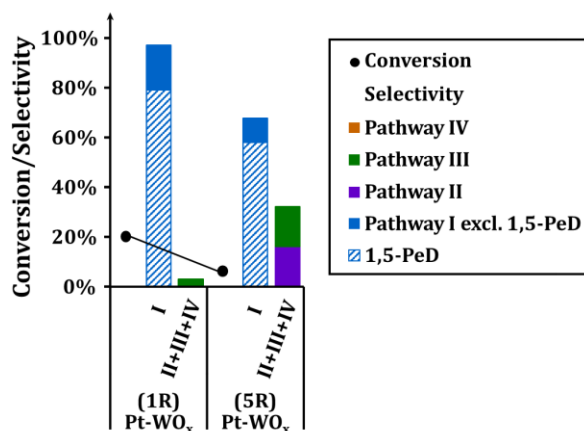


Figure 5.9 Conversion and selectivity for THFA hydrogenolysis over (1R) and (5R) $\text{Pt}|\text{WO}_x/\text{C}$ catalysts. Selectivity bars are grouped in pathway I and a sum of pathways II, III and IV. Reaction conditions: 473 K, 36 bar, 1-wt% THFA aqueous solution, space time = 1.67 min·g/mL.

5.4 Discussion

The results presented in this chapter agree with previous work which demonstrated synergy between specific $\text{M}^1\text{-M}^2\text{O}_x$ pairs for the reaction of THFA to form 1,5-PeD [2, 3, 8–12, 20, 21]. The enhanced activity and selectivity associated with the combination of metal/metal-oxide pairs, such as Pt-WO_x [92–95] and Pt-ReO_x , is remarkable. The dual-bed experiments reported here also show that direct contact between the metal and the oxide is required in order to achieve high catalytic performance. Simply having both components on the same support does not guarantee high activity.

Previous workers have reported that the role of the oxide is to act as a Brønsted-acid site for breaking C-O bonds and stabilizing the oxocarbenium-ion, while the metal is required for dissociation of H₂ [90]. My work could be consistent with this mechanism but it is interesting that only reducible oxides are effective in promoting the reaction, while non-reducible, acidic oxides, like Al₂O₃, are not effective. Also, not all catalytic metals (e.g. Pd) can be promoted, implying that there must be specific interactions between the metal and the metal oxide that are required to make an active catalytic site. The work from this chapter suggests that a key feature to the synergy between metal and metal oxide is that the metal oxide must be able to form a patchwork, monolayer coating over the metal, with most of the metal surface being covered by the oxide, but without having the metal oxide block access to the metal surface for H₂ adsorption and dissociation.

There are likely two reasons why only specific oxides are effective in promoting the reaction. First, reducible oxides are known form overlayers on metals under some conditions. This formation of an overlayer is responsible for the so-called Strong Metal Support Interactions (SMSI) phenomenon [141,142]. Non-reducible oxides generally do not “wet” metal surfaces and therefore tend not to form such coatings. Second, the most effective of the oxides, ReO_x, WO_x, and MoO_x, have all been shown to “leach” in the presence of water under some conditions [31,100,140]. This implies that they are mobile and able to migrate easily onto the metal surfaces.

It is interesting to consider that the proposed structure of Pt-Co catalysts for the hydrodeoxygenation of 5-hydroxymethylfurfural has similarities to the structure I am proposing here [45]. In that case, it was suggested that the active and selective phase of a

Pt₃Co₂ catalyst consisted of a Pt-rich core with a Co oxide surface monolayer. The oxide prevented side reactions while providing openings that allowed for selective reaction on the underlying Pt. For that reaction, the CoO_x overlayer was suggested to form spontaneously under reaction conditions. In the present example, the oxide overlayer formed either directly during preparation by ALD or by leaching.

The combination of metal and metal oxide for the selective reactions of biomass feedstocks appears to be a general concept that may well be applicable to a wide range of reactions. The insights gained from this study should help assist in the preparation of catalysts for these applications.

CHAPTER 6. MECHANISTIC STUDY OF THE DIRECT HYDRODEOXYGENATION OF *m*-CRESOL OVER WO_x-DECORATED Pt/C CATALYSTS⁵

Summary

This chapter describes my unsuccessful attempt to demonstrate universality of catalysts for HDO reactions of biomass model compounds. However, the work demonstrated that oxide-decorated Pt can be selective. The bimetallic catalysts that have previously shown good performance for HDO of HMF and furfural (see Chapter 3 and 4) are found to show poor activity or selectivity for the *m*-cresol HDO reaction. Surprisingly, a Pt-WO_x/C catalyst that was selective for ring-opening reaction of THFA to 1,5-PeD was found to be unusually active, stable, and selective to toluene. On the basis of Chapter 5, the work here discusses a deeper exploration into the Pt-WO_x synergy. Reactivity studies in combination with density functional theory (DFT) calculations reveal that the HDO reaction on Pt-WO_x/C proceeds via a direct hydrogenolysis of the C-O bond in *m*-cresol adsorbed on oxygen vacancy (or redox) sites on WO_x species. The DFT results also indicate that Pt helps stabilize the WO_x film while facilitating oxygen vacancy formation.

⁵This chapter was published as **C. Wang**, A.V. Mironenko, A. Raizada, T. Chen, X. Mao, A. Padmanabhan, D.G. Vlachos, R.J. Gorte, J.M. Vohs, ACS Catal. 8 (2018) 7749–7759. Reprinted with permission, copyright (2018) American Chemical Society.

6.1 Introduction

Fast pyrolysis of the lignin fraction of lignocellulosic biomass produces a bio-oil containing a range of phenolic and other aromatic oxygenates that have potential as feedstocks for the production of aromatic hydrocarbons. The high oxygen content of this bio-oil however makes it unstable, susceptible to polymerization, and limits its overall energy content. The need to partially or completely remove oxygen functionalities and yield high-value aromatic products has prompted research into the development of highly selective catalysts for hydrodeoxygenation (HDO) of oxygen-containing aromatics.

Early studies on HDO of lignin focused on using commercial Mo sulfide-based hydrotreating catalysts [52–54], but these were found to suffer from rapid deactivation due to coking [55,56]. While supported transition metal catalysts have been shown to be active for HDO reactions, they are also prone to deactivation and can promote ring hydrogenation [57–59]. In an attempt to address these issues many recent studies have focused on bimetallic catalysts, composed of a group 10 metal, such as Ni or Pt, alloyed with a second more oxophilic metal, such as Fe or Zn [49,63–68]. For some reaction conditions these catalysts have demonstrated good selectivity for hydrogenolysis of C-O bonds in lignin-derived oxygenates while maintaining the aromatic character of the molecule, although a range of both aromatic and ring-saturated products are typically still formed [63,64,66]. Bifunctional catalysts consisting of a transition metal either supported on or modified by an acidic metal oxide have shown some promise for selective HDO of phenolics and other aromatic oxygenates [69–76]. Examples here include Pt/F-Al₂O₃ [69], Pt/H-Beta [70], and Ru/WO_x-ZrO₂ [76].

The mechanism of HDO reactions on these supported metal catalysts is not well understood. For lignin model compounds, such as cresols, anisole and guaiacol, several different pathways have been proposed, including direct hydrogenolysis of the targeted C-O bond [68,72–74,77–80], and more complex pathways that proceed via tautomerization and partial hydrogenation of the aromatic ring, followed by a dehydration/dehydrogenation step to remove the oxygen. In this latter pathway, the group 10 metal is thought to catalyze partial ring hydrogenation, while the more oxophilic metal or metal oxide modifier provides sites for the subsequent dehydration reaction and potentially stabilizes the tautomer intermediate [59,64,67,68].

Here, I have examined the HDO of *m*-cresol, a model compound for lignin-derived phenolics, over carbon-supported Pt-WO_x catalyst. The use of Pt-WO_x/C was motivated in part by previous studies and patents [93,94], which have shown that Pt-WO_x catalysts are active for HDO of glycerol to produce 1,3-propanediol [143,144] and for the hydrogenolysis of tetrahydrofurfuryl alcohol to produce 1,5-pentanediol [95,145]. Reactivity studies were carried out using liquid *m*-cresol solution and H₂ reactants at 573 K and a total pressure of 36 bar. The Pt-WO_x/C was found to be unusually active and selective for the HDO of *m*-cresol with toluene selectivity being greater than 94% under steady-state reaction conditions with little to no deactivation occurring over a 7-hr test period. Comparison of these results to those for an unmodified Pt/C catalyst indicates that the HDO reaction on Pt-WO_x/C proceeds via a direct hydrogenolysis of the C-O bond in adsorbed *m*-cresol, a conclusion which is further supported by density functional theory (DFT) calculations for the adsorption and reaction of *m*-cresol on W₂O₆-decorated Pt(111).

6.2 Experimental

6.2.1 Catalyst Synthesis and Characterization

Carbon supported Pt, WO_x and Pt-WO_x were synthesized using a standard incipient wetness as described in detail in Chapter 1 and Chapter 5. Atomic layer deposition (ALD) was also used to modify Pt/C catalysts with WO_x. The catalyst referred to as (ALD) Pt-WO_x/C was prepared by depositing one ALD cycle of WO_x (1.6-wt% loading of WO₃) on an impregnated 10 wt% Pt/C. After completion of ALD the sample was heated in air up to 673K for 1 min to ensure complete removal of all of the organic ligands.

6.2.2 Reactivity Measurements and Catalyst Characterization

Characterization of the activity of the various catalysts for the HDO of *m*-cresol was carried out using a high-pressure continuous flow reactor that has been described in Chapter 2 and used in the studies featured in Chapters 3, 4 and 5. The liquid feed was a 2 mol % dodecane solution of oxygen-containing aromatics (either *m*-cresol, 99%, Alfa Aesar; 3-methylcyclohexanol, 98+%, ChemCruz; 3-methylcyclohexanone, 97%, Sigma Aldrich; anisole, 99.7%, Sigma Aldrich; or guaiacol, 98%, Sigma Aldrich). A H₂/reactant ratio of ~5 was used at steady state. Reactivity measurements were also conducted for a total pressure of 1 bar. These studies used the same reactor described above, except without the back pressure regulator. A 0.05 mL/min liquid feed of *m*-cresol was evaporated into a 12 mL/min H₂ flow prior to contact with the 50-mg catalyst bed. The H₂/reagent ratio at steady state was ~1. The space velocity (WHSV) reported in this study is defined as the weight of reagent per unit weight of the catalyst per hour.

For XPS analysis a model catalyst consisting of a Pt foil which was subjected to a single WO_x ALD deposition cycle was used. XPS spectra were collected using a dedicated ultra-high vacuum system equipped with an Al(K) x-ray source and a hemispherical electron energy analyzer. The binding energy scale of XPS spectra were referenced to the O(1s) peak which was assumed to be located at 530.5 eV. Catalyst total surface areas were measured using a custom-built BET apparatus with N_2 as the adsorbent. This apparatus was also used for selective CO chemisorption measurements which were used to estimate the Pt dispersion in each catalyst. The samples used for dispersion measurements were pretreated in 200-torr H_2 at 473 K for 30 min prior to adsorbing CO at room temperature.

6.2.3 Theoretical Approaches

In order to determine a representative Pt(111)- WO_x model structure, obtain insights into the synergy between WO_x and Pt, and assess the feasibility of the direct C-O scission on the Pt(111)- WO_x , we employed spin-polarized density functional theory (DFT) calculations using the VASP software [146–149]. The projector-augmented wave method [150,151] was employed to describe interactions of valence and core electrons. Slab calculations were performed using a 400 eV kinetic energy cutoff, (3 x 3 x 1) Monkhorst-Pack [152] k-point mesh, the RMM-DIIS electronic optimization algorithm, and the PBE exchange-correlation functional [153]. Convergence criteria for electronic and ionic loops were set to 10^{-4} eV and $0.05 \text{ eV}/\text{\AA}$, respectively. Transition state search was performed using the climbing image nudged elastic band [154–157] (10 - 12 images) and dimer [158] methods with the force tolerance set to $0.15 \text{ eV}/\text{\AA}$. The Pt- WO_x catalyst was modeled as a W_xO_{3x} cluster ($x = 2-4$) on top of a 3-layer Pt(111) slab with the (4 x 4) periodicity, a 20 \AA

vacuum separation along the z direction, and a relaxed top Pt layer. The Pt bulk lattice constant was pre-optimized using a standard procedure [159]. Tungsten oxide structures corresponding to global energy minima were determined by combining Born-Oppenheimer *ab initio* molecular dynamics (AIMD) and simulated annealing (SA) [160]. To minimize the computational cost, we took advantage of the observation that geometries converge faster with respect to the basis set size than energies [161], and that the energy ranking among adsorbate binding modes on a metal surface is well described using very approximate models (e.g., extended Hückel) and a single-layer metal substrate [162], indicating that low-level DFT calculations could yield reasonable global minimum energy structures. After placing W_3O_9 and W_6O_{18} on top of two separate frozen periodic Pt(111) single layers in a vacuum, we carried out spin-nonpolarized AIMD pre-equilibrations at 3000 K for 10 ps using a Nosé thermostat and a 5 fs time step, followed by SA with a 1.5 fs time step and a final temperature of 500 K, which was reached after 30 ps. System energies at each ionic step were calculated using the Γ -point Brillouin zone sampling, 300 eV energy cutoff, the RMM-DIIS electronic optimizer, and the Fermi smearing with $\sigma=0.172$ [163]. During the simulation, the W_6O_{18} cluster was split to W_2O_6 and W_4O_{12} bound to opposite sides of the Pt(111) layer (Movie2 in available in the electronic SI). Following SA, the cluster structures were further optimized using the standard computational setup (*vide supra*) with 2 extra Pt layers added to reconstruct the original 3-layer Pt(111) slab. The adequacy of the low-level DFT was confirmed by only minor structural relaxations, when the SA-optimized cluster was used as an input to the high-accuracy 3-layer calculations (see Figure 6.1 and Movie3 available in the electronic SI). The $WO_3(0001)$ surface was modeled using the (3 x 3 x 1) supercell with the bottom

stoichiometric layer frozen and the remaining layers relaxed; the $(\sqrt{2} \times \sqrt{2})R45^\circ$ surface reconstruction was employed [164].

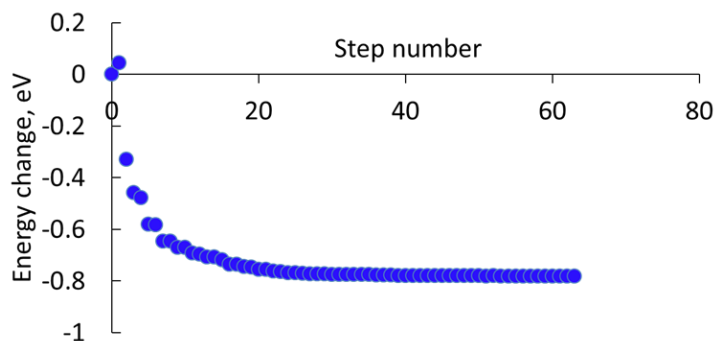


Figure 6.1 Structure optimization trajectory of $W_2O_6/3$ -layer Pt(111) at the standard (high) level of theory. The initial cluster structure was predicted by ab initio molecular dynamics/simulated annealing at the low level of theory.

6.3 Results

6.3.1 Reactivity Studies

The overall conversion and selectivity for the reaction of *m*-cresol on the Pt/C and Pt- WO_x /C catalysts were measured over a range of experimental conditions. As will be demonstrated throughout this section, over 90% selectivity to toluene (TOL) was always achieved for the Pt- WO_x /C catalyst for reaction temperatures between 473 and 623 K, regardless of the hydrogen pressure, reactant concentration, and space velocity. In contrast, much lower selectivity to toluene was obtained for the Pt/C catalyst for the same conditions with a range of other products also being detected. These products are shown in Figure 6.2 and include the hydrogenation products 3-methylcyclohexanol (OL), 3-methylcyclohexanone (ONE), and the hydrogenation/dehydration product methyl cyclohexane (MCH). Small amounts of products resulting from transalkylation and

bimolecular reactions (colored in gray in Figure 6.2) were also produced at high reaction temperatures when pure *m*-cresol was used as the reactant.

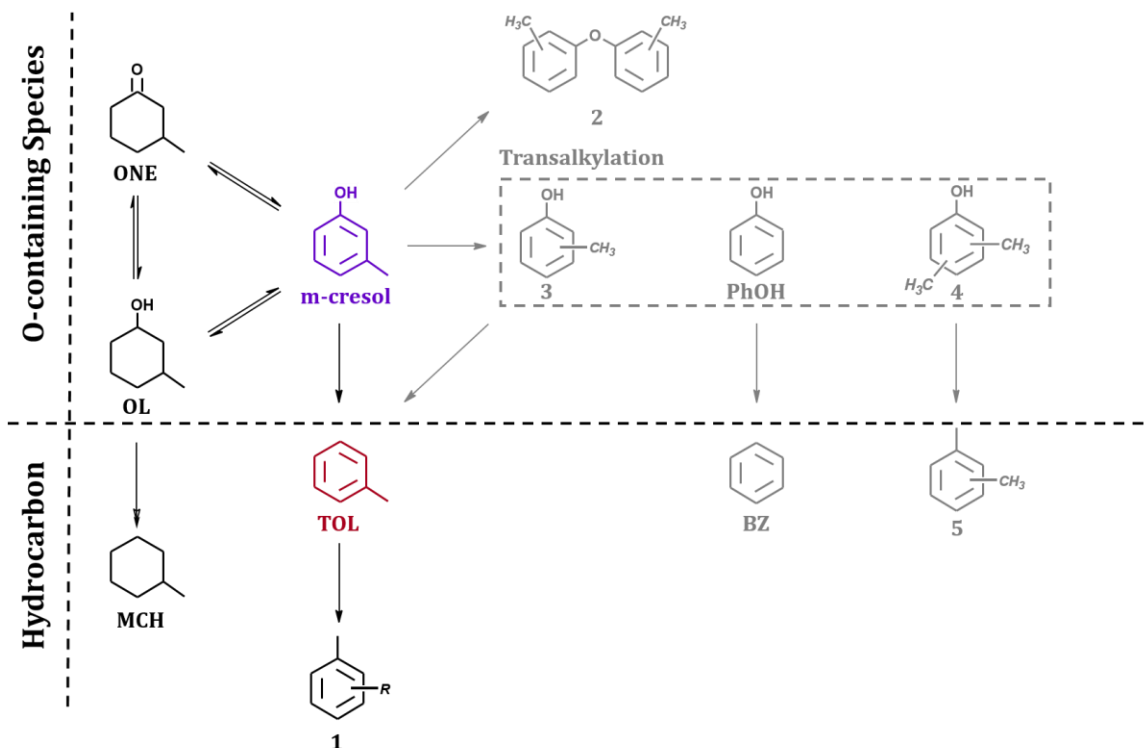


Figure 6.2 Reaction network for HDO of *m*-cresol. Species detected in the catalytic measurements are included. The products in grey were only observed during the 1-bar HDO reaction of pure *m*-cresol at 623K. ONE – methyl cyclohexanone; OL – methyl cyclohexanol; MCH – methyl cyclohexane; TOL – toluene; PhOH – phenol; BZ – benzene; 1 – alkyltoluenes; 2 – tolylethers; 3 – cresols; 4 – xylenols; 5 – xylenes.

Figure 6.3 compares the conversion and product selectivity at steady-state for the Pt-WO_x/C and Pt/C catalysts at 573 K and 36 bar using a liquid reactant stream consisting of 2 mol% *m*-cresol in dodecane and a WHSV of 0.6 hr⁻¹. For comparison purposes data for a WO_x/C catalyst is also included. These data show that the Pt/C catalyst had relatively low activity with only 8.3% conversion being obtained. While TOL (62%) was the primary

product over this catalyst, it also produced significant amounts of ONE (23%), OL (7.4%) and MCH (5.5%). These results are in stark contrast to those for the Pt-WO_x/C catalyst which was more active with over seven-fold higher conversion of *m*-cresol (61%) and much more selective with a 98% selectivity to TOL. The only other significant product was MCH (0.7%). Trace amounts of alkyltoluenes (**1** in Figure 6.2) were also observed, but we suspect that they resulted from reaction of the primary TOL product with light olefins produced by cracking of a small amount of the dodecane solvent. The large discrepancy in the product distribution from these two catalysts suggests that different reaction pathways occur over Pt/C and Pt-WO_x/C. It is also noteworthy that the WO_x/C catalyst was completely inactive, thus demonstrating that for Pt-WO_x/C, the high selectivity to TOL must result from synergistic interactions between the Pt and WO_x.

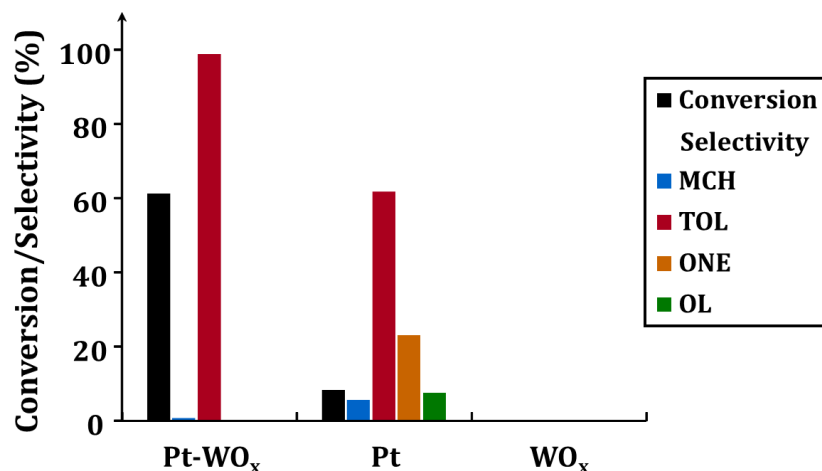


Figure 6.3 Conversion and selectivity for high-pressure HDO reaction of *m*-cresol over Pt-WO_x/C, Pt/C and WO_x/C catalysts. Reaction conditions: 573 K, 36 bar, 2-mol% *m*-cresol/dodecane solution, WHSV = 0.6 hr⁻¹.

Figure 6.4 shows the time evolution of conversion and selectivity for the Pt/C and Pt-WO_x/C catalysts for the aforementioned reaction conditions. Note that for the Pt/C

catalyst (panel b) the overall conversion decreases continuously for the first 5 h of operation until it stabilizes at the low value of 8.3% as reported above. For this operating temperature, 573 K, it is unlikely that this decrease in activity with time on stream is a consequence of Pt agglomeration and loss of metal surface area. As will be discussed below, we rather suspect that coking of the Pt is the primary factor leading to catalyst deactivation. In contrast, the time evolution data for the Pt-WO_x/C catalyst (panel a) shows that after an induction period that lasts several hours, the performance of the catalyst is quite stable with ~60% conversion and ~98% selectivity to the desired HDO product, TOL. It is noteworthy that significant changes in the product composition occur over the induction period with the selectivity to TOL increasing from 72% to 98% while concomitantly the selectivity to the complete hydrogenation product, MCH, decreasing from 28% to only trace amounts. Thus, the Pt-WO_x/C catalyst's ability to promote hydrogenation of the aromatic ring, which is initially nearly the same as that observed for the non-deactivated Pt/C catalyst, is essentially eliminated during the induction period. While it is tempting to attribute this change in selectivity to partial reduction or some other chemical change in the WO_x with time on stream, this seems unlikely since the catalyst was pretreated under the reaction conditions in a stream of pure dodecane and H₂. We instead speculate that, like what appears to be case for the Pt/C catalyst, coking of bare portions of the Pt surface (*i.e.* portions not modified by WO_x) poisons these sites while the remainder of the Pt surface that is coated by or adjacent to the WO_x deposits exhibits high activity for the HDO of *m*-cresol to produce TOL. This argument is further supported by CO adsorption data presented in the section below.

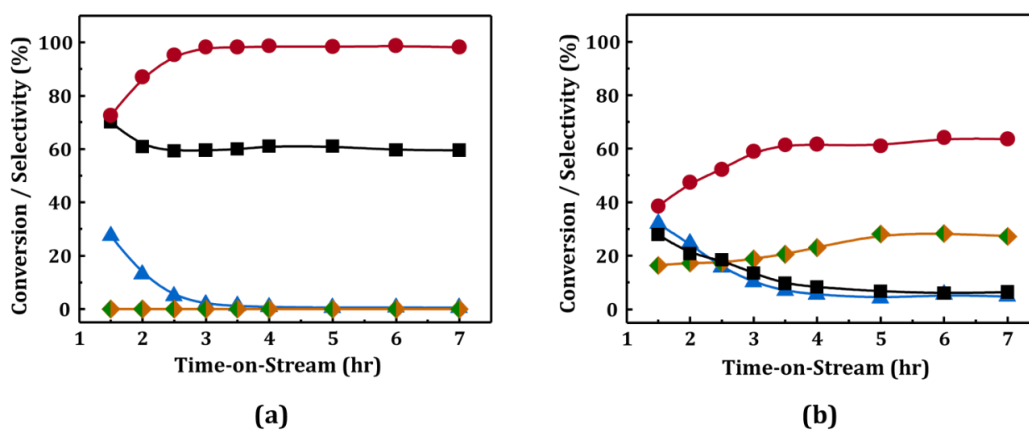


Figure 6.4 Time-on-stream experiments for high-pressure HDO reaction of *m*-cresol over (a) Pt-WO_x/C and (b) Pt/C catalyst. Reaction conditions: 573K, 36 bar, 2-mol% *m*-cresol/dodecane solution, WHSV = 0.6 hr⁻¹. Conversion of *m*-cresol (■); selectivity of TOL (●), MCH (▲) and the sum of ONE and OL (◆).

To characterize the reactivity of the Pt/C and Pt-WO_x/C catalysts towards TOL at lower hydrogen pressure and under solvent-free conditions, steady-state HDO experiments using pure *m*-cresol as reactant at 623 K, 1 bar of H₂, and a WHSV of 60 hr⁻¹ were conducted. As shown in Figure 6.5, the results of these experiments are analogous to those reported in Figure 6.3 for higher hydrogen pressure but lower temperature and *m*-cresol concentration. The Pt/C catalyst again exhibited low activity (11% conversion) with only modest selectivity to TOL (62%) and with significant amounts of ONE (32%) being produced. Much smaller amounts of OL (1.4%) and MCH (0.9%), as well as transalkylation and bimolecular products were also obtained. While relatively low conversion was obtained (27%) due to the high space velocity, the Pt-WO_x/C catalyst again exhibited an unusually high selectivity, 94%, to the desired HDO product, TOL. As was

the case for the Pt/C catalyst, small amounts of transalkylation and bimolecular products were obtained.

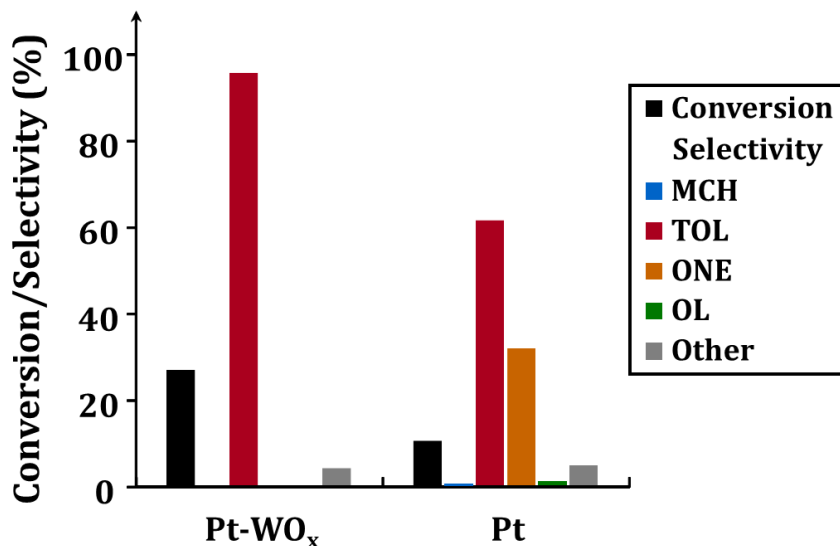


Figure 6.5 Conversion and selectivity for 1-bar HDO reaction of pure *m*-cresol over Pt-WO_x/C and Pt/C catalysts. Reaction conditions: 623 K, 1 bar. H₂ flow rate: 12 mL/min, WHSV = 60 hr⁻¹.

Several reports in the literature suggest that formation of aromatic hydrocarbons during HDO of lignin-derived aromatic oxygenates over supported noble metal catalysts is favored at high temperatures (>600 K) and low H₂ pressures (<10 bar), while products with saturated rings otherwise dominate [69,73,165,166]. For example, for the reaction of *m*-cresol over a Pt/C catalyst at 523 K, 20 bar, and a space velocity of 200 h⁻¹, Griffin *et al.* observed high selectivities to ONE (40%) and OL (52%) with only trace amounts of TOL produced. In contrast for reaction at 623 K, 5 bar, and a space velocity of 200 h⁻¹, they observed that the product contained 48% TOL and only 32% and 10% of ONE and OL, respectively [73]. They obtained analogous results for a Pt/TiO₂ catalyst, with the selectivity to TOL being 3% and 78% for the low- and high-temperature conditions. The

results obtained in the present study for Pt-WO_x/C are, therefore, somewhat surprising since >90% selectivity to TOL was obtained for a similar range of reaction temperatures and hydrogen pressures (Figure 6.6).

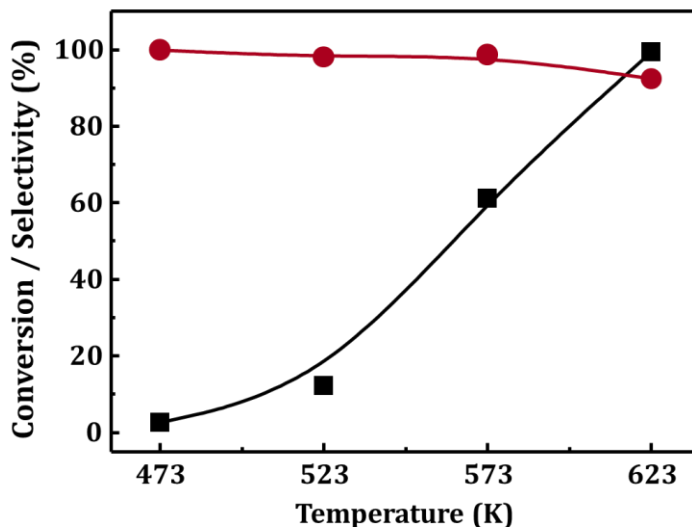


Figure 6.6 Conversion (■) and selectivity of toluene (●) as a function of temperature for high-pressure HDO reaction of *m*-cresol over Pt-WO_x/C catalyst. Reaction condition: 36 bar, 2-mol% *m*-cresol/dodecane solution, WHSV = 0.6 hr⁻¹.

The large discrepancies in the activity and selectivity of the Pt/C and Pt-WO_x/C catalysts suggest that different reaction pathways dominate on each catalyst. In order to provide additional insight into these pathways, data were collected for the reaction of ONE and OL (2-mol% in dodecane) over the two catalysts at 573 K and 36 bar. These data along with the analogous data for the *m*-cresol reactant for comparison are shown in Figure 6.7. To facilitate comparison, the products in this figure are grouped according to hydrocarbons (HC) that consist of TOL and MCH, and oxygen-containing hydrocarbons (O-HC) that consist of ONE, OL and/or *m*-cresol. As shown in Figure 6.7b, when ONE was fed as the reactant 100% and 45% conversions were obtained over the Pt-WO_x/C and Pt/C catalysts,

respectively. The former produced 66% TOL and 32% MCH, whereas the latter produced a spectrum of products including TOL (19%), MCH (16%), *m*-cresol (38%) and OL (27%). Note that for Pt-WO_x/C only hydrocarbons were produced, while for Pt/C 65% of the converted reagent did not have the oxygen removed. Figure 6.7c presents the results when OL was the reactant. In this case the Pt-WO_x/C catalyst exhibited 100% conversion with 13% selectivity to TOL and 85% selectivity to MCH. In comparison, the Pt/C catalyst was again considerably less active with only 66% conversion, and produced a wider range of products including both hydrocarbons and oxygenates: 11% TOL, 52% MCH, 28% ONE, and 10% *m*-cresol.

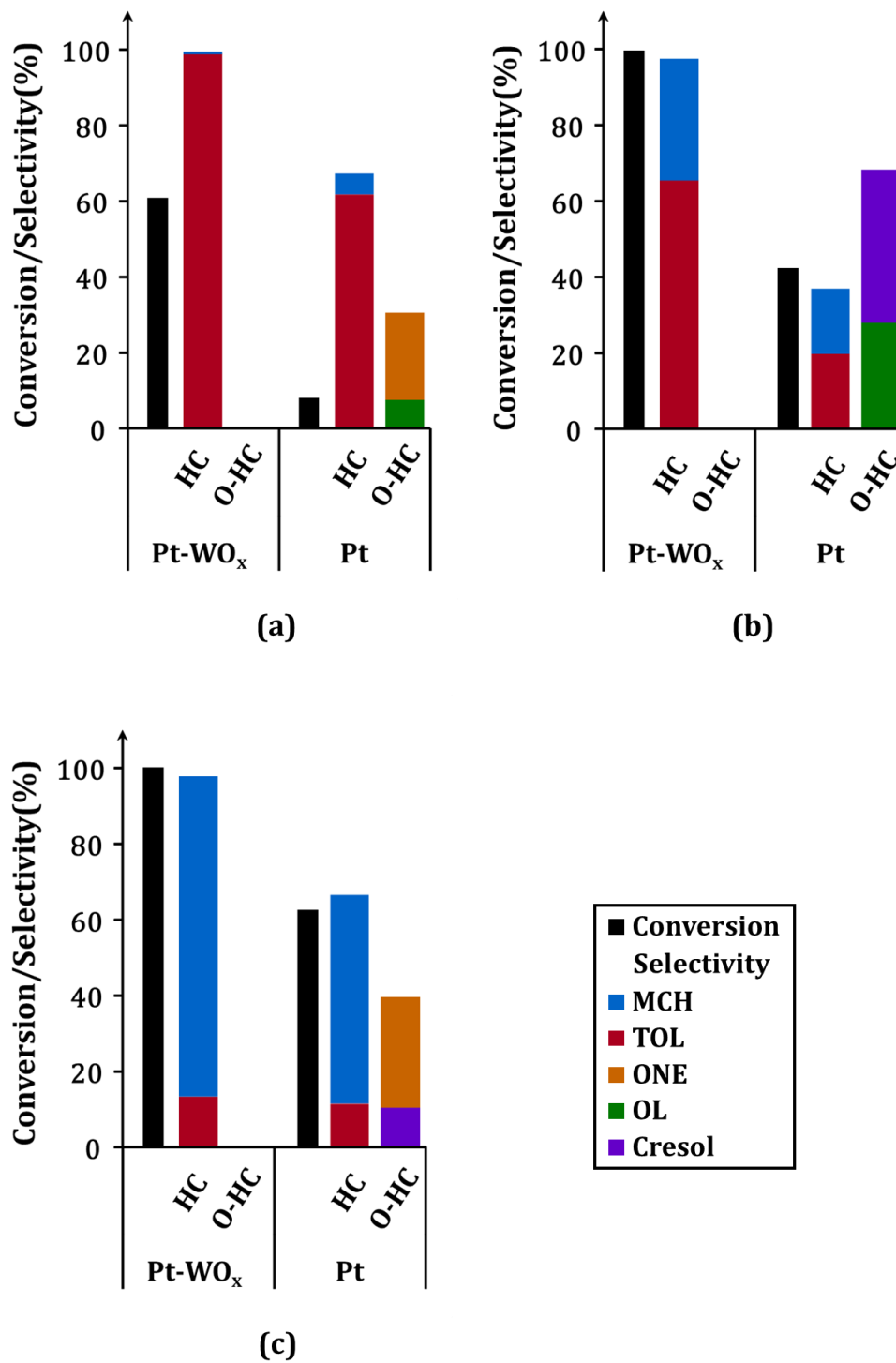


Figure 6.7 High-pressure HDO reaction of (a) *m*-cresol, (b) ONE and (c) OL over Pt-WO_x/C and Pt/C catalyst. Products are grouped as hydrocarbons (HC) and oxygen-containing

hydrocarbons (O-HC). Reaction conditions: 573 K, 36 bar, 2-mol% *m*-cresol/dodecane solution, WHSV = 0.6 hr⁻¹.

6.3.2 Additional Catalyst Characterization

XPS was used to provide insight into the oxidation state of the W in the Pt-WO_x/C catalyst. To ensure Pt-WO_x direct contact and enhance the signal-to-noise ratio of the XPS spectra, these studies made use of a model catalyst consisting of a Pt foil that had been subjected to a single ALD WO_x deposition cycle. XPS spectra were collected both immediately after ALD deposition of the W and after exposing the model WO_x-Pt catalyst to *m*-cresol HDO reaction conditions (H₂ plus 2-mol% *m*-cresol in dodecane, 36 bar total pressure, 573 K for 5 h (no measurable rates were obtained due to the extremely low surface area). Note that in both cases the samples were exposed to air prior to XPS analysis. Figure 6.8 displays the Pt(4f) and W(4f) spectra obtained from these samples. The W(4f_{5/2}) and W(4f_{7/2}) peaks for the freshly prepared catalyst are located at 38.1 and 36.1 eV, respectively, which is consistent with those reported in the literature [167] for W⁺⁶ indicating that the ALD procedure results in deposition of WO₃ on the Pt surface. Except for a reduction in peak intensity due to more carbon contamination, the W(4f) spectrum of the sample exposed to HDO reaction conditions was similar to that for the fresh sample, although some intensity is apparent at lower BE suggesting that some reduction of the WO₃ deposits may have occurred. While one must take into account that this sample was exposed to air prior to XPS analysis, the fact that both the W(4f) and Pt(4f) spectra provide no evidence for zero-valent W or alloy formation supports the conclusion that the W remains in an oxidized form under reaction conditions.

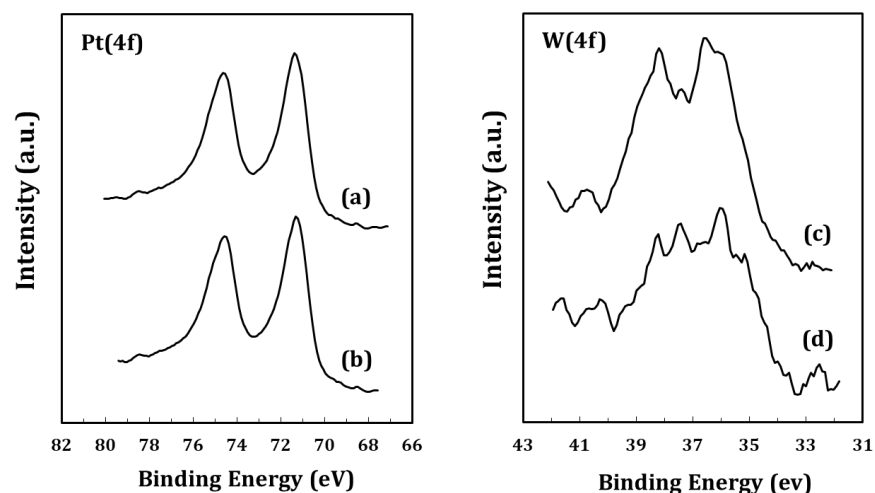


Figure 6.8 XPS spectra of the Pt(4f) and W(4f) energy regions of WO_x-decorated Pt model catalysts (a and c) before and (b and d) after exposing to *m*-cresol HDO reaction conditions (H₂ plus 2-mol% *m*-cresol in dodecane, 36 bar total pressure, 573 K) for 5 h.

Measurement of the Pt dispersion via selective CO chemisorption was also used to provide additional insight into the structure of the Pt-WO_x/C catalyst. These results along with those for Pt/C are reported in Table 6.1. As shown in this table, the Pt/C catalyst exhibited a relatively high Pt dispersion of 17%. In contrast, the apparent dispersion for the highly selective Pt-WO_x/C catalyst with 6.3-wt% WO_x loading was only 3%. Since I have previously shown that the Pt particle size is not altered upon WO_x deposition [145], this low dispersion value indicates that the majority of the Pt was coated with highly dispersed WO_x. Interestingly, the XRD patterns (Figure 6.9) for both pristine and consumed Pt-WO_x/C catalysts showed no features associated with WO_x. It suggests that the WO_x species are either amorphous or small enough in crystal size that they cannot be detected by XRD. This does not mean, however, that some small isolated WO_x species were also not present on the support. To further examine if intimate contact between Pt and WO_x is a prerequisite for obtaining >90% selectivity to TOL during HDO of *m*-cresol, a 10-wt% Pt-WO_x/C

catalyst was prepared in which the WO_x was added using ALD. It has been demonstrated previously using STEM-EDS mapping that the $\text{W}(\text{CO})_6$ ALD precursor preferentially reacts on the Pt and not on the carbon support [145], thus insuring intimate contact between the Pt and WO_x . The WO_x loading for this catalyst was only 1.6-wt% and it had an apparent Pt dispersion of only 5%. In contrast, an impregnated Pt- WO_x/C catalyst with the same 1.6-wt% WO_x loading had a 9% apparent dispersion, suggesting less intimate contact between the Pt and WO_x for this catalyst. The reactivities of these catalysts were also measured and as shown in Table 6.1 the conversion and selectivity to TOL for the reaction of *m*-cresol over ALD Pt- WO_x/C was 55% and 97%, respectively. Thus, direct interactions between the Pt and WO_x appear to play an important role in obtaining this unusually high selectivity for the HDO of *m*-cresol to produce TOL. Additionally, CO chemisorption was also performed on a consumed Pt/C catalyst to help evaluate the degree of coking. The apparent Pt dispersion decreased from 17% prior to reaction to 8% after reaction. This result is qualitatively consistent with our supposition that coking of bare Pt is in part responsible for the induction period shown in Figure 6.4.

Table 6.1 Metal dispersions for carbon supported catalysts after 573K reduction, assuming CO/Pt = 1. Conversion and selectivity for high-pressure HDO reaction of *m*-cresol. Reaction conditions: 573 K, 36 bar, 2-mol% *m*-cresol/dodecane solution, WHSV = 0.6 hr⁻¹.

Catalysts	WO_x Loading (wt%)	Pt Dispersion (%)	Conversion (%)	TOL selectivity (%)
Pt	0	17	8.3	62
Pt- WO_x	6.3	3	61	98
(ALD) Pt- WO_x	1.6	5	55	97

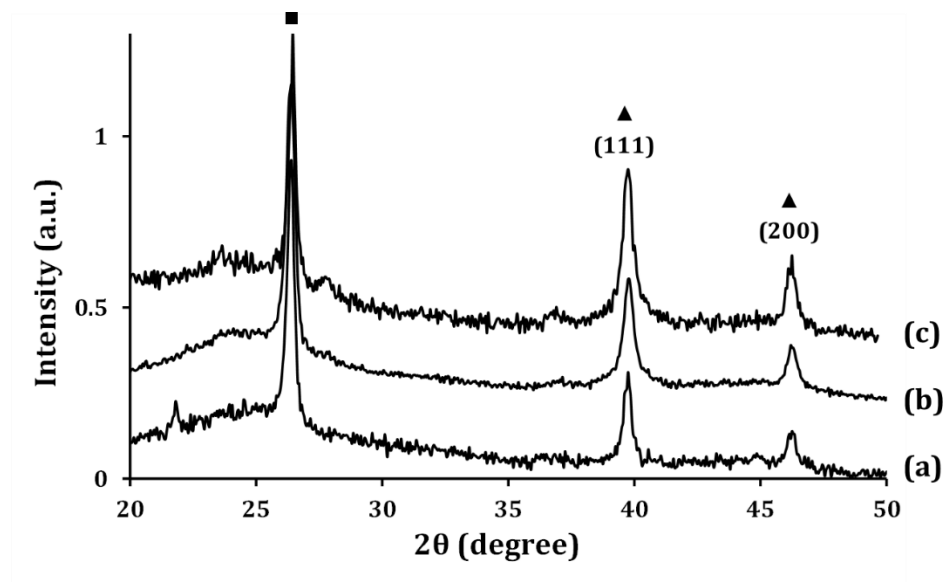


Figure 6.9 X-ray diffraction (XRD) pattern of (a) pristine Pt/C, (b) pristine Pt-WO_x/C and (c) consumed Pt-WO_x/C after exposing to *m*-cresol HDO reaction conditions (H₂ plus 2-mol% *m*-cresol in dodecane, 36 bar total pressure, 573 K) for 5 h. XRD patterns are normalized and referenced to graphite feature (■) at 26.5°. Pt facets are labeled by ▲.

6.3.3 Computational Studies

DFT calculations were used to provide additional insight into the synergistic interactions between WO_x and Pt and the mechanism of the HDO of *m*-cresol over Pt-WO_x/C catalysts. Optimized structures for W_xO_{3x} clusters supported on Pt(111) are depicted in Figure 6.10(A1-A3). The tungsten atoms are tetrahedrally coordinated to O in all of the clusters with the WO₃ units forming polymeric chains bound to each other via bridging O atoms and to the Pt surface via both W and O. The surface structure of the supported clusters differs from that in monoclinic bulk WO₃ with octahedrally coordinated tungsten, bearing striking similarity to WO₃ supported on HY/γ-Al₂O₃ [168], γ-Al₂O₃ [169], and TiO₂ [170], suggesting that the linked tetrahedral structure is general for WO₃

films on both oxide and metallic substrates. However, we find that cyclic tetrahedral $(\text{WO}_3)_3$, previously observed in the gas phase and on $\text{TiO}_2(110)$ [171], is 0.3 eV less stable than (A2) in Figure 6.10. This difference is attributed to strong direct Pt-W interaction, enabled on Pt(111) (*vide infra*).

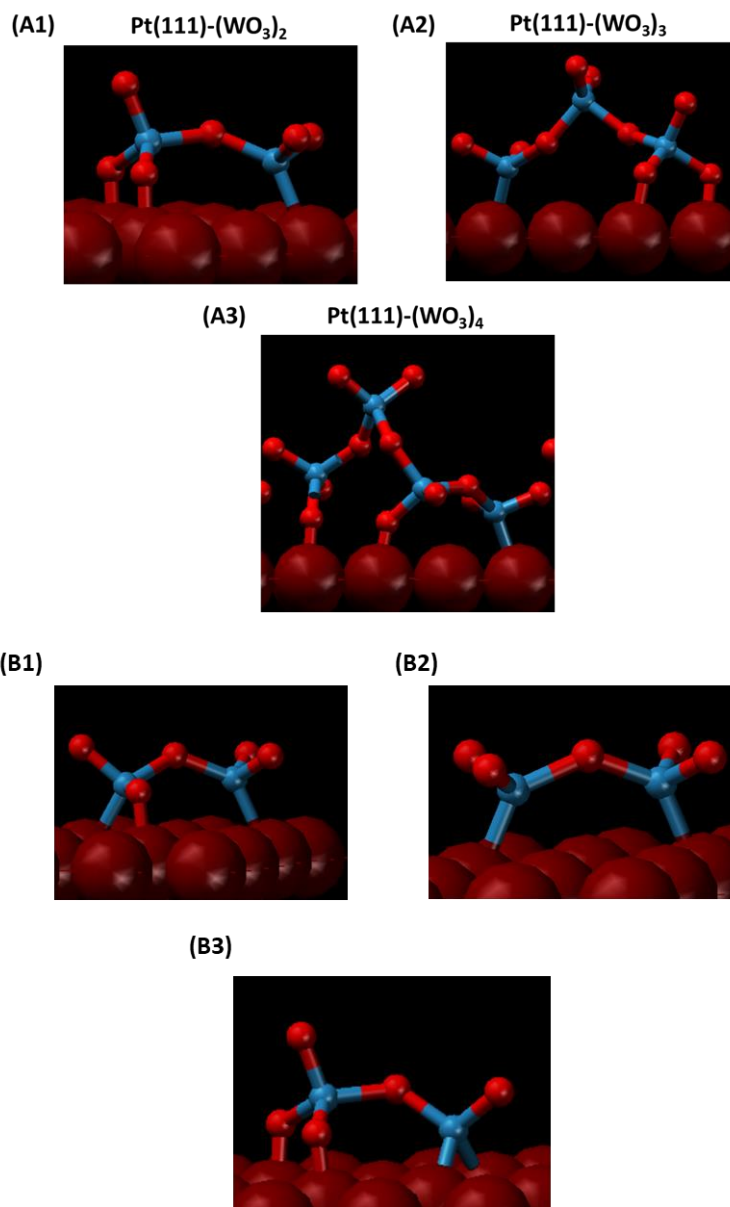


Figure 6.10 Simulated annealing-optimized W_2O_6 (A1), W_3O_9 (A2), and W_4O_{12} (A3) clusters, supported on Pt (111). (B1 – B3): partially reduced Pt (111)- W_2O_5 . B1/B2 and B3 correspond to O removal at WO_4 and WO_3 Pt tetrahedral units, respectively.

Pt(111)-W₂O₆ was selected as the simplest possible model of the Pt-WO_x/C catalyst for subsequent mechanistic study. Unlike W₃O₉ and W₄O₁₂ clusters, W₂O₆ does not contain tetrahedral units not bound to the Pt surface (Figure 6.10 A1-A3). Such WO₃ units are unlikely to participate in redox chemistry (*vide infra*).

To probe the redox properties of Pt-supported WO₃ structures, which are likely to be involved in selective HDO, we optimized six Pt(111)-W₂O₅ structures, formed by removing one out of six possible O atoms in the original W₂O₆ cluster. Three unique optimized structures are shown in Figure 6.10 (B1-B3). The B1 structure is the most energetically stable, with B2 and B3 being less stable by 0.18 and 0.67 eV, respectively. The large energy difference between the B1 and B3 structures indicates that oxygen vacancy formation is more facile at the more O-coordinated W sites (*i.e.*, more oxidized) with no direct W-Pt interaction. The bridging O atom in the W-O-W unit of W₂O₆ is extremely stable, as evident from its presence in all of the optimized W₂O₅ structures, even after attempting to remove it. Additionally, W-O-W motifs were intact during AIMD at 3000 K (Movie1 available in electronic SI), confirming their extreme stability. Consequently, the bridging O atoms are likely inert with respect to redox reactions and may be responsible for the observed high surface oxide stability.

Structural and energetic analysis reveals that the Pt substrate influences the WO₃ redox properties in two ways. First, it promotes the formation of the highly stable tetrahedral WO₃ structures as noted above. Consistent with prior reports on its stability [169], we find the W-O bonds in the tetrahedral WO₄ unit, which are not directly bound to the surface in the Pt(111)-supported W₃O₉ cluster, to be considerably stronger in comparison with those of WO₃(0001) (+2.33 eV vs. +1.28 eV bond cleavage energy at

frozen geometry, relative to H₂ and H₂O in a vacuum). Second, Pt stabilizes the reduced W₂O₅ states, facilitating oxygen vacancy formation. The latter is evident from the fact that all optimized Pt(111)-W₂O₅ structures contain an additional Pt-W bond, even if the initial structure did not possess Pt-W bonding (Figure 6.10), and a low formation energy of the B1-B3 structures (-0.87, -0.69, and -0.20 eV, respectively, relative to H₂, H₂O, and Pt(111)-W₂O₆). These values are comparable to or lower than the vacancy formation energy on pristine RuO₂(110) (-0.43 eV), previously reported to be an active site in HDO reactions [172], also suggesting that the Pt-supported WO₃ surface oxide most probably stays in a partially reduced form in a H₂-rich reaction environment. The stabilizing effect of the Pt substrate on the partially reduced WO₃ parallels the promoting effect of metal nanoparticles on oxide reduction in general [173] and of Pd on WO_x in particular [174]. We conclude that the metal substrate improves stability of the oxide film, while also facilitating vacancy formation at special sites on a metal/oxide interface.

Table 6.2 reports DFT-predicted reaction energies and barriers for C-O bond scission in *m*-cresol on Pt(111)-W₂O₅ to form physisorbed toluene and Pt(111)-W₂O₅-O* in comparison with those on a WO₃(0001) vacancy and a honeycomb Pt(111)-Co₃O₂ [45]. The latter some of us previously reported to be effective in C-O bond breaking in 2,5-bis-(hydroxymethyl)-furan (BHMF) [45]. The C-O scission barriers are very high on a WO₃(0001) vacancy and Pt(111)-Co₃O₂ (3.33 and 2.96 eV, respectively), consistent with negligible catalytic activity on WO_x/C and 10-wt% Pt₃Co₂/C. While the barrier on the WO₃Pt unit of the B1 structure of Pt(111)-W₂O₅ is also high (3.01 eV), we find that the WO₂Pt₂ unit of B3 (Figure 6.10) is much more efficient in breaking the C-O bond (2.00 eV barrier). The trend in Bader [175] tungsten atom charges parallels the C-O bond breaking

barriers: $\text{WO}_2\text{Pt}_2(+2.19) < \text{WO}_3\text{Pt}(+2.47) < \text{WO}_3(0001)(+2.58)$ and $\text{WO}_3(\text{bulk})(+2.70)$, revealing the beneficial role of the WO_x cluster reduction on HDO activity. On WO_2Pt_2 , the bond cleavage occurs together with the C-H bond formation in a concerted manner (Figure 6.11). The large C-O and C-H bond distances in the transition state (2.57 and 2.17 Å, respectively) indicate that the transition state most likely has a weakly bound radical character, similar to C-O scission transition states in furanics [45,172]. We note that the barriers reported herein are likely overestimated due to Pt- WO_x model limitations. Accounting for partial WO_x reduction and surface hydrogenation [172] under reaction conditions should improve absolute values.

Table 6.2 Concerted C-O scission DFT energies on various catalyst surfaces. BHMF stands for 2,5-bis(hydroxymethyl) furan, HMMF - 2-hydroxymethyl-5-methyl furan, TOL – toluene, O* - surface oxygen, V – oxygen vacancy. B1 and B3 refer to corresponding structures in Figure 6.10.

Reaction	Catalyst	Reaction energy, eV	Reaction barrier, eV
BHMF →HMMF+O*	Pt(111)- Co ₃ O ₂	0.74 [45]	1.19 [45]
		1.27	2.96
<i>m</i> -cresol→TOL+O*	Pt(111)- W ₂ O ₅ -B1	0.17	3.01
	Pt(111)- W ₂ O ₅ -B3	-0.19	2.00
	WO ₃ (0001)-V	0.77	3.33

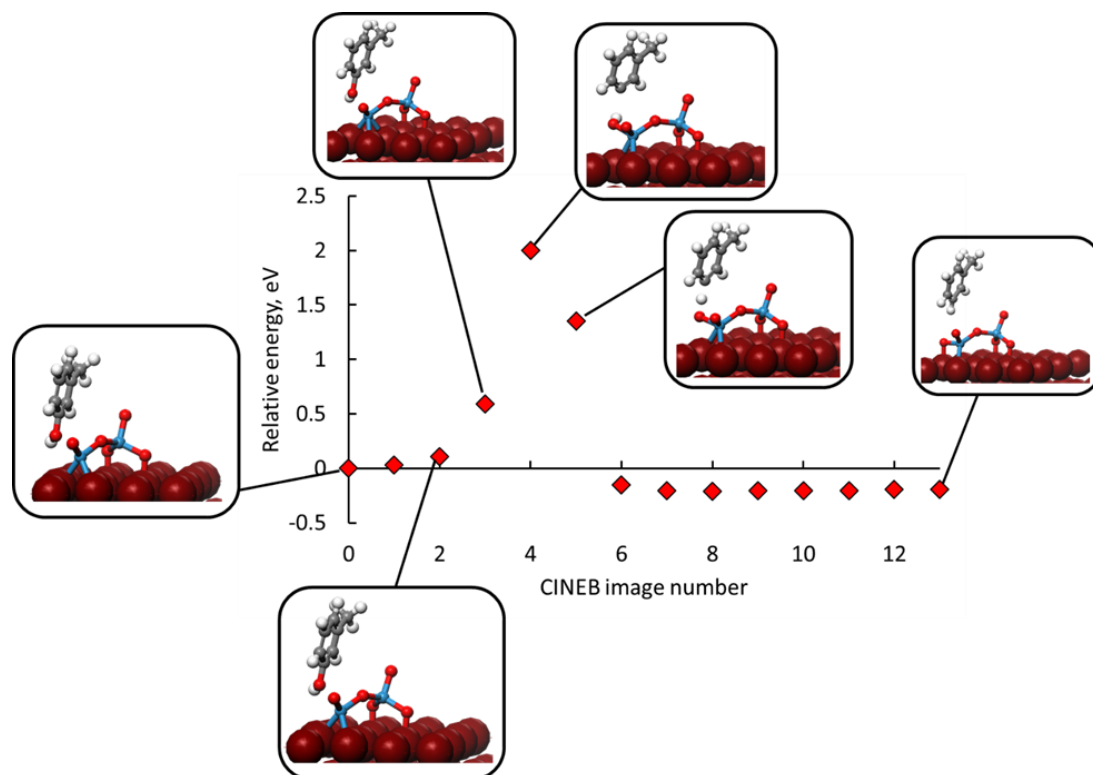


Figure 6.11 Computed reaction pathway for the concerted C-O bond scission/C-H bond formation in *m*-cresol on Pt(111)-W₂O₅-B3. Energy is plotted relative to the initial state energy, set to zero.

We attribute the enhanced HDO activity of reduced Pt(111)-WO_x to its higher oxophilicity – the O binding energy on (B3) Pt(111)-W₂O₅ relative to H₂ and H₂O is considerably less endothermic (+0.20 eV) than that on a honeycomb Pt(111)-Co₃O₂ (+1.70 eV). While weak oxophilicity of the latter was sufficient to activate the C-O bond in BHMF at low temperatures (433 K) due to extra stabilization of the transition/final state by conjugation [45], no such stabilization is possible in *m*-cresol-derived intermediates, necessitating a more oxophilic catalyst, as well as higher reaction temperatures (573 K), for the reaction to proceed.

6.4 Discussion

Before discussing the possible origin of the unusually high activity and selectivity of the Pt-WO_x/C catalyst for the HDO of *m*-cresol to produce TOL, it is useful to first compare the results obtained here for the Pt/C catalyst to those reported in previous studies of supported Pt catalysts. Our reactivity data for the Pt/C catalyst for the HDO of *m*-cresol appears to be in accord with that reported in the literature for Pt on non-acidic supports [59,69,73]. For example, Nie *et al.* studied the gas phase HDO of *m*-cresol over 1 wt% Pt/SiO₂ at 573 K and *m*-cresol and H₂ pressures of 1.25×10^{-2} atm and 1 atm, respectively, and observed that ONE was the primary product for space velocities between 8.5 and 110 hr⁻¹ with TOL and OL being secondary products [59]. Foster *et al.* performed similar experiments with 1.55 wt% Pt/SiO₂ (533 K, *m*-cresol and H₂ pressures of 7.5×10^{-3} atm and 0.5 atm) and observed that at lower space velocities TOL becomes the dominant product with much smaller amounts of OL and MCH being produced [69].

Using first-principles microkinetic modeling along with comparisons to the aforementioned studies Gu *et al.* [176] concluded that HDO of cresols on Pt proceeds via a pathway involving partial hydrogenation of three to five of the aromatic ring carbons with subsequent C-OH bond scission. Hydrogenation of the H-deficient-C (to the methyl group) in the resultant intermediate along with dehydrogenation of the other ring carbons leads to the production of TOL. As shown in Figure 6.12, a distinguishing feature of this

mechanism is that it does not necessarily require full hydrogenation of the ring as has been suggested in several previous studies in the literature [69,177–179] but rather involves a common pool of intermediates that leads to a range of side products [176]. This mechanism has some features in common with that proposed by Resasco and co-workers [59,67,68] which involves fast keto-enol tautomerization of the reactant followed by carbonyl hydrogenation to form a methyl cyclohexadienol intermediate which undergoes dehydration to produce TOL. In both of these scenarios complete ring hydrogenation products, such as ONE, OL and MCH, are produced only by side reactions and these species are not intermediates in the TOL producing pathway. This conclusion is consistent with the results obtained here as illustrated by the data in Figure 6.7 which shows that when ONE and OL are used as the reactant the selectivity to TOL is substantially less (19% and 11%, respectively) than that obtained when using *m*-cresol as the reactant (62%). Also note that for *m*-cresol, ONE and OL hydrogenation each reactant produces a group of all the other four major compounds, which confirms the presence of a pool of intermediates in the reaction network on Pt/C (Figure 6.12).

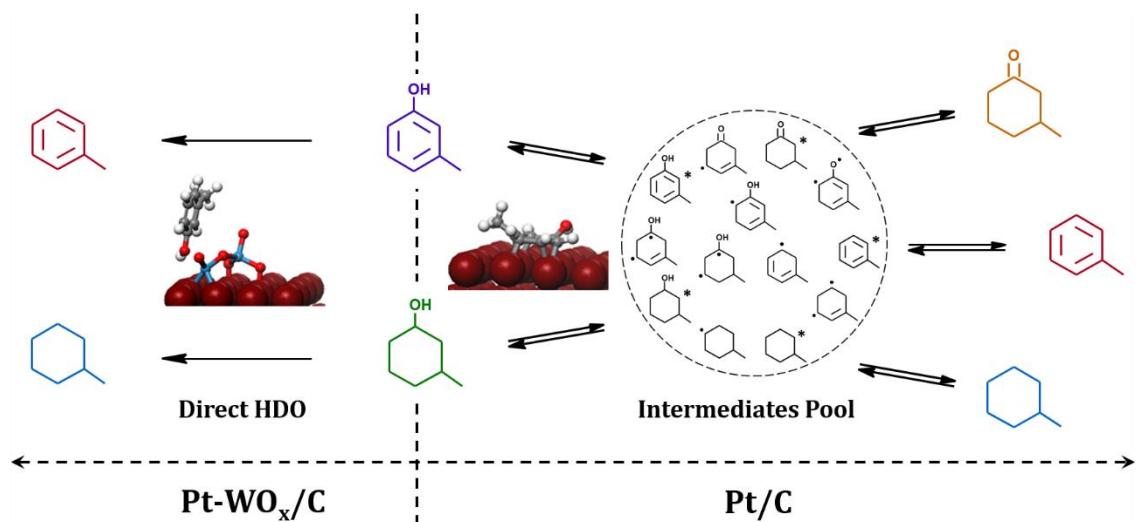


Figure 6.12 Comparison of simplified reaction networks and DFT-optimized adsorption structures for HDO reaction of *m*-cresol over Pt/C and Pt-WO_x/C catalysts.

While for the HDO reaction conditions used in the present study the Pt/C catalyst was shown to be somewhat selective for the production of TOL (see Figure 6.3), its initial overall activity was low and it underwent rapid deactivation over time (see Figure 6.4). As noted above, for the reaction temperatures used here it is unlikely that the deactivation was due to Pt agglomeration and loss of surface area. We instead attribute it to coking of the Pt surface. It is noteworthy that deactivation appears to have also been a problem in the aforementioned previous studies of HDO of *m*-cresol over Pt/SiO₂. For example, in the Nie *et al.* study it is noted that the H₂/*m*-cresol ratio was kept at 80:1 in order to minimize catalyst deactivation while running the reaction in the gas phase [59]. For the more industrially relevant liquid phase reaction conditions and H₂/*m*-cresol ratios, such as those used in the present study (H₂/*m*-cresol = 5), it is clear that catalyst deactivation over time will be problematic.

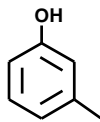
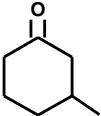
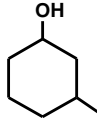
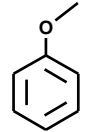
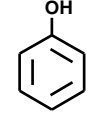
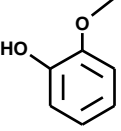
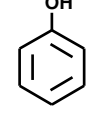
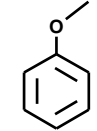
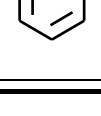
In contrast to Pt/C, which exhibited only modest selectivity and low stability for the HDO of *m*-cresol to produce TOL, the Pt-WO_x/C was unusually selective for this reaction with a selectivity to TOL of greater than 94% for all of the reaction conditions used in this study. Furthermore, this catalyst was highly stable and not prone to deactivation. It is clear that the reaction pathways for *m*-cresol and other oxygenates on Pt-WO_x/C are distinct from those on Pt/C. In addition to the high selectivity to TOL, evidence for this includes the fact that Pt-WO_x/C also exhibited high deoxygenation activity when ONE and OL were used as the reactants producing only hydrocarbon products in contrast to Pt/C which always produced a range of hydrocarbons and oxygenates (see Figure 6.7). These results along with the observation of essentially no secondary products during HDO of *m*-cresol demonstrates that the Pt-WO_x/C catalyst is highly selective for direct C-O bond cleavage (Figure 6.12) and has low activity for ring hydrogenation/dehydrogenation. The DFT results indicate that this lack of hydrogenation/dehydrogenation activity relative to Pt/C is due at least in part to the bonding configuration of *m*-cresol on each catalyst. As shown by the optimized adsorption structures in Figure 6.12, the aromatic ring in *m*-cresol bonds parallel to the Pt surface which facilitates ring hydrogenation, while it is oriented away from the underlying Pt when bonding to an oxygen vacancy site on WO_x via the hydroxyl group.

Since Pt is known to be a good catalyst for the hydrogenation of aromatic rings, the lack of ring hydrogenation products for the Pt-WO_x/C catalyst indicates that there is little to no direct interaction of the ring in *m*-cresol with the Pt surface in the TOL producing

pathway. Weak ring binding to an oxide surface has previously been found to be a key factor for selective C-O scission in furanics on Ru-RuO₂ [172] and Pt-CoO_x [45,180] catalysts. On Pt-WO_x/C, the reaction appears to proceed via bonding of the oxygen in the hydroxyl to a partially reduced, Pt-bound WO₂ unit on the WO_x surface layer (Figure 6.11). The DFT results presented above provide support for this conclusion and show that there is a moderate-energy concerted pathway for C-O bond scission in *m*-cresol on Pt(111)-W₂O₅ to form physisorbed toluene. In this direct pathway, which involves a redox site of the WO_x layer, the Pt appears to play the critical role of stabilizing the partially reduced W active sites (oxygen vacancies) through the formation of W-Pt bonds.

The results of this study indicate that Pt-WO_x/C has much promise as a highly active and selective catalyst for the HDO of the range of phenolic compounds that are produced via the fast pyrolysis of the lignin fraction of biomass. Indeed, I have already demonstrated that the excellent HDO performance of Pt-WO_x/C is not limited to *m*-cresol and that high selectivities to the desired aromatic hydrocarbons are also obtained during HDO anisole and guaiacol using reaction conditions similar to those used here for *m*-cresol (see data in Table 6.3). These results will be described in detail in a future paper.

Table 6.3 Conversion and selectivity for high-pressure HDO reaction of *m*-cresol, anisole and guaiacol over Pt-WO_x/C and Pt/C catalysts. Reaction conditions: 623K, 36 bar, 2-mol% reagent/dodecane solution, WHSV = 0.6 hr⁻¹.

Substrate	Catalysts	Conversion (%)	Product Selectivity (%)							
	Pt-WO _x	100		92		0		-	Other	8
	Pt	51		71		8		3	Other	18
	Pt-WO _x	64		80		9	-	Other	11	
	Pt	18		39		57	-	Other	4	
	Pt-WO _x	88		59		21		8	Other	11
	Pt	13		0		97		0	Other	3

CHAPTER 7. HYDRODEOXYGENATION OF *M*-cresol OVER Pt-WO_x/C USING H₂ GENERATED IN-SITU BY *N*-hexane DEHYDROGENATION⁶

Summary

The on-going study described in this chapter was a continuation of the cresol HDO project introduced in Chapter 6. I will demonstrate in this chapter that it is possible to replace expensive molecular hydrogen by using hydrogen generated *in-situ* by a simple dehydrogenation of *n*-hexane. The tandem reaction coupling dehydrogenation of *n*-hexane with HDO of *m*-cresol is ideal, because they both produce products that add value. Notably, the key observation that makes this possible is that the coking rates for dehydrogenation of *n*-hexane on Pt/C were found to be dramatically lower at high pressures. Two hypotheses will be proposed and discussed in the below sections in this chapter.

⁶This chapter was a manuscript prepared for submission, the work was contributed by **C. Wang**, C. Lin, R. Huang and R.J. Gorte.

7.1 Introduction

As I have discussed in Chapter 6, the products obtained from the initial depolymerization of lignocellulosic biomass remain highly functionalized and contain significant amounts of oxygen. To make the compounds stable and useful, it is necessary to remove at least some of the oxygen, usually by reaction with H₂ in hydrodeoxygenation (HDO) reactions [16,177]. Because H₂ is expensive, a great deal of effort has gone into preparing catalysts that are able to perform the HDO reactions selectively so as to minimize the amount of H₂ that is consumed. In the contributions from Chapters 3, 4, and 6, catalysts were developed to avoid consuming unnecessary H₂ for opening or saturating the furan and aromatic ring structures. Even so, the cost of H₂ is a significant impediment to the development of commercial processes that convert these compounds.

To avoid the cost of H₂, it can be useful to perform HDO using a different source of hydrogen. For example, this method for upgrading biomass feedstocks without directly adding H₂ is accomplished in Catalytic Transfer Hydrogenation (CTH) via the Meerwein-Ponndorf-Verley (MPV) reduction [76,181–184]. MPV reactions transfer hydrogen from a sacrificial alcohol, producing either a ketone or an aldehyde. However, it will still be necessary to consume H₂ in a separate reactor to restore the alcohol. An alternative to MPV involves generating molecular H₂ *in situ* by reforming light oxygenates in the same reactor in which HDO is performed [185–187]. The approach is challenging because the catalysts and reaction conditions required for reforming make selective HDO catalysis difficult. The requirement for sacrificial oxygenates is also an added cost and may require H₂ to produce.

Finally, hydrogen can be added to biomass by coupling hydrogenation and dehydrogenation reactions in tandem. This concept was demonstrated in a study where dehydrogenation of decalin and tetralin was used to supply hydrogen for HDO of phenolic compounds [188]. Again, H₂ would likely be required to convert the naphthalene that is produced back to the initial feed. An ideal situation would involve coupling hydrogenation and dehydrogenation reactions that both produce products that have value.

In Chapter 6, the work on HDO of *m*-cresol over Pt-WO_x/C showed that this catalyst exhibits high activity and selectivity to toluene, while exhibiting little to no deactivation over a wide range of reaction conditions. These results were intriguing, given that WO_x/C was not active for this reaction and that Pt/C showed poor activity, selectivity, and stability. The favorable properties of Pt-WO_x/C appear to be related to the fact that the surface of the Pt is decorated with a partially reduced WO_x species, which in turn causes the HDO reaction to proceed via a direct hydrogenolysis of the C-O bond in *m*-cresol. The use of carbon as the support is likely important in that WO_x prefers Pt to the non-acidic support [145]. The high stability of this catalyst led me to consider whether it could be used to carry out tandem, hydrogenation-dehydrogenation reactions.

I will show in this chapter that it is possible to use H₂ generated by dehydrogenation of *n*-hexane to hexene to perform HDO of *m*-cresol on a Pt-WO_x/C catalyst at high pressures (Figure 7.1). The key observation that makes this possible is that the coking rates for dehydrogenation of *n*-hexane on Pt/C were found to be dramatically lower at high pressures. While equilibrium conversions decrease with increasing pressure, the

consumption of H₂ by *m*-cresol over Pt-WO_x/C allows a higher conversion of *n*-hexane than would be possible by simple dehydrogenation.

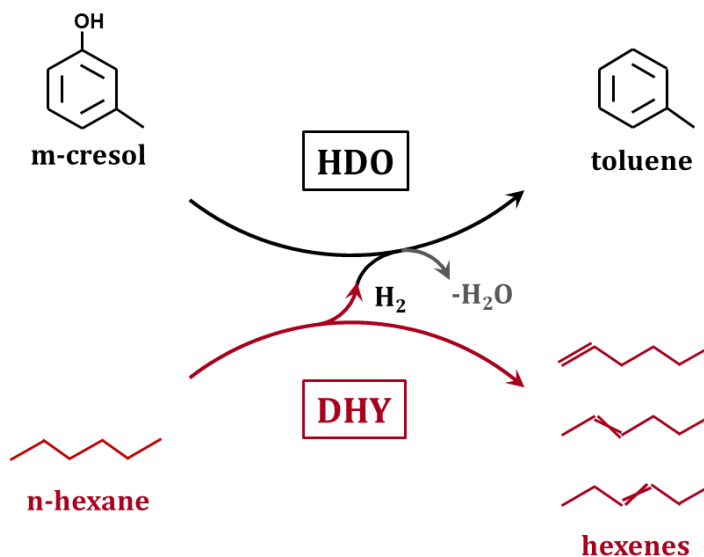


Figure 7.1 Reaction scheme for the tandem reactions of *m*-cresol HDO using *n*-hexane as H-donor.

7.2 Experimental

7.2.1 Catalyst synthesis

The carbon-supported Pt and Pt-WO_x catalysts were prepared using incipient wetness, as described in Chapters 2 and 6. The final Pt/C catalyst had a metal loading of 10-wt%, and the Pt-WO_x/C catalyst had a Pt:W elemental weight ratio of 2:1, which was equivalent to 6.3-wt% loading of WO₃.

7.2.2 Reactivity study

Reaction studies were performed in a high-pressure, tubular flow reactor similar to that described in Chapter 6 but without the inlet of molecular H₂. At the beginning of each experiment, air was displaced from the reactor using flowing He before switching to liquid feeds. The liquid feeds were either pure *n*-hexane (99+%, Acros) or *n*-hexane solutions with 5.7- to 20-mol% *m*-cresol (99%, Alfa Aesar). The feed was introduced to the reactor using an HPLC pump (Series I+, Scientific Systems Inc.) and the pressure was controlled by a back-pressure regulator (KPB series, Swagelok) at the reactor exit. Product analysis was performed in a GC-MS (QP-5000, Shimadzu), calibrated using standard *n*-hexane solutions of the products; but the GC column (Agilent, HP-INNOWax) did not allow separation of all hexene isomers.

7.3 Results

Representative results for the reaction of *m*-cresol with *n*-hexane over the Pt-WO_x/C, Pt/C, and WO_x/C catalysts are shown in Figure 7.2 for a feed that was 5.7-mol% *m*-cresol in *n*-hexane (5 g *m*-cresol/100 ml *n*-hexane). These experiments were carried out at 673 K and 36 bar, with a space time of 1 min·g_{cat}·mL⁻¹, conditions that are similar to those used in our previous HDO study of *m*-cresol [189], except that no H₂ was added to the liquid feed and the temperature here was higher. While WO_x/C was completely inactive, the Pt/C catalyst showed small conversions of both *n*-hexane and *m*-cresol. Although the conversion of *n*-hexane was only 1.0% on Pt/C, this is close to the equilibrium value that we calculated for this pressure and temperature, assuming that products were H₂, 1-hexene

and 2-hexenes. We were not able to separate the different hexene isomers but the selectivity to hexenes was about 90%. The conversion of *m*-cresol was very low, about 2.9%.

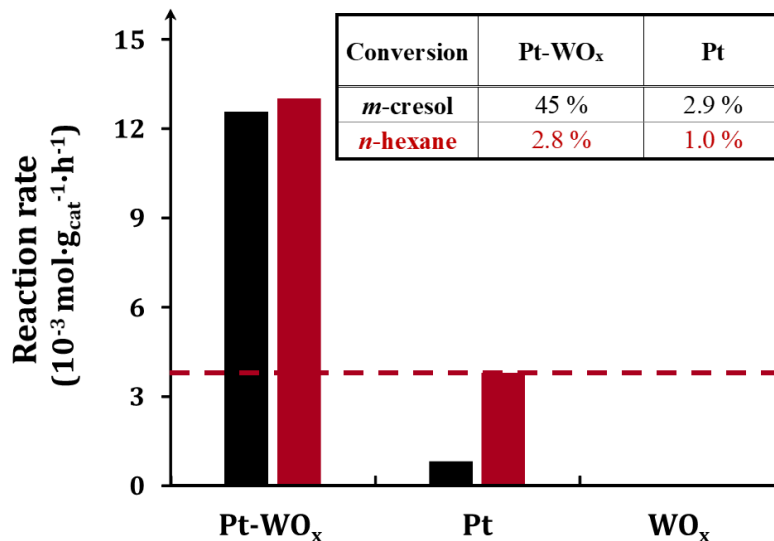


Figure 7.2 Reaction rates for high pressure tandem reactions of HDO of *m*-cresol (■) and DHY of *n*-hexane (■) over Pt-WO_x/C, Pt/C and WO_x/C catalysts at 673 K and 36 bar. The corresponding conversions are tabulated. Red dash line indicates equilibrium conversion (1%) of *n*-hexane determined by repeated experiments. Reagent concentration: 5.7·mol% *m*-cresol/*n*-hexane; space time = 1 min·g_{cat}⁻¹·mL⁻¹. Data obtained at 3 h on stream.

The rates and conversions on the Pt-WO_x/C catalyst were much more interesting. The *m*-cresol conversion under these conditions was 45%, with greater than 97% selectivity to toluene. The hydrogen used for the HDO reaction came from reaction of *n*-hexane, as shown by the fact that the rates for the conversion of *m*-cresol and *n*-hexane were almost identical. The selectivity of *n*-hexane to hexenes was 98% in this case; the fact that the *n*-hexane conversion, 2.8%, was above the equilibrium value calculated for Pt/C is explained by the consumption of H₂ in the HDO reaction over Pt-WO_x/C. Deactivation was negligible over the time required to make these measurements. It is noteworthy that, in a past HDO

study of *m*-cresol performed using molecular H₂ and the same catalyst, good conversions were achieved at 573 K, while reaction of *m*-cresol was negligible at that temperature in the present case, apparently because the equilibrium conversion of *n*-hexane is too low at the lower temperature.

A further demonstration that the HDO of *m*-cresol and dehydrogenation of *n*-hexane over Pt-WO_x/C are couple is shown in Figure 7.3. Here, steady-state rates and conversions are shown as a function of space time at 673 K and 36 bar. Figure 7.3a) is a plot of the conversions for both *m*-cresol and *n*-hexane as a function of space time, with Figure 7.3b) providing the integral reaction rates calculated from those conversions for both reactants. The data show that the reactions clearly occur in tandem. The reaction rates for *n*-hexane were slightly higher, consistent with the production of some molecular H₂ which can be observed at the exit of the reactor. The product selectivities also did not change.

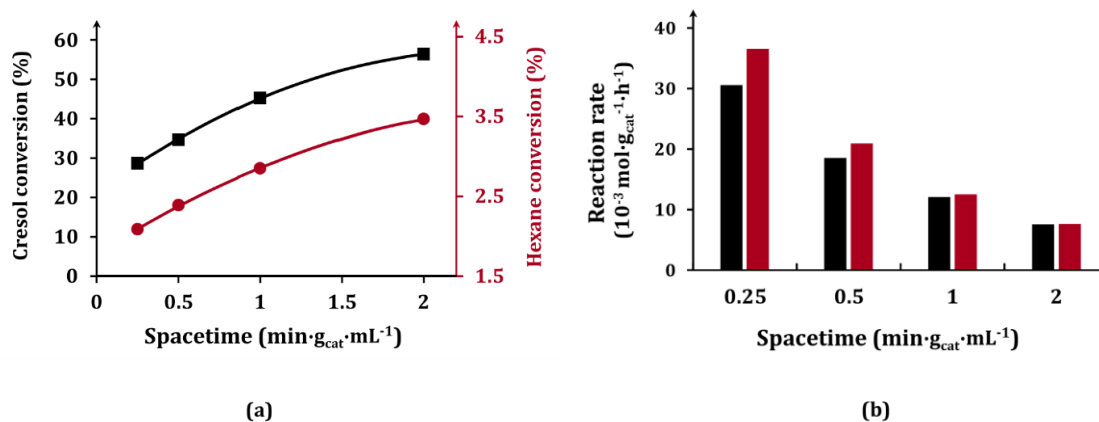


Figure 7.3 (a) Conversions and (b) reaction rates for high pressure tandem reactions of HDO of *m*-cresol (■) and DHY of *n*-hexane (●) as a function of space time at 673 K and 36 bar. Reagent concentration: 5.7-mol% *m*-cresol/*n*-hexane. Data obtained at 3 h on stream.

It is noteworthy that the integral reaction rates for *m*-cresol decreased by more than a factor of three when the space time increased from 0.25 to 2 min·g_{cat}·mL⁻¹. Since the conversions did not dramatically change over a period of several hours, the lower value at high space times cannot be due to poisoning of the catalyst. When we increased the *m*-cresol concentration to 19.8-mol% (20 g *m*-cresol in 100 mL *n*-hexane), the rate at a space time of 1 min·g_{cat}·mL⁻¹ was 16 mol·g_{cat}⁻¹·h⁻¹, compared to 12 mol·g_{cat}⁻¹·h⁻¹ when the *m*-cresol concentration was 5.7-mol%. Therefore, the reaction shows a relatively weak dependence on *m*-cresol concentration. We suggest that the reaction is limited by *n*-hexane dehydrogenation. This is consistent with the fact rates for *m*-cresol conversion on this catalyst were much higher in the presence of molecular H₂, even at lower temperatures [189].

The Pt-WO_x/C catalyst did show mild deactivation with time on stream under these conditions, as shown in Figure 7.4. Using a 5.7-mol% *m*-cresol solution and a space time of 1 min·g_{cat}·mL⁻¹, the HDO rate decreased from 12.0×10⁻³ mol·g_{cat}⁻¹·h⁻¹ at 3 h to 9.5×10⁻³ mol·g_{cat}⁻¹·h⁻¹ at 6 h on stream. The deactivation was slightly faster when the *m*-cresol concentration was 19.8 -mol%, decreasing from 16.2×10⁻³ mol·g_{cat}⁻¹·h⁻¹ at 3 h to 12.1×10⁻³ mol·g_{cat}⁻¹·h⁻¹ at 6 h. In the previous HDO study of *m*-cresol over this catalyst using H₂, the rates were stable for much longer times. However, since those measurements were also performed at lower temperatures, it is not clear whether the higher stability was due the presence of a higher H₂ pressure or the lower temperature.

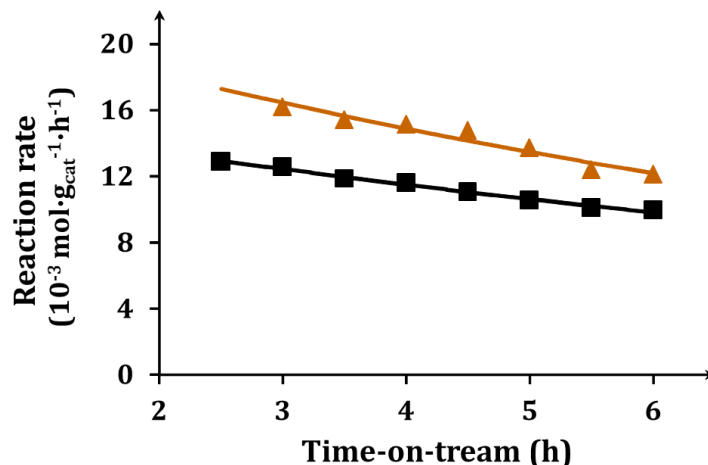


Figure 7.4 Time evolution for the HDO reaction rate over Pt-WO_x/C at 673 K and 36 bar using 5.7-mol% (■) and 19.8-mol% (▲) *m*-cresol/*n*-hexane solutions. space time = 1 min·g_{cat}·mL⁻¹.

The relatively slow deactivation observed in Figure 7.4 was surprising, since deactivation of Pt catalysts during alkane dehydrogenation is usually rapid [190], even in the absence of *m*-cresol. The high stability in the present case was related to the operating pressure. Figure 7.5 is a plot of the conversion of *n*-hexane over the Pt/C catalyst as a function of time at pressures varying between 1 and 36 bar. The feed in these experiments was pure *n*-hexane, the temperature was 773 K, and the space time was fixed at 0.25 min·g_{cat}·mL⁻¹. The calculated equilibrium conversions at each pressure are reported in Table 7.1. At 1 bar, deactivation was very rapid and the catalyst was essentially inactive after 30 min. The rate of deactivation decreased with pressure, so that deactivation was negligible for 5 h at 36 bar. The conversion at this pressure was also very close to the calculated equilibrium conversion. Since catalyst deactivation is likely related to formation of polyaromatics, the product distributions, listed in Table 7.2, are also of interest. Hexenes

were the major product at all pressures; but we observed a much higher conversion to cyclic compounds, including benzene, cyclohexane, and methyl cyclopentane, at the lower pressures. At 36 bar, the selectivity to hexenes was much higher and the side products were mainly C-1 to C-5 hydrocarbons.

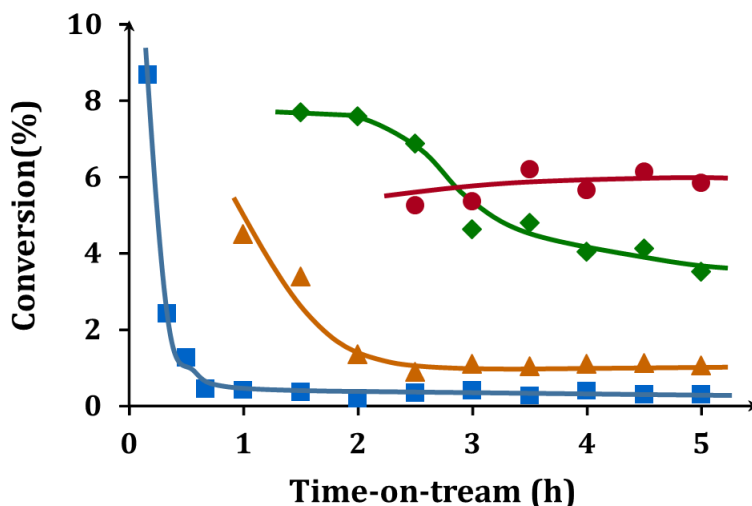


Figure 7.5 Time evolution for the conversions of the DHY reaction of *n*-hexane over Pt/C catalyst at 773 K and under total pressures of 1 bar (■), 8 bar (▲), 21 bar (◆), and 36 bar (●). Reaction condition: pure *n*-hexane feed, space time = 0.25 min·g_{cat}·mL⁻¹.

Table 7.1 Equilibrium conversions of *n*-hexane at 773 K and a range of total pressures. Data obtained from ASPEN PLUS™ using the Peng-Robinson equation of state.

Total pressure (bar)	Calculated equilibrium conversion of <i>n</i> -hexane
36	6.6 %
21	8.9 %
8	15.1 %

1	39.1 %
---	--------

Table 7.2 Selectivities for DHY reaction of *n*-hexane in the tandem reactions of *m*-cresol HDO using *n*-hexane as H-donor at 673 K and 36 bar. Reagent concentration: 5.7-mol% *m*-cresol/*n*-hexane; space time = 1 min·gcat·mL⁻¹. Data obtained at 3 h on stream.

	DHY Selectivity (%)			
	hexenes	cracking products	methyl cyclopentenes	benzene
Pt	87	6	4	3
Pt-WO_x	98	0.7	1.3	0

7.4 Discussion

In this chapter, I have demonstrated that it may be possible to perform HDO and dehydrogenation reactions simultaneously. The high selectivity of Pt-WO_x/C catalysts for HDO has been reported previously but the relatively high stability of a Pt/C catalyst for dehydrogenation at high pressures is new and surprising. The really interesting question is why there is a strong pressure dependence on the deactivation of Pt.

The work of Agirrezabal-Telleria and Iglesia [191] may provide an important clue for the mechanism behind the increased stability we observed at high pressures. In their investigation of ethylene dimerization over Ni catalysts supported on MCM-41, they reported dramatically increased stabilization of the catalyst when the pressure was increased above the value at which there was condensation in the pores. They argued that the presence of liquid reactants in the pores “stabilize the late transition states that mediate desorption of bound 1-butene before subsequent isomerization and C-C bond formation” produced larger products caused deactivation. In our case, there are no well-defined pores but surface condensation is possible. Using a simple Law of Corresponding States, we estimate that the bulk density of *n*-hexane at 773 K and 36 bar is approximately 10% of the liquid density; however, the concentration at the surface will certainly be much higher,

given that the heat of adsorption for *n*-hexane on carbons is in the range of 40 to 50 kJ/mol [192–194]. The fact that fewer cyclic products are produced at the higher pressures is also consistent with this picture.

Alternatively, surface crowdedness of *n*-hexane on Pt at high pressures may be important in preserving catalyst activity. It has been shown previously that crowding/packing effect has profound impact on reaction selectivities in heterogeneous catalysis [136,195,196]. For example, Vlachos *et al.* [136] have demonstrated in theory that it is energetically favorable for furfural to adsorb parallel on Pd (111) surface in hydrogenation reactions, and the adsorption species tends to tilt up from the surface at higher furfural/H₂ coverage. This gave rise to a higher selectivity of furfuryl alcohol (vs. decarbonylation to form furan) at higher furfural/H₂ partial pressures. The pressure dependence in product distributions for this reaction was later experimentally confirmed by our group using a Pt/C catalyst [135]. In the current work, we proposed a possible anti-coking mechanism in high-pressure alkane environment that is similar to the case in furfural hydrogenation reactions. The surface crowding may limit *n*-hexane from exposure parallel to the Pt surface and thus prevent further dehydrogenation, cyclization and polymerizations to form coke.

For the DHY reaction of *n*-hexane itself whether Pt particle is decorated by WO_x the activities appear to be identical. The tandem reaction as a composite, however, clearly requires the use of Pt-WO_x/C to simultaneously facilitate both side of the reactions (see Figure 7.6). Classic thermodynamics indicates that low equilibrium conversion should be an issue for alkane dehydrogenation at reasonable reaction temperatures, and it is particularly problematic at high pressures. For example, the equilibrium yields of hexenes from *n*-hexane are measured only ~1% at 673 K and 36 bar and 6.2% at 773 K and 36 bar. However, as is demonstrated in this work, incorporating HDO reaction of *m*-cresol on a highly active and selective Pt-WO_x/C can effectively push the conversion of *n*-hexane to hexenes. Apparently, the *m*-cresol can be viewed as a mild oxidant to facilitate an oxidative

dehydrogenation of *n*-hexane. Only in this work both sides of the tandem reaction are making useful products from less valuable reagents.

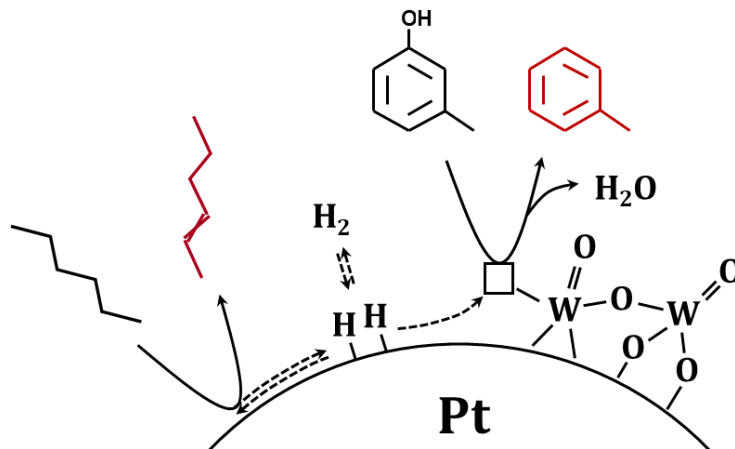


Figure 7.6 Proposed reaction mechanism for the tandem reactions of *m*-cresol HDO using *n*-hexane as H-donor.

Since I have demonstrated in Chapter 6 that HDO of *m*-cresol proceeds with the presence of molecular hydrogen, it is rather clear that the two reactions are connected by in-situ H₂ that is produced by *n*-hexane dehydrogenation followed by H₂ consumption from *m*-cresol HDO. At 673 K, the HDO of *m*-cresol and the DHY of *n*-hexane occur in near stoichiometry, and the rates of these two reactions appeared to increase in parallel with space times. Both evidences suggest that the overall reaction rates are limited by hydrogen production, and Pt-WO_x/C is able to efficiently utilize scarce hydrogen for the selective HDO reaction of *m*-cresol.

CHAPTER 8. A CHARACTERIZATION STUDY OF REACTIVE SITES IN ALD-SYNTHESIZED WO_x/ZrO_2 CATALYSTS⁷

Summary

ALD of WO_x was used to engineer the Pt- WO_x active interface in the studies featured in Chapters 5 and 6. However, characterization techniques that can directly demonstrate the uniform WO_x coverage were lacking due to the small surface area of Pt relative to the carbon support. Motivated in part by this limitation, I sought to demonstrate the utility of the ALD technique for designing overlayers catalysts by synthesizing tungstated zirconia, a well-known solid acid. Formation of a uniform, thin WO_x layer was verified by various techniques featured in this study. Together with the work that will be discussed in Chapter 9, I will show that the commonly accepted claim that W-Zr has super acidity is not correct that the W-Zr catalysts actually have weaker sites than those present in silica-alumina zeolites.

8.1 Introduction

In the 1980s, it was reported that tungstated zirconia (WO_x/ZrO_2) could be used as a solid acid catalyst; however, there are still many questions and apparent contradictions

⁷ This chapter was published as **C. Wang**, X. Mao, J. Lee, T. Onn, Y.-H. Yeh, C. Murray, R. Gorte, *Catalysts* 8 (2018) 292.

regarding the nature and strength of the acid sites in this material, as demonstrated in the recent review by Zhou *et al.* [197]. A major difficulty with tungstated-zirconia catalysts is that their properties depend on how they are made. It is likely, for this reason, that some studies indicated that the structure of the underlying ZrO₂, whether amorphous or crystalline (tetragonal or monoclinic), influences the activity of the sites [198], while other workers reported that the crystallographic structure of the zirconia is not important [199,200]. It was also suggested that the sites may be of varying strength, depending on the WO_x cluster size, with one theoretical study reporting that the Brønsted sites not only depend on cluster size, but can also approach super-acid strength [197]. However, the observations that it is necessary to add Pt in order for tungstated zirconia to exhibit alkane-isomerization activity [201,202] would suggest that the sites are less strong, in addition to tungstated zirconia being selective to ether formation in the dehydration of alcohols [203], without forming olefins, unlike with protonic zeolites.

Most researchers prepared their tungstated-zirconia catalysts via the aqueous impregnation of ammonium metatungstate ((NH₄)₁₀W₁₂O₄₁·5H₂O), followed by calcination [197]. In addition to the fact that this precursor consists of a relatively large number of tungsten atoms, the drying process itself can result in multiple clusters coming together before decomposing upon calcination [204]. While the WO_x species may spread over the support surface during calcination, the implications of there being so many tungsten atoms together in the initial state implies that there will likely be large clusters on the support in all cases. This is important because mono-tungstate species are not believed

to be the active component [197]. Furthermore, the fact that the catalytic properties are a function of the tungsten-oxide coverage and pretreatment conditions [205,206] implies that discrepancies in the results from different studies are likely due to differences in the detailed nature of the clusters that are formed in the catalysts.

Here, I set out to investigate the catalytic sites in WO_x/ZrO_2 catalysts prepared using atomic layer deposition (ALD). ALD is a self-limiting process in which WO_x is deposited through repeated, cyclic exposures of $\text{W}(\text{CO})_6$ and oxidants [145,207,208]. I have shown in Chapters 5 and 6 that this method could be used to deposit uniform WO_x overlayers preferentially on the Pt surfaces. Because the amount of WO_x deposited per cycle in ALD is low and the deposition is uniform, ALD ensures the formation of uniform, atomic-scale layers, which maximize the interfacial contact between WO_x and ZrO_2 . This allows the formation of isolated WO_x species, as well as much more control over the tungsten cluster sizes by increasing tungsten coverage. A complicating factor in the characterization is that zirconia itself exhibits activity in the reaction of amines and alcohols, and contributes to the activity of catalysts for some reactions. Fortunately, as demonstrated in this work, the chemistries on bare zirconia are oftentimes distinguishable from those that occur on WO_x/ZrO_2 interfaces, and thus, provide additional information on coverage and dispersion.

I also set out to test claims that tungstated-zirconia could show super-acidic properties. The quantification of Brønsted-acid strength in solid acids is difficult, and some common measures, such as heats of adsorption for ammonia or pyridine, were shown to be

uninformative [209]. A simple reaction that appears to depend only on the ability of the solid to protonate a weak base involves the H–D exchange between an aromatic molecule and deuterated acid sites [210]. In our case, we examined light-off curves for H–D exchange between D₂O and either toluene (C₇H₈) or chlorobenzene (C₆H₅Cl). Essentially, all hydroxides on solids exchange readily with D₂O [209,211], meaning that the presence of D₂O ensures a high concentration of deuterated acid sites. However, the deuteration of toluene (proton affinity = 784 kJ/mol) or chlorobenzene (proton affinity = 753 kJ/mol) requires the formation of a carbenium ion, so that the temperature at which exchange becomes rapid should be a reasonable measure of the acid strength. In agreement with expectations based on proton affinities, higher temperatures are required for H–D exchange with chlorobenzene compared to that with toluene; however, the Brønsted sites in tungstated zirconia appear to be significantly weaker than those in H-ZSM-5.

8.2 Experimental

8.2.1 Catalyst Synthesis

The ZrO₂ support was prepared by titrating (0.2 mL/s) 30% aqueous NH₄OH (Fischer) to a 5-wt% aqueous solution of ZrO(NO₃)₂•xH₂O (99%, Sigma Aldrich) with vigorous stirring. The precipitate was then dried at 333 K for 12 h before being calcined in a Muffle furnace at 773 K for 5 h. ALD was performed in a custom-built, static system that was described in Chapter 2. The nomenclature *x*W-Zr was used to refer to a sample exposed to *x* ALD cycles. For comparison purposes, a sample with 10-wt% WO_{*x*}/ZrO₂ (impW-Zr) was prepared via conventional aqueous incipient wetness of (NH₄)₁₀W₁₂O₄₁•5H₂O

(99.999%, Alfa Aesar), followed by a 4-h calcination at 773 K. To determine the effect of the support, a WO_x/SiO_2 sample (5W-Si) was prepared by depositing five ALD cycles onto a stabilized SiO_2 (Degussa AG, Ultrasil VN 3 SP, 140 m^2/g).

8.2.2 *Catalyst Characterization*

The temperature-programmed desorption/thermogravimetric analysis (TPD-TGA) measurements were performed on samples held in a system consisting of an evacuated CAHN 2000 microbalance, equipped with an SRI quadrupole mass spectrometer (RGA100), that is described in Chapter 2. The probe adsorbate, either 2-propanol (99.9%, Fisher), or 1-propanamine (99+%, Alfa Aesar), or 2-propanamine (99%, Alfa Aesar), was used to examine the reactive sites following the procedure described in Chapter 2.

Scanning transmission electron microscopy (STEM) and elemental mapping via energy-dispersive X-ray spectroscopy (EDS) were performed with a JEOL 2010F field-emission scanning transmission electron microscope (JEOL). Infrared spectra of adsorbed pyridine were performed on a Mattson Galaxy FTIR (Madison Instruments Inc.) with a diffuse-reflectance attachment (Collector IITM) in order to confirm the presence of Brønsted sites [212]. FTIR of adsorbed pyridine was also used to probe the Lewis and Brønsted acid sites. Raman spectra were obtained with an NTEGRA Spectra system (NT-MDT) with an excitation laser wavelength of 532 nm. Powder X-ray Diffraction (XRD) patterns were collected from a Rigaku Smartlab diffractometer equipped with a $\text{Cu K}\alpha$ source. Detailed description of these characterization techniques is shown in Chapter 2.

The steady-state reaction rates for various reactions (2-propanol dehydration, H–D exchange between toluene (C_7H_8) and D_2O , and H–D exchange between chlorobenzene (C_6H_5Cl) and D_2O) were measured in an ambient-pressure flow reactor described in Chapter 2. The results were compared to reaction measurements over an H-ZSM-5 catalyst ($Si/Al_2 = 280$; Zeolyst, CBV 28014). For the dehydration of 2-propanol, the inlet flow to the reactor was 5% 2-propanol in a 5 mL/min He flow. In the H–D exchange measurements, an equal molar fraction of 1% toluene (or chlorobenzene) and D_2O were co-fed in a 20 mL/min He flow. In both case, the reactant was added using syringe pumps. The conversions of H–D exchange were quantified via the deconvolution of mass fragmentations from m/e 91 to 97 for toluene, and from m/e 112 to 118 for chlorobenzene.

8.3 Results

8.3.1 Characterization of ALD-prepared W-Zr

The ZrO_2 substrate prepared for this study had an initial BET surface area of 65 m^2/g . As shown by the X-ray diffraction (XRD) pattern in Figure 8.1a, its phase was primarily monoclinic with a small amount of the tetragonal phase. The WO_x loadings were then determined as a function of the number of ALD cycles by measuring the sample weights. Table 8.1 shows these loadings, together with BET surface areas. In the first five ALD cycles, the sample weight increased almost linearly at 22 mg WO_x/g ZrO_2 per cycle. Assuming an O:W stoichiometry of three and uniform film growth over the entire ZrO_2 surface, this corresponds to a growth rate of 0.048 nm/cycle, a value that is reasonable for the size of the $W(CO)_6$ precursor, but that is somewhat larger than the value reported in the

literature for the growth of WO_3 films on flat surfaces (0.023 nm/cycle) for similar growth conditions [207,208]. It is interesting to notice that the growth rate of WO_x on the 140- m^2/g SiO_2 support, calculated from the amount deposited after five ALD cycles, was only 0.025 nm/cycle, implying that the substrate does influence the initial deposition rate. Finally, it is useful to consider that deposition of 22 mg of WO_3 onto the 65- m^2/g ZrO_2 sample corresponds to 8.8×10^{17} W atoms/ m^2 . This is a fraction of an oxide monolayer, which implies that, in the absence of surface migration, WO_x species are likely spatially isolated after a single ALD cycle.

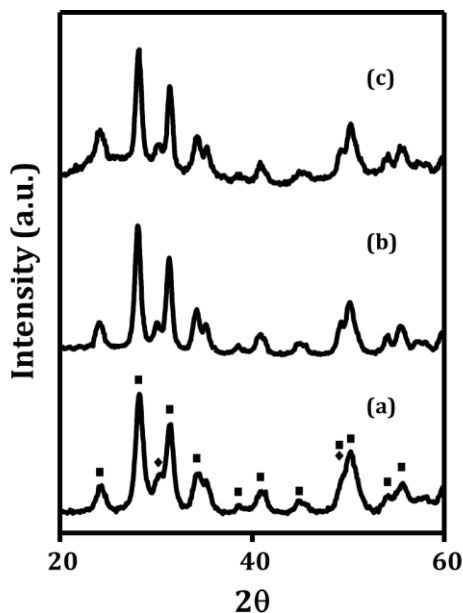


Figure 8.1 XRD patterns for (a) ZrO_2 , (b) 5W-Zr (5 ALD cycles), and (c) 40W-Zr (40 ALD cycles). Monoclinic phase (■); tetragonal phase (◆).

Table 8.1 Weight gain, surface area, and calculated layer thickness for W-Zr and W-Si materials. The layer thickness was calculated using a WO_3 density of 7.16 g/cm^3 . The nomenclature $x\text{W-Zr}$ is used to refer to a sample exposed to x ALD cycles.

SAMPLE	Weight Gain (mg/g of Substrate)	Surface Area (m²/g)	Layer Thickness (nm)
ZrO₂	0	65	0
1W-Zr	21	62	0.045
2W-Zr	47	60	0.10
3W-Zr	63	53	0.14
4W-Zr	87	47	0.19
5W-Zr	112	46	0.24
20W-Zr	430	36	0.92
40W-Zr	720	19	1.6
impW-Zr	111	58	-
5W-Si	120	135	0.12

After five ALD cycles, the BET surface area decreased to 46 m²/g. Some of the decrease was due to the increase in sample mass; however, the majority of the loss in surface area per mass of sample must be associated with the narrowing or blocking of pores. The WO_x added with five ALD cycles did not cause any changes in the XRD pattern (Figure 8.1b). Because of the decreasing surface area of the sample, the rate at which the weight changed decreased somewhat with the number of ALD cycles. After 40 ALD cycles, the WO_x loading was 42 wt%, or 0.72 g WO_x/g ZrO₂. Assuming that the film was uniform with a stoichiometry and density of bulk WO₃, the film thickness after 40 cycles was 1.5 nm, a thickness significantly greater than that of a monolayer. However, even with this relatively thick film, the XRD pattern (Figure 8.1c) showed no evidence of a well-defined crystalline WO_x phase. The only change in the XRD pattern with the addition of this large amount of WO_x was a slightly elevated baseline between 25 and 35 degrees 2θ, and again above 50 degrees 2θ. These broad features may be associated with a very small

fraction of mixed WO_x phases. However, if large, three-dimensional, crystalline clusters were being formed, it would have been apparent in the diffraction pattern.

Scanning transmission electron microscopy (STEM) imaging and energy-dispersive spectroscopy (EDS) elemental mapping on the 40W-Zr sample (Figure 8.2) demonstrate that the WO_x ALD films deposited uniformly over the ZrO_2 surface. While there were no obvious features in the image, despite the high WO_x coverage, the EDS mapping of W and Zr indicates the co-existence of W and Zr elements in the sample. The overlap in the signals reveals their uniform distribution.

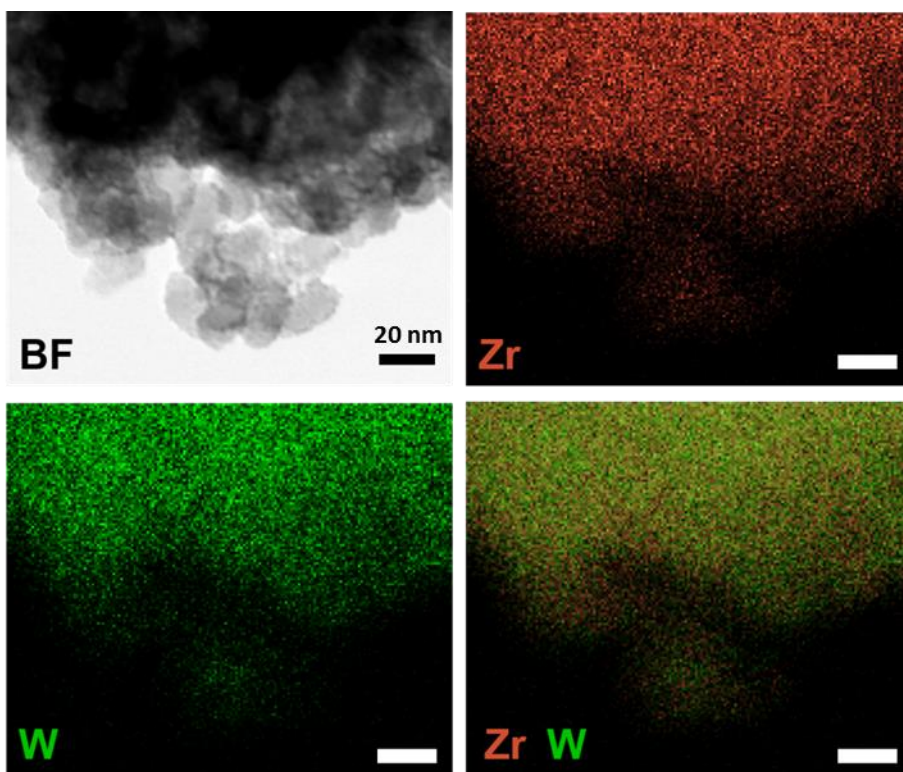


Figure 8.2 BF (Bright-Field) scanning transmission electron microscopy (STEM) image and energy-dispersive spectroscopy (EDS) elemental mapping of the 40W-Zr sample. The scale bars represent 20 nm.

To characterize the structure of the WO_x ALD films, Raman spectra of the ZrO_2 support and of the impW-Zr (10-wt% WO_x) and 5W-Zr samples were measured, both of which had WO_x loadings that were close to 10 wt%. The data for ZrO_2 (Figure 8.3a) show vibrational bands at $\sim 347, 380, 478, 616,$ and 636 cm^{-1} , which are well known to be due to ZrO_2 [213]. The spectrum for the impW-Zr sample (Figure 8.3b) exhibits the same bands, but with a new, broad feature centered at $\sim 962 \text{ cm}^{-1}$, which was previously assigned to the symmetric stretching mode of a terminal $\text{W}=\text{O}$ bond [213]. This broad feature may also include a contribution from a bridging $\text{W}-\text{O}-\text{Zr}$ bond at 915 cm^{-1} . The spectrum of the 5W-Zr sample (Figure 8.3c) is similar, except that the vibrational features associated with WO_x relative to those with ZrO_2 are significantly more intense, despite having the same WO_x loading. This is likely due to the WO_x being spread more uniformly over the ZrO_2 surface in the ALD-prepared sample.

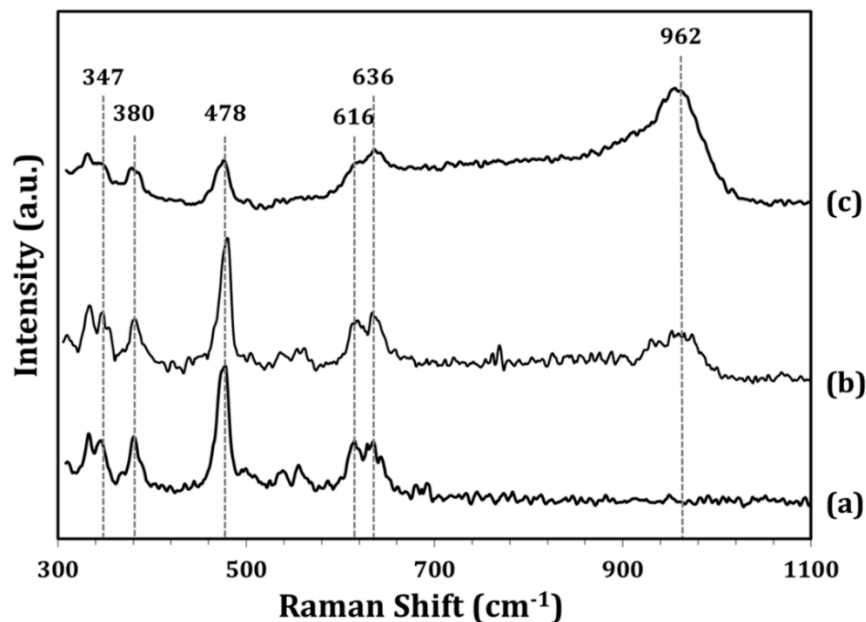


Figure 8.3 Raman spectra of (a) ZrO_2 , (b) impW-Zr (10-wt% WO_x), and (c) 5W-Zr samples under ambient conditions.

A further indication that the WO_x layer was more uniform on the ALD-prepared sample is demonstrated in Figure 8.4, which shows the TPD-TGA results for 2-propanol on the ZrO_2 , 5W-Zr, and impW-Zr samples. The TGA data show that the initial coverages following room-temperature adsorption and 1-h evacuation were slightly higher on the ZrO_2 and impW-Zr samples (between 250 and 300 $\mu\text{mol/g}$) compared to the 5W-Zr (200 $\mu\text{mol/g}$). However, this is almost certainly due to the lower surface area of the 5W-Zr sample. The initial specific coverages were roughly 2.7×10^{18} molecules/ m^2 for each of the samples. While some of the 2-propanol ($m/e = 45$) desorbed unreacted from all three samples, significant fractions of the 2-propanol desorbed from the samples as propene ($m/e = 41$) and H_2O due to reactions on either Lewis- or Brønsted-acid sites [127]. Water is not shown because it tends to desorb over a broad temperature range. What is more interesting

is that the dehydration reaction occurred at very different temperatures on ZrO_2 and on WO_x/ZrO_2 sites. On the ZrO_2 and 5W-Zr samples, the dehydration reaction occurred over narrow temperature ranges in peaks centered at 560 K on ZrO_2 , and 405 K on 5W-Zr. The TPD result of impW-Zr shows similarly sized peaks at both temperatures, suggesting that impW-Zr has regions of bare ZrO_2 and regions covered by WO_x . Even though the WO_x loadings were the same for 5W-Zr and impW-Zr, the distributions of WO_x were clearly different, with tungsten distributed much more uniformly on the sample prepared using ALD.

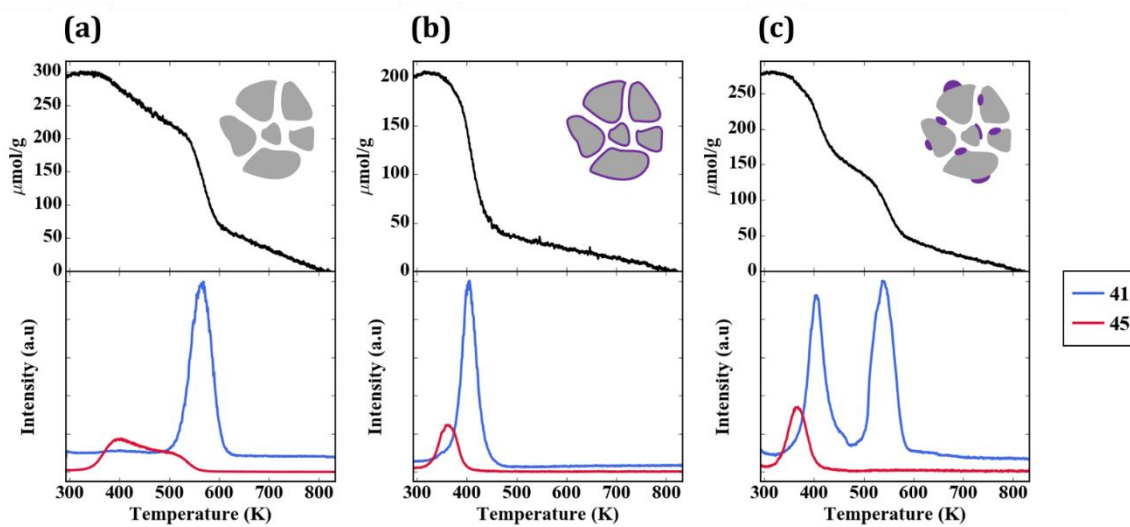


Figure 8.4 TPD-TGA of 2-propanol over (a) ZrO_2 , (b) 5W-Zr, and (c) impW-Zr. The desorption features correspond to propene ($m/e = 41$) and unreacted 2-propanol ($m/e = 45$). The graphic symbols are a schematic of the WO_x (purple) over the ZrO_2 support (gray).

To qualitatively assess the nature of the sites on the ZrO_2 and 5W-Zr samples, FTIR measurements were performed following adsorption of pyridine, with results shown in Figure 8.5. The spectrum for ZrO_2 (Figure 8.5a) shows only bands at 1440 and 1460 cm^{-1} , which are characteristic of adsorption at Lewis sites. In contrast to this, the spectrum of

pyridine on the ALD-prepared 5W-Zr (Figure 8.5b) also exhibits a band near 1540 cm^{-1} , which can be assigned to adsorbed pyridinium ions, implying 5W-Zr contains a significant concentration of Brønsted sites.

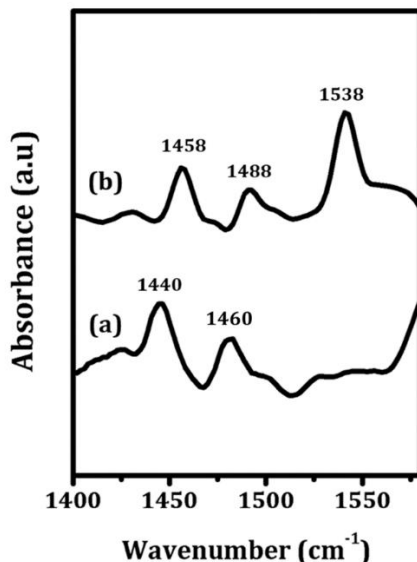


Figure 8.5 FTIR spectra of pyridine adsorbed on (a) ZrO₂ and (b) 5W-Zr. The samples were pretreated with helium at 373 K before pyridine was adsorbed onto the samples at room temperature.

8.3.2 Reactive sites on ALD-prepared W-Zr

To quantify the concentration of the sites, TPD-TGA measurements were performed using 2-propanamine as the probe molecule. On Brønsted sites, 2-propanamine forms 2-propylammonium which decompose during TPD to form ammonia and propylene between 573 and 650 K due to a Hoffman Elimination reaction [114,214], allowing site concentrations to be determined from this decomposition feature. Reaction of the amines can occur on catalytic sites other than Brønsted sites; however, the products that are formed and the temperature range in which the reactions occur are different and depend on the

nature of the site [215]. The TPD-TGA results for the WO_x/ZrO_2 samples show evidence for the presence of three different types of reactive sites, with concentrations of those sites dependent on the WO_x coverages. A summary of the three reaction pathways is illustrated in Figure 8.6.

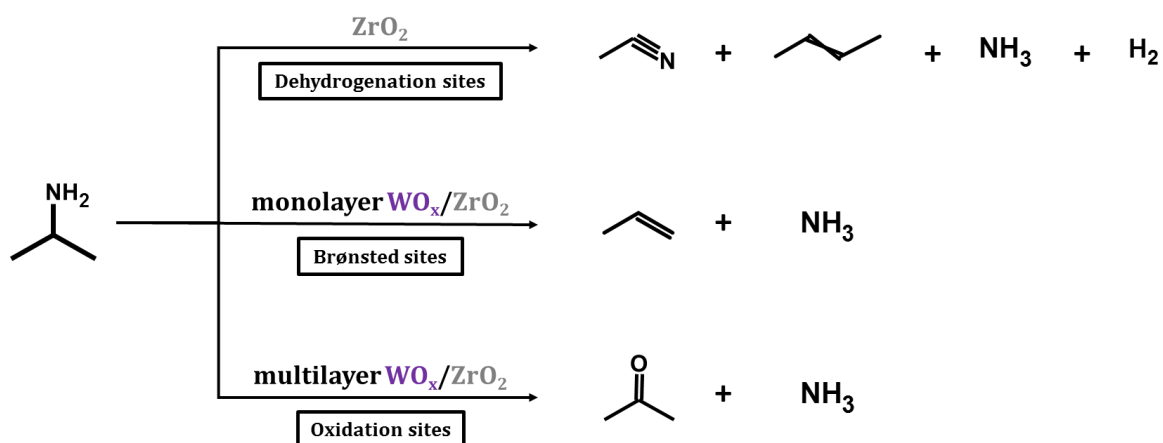


Figure 8.6 A summary of reaction pathways for the conversion of 2-propanamine on the WO_x/ZrO_2 samples observed in the TPD-TGA measurements.

Figure 8.7a provides the TPD-TGA result for 2-propanamine with pure ZrO_2 . Approximately half of the $300 \mu\text{mol/g}$ that remained on the sample after evacuation desorbed as unreacted amine ($m/e = 42, 43, 44$) below 500 K . Above that temperature, most of the amine molecules reacted in a feature centered at approximately 565 K to form H_2 ($m/e = 2$), a mixture of acetonitrile and butenes ($m/e = 41$), and ammonia ($m/e = 17$). The absence of a peak at $m/e = 42$ is particularly important for demonstrating that the high temperature peak at $m/e = 41$ is not propene, the product that would be formed on Brønsted sites. The identification of acetonitrile and propene as products was achieved by a more complete analysis of the mass spectra and was confirmed in steady-state flow-reactor

measurements over ZrO_2 at 673 K. The same products were observed in those measurements, with the addition of small amounts of dipropylamine. Apparently, ZrO_2 catalyzes the dehydrogenation of 2-propanamine to form the imine, which is unstable and reacts to form the smaller nitrile and butenes. The reaction of adsorbed 1-propanamine on ZrO_2 , shown in Figure 8.8, was simpler, forming primarily propionitrile and H_2 . However, because the products formed by 1-propanamine on sites formed by WO_x were more difficult to distinguish from those formed on ZrO_2 , most of our work focused on using 2-propanamine to characterize the samples. It is noteworthy that ZrO_2 was previously demonstrated to exhibit dehydrogenation chemistry under some conditions, and it is this functionality that is apparently responsible for the amine reactions [216].

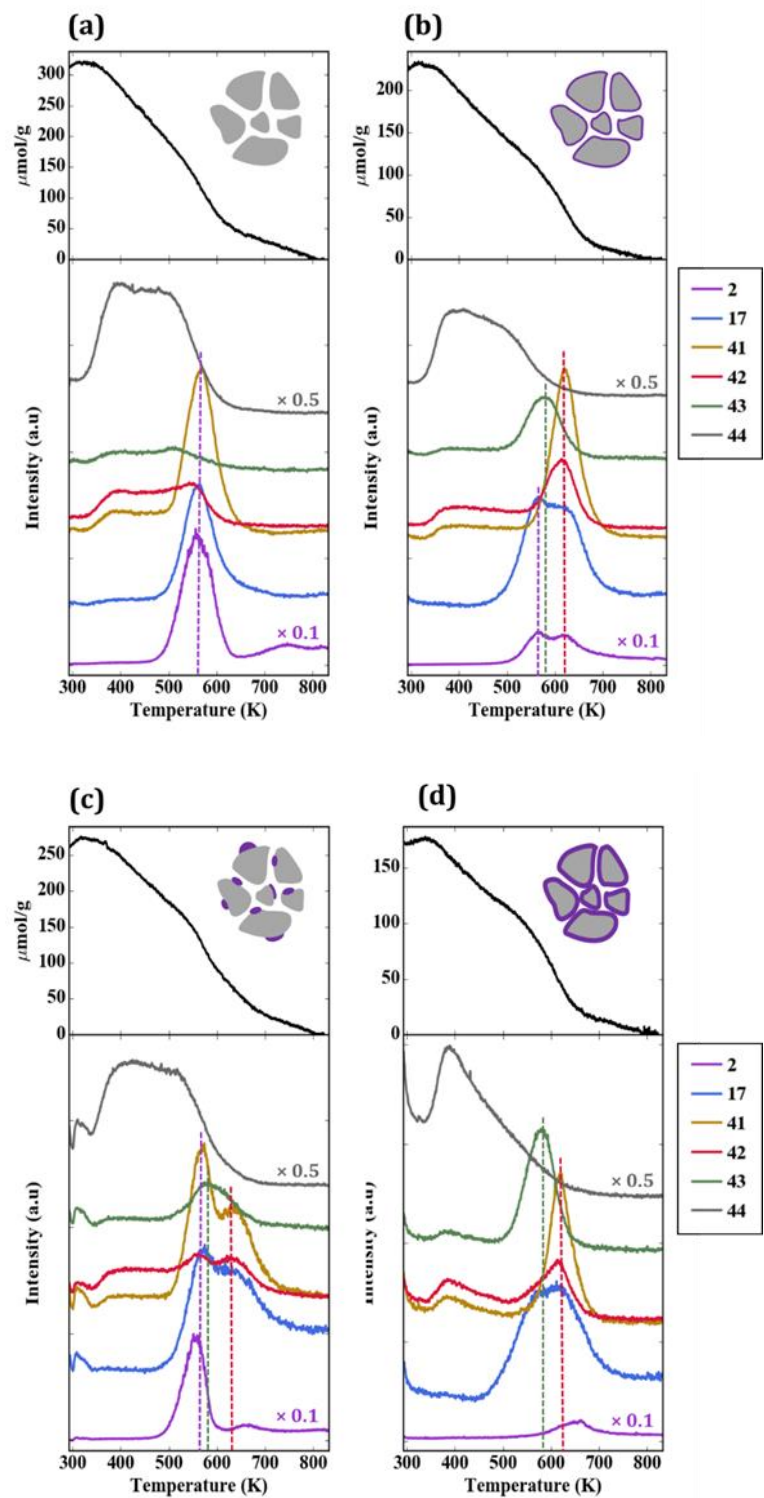


Figure 8.7 TPD-TGA of 2-propanamine over (a) ZrO_2 , (b) 5W-Zr, (c) impW-Zr, and (d) 20W-Zr. The desorption features correspond to hydrogen ($m/e = 2$), ammonia ($m/e = 17$), a mixture of butenes and acetonitrile ($m/e = 41$), acetone ($m/e = 43$), propene ($m/e = 41$ and 42), and unreacted 2-propanamine ($m/e = 44$).

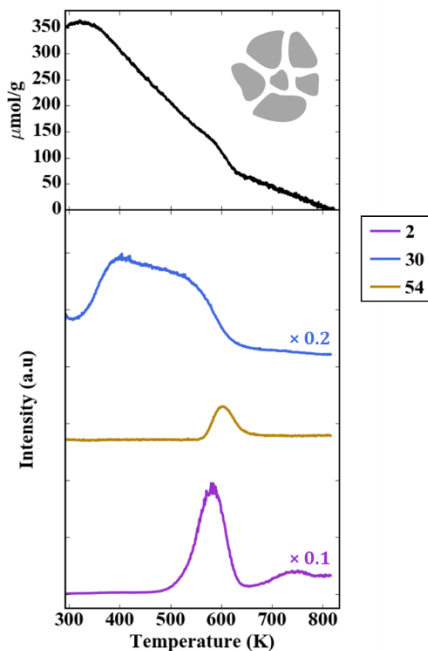


Figure 8.8 TPD-TGA of 1- propanamine over ZrO_2 . The desorption features correspond to hydrogen ($m/e = 2$), unreacted 1-propylamine ($m/e = 30$) and propionitrile ($m/e = 54$). The graphic symbols represent schematic ZrO_2 support (gray).

The TPD-TGA result for the 5W-Zr sample, shown in Figure 8.7b, differs significantly from that obtained on ZrO_2 . As in the case of 2-propanol, the initial coverage was slightly lower due to the lower specific surface area; similar to the case of ZrO_2 , unreacted amine desorbed from the sample below 500 K. However, on the 5W-Zr sample, there are two distinct reaction features at ~585 K and ~620 K, and the products formed in both peaks differ from that observed on ZrO_2 . The 620-K peak is characteristic of Brønsted-acid sites. The major products are propene ($m/e = 41$ and 42, in the correct ratio for

propene) and ammonia ($m/e = 17$), and these were formed via the Hoffman elimination at exactly the same temperature reported for the reaction of adsorbed 2-propanamine on acidic zeolites [114]. The lower-temperature peak at ~ 585 K may have a small contribution from the bare ZrO_2 , since the temperature is similar to the reaction temperature on ZrO_2 ; however, the major products formed in this case were very different. The major products determined from a complete analysis of the mass spectra in this temperature range were acetone ($m/e = 43$) and ammonia. Minimal amounts of acetonitrile and much less H_2 were formed, suggesting that most of the ZrO_2 was covered. The formation of acetone implies that partial oxidation took place. The total amount of 2-propanamine that reacted on the 5W-Z sample was ~ 100 $\mu\text{mol/g}$. By integrating the product peaks, we estimate that this sample had less than 10 $\mu\text{mol/g}$ of dehydrogenation sites (from the amount of H_2 and nitrile that formed), 80 $\mu\text{mol/g}$ of Brønsted sites (from propene and ammonia), and 15 $\mu\text{mol/g}$ of oxidation sites (acetone). These results are summarized in Table 8.2.

Table 8.2 Reaction site densities determined from the desorption features of 2-propanamine TPD, determined as described in the text. W/B = number of W atoms per Brønsted site.

SAMPLE	Reaction-Site Density ($\mu\text{mol/g}$)			W/B
	Dehydrogenation	Oxidation	Brønsted	
ZrO₂	123	0	0	-
1W-Zr	115	0	6	15
2W-Zr	77	0	24	8.5
3W-Zr	31	4	67	4.1
4W-Zr	20	5	74	5.2
5W-Zr	6	16	80	6.0
20W-Zr	5	32	41	32
40W-Zr	1	15	12	148
impW-Zr	63	9	40	13
5W-Si	0	24	9	30

TPD-TGA measurements were also performed for the impW-Zr sample (10-wt% WO_x), with the result shown in Figure 8.7c. This sample exhibited all three types of reaction features, with a clearly defined H₂ and acetonitrile/butene feature at 565 K, associated with ZrO₂. An estimate of the site densities gave 60 μmol/g of dehydrogenation sites, 40 μmol/g of Brønsted sites, and 10 μmol/g of oxidation sites. Figure 8.7d is the TPD-TGA result obtained for 20W-Zr, the sample prepared using ALD which had a 30-wt% WO_x loading, corresponding to a uniform film of ~1 nm. In comparison to the near-monolayer 5W-Zr sample, the TPD trace shows more intense features associated with oxidation sites at ~585 K, and smaller features associated with Brønsted sites at 620 K.

To understand the effect of WO_x coverage, TPD-TGA measurements of 2-propanamine were performed on samples exposed to a varying number of ALD cycles. All of the samples exhibited the same three features in the TPD-TGA but at different concentrations. A summary of the calculated site concentrations is reported in Table 8.2 and Figure 8.9. The concentration of accessible dehydrogenation sites decreased dramatically with the number of ALD cycles, and essentially disappeared after five ALD cycles. Using the deposition rate of 8.8×10^{17} W atoms/m² per cycle reported earlier, five ALD cycles corresponds to 4.4×10^{18} W atoms/m², a reasonable value for an oxide monolayer. In agreement with previous reports that individual W atoms do not form Brønsted sites, the Brønsted-site concentration was negligible after one cycle, and increased non-linearly thereafter, converging to a maximum after about five cycles. At higher WO_x coverages, the Brønsted-site concentration decreased, implying that contact

with the ZrO_2 substrate was essential for forming these sites. Confirmation of the importance of ZrO_2 came from the fact that the silica-supported sample, 5W-Si, showed a low Brønsted-site acidity. Finally, the concentration of oxidation sites, those responsible for forming acetone, were negligible below five ALD rounds, the point at which the dehydrogenation sites disappeared. This implies that the oxidation sites are associated with bulk WO_x that is not in contact with the ZrO_2 surface. It is also confirmed by the fact that oxidation-site density reached a maxima for 20W-Zr when multilayer WO_x was formed. However, the decrease in oxidation-site density for 40W-Zr was only due to a loss of surface area.

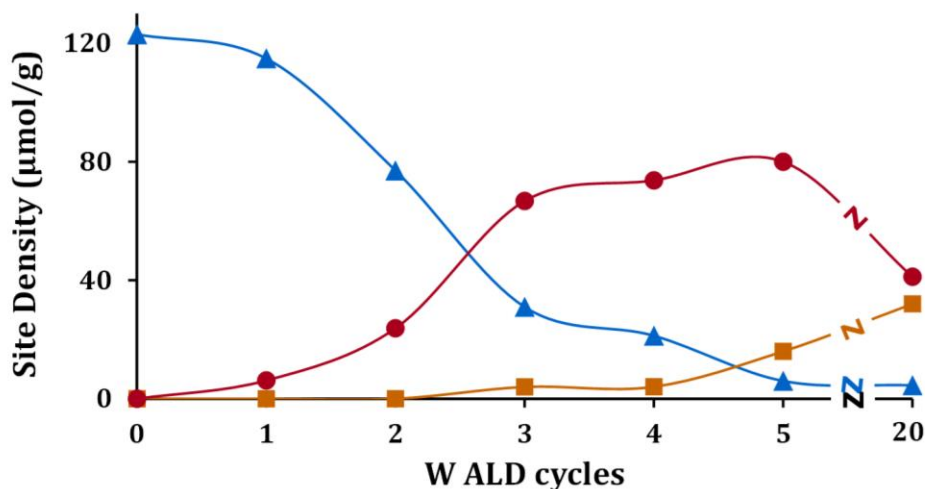


Figure 8.9 Reaction site densities of (▲) dehydrogenation sites, (●) Brønsted sites, and (■) oxidation sites as a function of the number of WO_x ALD cycles.

To determine the relationship between catalytic activity and the presence of Brønsted sites, the steady-state conversion of 2-propanol was performed on a series of ALD-prepared WO_x/ZrO_2 catalysts at 403 K and a Weight Hourly Space Velocity (WHSV) of 0.40 h^{-1} . Under these conditions, pure ZrO_2 was not catalytically active. As shown in

Figure 8.10, there was no significant conversion over catalysts prepared with one or two WO_x ALD cycles. With higher WO_x concentrations, the propanol reacted to a mixture of water with dipropyl ether (~60%) and propene (40%). Conversions were maximized after five ALD rounds, and there was a reasonable correspondence between the concentration of Brønsted sites on these samples and the conversions. The fact that the 40W-Zr sample showed a higher conversion than would be expected based on its Brønsted-site density suggests that the bulk WO_x also has some activity for alcohol dehydration.

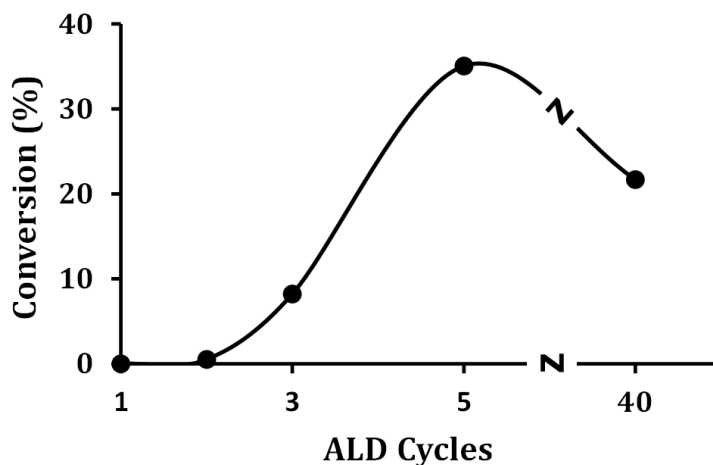


Figure 8.10 The 2-propanol conversions on $x\text{W-Zr}$ (where x is the number of ALD cycles) samples for the steady-state dehydration reaction at 403 K. Reaction conditions: 2-propanol $\text{WHSV} = 0.40 \text{ h}^{-1}$.

As discussed in the introduction, the quantification of Brønsted-acid strength in solid acids is difficult. Here, we measured light-off curves for H–D exchange between D_2O and either toluene (C_7H_8) or chlorobenzene ($\text{C}_6\text{H}_5\text{Cl}$) on the 5W-Zr sample, and compared the results to those obtained on an H-ZSM-5 zeolite which had a similar Brønsted-site density of $80 \mu\text{mol/g}$. Measurements began at room temperature, and were carried out in a

steady-state reaction environment after each increment of 10 K. The results are shown in Figure 8.11. Firstly, on both H-ZSM-5 and 5W-Zr, the light-off temperatures for chlorobenzene occurred at higher temperatures, roughly 60 degrees higher on H-ZSM-5 and 75 degrees higher on 5W-Zr. This is consistent with a lower barrier for the reaction of toluene due to its significantly higher proton affinity. Secondly, the temperatures at which H–D exchange occurred were significantly higher on the tungstated zirconia. Sorption effects and other factors can play a role in the observed rates on solid acids [217]; however, the fact that the reaction occurred at higher temperatures for both adsorbates suggests that tungstated zirconia has much weaker acid sites than does H-ZSM-5.

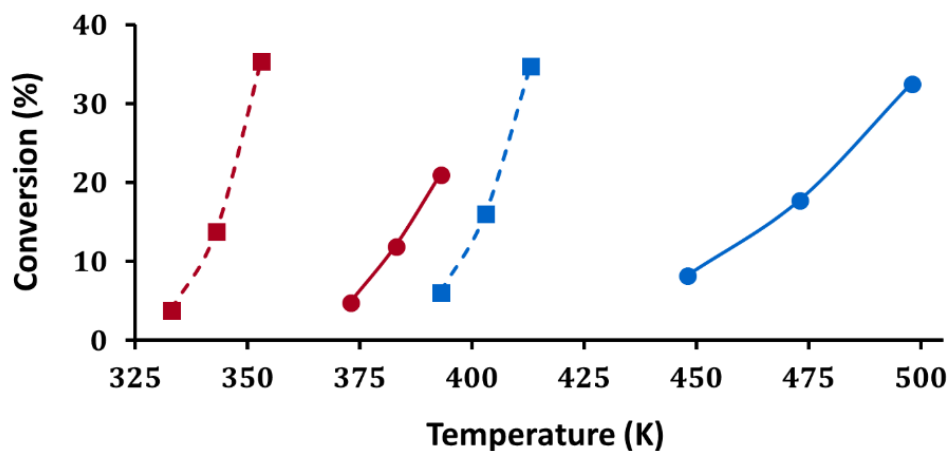


Figure 8.11 Conversions for H–D exchange of toluene (in red) and chlorobenzene (in blue) on (●) 5W-Zr and (■) H-ZSM-5 (280) as a function of temperature. The Brønsted-site densities for both materials were 80 $\mu\text{mol/g}$. Reaction conditions: 100 mg of catalyst, 1% toluene/chlorobenzene, and 1% D_2O in 20 mL/min He.

8.4 Discussion

In agreement with previous reports [197,213], the data shown in this chapter indicate that tungstated zirconia is a complex material that can exhibit Brønsted acidity,

Lewis acidity, and oxidation activity, along with dehydrogenation activity on ZrO_2 [216]. The concentrations of the various types of sites depend on how the material is made, as shown by the differences we observed in materials synthesized via impregnation and using ALD. This complexity almost certainly accounts for at least some of the differences reported by the various groups who have worked on tungstated zirconia. In the presented study, we focused on controlling the composition and structure by synthesizing catalysts using ALD because of the uniformity that this approach provides.

The TPD results also demonstrate the power of using reactive probe molecules, rather than simple bases like ammonia or pyridine, for characterizing the types of sites that are present on these materials. The application of TPD in this manner is certainly not new, and 2-propanol [127] and 2-propanamine [114] were previously used to characterize site concentrations for Lewis and Brønsted acids. However, the results demonstrate that additional information can also be obtained. For example, the comparison of 2-propanol results for WO_x/ZrO_2 samples prepared via impregnation gave a strong indication that the WO_x did not uniformly cover the ZrO_2 . The 2-propanamine results were also able to delineate concentrations of the various types of sites that were formed with increasing WO_x coverage.

Based on our reactivity studies, the Brønsted-acid sites formed in tungstated zirconia are relatively weak, certainly compared to the Brønsted-acid sites formed in zeolites. While site strengths may well depend on the detailed structure and method of synthesis, it is worth noting that others reported that WO_x/ZrO_2 is selective for the

etherification of alcohols [203], without forming olefins as with zeolites, which would again imply the sites are relatively weak. We suggest that the high activity sometimes observed at low temperatures in tungstated zirconia is due to the combination of oxidation sites and/or dehydrogenation sites, together with Brønsted sites, similar to that which was proposed for sulfated zirconia [218]. With sulfated zirconia, the oxidation sites were shown to transform alkanes to olefins, which were then more easily activated by the acid sites. A similar combination of sites likely explains at least some of the catalytic properties of tungstated zirconia. The combination of sites allows isomerization reactions to occur at low temperatures without the need for especially strong Brønsted sites.

It is interesting that there were essentially no Brønsted sites formed after the deposition of a single WO_x ALD cycle on the ZrO_2 . One would expect to form isolated WO_x species under these conditions, and the lack of Brønsted sites is interesting. The fact that more than one WO_x species must be present in order to form a Brønsted site was stated by others [197], who argued that the W:Brønsted-site ratio is about four. The value of four is indeed the approximate minimum value observed in Table 2, where the Brønsted-site concentrations are listed as a function of the number of ALD cycles added to the ZrO_2 . While this ratio suggests that a $(\text{WO}_x)_n$ cluster is required for forming Brønsted sites, it is worth noting that the ratio of four occurs after three cycles, at which point it is expected that most of the tungsten is deposited in the first monolayer, implying that the clusters would be two-dimensional and still in contact with ZrO_2 . The importance of zirconia is

confirmed by the fact that we do not form significant quantities of Brønsted sites when WO_x is deposited on silica.

Finally, the H–D exchange results imply that the Brønsted sites in WO_x/ZrO_2 are relatively weak compared to the sites in high-silica zeolites. The early work by Hino and Arata on the isomerization of small alkanes at low temperatures argued that these materials are very strong Brønsted acids [219]; similarly, the calculated deprotonation energies that were reported imply that tungstated zirconia should have much stronger sites than those present in zeolites [197]. However, the recent publication on dodecanol etherification showed that WO_x/ZrO_2 was more selective than acidic zeolites for forming ethers, and produced less olefin and oligomerization products [203], a result that would imply weaker Brønsted sites. We suggest that the high activity reported for alkane activation at low temperatures could be the result of a combination of oxidation sites and Brønsted sites. For example, the low-temperature activity of sulfated zirconia was associated in part with oxidation sites which form olefins that then go on to react over the Brønsted sites [205]. Since the tungsten clusters on zirconia were shown to be reducible, both in this study and previously [220], the low-temperature, isomerization activity may be the result of a combination of acidic and oxidation sites. Similarly, the presence of Pt in low-temperature isomerization catalysts likely leads to the formation of alkenes, which are much more easily protonated [221,222].

Obviously, there is still much to learn about the nature and properties of the catalytic sites in tungstated zirconia. I believe that the combination of controlled synthesis

using ALD with careful adsorption studies of the type performed here can help elucidate the nature of these sites.

CHAPTER 9. H-D EXCHANGE OF SIMPLE AROMATICS AS A MEASURE OF BRØNSTED-ACID SITE STRENGTHS IN SOLIDS⁸

Summary

In this chapter, I set out to determine the relative Brønsted-acid strengths of a series of solid-acid materials using the onset temperature for H-D exchange with the simple aromatics. The acidity ordering for these materials was previously not distinguishable using conventional techniques such as TPD-TGA of amines and pyridine IR. The results presented in this chapter suggest Brønsted-acid site strengths to be ordered as follows: H-[Al]ZSM-5 > H-[Fe]ZSM-5 > tungstated zirconia > P-SPP > H-[B]ZSM-5, in good agreement with expectations based on catalytic activities reported in the literatures.

9.1 Introduction

Solid, Brønsted-acid catalysts are used in a large number of industrially important reactions but characterization of site strengths and site densities remains a challenge. Temperature Programmed Desorption (TPD) of ammonia remains the most commonly used method for determining site strengths and densities but its utility has been challenged [114,223]. First, ammonia interacts with both Brønsted and Lewis sites, so that site

⁸This chapter was published as **C. Wang**, S. Li, X. Mao, S. Caratzoulas, R.J. Gorte, *Catalysis Letters* 148 (2018) 3548–3556. . Reprinted by permission from Springer Nature.

concentrations determined from ammonia TPD on complex materials are unreliable for determining Brønsted-site concentrations [223]. Second, while it is common practice to infer site strengths from TPD peak temperatures, it has been shown that peak temperatures in ammonia TPD depend on a number of experimental parameters [224], not simply site strengths. Furthermore, calorimetric measurements of ammonia on H-[Al]ZSM-5 and H-[Fe]ZSM-5 (zeolites with the MFI structure but having either Al or Fe in the framework) have shown that heats of adsorption for both ammonia and pyridine cannot distinguish between materials with very different catalytic activities [209].

There are reliable methods to measure Brønsted-site concentrations, at least for relatively strong Brønsted sites. Infrared spectra of adsorbed pyridine are able to distinguish pyridinium ions from non-protonated pyridine and site concentrations can then be determined from the intensity of the absorption bands for the pyridinium ions [225]. TPD of alkyl amines is another method that is able to distinguish Brønsted and Lewis sites [114,226]. In this case, protonated amines decompose to ammonia and the corresponding olefin via a Hofmann elimination at elevated temperatures, allowing the Brønsted sites to be counted from the amount of product that is formed. However, both of these techniques require that the Brønsted sites be sufficiently strong to protonate relatively strong bases; and, in the case of alkyl amine TPD, the sites must be sufficiently strong to stabilize the alkyl ammonium ions to the temperature required for reaction. While this criterion is usually satisfied in materials that are catalytically active, there is the recent example of phosphorus-containing self-pillared pentasil (SPP) zeolite [227] that shows activity for

some reactions that are believed to be Brønsted-acid catalyzed without exhibiting Brønsted sites as measured by pyridine IR or 2-propanamine TPD [228].

The best measure of Brønsted-acid strength is the deprotonation energy of the solid but this is not directly measurable experimentally. The intrinsic acidity can, however, be inferred from careful reaction measurements coupled with density functional theory (DFT), as shown by Deshlahra and Iglesia [229]. By examining a series of Mo- and W-based polyoxometalate clusters and the isomorphous-substituted MFI silicates (H-[Al]ZSM-5, H-[Fe]ZSM-5, H-[Ga]ZSM-5, and H-[B]ZSM-5) using methanol dehydration and 2-methylpentene isomerization, they were able to infer relative acid strengths for each of the materials and determine the nature of bonding between the solids and the intermediates. One potential issue with alcohol dehydration is that this reaction can be catalyzed by Lewis-acid sites [230] and it may be difficult to distinguish the Lewis sites from very weak Brønsted sites in some cases.

A conceptually simpler set of Brønsted-acid-catalyzed reactions is the H-D exchange between the deuterated zeolite and the hydrogen form of substituted benzenes [231–233]. The products in this case are chemically identical to the reactants and there is no thermodynamic bias to influence the rates. The basicity of the substituted benzenes can also be varied substantially through substitution. For example, the proton affinities of toluene and chlorobenzene, the two probes used in the present study, are 784 and 753 kJ/mol, respectively; and m-xylene, with a proton affinity of 812 kJ/mol, is significantly more basic than most simple alcohols. Because Brønsted sites undergo H-D exchange with

D₂O very rapidly and at low temperatures, the steady-state reaction can be performed by co-feeding D₂O with the protonated form of the solid acid. Multiple exchange reactions complicate the analysis but we report here that the onset-of-reaction temperature appears to be a good qualitative measure of the acid strength.

Here, I have used H-D exchange measurements with toluene and chlorobenzene to study the Brønsted acidity of H-[Al]ZSM-5, H-[Fe]ZSM-5, H-[B]ZSM-5, silicalite, P-SPP, tungstated zirconia, ZrO₂, and γ -Al₂O₃. The results show clear differences between materials that are expected to be Lewis acids and those that are expected to be Brønsted acids. The ordering of acidities is also in good agreement with expectations based on catalytic activities reported in the literature.

9.2 Experimental

9.2.1 Catalyst Synthesis and Characterization

Two H-[Al]ZSM-5 samples with Si/Al₂ ratios of 50 (CBV 5524G, Zeolyst) and 280 (CBV 28014, Zeolyst) were obtained by calcination of their NH₄ forms to 500 °C in flowing air. The H-[Fe]ZSM-5 sample (Si/Fe₂ = 56) is the same sample used in previous studies [209]. It was prepared using fumed silica (Cab-O-Sil, Cabot) in order to be as free as possible of any Al. The synthesis and characterization of the H-[B]ZSM-5 (Si/B₂ = 120) are described in detail in another publication [234], as is the synthesis of the purely siliceous ZSM-5 sample (Si-MFI) [235]. The P-SPP sample was synthesized at the University of Minnesota and is described in other publications [228,236,237]. It was

prepared by impregnation of phosphoric acid into the siliceous form of SPP to have a Si/P ratio of 27. Notably, this SPP sample was prepared from an ultra-pure silica source to avoid any alumina contamination. ZrO₂ substrate was prepared using conventional impregnation which was reported in Chapter 8. The tungstated zirconia (5W-Zr) was prepared by adding 5 ALD cycles of WO_x onto the ZrO₂, as described in Chapter 8. The WO₃ loading on this sample was 10-wt% and the sample had a surface area of 46 m²/g. The γ -Al₂O₃ sample was purchased from Strem Chemicals and was stabilized by calcination at 900 °C. It had a BET surface area of 110 m²/g.

Concentrations of strong Brønsted sites on each of the samples were estimated using TPD-TGA (thermogravimetric analysis) of 2-propanamine [114]. The site densities were determined by the amount of amine that reacted to propene and ammonia between 575 and 650 K. A listing of each of the samples, together with their Brønsted-site densities, is reported in Table 1.

Table 9.1 A summary of strong Brønsted-site densities (determined by TPD-TGA of 2-propanamine) and onset temperatures for H-D exchange of toluene and chlorobenzene on the samples tested in this study.

SAMPLE	Brønsted-Site Density ($\mu\text{mol/g}$)	Reference	Onset Temperature of H-D exchange ($^{\circ}\text{C}$)	
			toluene	chlorobenzene
H-[Al]ZSM-5(50)	500	[234]	60	100
H-[Al]ZSM-5(280)	90	[238]	65	125
H-[Fe]ZSM-5	420	[234]	70	140
H-[B]ZSM-5	--	--	340	-
Si-MFI	< 10	[238]	-	-

5W-Zr	80	[239]	100	175
P-SPP	0	[228]	175	-
ZrO₂	0	[127]	375	350
Al₂O₃	0	[127]	375	375

Two types of H-D exchange experiments were performed. An initial indication of the H-D exchange rates on the H-[Al]ZSM-5(50), H-[Fe]ZSM-5, and P-SPP samples was achieved by adsorption of either toluene-*h*₈ (99.9%, Fisher Scientific) or chlorobenzene-*h*₅ (99.5%, Acros) onto the deuterated samples in the TPD-TGA system.

H-D exchange experiments were also performed under steady-state conditions by co-feeding D₂O and toluene/chlorobenzene in a continuous flow reactor. The conversions for the H-D exchange were quantified by deconvolution of mass fragmentations from $m/e = 91$ to 97 for toluene and from $m/e = 112$ to 118 for chlorobenzene. Steady-state conversions were obtained after temperature increments of either 5, 10, or 25 degrees, depending on the temperature range. No evidence for catalyst deactivation was observed and the conversions were always the same whether the sample temperature was approached from the high or low side.

9.2.2 Theoretical Approaches

The DFT calculations in this work were performed with Gaussian 09 [240]. The H-[Al]ZSM-5 model was constructed by substituting Al for Si in the T12 position of the MFI unit cell and incorporating a proton on an adjacent oxygen atom. To build the cluster, we

employed the method of overlapping spheres centered at the adsorbed toluene atoms and at the active site atoms within the first coordination sphere of the Al atoms using a cutoff radius of 7 Å [241]. The resulting cluster contains 55 tetrahedral atoms (55T) and all terminal silicon atoms were saturated with hydrogen atoms with a bond distance of 1.47 Å. The Si and Al atoms were modeled at the M06-2X/LANL2DZ theory level [242], while the rest of the system was modelled at the M06-2X/6-31G(d,p) theory level [243]. Ground and transition states were characterized by frequency analysis and the latter were also corroborated by intrinsic reaction coordinate (IRC) [244] calculations. Thermal corrections to the electronic energies were computed using the harmonic oscillator approximation.

9.3 Results

9.3.1 TPD-TGA Measurements

Previous TPD-TGA studies of toluene-h₈ on the deuterated zeolite, D-[Al]ZSM-5, had shown that toluene can be completely removed from the sample by prolonged evacuation at room temperature and that the desorption product in these experiments underwent significant H-D exchange with the acid sites [211]. Therefore, the present studies were performed at -30 °C with a lower initial exposure of the samples to toluene in order to catch the initial phases of the reaction. The three samples that were studied using adsorption methods, H-[Al]ZSM-5(50), H-[Fe]ZSM-5, and P-SPP, were chosen because they have the same MFI structure but very different types of acid sites. H-[Fe]ZSM-5 has

a much lower activity for hydrocarbon cracking and olefin oligomerization compared to H-[Al]ZSM-5 [209,245]. P-SPP appears to have Brønsted sites that are too weak to even protonate pyridine [228].

Results for TPD-TGA of toluene- h_8 on each of the deuterated samples are shown in Figure 9.1. Initially, the samples were exposed to approximately 800 $\mu\text{mol/g}$ of toluene- h_8 at $-30\text{ }^\circ\text{C}$ before 1-h evacuation. This exposure corresponds to a coverage that is slightly more than one molecule per Brønsted site, at least for the H-[Al]ZSM-5 and H-[Fe]ZSM-5 samples. On the H-[Al]ZSM-5(50) sample, Figure 9.1a), a small amount of toluene was removed during evacuation, leaving an initial coverage of 670 $\mu\text{mol/g}$. Desorption from the sample became significant above $0\text{ }^\circ\text{C}$ but the products below $50\text{ }^\circ\text{C}$ showed peaks at only $m/e=91$ and 92 , with no discernable features at $m/e=93$ or 94 . Because the mass spectrum of toluene- h_8 exhibits peaks at $m/e=91$ and 92 in a ratio of approximately 2:1, the toluene leaving the sample below $50\text{ }^\circ\text{C}$ remains undeuterated. At approximately $50\text{ }^\circ\text{C}$, there is a sharp change in the ratio of the $m/e=91$ and 92 peaks, followed by a rise in the $m/e=93$ and 94 peaks at a slightly higher temperature. This is clear evidence that H-D exchange occurs above $50\text{ }^\circ\text{C}$. The presence of a peak at $m/e=94$, along with the fact that the $m/e=93$ peak is larger than the $m/e=92$ peak, shows that multiple exchanges occur. Although it is difficult to quantify the amount of deuterium leaving the sample in the deuterated products, the amount appears to be larger than the number of Brønsted sites. This was also observed in the previous TPD-TGA study and was shown by IR spectroscopy to be caused by H-D exchange between the Brønsted sites and silanol defects in the zeolite

[211]. That previous work showed that the number of hydroxyls associated with defects in H-[Al]ZSM-5 could significantly exceed the number of hydroxyls associated with framework Al sites.

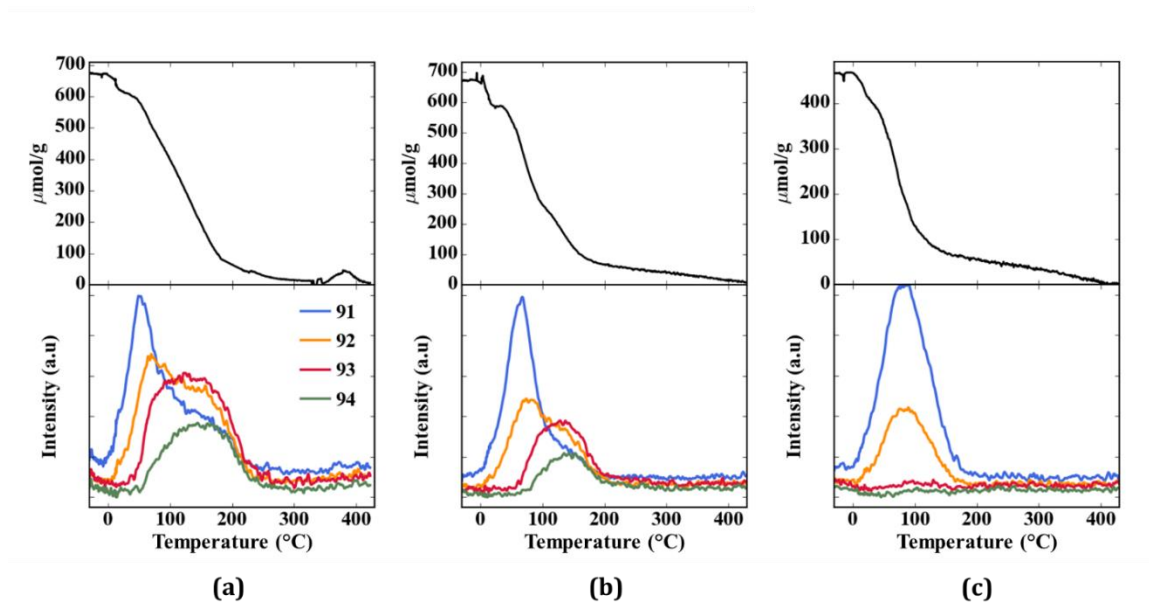


Figure 9.1 TPD-TGA of toluene-h₈ over deuterated (a) H-[Al]ZSM-5(50), (b) H-[Fe]ZSM-5, and (c) P-SPP.

The TPD-TGA data for the H-[Fe]ZSM-5 sample, Figure 9.1b), were qualitatively the same but the temperature at which H-D exchange occurred was shifted up by more than 30 degrees. This is a strong indication that the Brønsted sites are weaker. Finally, in the P-SPP sample, Figure 9.1c), the initial coverage at the start of the TPD-TGA measurement was slightly lower due to removal of some toluene during the evacuation at -30 $^{\circ}\text{C}$. More significantly, all of the toluene-h₈ desorbed intact, with no evidence for any H-D exchange into the desorbing toluene.

Because chlorobenzene (PA = 753 kJ/mol) is a much weaker base than toluene (PA = 784 kJ/mol), we performed similar TPD-TGA measurements with chlorobenzene- h_5 on the deuterated forms of H-[Al]ZSM-5(50) and H-[Fe]ZSM-5 samples to better distinguish the strengths of the sites in these two solid acids. The experiments were performed in the same manner as with toluene and the results are reported in Figure 9.2. Peak desorption temperatures for chlorobenzene are similar to that for toluene, an indication that the dispersion forces are similar for chlorobenzene and toluene with the siliceous zeolite cavities. Figure 9.2a) demonstrates that there is no H-D exchange between chlorobenzene and the acid sites below about 100 °C on H-[Al]ZSM-5(50), as shown by the fact that the product exhibits a peak at $m/e=77$ but none at 78, 79, or 80. Above 100 °C, peaks at $m/e=78$ and 79 appear in the mass spectra of the products, demonstrating H-D exchange. By contrast, Figure 9.2b) shows that there was negligible H-D exchange for the H-[Fe]ZSM-5 sample up to the desorption temperature of 200 °C.

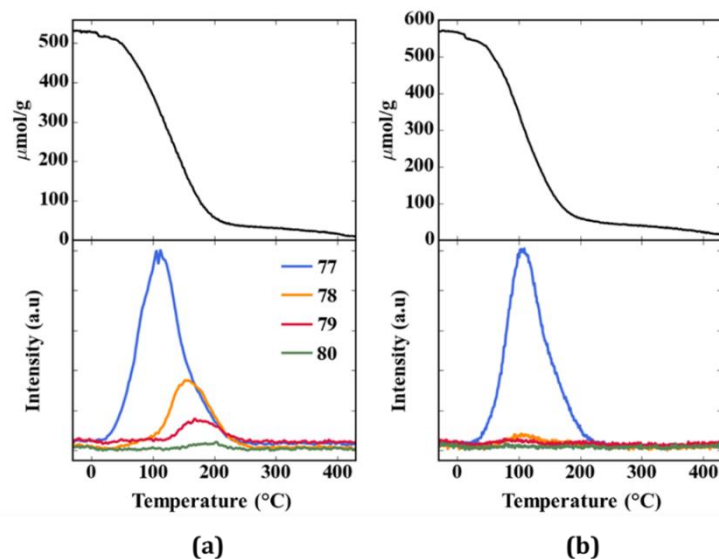


Figure 9.2 TPD-TGA of chlorobenzene- h_5 over deuterated (a) H-[Al]ZSM-5(50) and (b) H-[Fe]ZSM-5.

9.3.2 Steady-State Reaction Measurements

The TPD-TGA measurements suggest that the temperature at which acid sites catalyze H-D exchange is a useful measure of acid strength; however, the temperature range at which H-D exchange can be observed in TPD is limited to temperatures at which some adsorbate remains in the sample. To access higher temperatures, we performed steady-state reaction measurements in a flow reactor with 1% of both D_2O and the aromatic compound in He. The presence of D_2O maintains the solid acids in the deuterated form, while the onset temperature of deuterated hydrocarbon products is an indication of the ability of the solid to activate the hydrocarbon.

The initial experiments were performed with toluene- h_8 on the series of samples which had the MFI structure, with results that are shown in Figure 9.3 and summarized in

Table 9.1. For this study, we defined the onset reaction temperature as that value for which 10% toluene- h_8 was deuterated. H-D exchange on H-[Al]ZSM-5(50) began at 60 °C, very close to the value for the onset temperature estimated from in-vacuo TPD-TGA measurements. To determine the effect of acid-site density, we also performed measurements with H-[Al]ZSM-5(280), a sample with the same type of sites but six times fewer of them. The reaction onset temperature in this case was 65 °C. The fact that the onset reaction temperature is only weakly dependent on site density is likely due to the fact that reaction rates increase exponentially with temperature but only linearly with site density. This is a potential problem when comparing different solid acids since minority sites could affect results. The onset reaction temperature for the H-[Fe]ZSM-5, which had a similar site density as the H-[Al]ZSM-5(50) sample, was 70 °C. While this difference is small, we believe it is a real indication of the difference in the strength of the acid sites. As expected, there was no reaction on the Si-MFI sample up to at least 450 °C because that sample has no acid sites. H-D exchange over H-[B]ZSM-5 began at approximately 340 °C. Since there was no reaction on the Si-MFI sample, it would appear that the reaction on H-[B]ZSM-5 is due to the very weak acid sites associated with framework B; but we cannot completely rule out the possibility that reaction on this sample could be due to trace Al impurities that may have been introduced in the synthesis.

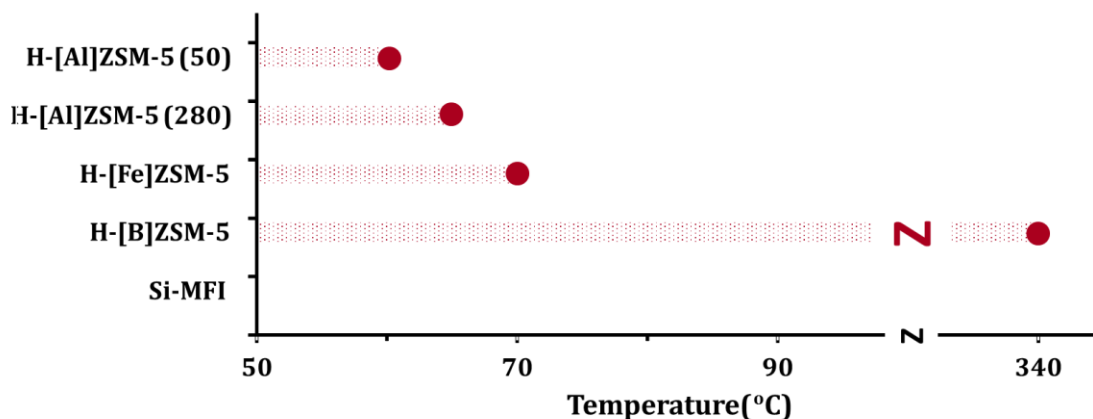


Figure 9.3 Onset-of-reaction temperatures for steady-state H-D exchange between toluene- h_8 and D_2O in a continuous flow reactor over a series of MFI-structured zeolites. 10% conversion of H-D exchange was observed on each material at the highlighted temperature. Reaction conditions: 100-mg catalyst, 1% toluene- h_8 and 1% D_2O in a 20-mL/min He flow.

H-D exchange measurements were also performed on the tungstated zirconia (5W-Zr), P-SPP, ZrO_2 , and Al_2O_3 samples, with results provided in Figure 9.4 and summarized in Table 9.1. The H-D exchange reaction on the 5W-Zr sample began at 100 °C, suggesting that this material has sites which are significantly weaker than those in H-[Al]ZSM-5 and H-[Fe]ZSM-5. While there are claims that tungstated zirconia can have very strong acid sites, this may depend on the synthesis conditions [197]. As discussed elsewhere [239], samples prepared in our lab were not active for alkane cracking or olefin oligomerization and appear to have sites much weaker than those associated with either framework Al or Fe in siliceous zeolites. Therefore, the higher onset reaction temperature observed here is consistent with observations from catalytic studies. Interestingly, the weakly acidic P-SPP sample exhibits H-D exchange above approximately 175 °C. Because this sample was prepared using very pure silica sources, the results cannot be associated with impurities.

The reaction temperature places the acid strength of this sample between that of H-[Fe]ZSM-5 and H-[B]ZSM-5. Finally, isotope exchange was also observed with ZrO₂ and Al₂O₃, but only at temperatures above 375 °C.

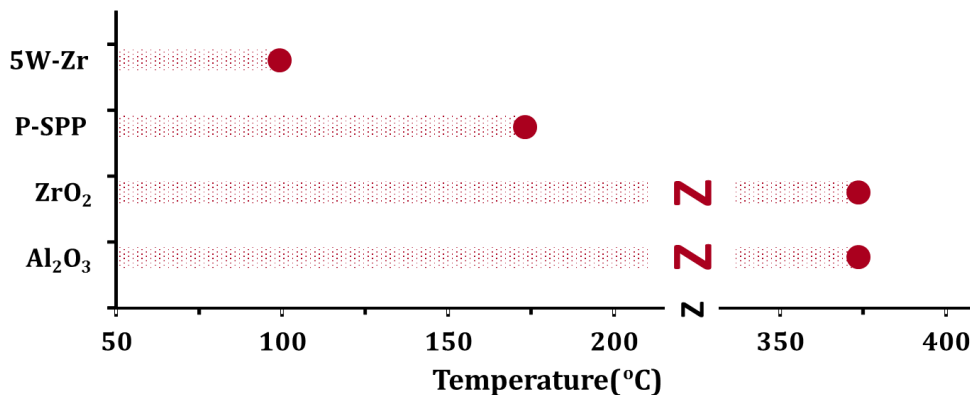


Figure 9.4 Onset-of-reaction temperatures for steady-state H-D exchange between toluene-h₈ and D₂O in a continuous flow reactor over 5W-Zr, P-SPP, ZrO₂, and Al₂O₃. 10% conversion of H-D exchange was observed on each material at the highlighted temperatures. Reaction conditions: 100-mg catalyst, 1% toluene-h₈ and 1% D₂O in a 20-mL/min He flow.

The steady-state reaction experiments were repeated with chlorobenzene-h₅ and the results are tabulated in Figure 9.5 and Table 9.1. With the exceptions of Al₂O₃ and ZrO₂, the two samples which are Lewis rather than Brønsted acids, the onset of reaction was shifted to higher temperatures for each of the materials compared to what was observed with toluene, as expected. However, the ranking of the materials was the same in each case. Reaction occurred at the lowest temperature over H-[Al]ZSM-5(50), followed by H-[Fe]ZSM-5 and 5W-Zr. With chlorobenzene, no reaction was observed over H-[B]ZSM-5 or P-SPP, even at 450 °C.

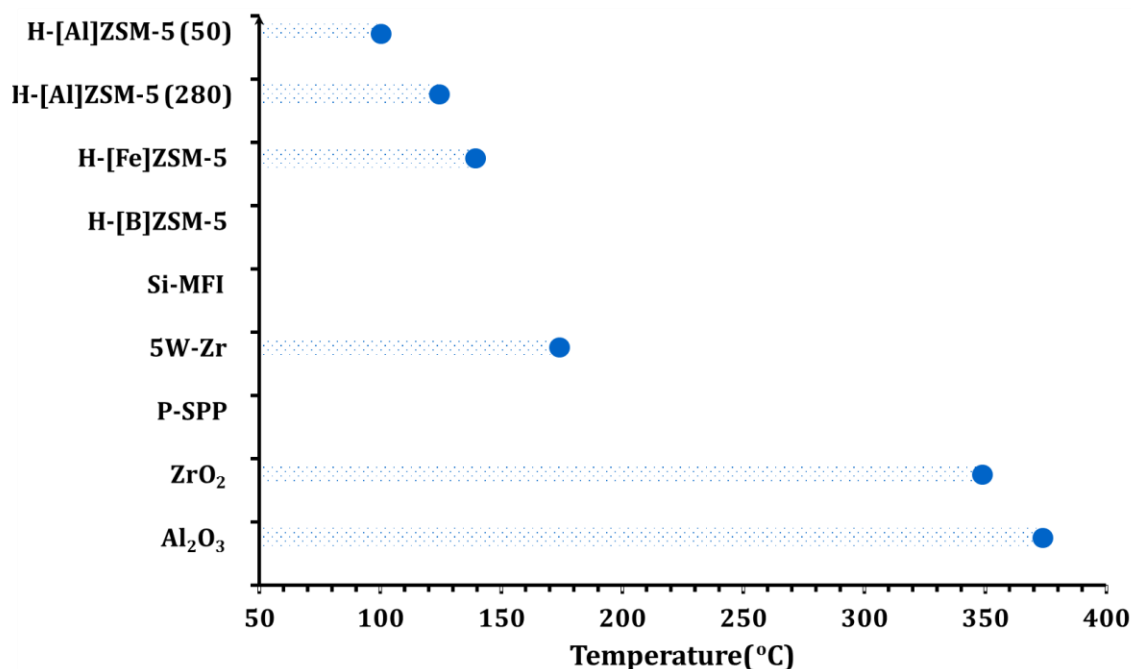


Figure 9.5 Onset-of-reaction temperatures for steady-state H-D exchange between chlorobenzene-h₅ and D₂O in a continuous flow reactor. 10% conversion of H-D exchange was observed on each material at the highlighted temperature. Reaction conditions: 100-mg catalyst, 1% chlorobenzene-h₅ and 1% D₂O in a 20-mL/min He flow.

It is interesting to consider why the reaction onset temperature over Al₂O₃ and ZrO₂ remained nearly the same for toluene and chlorobenzene. We suggest that reaction on these materials involves a different mechanism. If reaction were due to Brønsted sites associated with impurities or Brønsted sites associated with adsorption of D₂O on the Lewis sites, one would expect that the onset temperature would increase for chlorobenzene due to the lower proton affinity of the reactant. If protonation of the reactant is not required, the reaction temperature would not be expected to change.

9.3.3 DFT calculations

To better understand the reaction mechanism and energetics, we performed DFT calculations for the H-D exchange between toluene and D-[Al]ZSM-5. Two exchange positions were explored for toluene, *para* and *meta*. Free-energy profiles for both pathways are shown in Figure 6. We find that exchange at the *para*-position is more favorable by ca. 2 kcal/mol, in agreement with published experimental work [211]. The reaction follows the two-step mechanism through the Wheland intermediate, which forms upon D⁺ transfer from the active site to the aromatic ring and is very unstable (inset in Figure 9.6). This is the rate-limiting step of the H-D exchange, with an intrinsic free energy barrier of 16.9 kcal/mol and an apparent one of 15.6 kcal/mol for the *para* position, at 60 °C (the onset-of-reaction temperature); an image of the first transition state is shown in Figure 9.7. A little less than 3 kcal/mol of activation is required for the Wheland intermediate to donate its proton back to the active site and decay to product. The intrinsic barrier value reported here is much smaller than the 27-31 kcal/mol calculated by Limtrakul [232] and Bell [246] for benzene and ethylbenzene using much smaller cluster models.

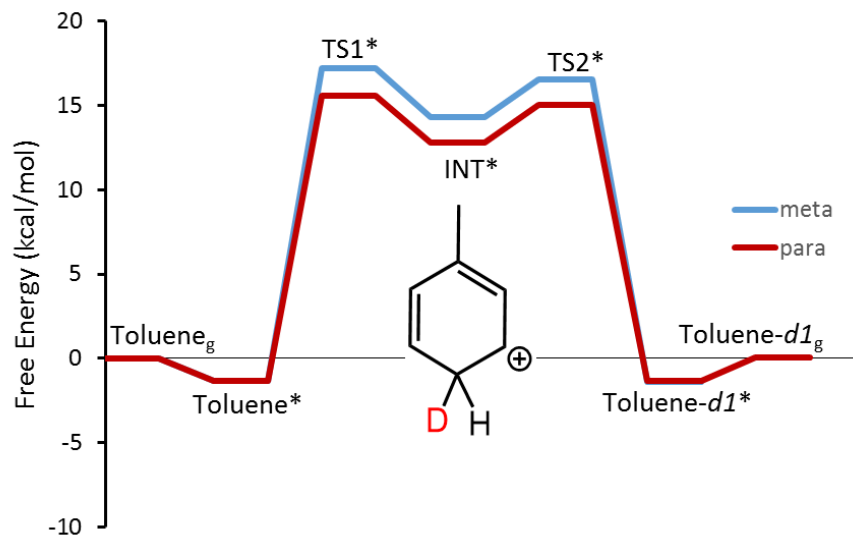


Figure 9.6 Free energy profiles of the H-D exchange reaction between deuterated H-[Al]ZSM-5 and toluene at the *para* (red line) and *meta* (blue line) positions, at 60 °C. The zero-energy reference is gas-phase toluene at infinite separation from deuterated H-[Al]ZSM-5. The reaction follows the two-step mechanism via the Wheland intermediate.

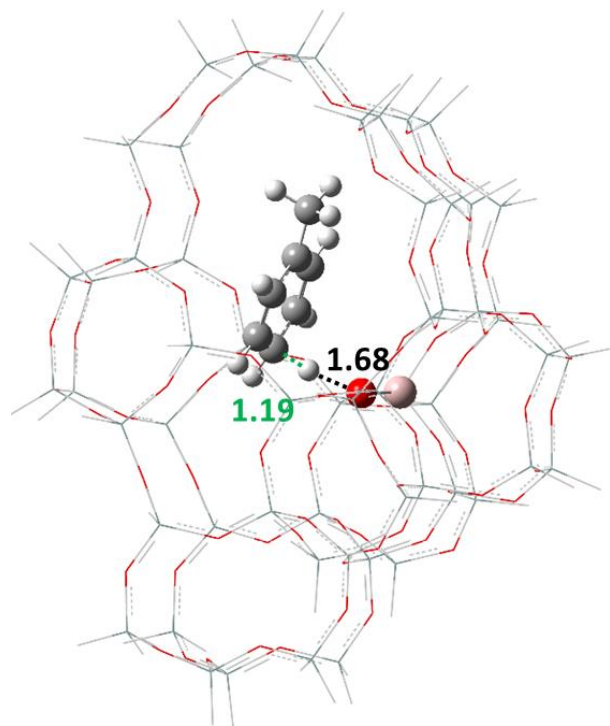


Figure 9.7 Transition state geometry of deuterium cation transfer from the D-[Al]ZSM-5 active site to the para position of toluene. The deuterium-donor/acceptor distances are shown in Å. For clarity, only toluene and the active site atoms are shown in the ball-and-stick representation; the rest of the system is shown in the wireframe representation. Color codes: pink, Al; red, O; white, H; grey, C.

9.4 Discussion

As discussed in the Introduction, measurements of Brønsted-acid strength, as opposed to site densities, is difficult. Heats of adsorption for common probe molecules, such as ammonia, do not necessarily correlate with catalytic activity [226]. For many reactions, rates can depend on factors other than intrinsic acidity. For example, it has been shown that differences in the rates for *n*-hexane cracking on various zeolites is at least partially explained by differences in the sorption properties of the zeolite structures [247]. The H-D exchange experiments discussed here also have limitations but the simplicity of

the reaction has the advantage of being directly related to the ability of the solid to donate a proton and does not appear to be masked by the presence of Lewis sites.

A very important advantage of H-D exchange measurements is that they allowed me to observe the presence of Brønsted sites in P-SPP, a material that has such weak acid sites that we were not able to detect them using adsorption of amines or pyridine. For a Brønsted site to be detectable by pyridine, the proton transfer reaction must be energetically favorable, whereas the H-D exchange reaction can occur even if the protonated form of the adsorbate is not stable. While pyridine is a relatively strong base (Proton Affinity of 924 kJ/mol), the unprotonated pyridine is more stable in weak solid acids, such as P-SPP. A serious disadvantage to using H-D exchange measurements to measure acidity is the sensitivity of the reaction to small concentrations of strong Brønsted sites. It is noteworthy that this sensitivity to impurities can also be a problem with other reaction probes. For example, alkane cracking activity in some early studies of siliceous ZSM-5 zeolites were later shown to be due to Al contaminants in the structure [248].

It is interesting to consider how well the calculated activation barrier agrees with experimental values for H-D exchange between H-[Al]ZSM-5 and toluene. Unfortunately, it was not possible for me to calculate an activation barrier from the steady-state rate measurements in our reactor because of multiple exchange and other complicating factors. However, the TPD results suggest that the reaction between adsorbed toluene-h₈ and D-[Al]ZSM-5 becomes significant above 50 °C. When re-adsorption is not important, TPD

peak temperatures (T_p) can be used to estimate activation energies (E) for desorption using the Redhead Equation:

$$\frac{E\beta}{\nu RT_p^2} = \exp\left\{\frac{-E}{RT_p}\right\}$$

In this equation, β is the heating rate and ν is the reaction pre-exponential (commonly assumed to be $10^{13}/\text{s}$). Using the value of 16.9 kcal/mol from the calculation and the experimental parameters of our experiment, the peak temperature would be estimated to have a value of 255 K. This is significantly lower than the temperature at which deuterated products begin to desorb, which suggests that the actual barrier to H-D exchange is higher than what we have estimated here.

I have admittedly taken a very simplistic view of Brønsted-acid-catalyzed reactions in this work. In real systems, bonding interactions between the adsorbate and the solid will be important [229,231]. Still, I believe that the H-D exchange reaction provides important insights into the nature of the acid sites.

CHAPTER 10. CONCLUSIONS

This dissertation has demonstrated the viability of utilizing bimetallic and metal-oxide-promoted metal catalysts to upgrade biomass-derived oxygenates by selective C-O bond scissions. Useful fuels and chemicals are produced from model compounds which represent the main fractions of lignocellulosic biomass. Using catalysts with well-defined sizes, structures and compositions, I have made progress on gaining insights into the underlying reaction mechanisms and structure-activity relationships. These contributions from the fundamentals should help developing catalysts that are suitable for practical applications.

The work in Chapter 3 highlighted base-metal, Ni-Cu alloys that have achieved 95+ % DMF yields in the high-pressure HDO reaction of HMF. In contrast, monometallic Ni and Cu catalysts only exhibit low performance under the same reaction conditions due to over-hydrogenation on Ni and low reactivity on Cu. The surface composition and chemical state of the active phase were clearly identified by state-of-the-art NAP-XPS analysis on Ni-Cu catalysts based on bimetallic nanocrystals of controlled dimensions and compositions. In both nanocrystal NiCu- and NiCu₃-based catalysts, Ni and Cu were completely reduced at 250 °C in 1 mbar of H₂ and an exposed surface in a 1 : 1 molar ratio. It strongly indicates that an oxide overlayer, which have previously shown to be a critical component for the selective Pt-Co catalysts, is not necessary for Ni-Cu alloys to achieve high DMF yields in the HDO reaction of HMF.

Although the mechanisms behind the high selectivity for the various metal alloys appear to differ, they all require suppression of over-hydrogenation so long as the HDO reactions are performed at high pressures. At low pressures, however, the reduced selectivity in the HDO reactions is primarily due to a separate, decarbonylation pathway. In Chapter 4, I investigated the HDO of furfural at high- and low-pressures. The Ni-Fe bimetallic catalysts that have previously been demonstrated to suppress decarbonylation at low pressures are shown to also suppress over hydrogenation of MF at high pressures. Likewise, the Pt-Co nanocrystals that were previously shown to prevent over hydrogenation of MF are now demonstrated to suppress decarbonylation furfural. These results suggest that a similar process is involved in both the decarbonylation and over-hydrogenation reactions.

In Chapter 5, I investigated the ring opening reaction of THFA. A series of carbon-supported, metal oxide-promoted, metal catalysts were shown to exhibit special activity and selectivity to produce 1,5-PeD, even though the individual components were not active or selective. Only reducible oxides produced selective catalysts. A more comprehensive study of the Pt-WO_x system indicated that the active form of the catalyst exists as a thin, submonolayer film of the oxide on the Pt surface. This film could be formed by atomic layer deposition (ALD) of W(CO)₆ onto the Pt nanocrystals and STEM-EDS mapping demonstrated that ALD deposition occurred selectively on the Pt. Since all of the metal oxides that exhibited promotional effects (WO_x, MoO_x and ReO_x) could be partially reduced and have been demonstrated to exhibit mobility in aqueous environments, it is

suggested that the formation of an oxide overlayer is generally a key feature required to produce active and selective catalysts for this system.

The work presented in Chapter 6 investigated the HDO reaction *m*-cresol, a model compound for the lignin fractions of biomass. Due in part to the persistent conjugation of the aryl C-O bond, none of the catalysts that have previously shown to be selective for HDO of HMF and furfural (see Chapters 3 and 4) promotes the HDO of *m*-cresol. However, the results shown in Chapter 6 demonstrate that Pt-WO_x/C has high activity and selectivity for the HDO of *m*-cresol. Over 94% selectivity to the desired product, toluene, was achieved under a range of reaction conditions with the catalyst being highly stable and not prone to deactivation via coking. This behavior is contrast to what is observed for unmodified Pt/C which is much less selective for the production of toluene during HDO of *m*-cresol with a significant amount of products with saturated rings, such as 3-methylcyclohexanone, also being produced.

On Pt/C, the results obtained indicate that HDO of phenolics, like *m*-cresol, proceeds through a complex pathway that involves partial ring hydrogenation followed by dehydration and hydrogenation, a pathway that produces a pool of reaction intermediates which limits the selectivity to the desired aromatic hydrocarbons. Both the experimental and theoretical results reported in Chapter 6 indicate that for Pt-WO_x/C the HDO reaction proceeds in a much more direct manner. Direct bonding between the Pt and supported WO_x complexes both stabilizes the oxide and lowers the barrier to oxygen vacancy formation. The latter plays a pivotal role in the formation of redox sites on the WO_x which are active

for direct C-O bond hydrogenolysis in adsorbed phenolic compounds. Adsorption on these sites also limits interaction of the aromatic ring with the Pt surface thereby precluding ring hydrogenation.

Chapter 7 discussed the results for the selective HDO reaction of *m*-cresol, but using *in-situ* hydrogen generated by a tandem reaction of *n*-hexane dehydrogenation. While the Pt/C catalyst showed very small conversions of both *n*-hexane and *m*-cresol, the Pt-WO_x/C catalyst was able to significantly promote both HDO and dehydrogenation activity, and both reactions achieved over 95 % selectivity to the desired products, hexenes and toluene. In addition, the enhanced performance are shown to be relatively stable in 6 h on stream. The key observation that makes this possible is that the coking rates for dehydrogenation of *n*-hexane on Pt/C were found to be dramatically lower at high pressures. Two hypotheses were proposed in an attempt to explain the pressure dependence of Pt deactivation: (1) The surface crowding may limit *n*-hexane from exposure parallel to the Pt surface and thus prevent further dehydrogenation, cyclization and polymerizations to form coke; alternatively, (2) *n*-hexane inside the micro pores of carbon support may be liquid-like, the dense fluid near the surface may assist desorption of products before further reacting to form coke.

Chapter 8 reported a novel synthesis method for preparing tungstated zirconia by atomic layer deposition (ALD). Results confirmed that ALD of W(CO)₆ on ZrO₂ allows the deposition of uniform layers of WO_x, with coverages varying from sub-monolayer to multilayer. The TPD measurements with 2-propanamine on the WO_x/ZrO₂ samples

identified three types of sites: dehydrogenation sites associated with uncovered ZrO_2 , Brønsted sites formed by monolayer clusters of WO_x , and redox sites associated with multilayers of WO_x . The densities of these reactive sites were correlated to the surface WO_x coverage, it reveals that the formation of Brønsted sites for WO_x/ZrO_2 requires the presence of multiple W atoms. However, the Brønsted sites in WO_x/ZrO_2 were shown to be significantly weaker than the Brønsted sites in an H-ZSM-5 zeolite demonstrated by H–D exchange with toluene and chlorobenzene.

The work in Chapter 9 further demonstrated that it is possible to determine relative Brønsted-acid strengths using the onset temperature of H-D exchange with the simple aromatics. Reactivity studies of H-D exchange in combination with TPD-TGA results using toluene- h_8 and chlorobenzene- h_5 allowed the Brønsted-acid site strengths of a series of solids to be ordered as follows: H-[Al]ZSM-5 > H-[Fe]ZSM-5 > tungstated zirconia > P-SPP > H-[B]ZSM-5. This ordering is in good agreement with expectations based on catalytic activities reported in the literature. DFT calculation suggests that H-D exchange reaction with toluene- h_8 is rate-limited by the isotope exchange step through a Wheland intermediate with an intrinsic free energy barrier of 16.9 kcal/mol.

BIBLIOGRAPHY

- [1] D.M. Alonso, S.G. Wettstein, J.A. Dumesic, *Chemical Society Reviews* 41 (2012) 8075–8098.
- [2] Y. Nakagawa, M. Tamura, K. Tomishige, *ACS Catalysis* 3 (2013) 2655–2668.
- [3] J.C. Serrano-Ruiz, J.A. Dumesic, *Energy & Environmental Science* 4 (2011) 83–99.
- [4] A. Corma, S. Iborra, A. Velty, *Chemical Reviews* 107 (2007) 2411–2502.
- [5] C.-H.C. Zhou, J.N. Beltramini, Y.-X. Fan, G.M. Lu, *Chemical Society Reviews* 37 (2008) 527–549.
- [6] J.N. Chheda, G.W. Huber, J.A. Dumesic, *Angewandte Chemie International Edition* 46 (2007) 7164–7183.
- [7] G.W. Huber, S. Iborra, A. Corma, *Chemical Reviews* 106 (2006) 4044–4098.
- [8] A.A. Kiss, A.C. Dimian, G. Rothenberg, *Energy & Fuels* 22 (2007) 598–604.
- [9] International Energy Agency, *Renewables 2018 Market Analysis and Forecast from 2018 to 2023*, International Energy Agency, 2018.
- [10] G. Kumar, P. Bakonyi, S. Periyasamy, S. Kim, N. Nemestóthy, K. Bélafi-Bakó, *Renewable and Sustainable Energy Reviews* 44 (2015) 728–737.
- [11] D.N.-S. Hon, N. Shiraishi, *Wood and Cellulosic Chemistry, Revised, and Expanded*, CRC press, 2000.
- [12] F.H. Isikgor, C.R. Becer, *Polymer Chemistry* 6 (2015) 4497–4559.
- [13] P. De Wild, H. Reith, E. Heeres, *Biofuels* 2 (2011) 185–208.
- [14] S. Wang, Z. Luo, *Pyrolysis of Biomass*, Walter de Gruyter GmbH & Co KG, 2016.
- [15] L.D. Schmidt, P.J. Dauenhauer, *Nature* 447 (2007) 914.
- [16] G.W. Huber, S. Iborra, A. Corma, *Chemical Reviews* 106 (2006) 4044–4098.
- [17] J.A. Melero, J. Iglesias, A. Garcia, *Energy & Environmental Science* 5 (2012) 7393–7420.
- [18] P. Gallezot, *Chemical Society Reviews* 41 (2012) 1538–1558.
- [19] C.O. Tuck, E. Pérez, I.T. Horváth, R.A. Sheldon, M. Poliakoff, *Science* 337 (2012) 695–699.
- [20] G.W. Huber, J.A. Dumesic, *Catalysis Today* 111 (2006) 119–132.
- [21] J.A. Geboers, S. Van de Vyver, R. Ooms, B.O. de Beeck, P.A. Jacobs, B.F. Sels, *Catalysis Science & Technology* 1 (2011) 714–726.
- [22] H.J. Brownlee, C.S. Miner, *Industrial & Engineering Chemistry* 40 (1948) 201–204.
- [23] Grand View Research, *Global Furfural Market By Application (Furfuryl Alcohol, Solvents) Expected To Reach USD 1,200.9 Million By 2020*, Grand View Research, 2015.
- [24] T. Wang, M.W. Nolte, B.H. Shanks, *Green Chemistry* 16 (2014) 548–572.
- [25] M. Dashtban, A. Gilbert, P. Fatehi, *Rsc Advances* 4 (2014) 2037–2050.
- [26] A.I. Torres, P. Daoutidis, M. Tsapatsis, *Energy & Environmental Science* 3 (2010) 1560–1572.
- [27] M. Chidambaram, A.T. Bell, *Green Chemistry* 12 (2010) 1253–1262.
- [28] A. Demirbas, *Fuel Processing Technology* 88 (2007) 591–597.
- [29] B.-O.C.D.D. Ensyn, Ensyn, Wilmington, Delaware (2001).
- [30] D.E. Resasco, S. Sitthisa, J. Faria, T. Prasomsri, M.P. Ruiz, *Solid Waste as a Renewable Resource Methodologies* (2011) 103.

- [31] S. Koso, I. Furikado, A. Shima, T. Miyazawa, K. Kunimori, K. Tomishige, *Chemical Communications* (2009) 2035–2037.
- [32] O. Casanova, S. Iborra, A. Corma, *Journal of Catalysis* 275 (2010) 236–242.
- [33] S. Liu, T.R. Josephson, A. Athaley, Q.P. Chen, A. Norton, M. Ierapetritou, J.I. Siepmann, B. Saha, D.G. Vlachos, *Science Advances* 5 (2019) eaav5487.
- [34] Y. Ji, J. Pan, P. Dauenhauer, R.J. Gorte, *Applied Catalysis A: General* (2019).
- [35] A.M. Robinson, J.E. Hensley, J.W. Medlin, *ACS Catalysis* 6 (2016) 5026–5043.
- [36] M. Saidi, F. Samimi, D. Karimipourfard, T. Nimmanwudipong, B.C. Gates, M.R. Rahimpour, *Energy & Environmental Science* 7 (2014) 103–129.
- [37] Q. Bu, H. Lei, A.H. Zacher, L. Wang, S. Ren, J. Liang, Y. Wei, Y. Liu, J. Tang, Q. Zhang, *Bioresource Technology* 124 (2012) 470–477.
- [38] J. Luo, L. Arroyo-Ramírez, J. Wei, H. Yun, C.B. Murray, R.J. Gorte, *Applied Catalysis A: General* 508 (2015) 86–93.
- [39] Y. Huang, M. Chen, L. Yan, Q. Guo, Y. Fu, *ChemSusChem* 7 (2014) 1068–1072.
- [40] S. Nishimura, N. Ikeda, K. Ebitani, *Catalysis Today* 232 (2014) 89–98.
- [41] S. Sitthisa, W. An, D.E. Resasco, *Journal of Catalysis* 284 (2011) 90–101.
- [42] M. Myint, Y. Yan, J.G. Chen, *The Journal of Physical Chemistry C* 118 (2014) 11340–11349.
- [43] J. Lee, Y.T. Kim, G.W. Huber, *Green Chemistry* 16 (2014) 708–718.
- [44] Y. Zu, P. Yang, J. Wang, X. Liu, J. Ren, G. Lu, Y. Wang, *Applied Catalysis B: Environmental* 146 (2014) 244–248.
- [45] J. Luo, H. Yun, A.V. Mironenko, K. Goulas, J.D. Lee, M. Monai, C. Wang, V. Vorotnikov, C.B. Murray, D.G. Vlachos, *ACS Catalysis* 6 (2016) 4095–4104.
- [46] J. Luo, J.D. Lee, H. Yun, C. Wang, M. Monai, C.B. Murray, P. Fornasiero, R.J. Gorte, *Applied Catalysis B: Environmental* 199 (2016) 439–446.
- [47] Y. Román-Leshkov, C.J. Barrett, Z.Y. Liu, J.A. Dumesic, *Nature* 447 (2007) 982.
- [48] G.-H. Wang, J. Hilgert, F.H. Richter, F. Wang, H.-J. Bongard, B. Spliethoff, C. Weidenthaler, F. Schüth, *Nature Materials* 13 (2014) 293.
- [49] D. Shi, L. Arroyo-Ramírez, J.M. Vohs, *Journal of Catalysis* 340 (2016) 219–226.
- [50] C. Li, X. Zhao, A. Wang, G.W. Huber, T. Zhang, *Chemical Reviews* 115 (2015) 11559–11624.
- [51] H.L. Chum, D.K. Johnson, *Liquid Fuels from Lignins: Annual Report*, National Renewable Energy Lab.(NREL), Golden, CO (United States), 1986.
- [52] H. Weigold, *Fuel* 61 (1982) 1021–1026.
- [53] E.O. Odebunmi, D.F. Ollis, *Journal of Catalysis* 80 (1983) 56–64.
- [54] R. Wandas, J. Surygala, E. Śliwka, *Fuel* 75 (1996) 687–694.
- [55] H. Wang, J. Male, Y. Wang, *ACS Catalysis* 3 (2013) 1047–1070.
- [56] M. Badawi, J. Paul, S. Cristol, E. Payen, Y. Romero, F. Richard, S. Brunet, D. Lambert, X. Portier, A. Popov, *Journal of Catalysis* 282 (2011) 155–164.
- [57] H. Wan, R.V. Chaudhari, B. Subramaniam, *Topics in Catalysis* 55 (2012) 129–139.
- [58] C. González, P. Marín, F.V. Díez, S. Ordóñez, *Industrial & Engineering Chemistry Research* 55 (2016) 2319–2327.
- [59] L. Nie, D.E. Resasco, *Journal of Catalysis* 317 (2014) 22–29.
- [60] A. Ardiyanti, A. Gutierrez, M. Honkela, A. Krause, H. Heeres, *Applied Catalysis A: General* 407 (2011) 56–66.

- [61] Y.-C. Lin, C.-L. Li, H.-P. Wan, H.-T. Lee, C.-F. Liu, *Energy & Fuels* 25 (2011) 890–896.
- [62] T. Nimmanwudipong, R.C. Runnebaum, D.E. Block, B.C. Gates, *Energy & Fuels* 25 (2011) 3417–3427.
- [63] F. Yang, D. Liu, H. Wang, X. Liu, J. Han, Q. Ge, X. Zhu, *Journal of Catalysis* 349 (2017) 84–97.
- [64] A. Robinson, G.A. Ferguson, J.R. Gallagher, S. Cheah, G.T. Beckham, J.A. Schaidle, J.E. Hensley, J.W. Medlin, *ACS Catalysis* 6 (2016) 4356–4368.
- [65] D. Ballesteros-Plata, A. Infantes-Molina, M. Rodríguez-Cuadrado, E. Rodríguez-Aguado, P. Braos-García, E. Rodríguez-Castellón, *Applied Catalysis A: General* 547 (2017) 86–95.
- [66] P.T. Do, A.J. Foster, J. Chen, R.F. Lobo, *Green Chemistry* 14 (2012) 1388–1397.
- [67] L. Nie, P.M. de Souza, F.B. Noronha, W. An, T. Sooknoi, D.E. Resasco, *Journal of Molecular Catalysis A: Chemical* 388 (2014) 47–55.
- [68] X. Liu, W. An, C.H. Turner, D.E. Resasco, *Journal of Catalysis* 359 (2018) 272–286.
- [69] A.J. Foster, P.T. Do, R.F. Lobo, *Topics in Catalysis* 55 (2012) 118–128.
- [70] X. Zhu, L. Nie, L.L. Lobban, R.G. Mallinson, D.E. Resasco, *Energy & Fuels* 28 (2014) 4104–4111.
- [71] H. Ohta, B. Feng, H. Kobayashi, K. Hara, A. Fukuoka, *Catalysis Today* 234 (2014) 139–144.
- [72] Y.-B. Huang, L. Yan, M.-Y. Chen, Q.-X. Guo, Y. Fu, *Green Chemistry* 17 (2015) 3010–3017.
- [73] M.B. Griffin, G.A. Ferguson, D.A. Ruddy, M.J. Bidy, G.T. Beckham, J.A. Schaidle, *ACS Catalysis* 6 (2016) 2715–2727.
- [74] I.T. Ghampson, R. Canales, N. Escalona, *Applied Catalysis A: General* 549 (2018) 225–236.
- [75] A.A. Dwiatmoko, I. Kim, L. Zhou, J.-W. Choi, D.J. Suh, J. Jae, J.-M. Ha, *Applied Catalysis A: General* 543 (2017) 10–16.
- [76] T. Guo, Q. Xia, Y. Shao, X. Liu, Y. Wang, *Applied Catalysis A: General* 547 (2017) 30–36.
- [77] T. Prasomsri, T. Nimmanwudipong, Y. Román-Leshkov, *Energy & Environmental Science* 6 (2013) 1732–1738.
- [78] T. Prasomsri, M. Shetty, K. Murugappan, Y. Román-Leshkov, *Energy & Environmental Science* 7 (2014) 2660–2669.
- [79] Q. Sun, G. Chen, H. Wang, X. Liu, J. Han, Q. Ge, X. Zhu, *ChemCatChem* 8 (2016) 551–561.
- [80] T.O. Omotoso, B. Baek, L.C. Grabow, S.P. Crossley, *ChemCatChem* 9 (2017) 2642–2651.
- [81] Q. Tan, G. Wang, L. Nie, A. Dinse, C. Buda, J. Shabaker, D.E. Resasco, *ACS Catalysis* 5 (2015) 6271–6283.
- [82] S. Sitthisa, D.E. Resasco, *Catalysis Letters* 141 (2011) 784–791.
- [83] V. Vetere, A.B. Merlo, J.F. Ruggera, M.L. Casella, *Journal of the Brazilian Chemical Society* 21 (2010) 914–920.
- [84] S. Koso, N. Ueda, Y. Shinmi, K. Okumura, T. Kizuka, K. Tomishige, *Journal of Catalysis* 267 (2009) 89–92.
- [85] C.J. Kliewer, C. Aliaga, M. Bieri, W. Huang, C.-K. Tsung, J.B. Wood, K. Komvopoulos, G.A. Somorjai, *Journal of the American Chemical Society* 132 (2010) 13088–13095.
- [86] J. Tuteja, H. Choudhary, S. Nishimura, K. Ebitani, *ChemSusChem* 7 (2014) 96–100.
- [87] A.D. Sutton, F.D. Waldie, R. Wu, M. Schlaf, A. Louis III, J.C. Gordon, *Nature Chemistry* 5 (2013) 428.
- [88] M. Schlaf, *Dalton Transactions* (2006) 4645–4653.
- [89] L. Schniepp, H. Geller, *Journal of the American Chemical Society* 68 (1946) 1646–1648.

- [90] M. Chia, Y.J. Pagán-Torres, D. Hibbitts, Q. Tan, H.N. Pham, A.K. Datye, M. Neurock, R.J. Davis, J.A. Dumesic, *Journal of the American Chemical Society* 133 (2011) 12675–12689.
- [91] T. Buntara, I. Melián-Cabrera, Q. Tan, J.L. Fierro, M. Neurock, J.G. De Vries, H.J. Heeres, *Catalysis Today* 210 (2013) 106–116.
- [92] E.L. Dias, J.A. Shoemaker, T.R. Boussie, V.J. Murphy, (2014).
- [93] A.M. Allgeier, D.R. Corbin, W.I.N. De Silva, E. Korovessi, C.A. Menning, J.C. Ritter, S.K. Sengupta, (2014).
- [94] V. Sokolovskii, M. Lavrenko, A. Hagemeyer, E.L. Dias, J.A. Shoemaker, V.J. Murphy, (2017).
- [95] S. Feng, A. Nagao, T. Aihara, H. Miura, T. Shishido, *Catalysis Today* 303 (2018) 207–212.
- [96] S. Koso, Y. Nakagawa, K. Tomishige, *Journal of Catalysis* 280 (2011) 221–229.
- [97] S. Koso, H. Watanabe, K. Okumura, Y. Nakagawa, K. Tomishige, *Applied Catalysis B: Environmental* 111 (2012) 27–37.
- [98] K. Chen, K. Mori, H. Watanabe, Y. Nakagawa, K. Tomishige, *Journal of Catalysis* 294 (2012) 171–183.
- [99] B. Pholjaroen, N. Li, Y. Huang, L. Li, A. Wang, T. Zhang, *Catalysis Today* 245 (2015) 93–99.
- [100] J. Guan, G. Peng, Q. Cao, X. Mu, *The Journal of Physical Chemistry C* 118 (2014) 25555–25566.
- [101] Y. Amada, Y. Shinmi, S. Koso, T. Kubota, Y. Nakagawa, K. Tomishige, *Applied Catalysis B: Environmental* 105 (2011) 117–127.
- [102] M.V. Juskelis, J.P. Slanga, T.G. Roberie, A.W. Peters, *Journal of Catalysis* 138 (1992) 391–394.
- [103] J. Luo, L. Arroyo-Ramírez, R.J. Gorte, D. Tzoulaki, D.G. Vlachos, *AIChE Journal* 61 (2015) 590–597.
- [104] C.B. Murray, a C. Kagan, M. Bawendi, *Annual Review of Materials Science* 30 (2000) 545–610.
- [105] S.M. George, *Chemical Reviews* 110 (2009) 111–131.
- [106] B.J. O’Neill, D.H. Jackson, J. Lee, C. Canlas, P.C. Stair, C.L. Marshall, J.W. Elam, T.F. Kuech, J.A. Dumesic, G.W. Huber, *ACS Catalysis* 5 (2015) 1804–1825.
- [107] J. Lu, J.W. Elam, P.C. Stair, *Accounts of Chemical Research* 46 (2013) 1806–1815.
- [108] T. Onn, R. Küngas, P. Fornasiero, K. Huang, R. Gorte, *Inorganics* 6 (2018) 34.
- [109] R. Demmin, R. Gorte, *Journal of Catalysis* 90 (1984) 32–39.
- [110] R.J. Gorte, *Journal of Catalysis* 75 (1982) 164–174.
- [111] M.T. Aronson, R.J. Gorte, W.E. Farneth, *Journal of Catalysis* 98 (1986) 434–443.
- [112] W.E. Farneth, R.J. Gorte, *Chemical Reviews* 95 (1995) 615–635.
- [113] D.J. Parrillo, A.T. Adamo, G.T. Kokotailo, R.J. Gorte, *Applied Catalysis* 67 (1990) 107–118.
- [114] R.J. Gorte, *Catalysis Letters* 62 (1999) 1–13.
- [115] J.G. Tittensor, R.J. Gorte, D.M. Chapman, *Journal of Catalysis* 138 (1992) 714–720.
- [116] B. Saha, C.M. Bohn, M.M. Abu-Omar, *ChemSusChem* 7 (2014) 3095–3101.
- [117] D. Scholz, C. Aellig, I. Hermans, *ChemSusChem* 7 (2014) 268–275.
- [118] G.C.A. Luijkx, N.P.M. Huck, F. van Rantwijk, *Heterocycles* 77 (2009) 1037–1044.
- [119] L. Yu, L. He, J. Chen, J. Zheng, L. Ye, H. Lin, Y. Yuan, *ChemCatChem* 7 (2015) 1701–1707.
- [120] B. Chen, F. Li, Z. Huang, G. Yuan, *Applied Catalysis B: Environmental* 200 (2017) 192–199.

- [121] M. Cargnello, V.V.T. Doan-Nguyen, T.R. Gordon, R.E. Diaz, E.A. Stach, R.J. Gorte, P. Fornasiero, C.B. Murray, *Science* 341 (2013) 771–773.
- [122] Z.J. Huba, E.E. Carpenter, *CrystEngComm* 15 (2013) 8919–8923.
- [123] E. Pellicer, A. Varea, K.M. Sivaraman, S. Pané, S. Suriñach, M.D. Baró, J. Nogués, B.J. Nelson, J. Sort, *ACS Appl. Mater. Interfaces* 3 (2011) 2265–2274.
- [124] S. Sitthisa, T. Pham, T. Prasomsri, T. Sooknoi, R.G. Mallinson, D.E. Resasco, *Journal of Catalysis* 280 (2011) 17–27.
- [125] S. Sitthisa, T. Sooknoi, Y. Ma, P.B. Balbuena, D.E. Resasco, *Journal of Catalysis* 277 (2011) 1–13.
- [126] L. Bui, H. Luo, W.R. Gunther, Y. Román-Leshkov, *Angewandte Chemie International Edition* 52 (2013) 8022–8025.
- [127] J. Luo, J. Yu, R.J. Gorte, E. Mahmoud, D.G. Vlachos, M.A. Smith, *Catal. Sci. Technol.* 4 (2014) 3074–3081.
- [128] Y. Yao, D.W. Goodman, *Journal of Molecular Catalysis A: Chemical* 383–384 (2014) 239–242.
- [129] J.H. Sinfelt, *Acc. Chem. Res.* 10 (1977) 15–20.
- [130] K. Xiong, W. Wan, J.G. Chen, *Surface Science* 652 (2016) 91–97.
- [131] K. Bakhmutsky, N.L. Wieder, T. Baldassare, M.A. Smith, R.J. Gorte, *Applied Catalysis A: General* 397 (2011) 266–271.
- [132] R.V. Sharma, U. Das, R. Sammynaiken, A.K. Dalai, *Applied Catalysis A: General* 454 (2013) 127–136.
- [133] G. Chen, Y. Shen, Q. Zhang, M. Yao, Z. Zheng, H. Liu, *Energy* 54 (2013) 333–342.
- [134] H.-Y. Zheng, Y.-L. Zhu, B.-T. Teng, Z.-Q. Bai, C.-H. Zhang, H.-W. Xiang, Y.-W. Li, *Journal of Molecular Catalysis A: Chemical* 246 (2006) 18–23.
- [135] J. Luo, M. Monai, H. Yun, L. Arroyo-Ramírez, C. Wang, C.B. Murray, P. Fornasiero, R.J. Gorte, *Catalysis Letters* 146 (2016) 711–717.
- [136] S. Wang, V. Vorotnikov, D.G. Vlachos, *ACS Catalysis* 5 (2015) 104–112.
- [137] M.J. Taylor, L. Jiang, J. Reichert, A.C. Papageorgiou, S.K. Beaumont, K. Wilson, A.F. Lee, J.V. Barth, G. Kyriakou, *The Journal of Physical Chemistry C* 121 (2017) 8490–8497.
- [138] W. Yu, K. Xiong, N. Ji, M.D. Porosoff, J.G. Chen, *Journal of Catalysis* 317 (2014) 253–262.
- [139] T.M. Onn, S. Zhang, L. Arroyo-Ramírez, Y. Xia, C. Wang, X. Pan, G.W. Graham, R.J. Gorte, *Applied Catalysis B: Environmental* 201 (2017) 430–437.
- [140] A. Wang, T. Zhang, *Accounts of Chemical Research* 46 (2013) 1377–1386.
- [141] J. Santiesteban, D. Calabro, W. Borghard, C. Chang, J. Vartuli, Y. Tsao, M. Natal-Santiago, R. Bastian, *Journal of Catalysis* 183 (1999) 314–322.
- [142] S. Zhang, P.N. Plessow, J.J. Willis, S. Dai, M. Xu, G.W. Graham, M. Cargnello, F. Abild-Pedersen, X. Pan, *Nano Letters* 16 (2016) 4528–4534.
- [143] S. García-Fernández, I. Gandarias, J. Requies, F. Soulimani, P.L. Arias, B.M. Weckhuysen, *Applied Catalysis B: Environmental* 204 (2017) 260–272.
- [144] S. Zhu, X. Gao, Y. Zhu, Y. Li, *Journal of Molecular Catalysis A: Chemical* 398 (2015) 391–398.
- [145] C. Wang, J.D. Lee, Y. Ji, T.M. Onn, J. Luo, C.B. Murray, R.J. Gorte, *Catalysis Letters* 148 (2018) 1047–1054.
- [146] G. Kresse, J. Hafner, *Physical Review B* 47 (1993) 558.

- [147] G. Kresse, J. Hafner, *Physical Review B* 49 (1994) 14251.
- [148] G. Kresse, J. Furthmüller, *Physical Review B* 54 (1996) 11169.
- [149] G. Kresse, J. Furthmüller, *Computational Materials Science* 6 (1996) 15–50.
- [150] P.E. Blöchl, *Physical Review B* 50 (1994) 17953.
- [151] G. Kresse, D. Joubert, *Physical Review B* 59 (1999) 1758.
- [152] H.J. Monkhorst, J.D. Pack, *Physical Review B* 13 (1976) 5188.
- [153] J.P. Perdew, K. Burke, M. Ernzerhof, *Physical Review Letters* 77 (1996) 3865.
- [154] G. Henkelman, B.P. Uberuaga, H. Jónsson, *The Journal of Chemical Physics* 113 (2000) 9901–9904.
- [155] D. Sheppard, G. Henkelman, *Journal of Computational Chemistry* 32 (2011) 1769–1771.
- [156] D. Sheppard, R. Terrell, G. Henkelman, *The Journal of Chemical Physics* 128 (2008) 134106.
- [157] D. Sheppard, P. Xiao, W. Chemelewski, D.D. Johnson, G. Henkelman, *The Journal of Chemical Physics* 136 (2012) 074103.
- [158] G. Henkelman, H. Jónsson, *The Journal of Chemical Physics* 113 (2000) 9978–9985.
- [159] A.V. Mironenko, M.J. Gilkey, P. Panagiotopoulou, G. Facas, D.G. Vlachos, B. Xu, *The Journal of Physical Chemistry C* 119 (2015) 6075–6085.
- [160] G. Kresse, W. Bergermayer, R. Podloucky, E. Lundgren, R. Koller, M. Schmid, P. Varga, *Applied Physics A* 76 (2003) 701–710.
- [161] W. Koch, M.C. Holthausen, *A Chemist's Guide to Density Functional Theory*, John Wiley & Sons, 2015.
- [162] G. Papoian, J.K. Nørskov, R. Hoffmann, *Journal of the American Chemical Society* 122 (2000) 4129–4144.
- [163] (2018).
- [164] F. Wang, C. Di Valentin, G. Pacchioni, *The Journal of Physical Chemistry C* 116 (2012) 10672–10679.
- [165] D.C. Elliott, T.R. Hart, *Energy & Fuels* 23 (2009) 631–637.
- [166] C. Zhao, J. He, A.A. Lemonidou, X. Li, J.A. Lercher, *Journal of Catalysis* 280 (2011) 8–16.
- [167] A. Katrib, F. Hemming, P. Wehrer, L. Hilaire, G. Maire, *Journal of Electron Spectroscopy and Related Phenomena* 76 (1995) 195–200.
- [168] H. Liu, S. Huang, L. Zhang, S. Liu, W. Xin, L. Xu, *Catalysis Communications* 10 (2009) 544–548.
- [169] J. Horsley, I. Wachs, J. Brown, G. Via, F. Hardcastle, *Journal of Physical Chemistry* 91 (1987) 4014–4020.
- [170] F. Hilbrig, H.E. Goebel, H. Knoezinger, H. Schmelz, B. Lengeler, *The Journal of Physical Chemistry* 95 (1991) 6973–6978.
- [171] O. Bondarchuk, X. Huang, J. Kim, B.D. Kay, L. Wang, J. White, Z. Dohnálek, *Angewandte Chemie International Edition* 45 (2006) 4786–4789.
- [172] A.V. Mironenko, D.G. Vlachos, *Journal of the American Chemical Society* 138 (2016) 8104–8113.
- [173] A. Ruiz Puigdollers, P. Schlexer, S. Tosoni, G. Pacchioni, *ACS Catalysis* 7 (2017) 6493–6513.
- [174] Y. Amada, N. Ota, M. Tamura, Y. Nakagawa, K. Tomishige, *ChemSusChem* 7 (2014) 2185–2192.
- [175] R. Bader, *Acc Chem Res* (1990) 9–15.

- [176] G.H. Gu, C.A. Mullen, A.A. Boateng, D.G. Vlachos, *ACS Catalysis* 6 (2016) 3047–3055.
- [177] P.M. Mortensen, J.-D. Grunwaldt, P.A. Jensen, A.D. Jensen, *ACS Catalysis* 3 (2013) 1774–1785.
- [178] W. Song, Y. Liu, E. Baráth, C. Zhao, J.A. Lercher, *Green Chemistry* 17 (2015) 1204–1218.
- [179] L. Nie, B. Peng, X. Zhu, *ChemCatChem* 10 (2018) 1064–1074.
- [180] C. Wang, J. Luo, V. Liao, J.D. Lee, T.M. Onn, C.B. Murray, R.J. Gorte, *Catalysis Today* 302 (2018) 73–79.
- [181] X. Wang, R. Rinaldi, *Energy & Environmental Science* 5 (2012) 8244–8260.
- [182] X. Wang, R. Rinaldi, *Angewandte Chemie International Edition* 52 (2013) 11499–11503.
- [183] M. Kim, J.-M. Ha, K.-Y. Lee, J. Jae, *Catalysis Communications* 86 (2016) 113–118.
- [184] H.P.R. Kannapu, C.A. Mullen, Y. Elkasabi, A.A. Boateng, *Fuel Processing Technology* 137 (2015) 220–228.
- [185] C.A. Fisk, T. Morgan, Y. Ji, M. Crocker, C. Crofcheck, S.A. Lewis, *Applied Catalysis A: General* 358 (2009) 150–156.
- [186] Y. Zeng, Z. Wang, W. Lin, W. Song, J.M. Christensen, A.D. Jensen, *Catalysis Communications* 82 (2016) 46–49.
- [187] Y. Zeng, Z. Wang, W. Lin, W. Song, *Chemical Engineering Journal* 320 (2017) 55–62.
- [188] H. Shafaghat, P.S. Rezaei, W.M.A.W. Daud, *Journal of the Taiwan Institute of Chemical Engineers* 65 (2016) 91–100.
- [189] C. Wang, A.V. Mironenko, A. Raizada, T. Chen, X. Mao, A. Padmanabhan, D.G. Vlachos, R.J. Gorte, J.M. Vohs, *ACS Catal.* 8 (2018) 7749–7759.
- [190] N. Kaylor, R.J. Davis, *Journal of Catalysis* 367 (2018) 181–193.
- [191] I. Agirrezabal-Telleria, E. Iglesia, *Journal of Catalysis* 352 (2017) 505–514.
- [192] G. Wang, B. Dou, Z. Zhang, J. Wang, H. Liu, Z. Hao, *Journal of Environmental Sciences* 30 (2015) 65–73.
- [193] W.G. Shim, J.W. Lee, H. Moon, *Separation Science and Technology* 38 (2003) 3905–3926.
- [194] Shin JW, Yoo KS, Park SY, Song KS, *J. Ind. Eng. Chem.* 12 (2006) 418–424.
- [195] S.H. Pang, J.W. Medlin, *J. Phys. Chem. Lett.* 6 (2015) 1348–1356.
- [196] S. Chen, R. Wojcieszak, F. Dumeignil, E. Marceau, S. Royer, *Chem. Rev.* 118 (2018) 11023–11117.
- [197] W. Zhou, N. Soutanidis, H. Xu, M.S. Wong, M. Neurock, C.J. Kiely, I.E. Wachs, *ACS Catalysis* 7 (2017) 2181–2198.
- [198] V. Lebarbier, G. Clet, M. Houalla, *The Journal of Physical Chemistry B* 110 (2006) 13905–13911.
- [199] E. Rossmedgaarden, W. Knowles, T. Kim, M. Wong, W. Zhou, C. Kiely, I. Wachs, *Journal of Catalysis* 256 (2008) 108–125.
- [200] F. Digregorio, *Journal of Catalysis* 225 (2004) 45–55.
- [201] E. Iglesia, D.G. Barton, S.L. Soled, S. Miseo, J.E. Baumgartner, W.E. Gates, G.A. Fuentes, G.D. Meitzner, in: *Studies in Surface Science and Catalysis*, Elsevier, 1996, pp. 533–542.
- [202] C.D. Baertsch, S.L. Soled, E. Iglesia, *The Journal of Physical Chemistry B* 105 (2001) 1320–1330.
- [203] J. Rorrer, Y. He, F.D. Toste, A.T. Bell, *Journal of Catalysis* 354 (2017) 13–23.
- [204] S. Jung, C. Lu, H. He, K. Ahn, R.J. Gorte, J.M. Vohs, *Journal of Power Sources* 154 (2006) 42–50.

- [205] D.G. Barton, S.L. Soled, G.D. Meitzner, G.A. Fuentes, E. Iglesia, *Journal of Catalysis* 181 (1999) 57–72.
- [206] M. Scheithauer, R. Jentoft, B. Gates, H. Knözinger, *Journal of Catalysis* 191 (2000) 271–274.
- [207] J. Malm, T. Sajavaara, M. Karppinen, *Chemical Vapor Deposition* 18 (2012) 245–248.
- [208] D.K. Nandi, S.K. Sarkar, *Energy Procedia* 54 (2014) 782–788.
- [209] O. Kresnawahjuesa, G.H. Kuhl, R.J. Gorte, C.A. Quierini, *Journal of Catalysis* 210 (2002) 106–115.
- [210] K. Chen, J. Damron, C. Pearson, D. Resasco, L. Zhang, J.L. White, *ACS Catalysis* 4 (2014) 3039–3044.
- [211] W.E. Farneth, D.C. Roe, T.G. Kofke, C.J. Tabak, R.J. Gorte, *Langmuir* 4 (1988) 152–158.
- [212] J. Yu, S. Zhu, P.J. Dauenhauer, H.J. Cho, W. Fan, R.J. Gorte, *Catal. Sci. Technol.* 6 (2016) 5729–5736.
- [213] E.I. Ross-Medgaarden, I.E. Wachs, *The Journal of Physical Chemistry C* 111 (2007) 15089–15099.
- [214] T.G. Kofke, R.J. Gorte, W.E. Farneth, *Journal of Catalysis* 114 (1988) 34–45.
- [215] Y.-H. Yeh, S. Zhu, P. Staiber, R.F. Lobo, R.J. Gorte, *Industrial & Engineering Chemistry Research* 55 (2016) 3930–3938.
- [216] M.-Y. He, J.G. Ekerdt, *Journal of Catalysis* 87 (1984) 238–254.
- [217] J. Luo, R. Gorte, *Catalysis Letters* 143 (2013) 313–316.
- [218] K.T. Wan, C.B. Khouw, M.E. Davis, *Journal of Catalysis* 158 (1996) 311–326.
- [219] M. Hino, K. Arata, *Journal of the Chemical Society, Chemical Communications* (1988) 1259–1260.
- [220] M. Occhiuzzi, D. Cordischi, D. Gazzoli, M. Valigi, P.C. Heydorn, *Applied Catalysis A: General* 269 (2004) 169–177.
- [221] S. Kuba, M. Che, R.K. Grasselli, H. Knözinger, *The Journal of Physical Chemistry B* 107 (2003) 3459–3463.
- [222] T.M. Onn, M. Monai, S. Dai, E. Fonda, T. Montini, X. Pan, G.W. Graham, P. Fornasiero, R.J. Gorte, *Journal of the American Chemical Society* (2018).
- [223] M.V. Juskelis, J.P. Slanga, T.G. Roberie, A.W. Peters, *Journal of Catalysis* 138 (1992) 391–394.
- [224] W.E. Farneth, R.J. Gorte, *Chemical Reviews* 95 (1995) 615–635.
- [225] E. Parry, *Journal of Catalysis* 2 (1963) 371–379.
- [226] O. Kresnawahjuesa, R.J. Gorte, D. De Oliveira, L. Lau, *Catalysis Letters* 82 (2002) 155–160.
- [227] X. Zhang, D. Liu, D. Xu, S. Asahina, K.A. Cychoz, K.V. Agrawal, Y. Al Wahedi, A. Bhan, S. Al Hashimi, O. Terasaki, *Science* 336 (2012) 1684–1687.
- [228] H.J. Cho, L. Ren, V. Vattipalli, Y. Yeh, N. Gould, B. Xu, R.J. Gorte, R. Lobo, P.J. Dauenhauer, M. Tsapatsis, *ChemCatChem* 9 (2017) 398–402.
- [229] P. Deshlahra, E. Iglesia, *ACS Catalysis* 6 (2016) 5386–5392.
- [230] S. Roy, G. Mpourmpakis, D.-Y. Hong, D.G. Vlachos, A. Bhan, R.J. Gorte, *ACS Catalysis* 2 (2012) 1846–1853.
- [231] W.E. Farneth, R.J. Gorte, *Chemical Reviews* 95 (1995) 615–635.
- [232] B. Boekfa, S. Choomwattana, P. Khongpracha, J. Limtrakul, *Langmuir* 25 (2009) 12990–12999.

- [233] K. Chen, A. Gumidyala, M. Abdolrhmani, C. Villines, S. Crossley, J.L. White, *Journal of Catalysis* 351 (2017) 130–135.
- [234] Y.-H. Yeh, R.J. Gorte, *Industrial & Engineering Chemistry Research* 55 (2016) 12795–12805.
- [235] Y. Zhang, J. Yu, Y.-H. Yeh, R.J. Gorte, S. Rangarajan, M. Mavrikakis, *The Journal of Physical Chemistry C* 119 (2015) 28970–28978.
- [236] O.A. Abdelrahman, D.S. Park, K.P. Vinter, C.S. Spanjers, L. Ren, H.J. Cho, K. Zhang, W. Fan, M. Tsapatsis, P.J. Dauenhauer, *ACS Catalysis* 7 (2017) 1428–1431.
- [237] O.A. Abdelrahman, D.S. Park, K.P. Vinter, C.S. Spanjers, L. Ren, H.J. Cho, D.G. Vlachos, W. Fan, M. Tsapatsis, P.J. Dauenhauer, *ACS Sustainable Chemistry & Engineering* 5 (2017) 3732–3736.
- [238] Y.-H. Yeh, R.J. Gorte, S. Rangarajan, M. Mavrikakis, *The Journal of Physical Chemistry C* 120 (2016) 12132–12138.
- [239] C. Wang, X. Mao, J. Lee, T. Onn, Y.-H. Yeh, C. Murray, R. Gorte, *Catalysts* 8 (2018) 292.
- [240] M. Frisch, G. Trucks, H. Schlegel, G. Scuseria, M. Robb, J. Cheeseman, G. Scalmani, V. Barone, B. Mennucci, G. Petersson, Inc, Wallingford CT Google Scholar (2013).
- [241] A.N. Migués, A. Muskat, S.M. Auerbach, W. Sherman, S. Vaitheeswaran, *ACS Catalysis* 5 (2015) 2859–2865.
- [242] W.R. Wadt, P.J. Hay, *The Journal of Chemical Physics* 82 (1985) 284–298.
- [243] Y. Zhao, D.G. Truhlar, *Theoretical Chemistry Accounts* 120 (2008) 215–241.
- [244] K. Fukui, in: *Frontier Orbitals And Reaction Paths: Selected Papers of Kenichi Fukui*, World Scientific, 1997, pp. 471–476.
- [245] D.J. Parrillo, C. Lee, R.J. Gorte, D. White, W.E. Farneth, *The Journal of Physical Chemistry* 99 (1995) 8745–8749.
- [246] J.A. Ryder, A.K. Chakraborty, A.T. Bell, *The Journal of Physical Chemistry B* 104 (2000) 6998–7011.
- [247] W. Haag, in: *Studies in Surface Science and Catalysis*, Elsevier, 1994, pp. 1375–1394.
- [248] D. Olson, W. Haag, R. Lago, *Journal of Catalysis* 61 (1980) 390–396.